Physik-Department
Technische Universität München

Particle Detection and Proton Asymmetry in Neutron Beta Decay

Christoph Marcus Roick

Vollständiger Abdruck der von der Fakultät für Physik der Technischen Universität München zur Erlangung des akademischen Grades eines

Doktors der Naturwissenschaften (Dr. rer. nat.)

genehmigten Dissertation.

Vorsitzender:
Prof. Dr. Norbert Kaiser

Prüfende der Dissertation:
1. Prof. Dr. Bastian Märkisch
2. Prof. Dr. Stefan Schönert

Die Dissertation wurde am 14.08.2018 bei der Technischen Universität München eingereicht und durch die Fakultät für Physik am 27.09.2018 angenommen.

Abstract

Experimental studies of the nature of the neutron beta decay are a powerful tool to test the current Standard Model of particle physics. Correlations between particles involved in the decay are used to characterize the weak interaction and to search for so far undiscovered couplings between nuclei and leptons.
In this work, a comprehensive study of electron detection with plastic scintillators is presented, which aims to address all important contributions towards the determination of the electron asymmetry and a clean description of the measured electron spectrum with the instruments PERKEO III and PERC. Important steps are a refined description of calibration sources, a supplementary method for detector calibration using time of flight, a method to convolute the spread of electron sources with a spatially dependent detector function and an almost complete trigger function which is used to determine an important systematic correction of the electron asymmetry measurement. The new measurement improves the relative precision of the ratio between axial-vector and vector coupling to $4.4 \cdot 10^{-4}$, four times more precise than the current world average.
In the second part, the finalized data analysis of a new measurement of the proton asymmetry with PERKEO III is provided. The proton asymmetry is sensitive to hypothetical right-handed currents and scalar and tensor couplings. Analyses of systematic effects provide the basis for a $\sim 10^{-3}$ measurement with the upcoming instrument PERC. A model for a formerly neglected influence of an energy dependent trigger efficiency in the proton detection is deduced. The only published measurement, taken with PERKEO II, will be improved.

Zusammenfassung

Ein wichtiger Bestandteil verschiedener Tests zur Überprüfung des Standardmodells der Teilchenphysik sind experimentelle Untersuchungen des Neutronenbetazerfalls. Verschiedene Korrelationskoeffizienten die diesen Zerfall beschreiben, ermöglichen eine Charakterisierung der schwachen Wechselwirkung und darüber hinaus die Suche nach bisher unentdeckten Kopplungen zwischen Kernen und Leptonen.
In dieser Arbeit wird eingehend die Elektronendetektion mit Plastikszintillatoren untersucht, wobei versucht wird, auf alle wichtigen Bestandteile zur Bestimmung der Elektronenasymmetrie mit dem Instrument PERKEO III einzugehen. Dies beinhaltet eine umfassende Beschreibung des gemessenen Betaspektrums.
Die wichtigsten Schritte hierfür sind eine verbesserte Beschreibung von Kalibrationsquellen, die Beschreibung einer neuen Methode zur Detektoreichung mittels Flugzeitmessung, eine Methode zur Faltung von räumlichen Elektronenverteilungen mit ortsabhängigen Detektorfunktionen und letztlich eine deutlich verfeinerte Beschreibung der Detektortriggerfunktion, welche verwendet wird, um eine wichtige systematische Korrektur für die Messung der Elektronenasymmetrie zu bestimmen. Diese neue Messung ermöglicht eine verbesserte Bestimmung des Verhältnisses zwischen Axialvektor- und Vektorkopplung mit einer relativen Präzision von $4.4 \cdot 10^{-4}$, was die Präzision des aktuellen Weltmittelwerts um einen Faktor vier verbessert.
Der zweite Teil schließt die Datenanalyse einer neuen Messung der Protonenasymmetrie mit PERKEO III ab. Die Protonenasymmetrie ist sensitiv auf hypothetische rechtshändige Ströme und Skalar- und Tensorkopplungen. Die systematischen Analysen dieser Arbeit schaffen die Grundlage für eine $\sim 10^{-3}$-Messung mit dem neuen Instrument PERC. Unter anderem wird eine Korrektur für die bisher vernachlässigte Abhängigkeit der Detektionseffizienz von der Protonenenergie abgeleitet. Die neue Messung wird das bisher einzige Resultat, welches mit PERKEO II erreicht wurde, verbessern.

Contents

1 Neutron Beta Decay

Beta decay has been discovered more than 100 years ago and its nature been explained by a beforehand unexpected uncharged particle, the neutrino. Even 80 years after the first theoretical description by Wolfgang Pauli and Enrico Fermi [Fer34], beta decay is subject to investigation, even though facilities like the LHC provide access to more exotic new particles than electron and proton emerging from neutron decay. But instead of directly searching for new particles, unknown processes may also be discovered by precisely measuring assumedly known quantities.

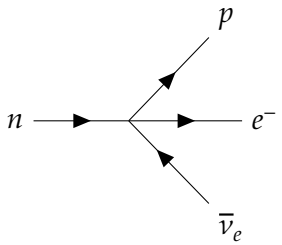

(1.1)

In the Standard Model of particle physics, beta decay (1.1) as an example for the weak interaction is regarded as a process of vector and axial-vector coupling [FG58; SM58]. That means, the interaction between mother nucleus and decay products is mediated by a massive charged particle. This point of view is based on experimental observations. Despite having small influence, additional components of scalar and tensor coupling might still be present, i.e. by a not yet discovered particle or coupling. A general phenomenological description of beta decay is provided by the differential decay width [JTW57]:

$$\begin{aligned} \mathrm{d}\,\Gamma = & \frac{{G_\mathrm{F}}^2\,|V_{ud}|^2}{(2\pi)^5} E_\nu E \sqrt{E^2 - m_e^2}\,\mathrm{F}\,(E)\,|M_\mathrm{fi}|^2\,\mathrm{d}\,\Omega_e\,\mathrm{d}\,\Omega_\nu \\ & \times \left[1 + a\frac{\vec{p}_e \cdot \vec{p}_\nu}{E_e E_\nu} + b\frac{m_e}{E_e} + \langle \vec{\sigma}_n \rangle \cdot \left(A\frac{\vec{p}_e}{E_e} + B\frac{\vec{p}_\nu}{E_\nu} + D\frac{\vec{p}_e \times \vec{p}_\nu}{E_e E_\nu} \right) \right]. \end{aligned} \tag{1.2}$$

It lists all possible quantities accessible by experiments. The instrument covered in this work is the spectrometer PERKEO III which investigates the neutron decay in particular. It provides access to the correlation parameters A, B, C and scalar and tensor interactions which are condensed in the Fierz term parameter b [Fie37]. C does not appear here, but will attain attention later on.

Experiments of the PERKEO-series are most known for the measurement of the so-called electron asymmetry parameter A. It is entirely determined by the relation between electron momentum and neutron spin $\vec{\sigma}_n$. The quantity which is actually measured is the experi-

mental electron asymmetry:

$$A_{\text{exp}} = \frac{\int_0^1 \mathrm{d}(\cos\theta)[(1 + b\frac{m_e}{E_e} + \beta_e AP\cos\theta) - (1 + b\frac{m_e}{E_e} - \beta_e AP\cos\theta)]}{\int_0^1 \mathrm{d}(\cos\theta)[(1 + b\frac{m_e}{E_e} + \beta_e AP\cos\theta) + (1 + b\frac{m_e}{E_e} - \beta_e AP\cos\theta)]} \tag{1.3}$$

$$= \frac{N^{\uparrow}(E_e) - N^{\downarrow}(E_e)}{N^{\uparrow}(E_e) + N^{\downarrow}(E_e)} = \frac{1}{2}\frac{\beta_e AP}{1 + b\frac{m_e}{E_e}}. \tag{1.4}$$

In this formulation $N^{\uparrow}(E_e)$ denotes the number of electrons of an energy E_e emitted in neutron spin direction and is compared to the number of electrons emitted against neutron spin direction $N^{\downarrow}(E_e)$. θ is the angle of the electron momentum to the neutron polarization. P is called the neutron polarization and expresses the ratio of neutrons with spin oriented in one or the other direction. Many details on the measurement of A with Perkeo III are covered in chapter 2. The current most precise value was determined with Perkeo II by [Mun+13] to

$$A_{\text{Mund et al.}} = -0.11972(^{+53}_{-65}). \tag{1.5}$$

A recent result by the UCNA collaboration where ultra cold neutrons are used is [Bro+18]

$$A_{\text{Brown et al.}} = -0.12015(72). \tag{1.6}$$

The new result with Perkeo III improves the relative precision of this quantity to $17.4 \cdot 10^{-4}$.

An experiment which detects electrons to determine A is entirely conceivable. A setup to directly measure the relation between neutrino momentum and neutron spin – the neutrino asymmetry parameter B – is more difficult to imagine. The direct detection of neutrinos and assignment to a decay within the experiment is simply not possible for the required number of events. Instead of pursuing neutrino counting, the proton as last participant in the decay comes at help. By detecting proton and electron in coincidence, energy and momentum conservation allows to infer on the movement of the related neutrino. B is currently the most precise relative measurement, performed with Perkeo II as well [Sch+07]:

$$B_{\text{Schumann et al.}} = 0.9802(50). \tag{1.7}$$

A precise value for the proton asymmetry parameter C has been determined in the same measurement [Sch+08], identically by considering coincident events. C is special in a sense that it does not appear in equation (1.2) and therefore has no unique definition. Commonly the average asymmetry (1.11) over the entire proton energy range is provided:

$$C_{\text{Schumann et al.}} = -0.2377(26). \tag{1.8}$$

The determination of C with Perkeo III is described in chapter 3. The data may also be used to extract a new value for the neutrino asymmetry B. This subject will not be covered in this work though.

1.1 Axialvector and Vector Coupling

In the following the relation of fundamental interactions to these parameters is discussed and why properties of decay products would depend on the neutron spin at all.

The key is the coupling of the so-called W-boson only to left-handed particles and right-handed antiparticles. The W-boson enables the beta decay, since it is the only particle

in the Standard Model which allows to change quark flavors and therefore makes the transformation of neutrons into protons possible. It refines the decay (1.1) to

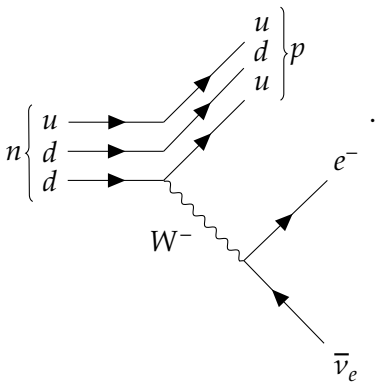

(1.9)

This follows from the most general Hamiltonian [LY56]

$$H_{\text{int}} = \frac{G_F V_{ud}}{\sqrt{2}} \Big([\overline{u}_p \gamma_\mu u_n][\overline{u}_e \gamma^\mu (C_V + \overline{C}_V \gamma_5) u_\nu] + [\overline{u}_p \gamma_\mu \gamma_5 u_n][\overline{u}_e \gamma^\mu \gamma_5 (C_A + \overline{C}_A \gamma_5) u_\nu] + [\overline{u}_p u_n][\overline{u}_e (C_S + \overline{C}_S \gamma_5) u_\nu] + \frac{1}{2}[\overline{u}_p \sigma_{\mu\nu} u_n][\overline{u}_e \sigma^{\mu\nu} (C_T + \overline{C}_T \gamma_5) u_\nu] \Big) + h.c., \tag{1.10}$$

where in the Standard Model $C_S = \overline{C}_S = C_T = \overline{C_T} = 0$, $C_V = -\overline{C}_V = 1$ and $C_A = -\overline{C}_A = -\lambda$. For purely leptonic decays the ratio between axial-vector and vector coupling $\lambda = -1$. For the conversion from neutron to proton, QCD renormalization leads to an effective axial-vector coupling different from unity, however.

In the Standard Model, the correlation coefficients A, B and C may be expressed by λ [Abe00] using

$$A = -2\frac{\lambda(1+\lambda)}{1+3\lambda^2}, \quad B = -2\frac{\lambda(1-\lambda)}{1+3\lambda^2}, \quad C = -x_C(A+B) = x_C \frac{4\lambda}{1+3\lambda^2}, \tag{1.11}$$

where λ is considered to be purely real and radiative and recoil corrections are neglected. x_C is a kinematic factor which follows from energy and momentum conservation and will be explained in more detail in chapter 3. These expressions allow a direct measurement of the ratio between axial-vector and vector coupling. The current most precise value is deduced in [Mun+13]:

$$\lambda_{\text{Mund et al.}} = -1.2761(^{+14}_{-17}) \tag{1.12}$$

In practice, all measurements of the angular correlation coefficients are measurements of λ. The electron asymmetry measurement with Perkeo III improves this precision by a factor of 2.5.

Calculations using Lattice QCD which model the complex processes which lead to the effective ratio of coupling constants are constantly approaching experimental uncertainties. A recent publication [Cha+18] obtains

$$\lambda_{\text{LQCD}} = -1.2711(103)_{\text{stat}}(70)_{\text{sys}}, \tag{1.13}$$

which hints to the possibility of actually comparing experimental and theoretical results not too far in the future.

As previously noted, beta decay is not restricted to vector and axial-vector coupling per se. Next to the decay of ^{6}He, neutron decay is a very suitable tool for searches of scalar and

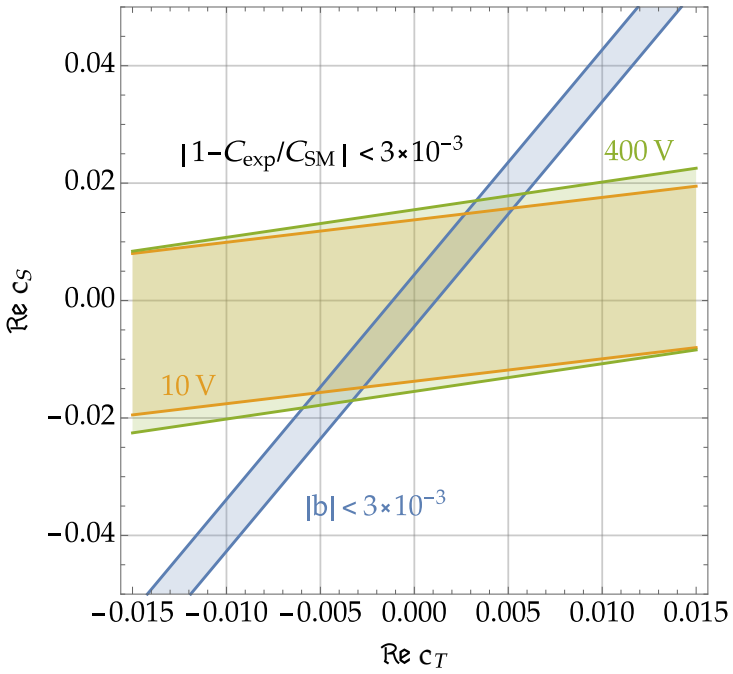

Figure 1.1: Measurements of λ are most precise using the electron asymmetry. With that parameter fixed, the Fierz term b from the electron spectrum and changes in the proton asymmetry parameter C may disentangle scalar and tensor couplings exclusively from neutron decay measurements.

tensor couplings g_S and g_T [GN16]. Interactions of this kind would appear as an additional term $b\frac{m_e}{E_e}$ in the phase space factor (1.2), which is zero within the Standard Model.

The effective coupling $b = \frac{4}{1+3\lambda^2}(g_S + 3\lambda g_T)$ enters differently in all measurable spectra. For example the neutrino asymmetry is only sensitive to a correction $1 - \frac{(1+\lambda)(1-3\lambda)}{2\lambda(1-\lambda)} c_{ST} \frac{m_e}{E_e}$, where $c_{ST} = \frac{4}{1+3\lambda^2}(\lambda g_S - g_T)$ [IPT13] is introduced as an additional observable for convenience. Combined analyses of different experiments which measure b and c_{ST} allow the decorrelation of scalar and tensor couplings. One set of such measurements is the determination of the electron asymmetry combined with a new measurement of the proton asymmetry with Perkeo III. Figure 1.1 shows the sensitivity to both couplings. Although these measurements are mostly independent, a few correlated systematic effects remain and must be taken into account. It is the task of the experimentalists to evaluate these effects to enable the deduction of combined limits to scalar and tensor couplings.

1.2 Perkeo III

The instrument Perkeo III [Mär+09; Mär06] is the successor of Perkeo II [Abe+97], which again is the successor of Perkeo [Bop+88]. All of these instruments are designed to allow 4π-detection-coverage for charged decay particles from a cold neutron beam. *Cold* refers to the low temperature of neutrons, which have a wavelength of $\approx 5\,\text{Å}$ or a velocity of $\approx 800\,\text{m/s}$. This corresponds to $40\,\text{K}$ or a mean energy of $3\,\text{meV/c}^2$. The key idea of the setup is to let the neutrons decay in the same homogeneous magnetic field which also defines their spin direction. This way, electrons and protons from the neutron decay may either be emitted and transported into the half-sphere against neutron spin direction, or

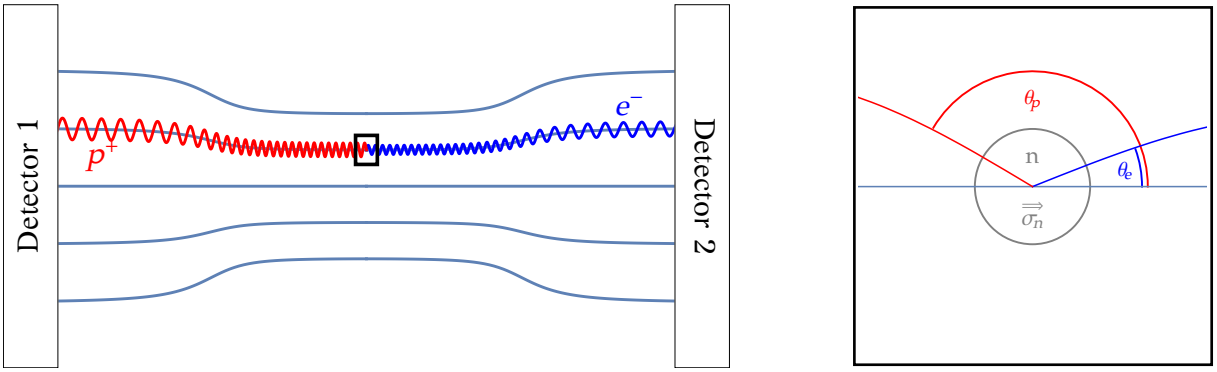

Figure 1.2: A sketch of the Perkeo principle depicts two detectors which are connected by a magnetic field. In the center, the magnetic field density has its maximum and defines the neutron spin direction. A zoom to a neutron decay shows the definition of the polar angle between proton or electron momentum and the neutron spin.

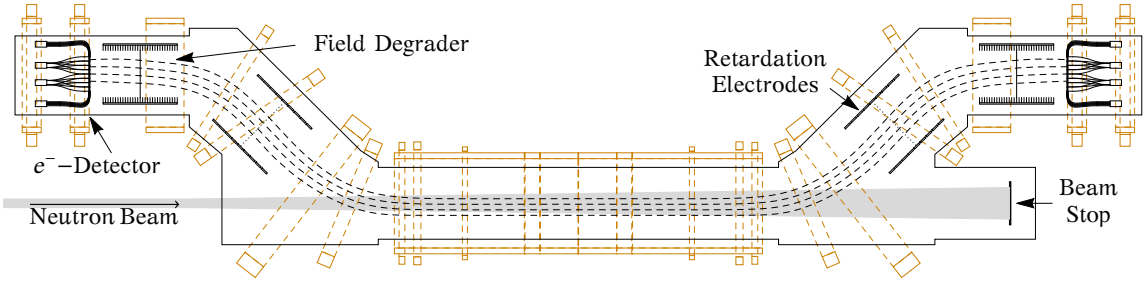

Figure 1.3: A sketch of the experiment Perkeo III shows the substantial components required for the measurement of the proton asymmetry parameter C. Retardation electrodes for proton blocking and proton-to-electron conversion devices, referred to as Field Degraders, are not required for a measurement of the electron asymmetry parameter A and were not present in the measurement of 2009. A more detailed view onto one of the detector sections can be found in Figure 3.1b.

the opposite, depending on their direction of emission. The sign of $\vec{\sigma}_n \cdot \vec{p}_e$ and $\vec{\sigma}_n \cdot \vec{p}_p$ from the decay width (1.2) with $\vec{p}_p = -(\vec{p}_e + \vec{p}_\nu)$ can finally be measured by counting particles with detectors placed inside the magnetic field which is connected to the decay volume. Figure 1.2 illustrates the basic idea.

For Perkeo II the neutron beam is traveling perpendicular to the magnetic field lines. This allows a simple magnetic field setup with direct sight of the detectors onto the neutron beam. In Perkeo III on the other hand, neutrons are traveling in longitudinal field direction. This setup has the advantage of a larger decay volume at similar detector size. While for Perkeo II the detector size is linearly increasing with the decay volume, Figure 1.3 illustrates that in Perkeo III only the beam divergence is a limiting factor.

For a continuous neutron beam of $2 \cdot 10^{10}\mathrm{cm}^{-2}\mathrm{s}^{-1}$ capture flux density, such as the one provided by PF1B at the Institut Laue-Langevin (ILL) [Abe+06] in Grenoble, a decay rate of $5 \cdot 10^4\mathrm{s}^{-1}$ [Mär+09] can be reached. In the same mode, with Perkeo II only $400\,\mathrm{s}^{-1}$ may be observed [Mun06]. The advantage of a much higher decay rate comes at the price of a more complicated field design. In order to not let neutrons pass the particle detectors, the magnetic field must separate neutron beam and charged particles. The influence of that feature on drifts of charged particles is treated in section 3.2.2.

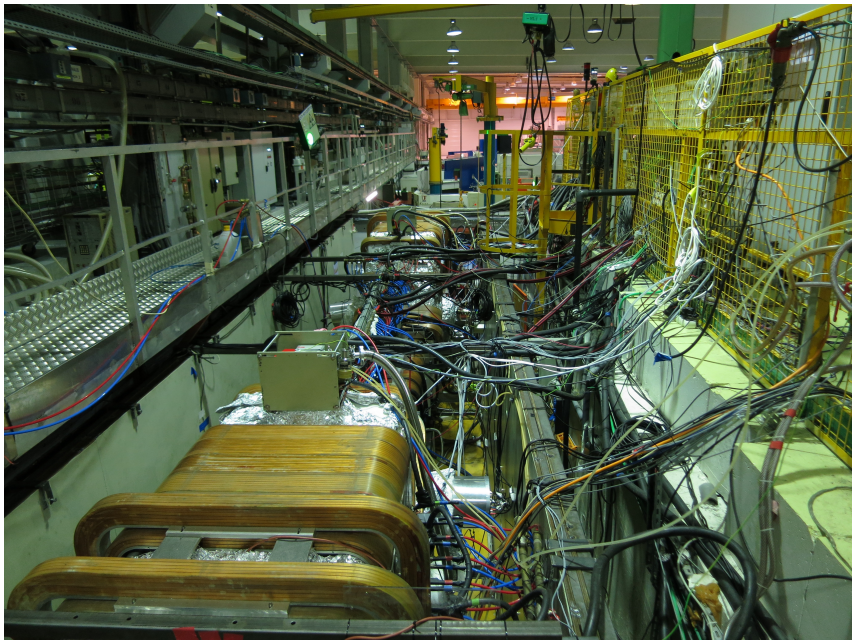

Figure 1.4: PERKEO III set up at cold neutron beam PF1B at the ILL in Grenoble for the measurement of the proton asymmetry parameter C. The detector vessel in the front pointing towards the city center of Grenoble hides the central part of the magnet system where the neutrons decay. The rear part is referred to as the Lyon detector vessel and is located in the downstream direction of the neutron beam. The experimental zone is not accessible when the neutron beam shutter is opened. Blue and red hoses are feed and return lines for the cooling water, which keeps the conventional magnets below 60 °C despite the 300 kW of energy consumption.

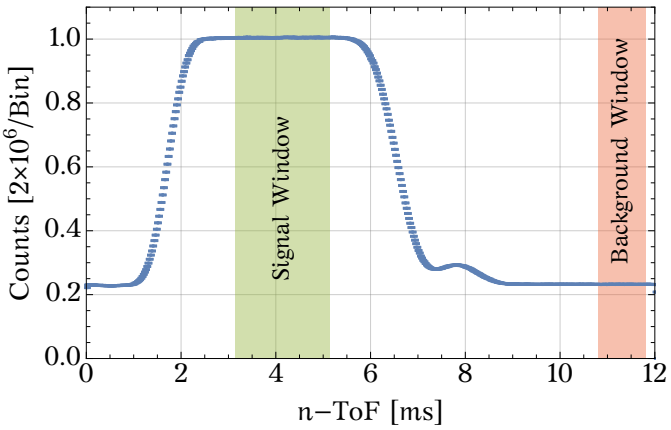

Figure 1.5: Detector counts depending on the neutron flight time. By using a chopper the neutron beam can be chopped into pulses. These pulses define a signal time window where neutron decay takes place and a background time window where the background spectra can be measured. This allows an immediate subtraction of background and yields clean signal spectra even for quickly varying background levels.

The high instantaneous decay rate of Perkeo III allows the use of a pulsed beam. Instead of having a continuous beam of neutrons, only pulses are permitted to enter the decay volume. Figure 1.5 shows how this enables a clean separation of signal events from background events.

Previously background was measured by stopping the beam before the decay volume by using a shutter. This changes the nature of the background spectrum since it misses background contributions from the beam stop and introduces the shutter as additional source of background signals on the other hand. The background contribution may therefore only be determined with a relatively large uncertainty, see Table 1.1 for reference. For a chopped measurement, the timing may be chosen such that environmental properties remain the same for signal and background measurement: The chopper is closed and no neutrons hit the beam stop.

Two beam times were conducted using Perkeo III to measure the electron asymmetry A_{exp}. Experiences from the first run which was performed with a continuous beam, lead to a second run using a pulsed beam and resulted in the so far largest concise data set for the determination of the electron asymmetry parameter [Mes11; Sau18]. In this work this will be referred to as Perkeo III 2009 and significant parts of the analysis are treated in chapter 2. It focuses on the steps which reduce the uncertainty due to the electron detector description. Contributions due to this work are marked in bold in Table 1.1. An impression of the completed experimental setup for the third run, where the proton asymmetry C was measured, is captured in Figure 1.4.

1.2.1 Beamline

Before neutrons enter Perkeo III, the neutron beam has to be prepared. First of all, neutrons have to be released. In the case of the Perkeo measurements, this is done inside the research reactor of the ILL. The use of heavy water only moderates neutrons and allows thermalization without complete neutron absorption, which occurs in light water reactors. The released power of 58.3 MW in normal operation [Ins17] is not further used and dissipates into the neighbouring river Drac by a cooling system. Neutrons are moderated to cold

Type of Uncertainty	Relative Uncertainty (10^{-3}) PERKEO II	PERKEO III
Neutron Polarization Spin Flip Efficiency	1.4	0.64
Magnetic Mirror Effect	0.2	0.45
Background	1.0	0.11
Edge Effect	0.5	
Detector Uniformity	2.5	0.21
Detector Drift		0.37
Detector Nonlinearity		0.4
Calibration Source Description		0.1
Electron Backscattering (detectors)	0.04	0.21
Electron Backscattering (baffles)	+0.6, −0.0	
Dead Time	0.1	0.035
Radiative Correction	0.5	0.1
Total Systematic Uncertainty	+3.6, −2.7	1.02
Statistical Uncertainty	3.8	1.4
Total	+5.4, −4.4	1.73

Table 1.1: A comparison of uncertainties of the electron asymmetry measurements shows the main improvements going from PERKEO II to PERKEO III. In this work and [Sau18] the major uncertainties of the detector response could be reduced by a factor of four. Improvements of the background handling are mainly due to using a chopped neutron beam with PERKEO III.

neutrons by letting them pass through a vessel of liquid deuterium. Most of their energy is transferred to the deuterium and the neutrons remain with a kinetic energy of roughly 3 meV. To be able to transport neutrons from the reactor to the experimental sites, neutron guides are used. The neutron optical potential of most materials is repulsive and enables the use of supermirrors to guide the neutrons over long sections. Consequently, the beam site PF1B can be situated 72 m away from the reactor and still provide the worlds strongest cold neutron beam for particle physics [Abe+06].

Polarization of the neutrons, i.e. selecting a preferred neutron spin direction relative to a guiding magnetic field, may be achieved by several ways. Common to all methods is that there is no way to rearrange spins of an unpolarized beam, such that all spins finally point in the same direction. Instead, the goal is reached by filtering out the unwanted spin direction. This is done using cells of polarized ^{3}He, supermirror polarizers or a more recent development, crystalline supermirror polarizers [Pet+16]. ^{3}He-cells provide good transmission for the requested spin direction, but do not keep their internal polarization over a longer period of time. Therefore, they are commonly not used for longer measurements, but allow a precise characterization of the polarization of a beam [Kla+13]. For PERKEO III measurements, a supermirror polarizer is used. By using Co as one of the reflecting materials, polarization is achieved by exploiting different repelling potentials for different neutron spin directions. The obtained polarization is on the order of 95 to 99 %, but comes at the price of a flux loss of roughly 80 %. Since neutron mirrors and especially polarizer mirrors are subject to aging, the first stage after the neutron guide from the reactor is wavelength selection though: A boron coated turbine spins at a fixed speed and allows passage only for neutrons with a small velocity range. Combining the transmission function with the spectrum of the cold source, the outgoing wavelength spectrum is approximately triangu-

larly shaped with a width of 10 %. All neutrons of the wrong velocity are captured in the boron coating and may therefore not degenerate the polarizer. Once neutrons are polarized, it is rather easy to switch their spin direction using a so-called adiabatic fast passage spin flipper. This spin flipper exploits the motion of the neutron and generates a rotating magnetic field in the rest frame of the neutron. This kind of flipper commonly has an efficiency of 1, which also means, that any degree of polarization is conserved and allows to create a mirrored experimental setup from the viewpoint of the neutron. That fact is important: Although PERKEO III provides an overall symmetric setup, it is not possible to produce two exactly equivalent detectors, create an exactly symmetric magnetic field or avoid any divergence of the neutron beam inside the instrument. Instead, the spin flip makes it possible to perform two experiments at the same time and only exploit the symmetry of the setup to suppress systematic effects, such as electron backscattering.

Inside PERKEO III there are no neutron guides which could keep the neutrons on track. Any transversal velocity component leads to a spread of the beam up to a point where it does not make sense to further increase the length of the decay volume. Five ^{6}LiF-apertures in the last section of the beamline trim the neutron beam to a cross section of $6\times6\,\mathrm{cm}^2$ with a divergence of $\approx 1.5\,\mathrm{cm/m}$, making it possible to have reasonably sized detectors which may capture all decay particles.

The end of the beamline is marked by the disk-chopper [Wer09]. ^{6}LiF-tiles are turning at a speed of up to 100 Hz and allow the neutrons to pass through an opening of 22.2°. The chopper position defines signal and background time windows.

1.2.2 Calibration Source Scanner

In order to measure electron spectra, reference sources must be used to calibrate the electron detectors. These sources are used to determine a relation between electron energy and detector signal. Since the energy of the emitted electrons does not depend on environmental parameters, they are also used to monitor drifts of the detector response frequently. It is not possible to manually install or remove calibration sources during the measurements. Instead, the sources have to be moved automatically inside the vacuum. This is especially delicate since the calibration sources are located on very thin and fragile carbon foils to minimize energy losses.

The device in Figure 1.6 which fulfills these requirements is called scanner and allows the positioning of five individual calibration sources within a wide range of coordinates. This furthermore enables a characterization of the detector response depending on the position on the detector.

1.2.3 Electron Detectors

Electrons are detected using plastic scintillators in combination with photomultiplier tubes (PMTs). Their main advantages are a small response time and a low electron backscattering probability, which reduces a major systematic effect. Although the relative energy resolution is small compared to semiconductor detectors, plastic scintillators have the advantage of being relatively cheap and are reasonably well understood – in spite of the studies in section 2.3.3. Figure 1.7a and Figure 1.7b show two designs of PERKEO III detectors which have in common that light is read out from the sides.

Most of the effects which are discussed in the following chapter are related to detection with plastic scintillators. The detection of protons is described in chapter 3.

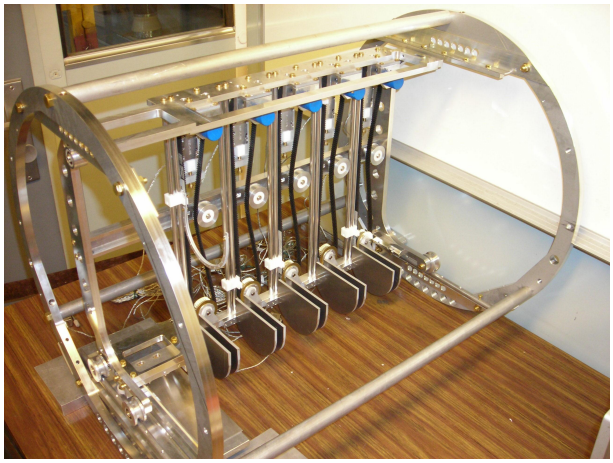

Figure 1.6: The scanner device which is used to position calibration sources in front of the electron detectors [Wil07]. In horizontal direction, the whole sled is moving, while vertically the sources can be moved away from their shields individually. Meanwhile, the rubber belts have been replaced by steel wires to improve vacuum compatibility and reduce friction.

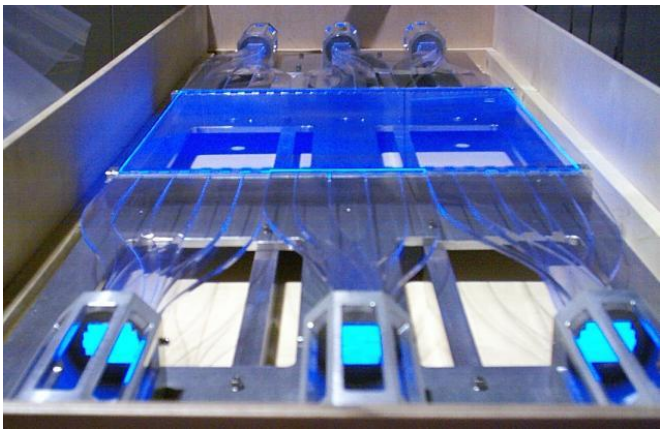

(a) For the beam time of 2009, a large scintillator of 43 cm × 45 cm × 5 mm was used and allowed electron detection without edge effect [Mes11]. The large size required installation of the detector before PERKEO III could actually be set in place at PF1B.

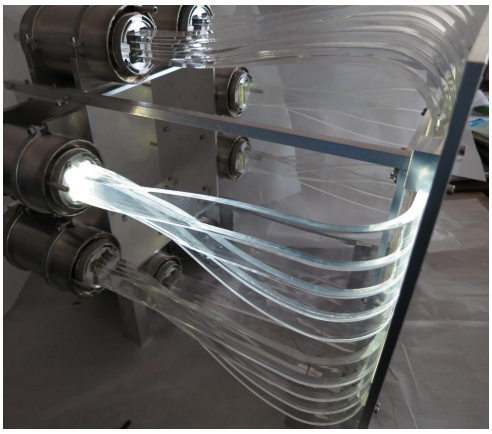

(b) A smaller detector designed by Lukas Raffelt was used for the beam time of 2014. It has the advantage of being installed from the back of PERKEO III [Raf15].

Figure 1.7: In PERKEO III, electrons are detected with plastic scintillators. They provide a large detection area and can be read out with little effort using photomultipliers.

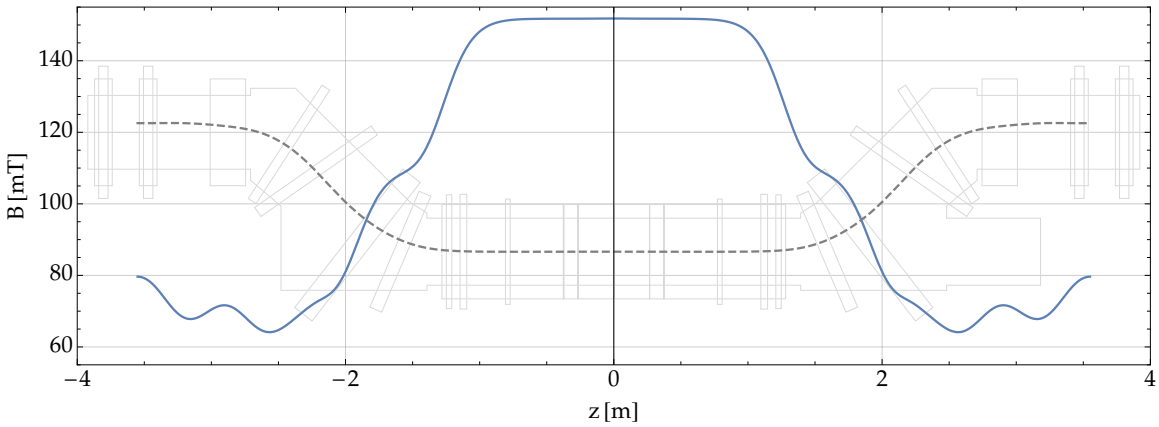

Figure 1.8: The absolute magnetic field density in Perkeo III is largest in the central volume and decreases when following the charged particles along the dashed line towards the detector vessels. There are no field minima in the decay volume to have a well defined angular coverage of the particle detectors.

1.2.4 Guidance of Charged Particles

The guidance of decay particles to the detectors is crucial for the Perkeo experiments. It must be treated accurately to reduce uncertainties which are related to the solid angle coverage of the detectors.

An important property of the employed magnetic fields is that they allow adiabatic transport of neutron spins and electrons and protons. *Adiabatic* means, that locally the magnetic field can always be considered homogeneous, which leads to radial movement of protons and electrons around the field lines with a radius of gyration

$$r = \frac{p}{eB} \sin\theta. \tag{1.14}$$

For momenta p of up to 1.2 MeV/c, in the central magnetic field of 152 mT, $r < 2.6$ cm. Naturally, the radius decreases if the particle momentum is more parallel to the magnetic field lines: $\theta \to 0$.

If $\theta = 0$ is defined as particles moving in the direction of the neutron beam – downstream – then the angular range covered by the downstream *Lyon* detector is defined for $\theta \in (0, \pi/2)$ and the range covered by the upstream *Grenoble* detector by $\theta \in (\pi/2, \pi)$. This only holds for a magnetic field which is completely homogeneous in the neutron decay region. Practically the field has the highest density in the center of the central volume and slightly decreases towards the outer region. This has an implication on the accepted angular ranges of the decay particles by the individual detectors: The magnetic flux which is enclosed by a gyrating particle is an adiabatic invariant, i.e.

$$\begin{aligned} &\pi r_1^2 \cdot B_1 = \pi r_2^2 \cdot B_2, \quad \text{for slowly changing } B \\ \Leftrightarrow\ &\frac{p^2}{e^2 B_1} \sin^2\theta_1 = \frac{p^2}{e^2 B_2} \sin^2\theta_2 \\ \Rightarrow\ &\sin\theta_2 = \sqrt{\frac{B_2}{B_1}} \sin\theta_1. \end{aligned} \tag{1.15}$$

On one hand this implies a decreasing polar angle $\theta_1 \to \theta_2$ for $B_2 < B_1$, which makes particles advance faster along the magnetic field such as in Figure 1.8 for $|z| > 1$ m. On the

other hand there may also be a point of $\sin\theta = 1$, if the magnetic field is increasing in the longitudinal direction of motion. At this point, the particle turns around and continues in the opposite direction. This is called the magnetic mirror effect and leads to a change of integration region for the angular coverage of the detectors and implies an important correction to the measured asymmetry. For the electron asymmetry measurement this effect is summarized in [Wan13] and will be investigated in [Klo18] for the proton asymmetry measurement.

For the protons, which have small kinetic energies $< 1\,\mathrm{keV}$, also electrostatic fields are involved which in contrast to magnetic fields may change the kinetic energy of charged particles. For electric fields parallel to the magnetic guiding field, the longitudinal component of the momentum increases or decreases depending on the charge of the particle q and the electric potential. While the transversal momentum remains the same, the overall momentum decreases, which again changes the polar angle:

$$\sin\theta_1 = \frac{p_1 \sin\theta_1}{p_1} \rightarrow \frac{p_1 \sin\theta_1}{p_2} = \frac{p_2 \sin\theta_2}{p_2} = \sin\theta_2. \tag{1.16}$$

In the nonrelativistic limit the change of the polar angle can be simply expressed by

$$\sin\theta_2 = \sqrt{\frac{E_{\mathrm{kin},1} + q(U_2 - U_1)}{E_{\mathrm{kin},1}}}\,\sin\theta_1. \tag{1.17}$$

Again, there may be a point where $\sin\theta = 1$ and the particle turns around. This is used in section 3.2 to build up an electrostatic barrier for protons below a certain kinetic energy.

1.3 PERC

Experiments described in this work, namely the measurement of the electron and proton asymmetry of the neutron beta decay, will be enhanced with the upcoming instrument PERC (proton-electron-radiation-channel). It will break with the tradition of symmetric setups and provide a port for decay electrons and protons only on one end. It is intended as a user facility and provides the opportunity to measure with secondary spectrometers other than those of the Perkeo-collaboration. The main improvement over previous experiments is an eight-meter-long non-depolarizing neutron guide inside an equally long superconducting solenoid. The use of a neutron guide to limit the decay section solves the problems with diverging beams and therefore allows much longer neutron pulses and higher average decay rates. PERC is going to be set up at the new beam site MEPHISTO, at the Forschungsreaktor München (FRM II), where a similar cold neutron flux is expected, compared to PF1B. Especially the studies of the proton asymmetry measurement should be regarded as preparatory work for measurements with PERC, which provides a cleaner environment with neutron decay region and particle detection being separated more strictly. Figure 1.9 shows a schematic setup of PERC.

Figure 1.9: The superconducting magnet system of PERC defines an eight meter long decay region. Decay particles whose momentum polar angle is above a certain threshold may be filtered by a 3 to 6 T selector magnet. Neutron beam divergence is addressed by using a non-depolarizing neutron guide within the decay region. User experiments can be attached to the right end of the instrument.

2 Electron Detection and Electron Asymmetry A

A major task of an experiment with the goal to measure the spectrum of a particle decay is to understand and model the processes from the source to the detector. In the case of beta decay measurements, this includes the understanding of the theoretical decay spectrum at the source, the transport of the decay particles to the detector and the detection process. For scintillation detection, the conversion of kinetic particle energy into light and after the light transport, the conversion of light back to electrons to a measured pulse amplitude must be understood.

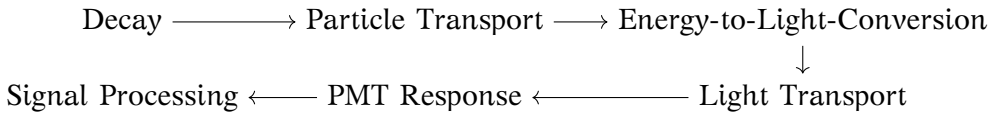

Although some of these processes cannot easily be separated into independent parts, the above diagram shows the outline of this chapter. Corrections to the electron asymmetry measurement will be deduced as a result of the studied effects. Some results presented here are not explicitly applied in this work, but find their use in [Sau18].

2.1 Electron Spectra

Within this section a refined theoretical description of beta decay electron sources, as well as electron capture sources will be presented. Parts of this section are a further evolution of [Roi10], with the goal of employing all information available. It finally allows to determine the electron detector response function independently of the neutron beta decay spectrum, which was previously not possible. The major systematic effect of the measurement with PERKEO II can be reduced by a factor of four, see Table 1.1. The theoretical description of the calibration sources finally only has a relative uncertainty of 10^{-4} on the electron asymmetry.

2.1.1 Beta Decay

The electron spectrum of beta decay may be fully described by equation (1.2). Being a three-body-decay, the energies of the final state particles are continuously distributed. By summing over all spins and neglecting couplings beyond the Standard Model – namely the Fierz interference term $b = 0$ – the electron phase space density in units of electron masses can be written as:

$$N(T) \propto pW(W_0 - T)^2 C(T) F(Z,T) = \sqrt{T^2 + 2T}(T+1)(W_0 - W)^2 C(T) F(Z,T)(1 + \delta_R(T, W_0)). \quad (2.1)$$

Here p is the electron momentum, W the total electron energy, $W_0 = Q{+}1$ the complete energy release, i.e. the mass difference between mother and daughter nucleus, T the kinetic energy of the electron and Z the charge of the daughter nucleus. The shape factor $C(T)$ accounts for the forbiddenness of the decay. It is unity for allowed decays such as the neutron decay.

For so-called unique forbidden decays the shape factor has a general form, while for non-unique decays $C(T)$ usually has to be determined experimentally. The Fermi function F is a correction which changes the emission spectrum due to the Coulomb interaction of the $\beta^{\pm}$-particle with the nucleus. δ_R accounts for external radiative corrections, due to emission of real or virtual photons, given in [Sir67] to first order in α. Only higher order contributions couple to the nucleus and have a low impact on the shape of the beta spectrum [BB82]. By using the term $q = (W_0 - W)$ for the momentum of the antineutrino, the recoil energy of the daughter nucleus and a finite neutrino mass are neglected. In most cases this is a valid assumption; for the neutron beta decay the proton may carry up to 1‰ of the total kinetic energy and its momentum should be considered in precision measurements.

The shape factor $C(T)$ has been described by [KU41] whereas $F(Z,T)$ was proposed in [Fer34] already. In this work a method by [BB82] was implemented to calculate the Coulomb amplitudes of the electron radial wave functions $\alpha_k(T)$. These may be used to obtain the corrections

$$F(Z,T) = F_0 L_0 = \frac{\alpha_{-1}^2 + \alpha_1^2}{2p^2}, \tag{2.2}$$

$$C(T) = (2L-1)! \sum_{k=1}^{L} \lambda_k \frac{p^{2(k-1)} q^{2(L-k)}}{(2k-1)!(2(L-k)+1)!}, \tag{2.3}$$

$$\lambda_k = \frac{\alpha_{-k}^2 + \alpha_k^2}{\alpha_{-1}^2 + \alpha_1^2}, \tag{2.4}$$

for an (L-1)th forbidden unique transition. Except for the beta decay of the neutron and completely stripped atoms, electrons of the atomic shell may alter the Coulomb potential of the mother nucleus and therefore change the shape factors. The parametrization by [Sal+87] for the screening potential is used as compensation. The resulting spectra are in agreement with the program `BetaShape` [Mou15]. Theoretical uncertainties arise from the assumption that the charge distribution inside the nucleus be uniform. [BB82] show that the energy dependent difference to other charge distributions is negligible for $F(T)$ and $< 1\%$ for $C(T)$. The detector calibration does not suffer from these uncertainties.

Neutron

The neutron, only having an allowed decay channel, has small corrections to the shape of the decay electron spectrum. $C(T) = 1$ only leaves radiative corrections [Sir67; Sha71; IPT13] and the Fermi function $F(Z,T)$. The latter is often described by

$$F(Z,T) \approx \frac{2\pi\eta}{1 - e^{-2\pi\eta}},\ \eta = \frac{\alpha Z}{\beta}, \tag{2.5}$$

valid for small electron energies and low Z [MM33]. For precise calculations, either the relativistic Fermi function [Fer34]

$$F(Z,T) = \left(1 + \frac{1}{2}S\right) \frac{4(2r_p m_e \beta)^{2S}}{\Gamma^2(3+2S)} \frac{e^{\pi\eta}}{(1-\beta^2)^S} \left|\Gamma\left(1 + S + i\eta\right)\right|^2,\ S = \sqrt{1 - \alpha^2 Z^2} - 1 \tag{2.6}$$

should be used or even equation (2.2), which respects the recoil of the daughter nucleus and spares the application of a correction [Wil82]. It should be noted, that the nuclear charge radius r_p refers to a uniformly charged sphere [BB82] and is related to the measured [AM13] root mean square radii by $\sqrt{\langle r^2 \rangle} = \sqrt{\frac{3}{5}} r$. Figure 2.1b shows that the approximation

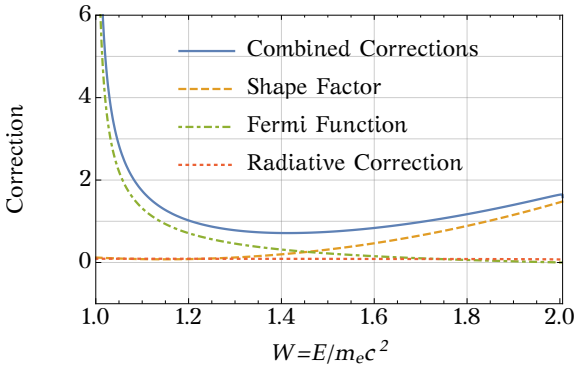

(a) Several corrections have to be applied to calculate the inner branch of the $^{137}_{55}$Cs beta decay spectrum. The Fermi function is important at low energies, while the shape factor alters the spectrum at high energies. Radiative corrections only have little impact.

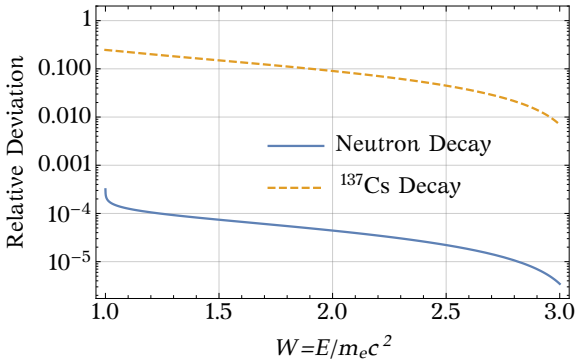

(b) Often equation (2.5) is applied to correct for the attracting potential of the mother nucleus in beta decay. For neutrons the approximation is justified with a relative deviation $< 10^{-3}$, for nuclei with large Z, the relation cannot be used.

Figure 2.1: In the approximation of radial electron wavefunctions the Fermi function may be calculated to sufficient precision. The same assumption is used for the calculation of shape factors of forbidden beta decays. The Fermi function gets very large for high-Z-nuclei.

(2.5) may not be used for large Z, but was sufficiently precise for the description of neutron decay spectra in the past.

An interesting extension to the Standard Model of particle physics is an additional factor $(1+b/W)$ which is called the Fierz term and accounts for possible scalar and tensor couplings. A first measurement of b was performed by [Hic+17] and provides agreement with zero. The data set of the PERKEO III electron asymmetry measurement has potential to significantly improve the precision of this measurement.

Cesium-137

A common calibration source is $^{137}_{55}$Cs, an emitter of a continuous spectrum of electrons as well as of internal conversion electrons (see section 2.1.2) and transition gammas. Corrections to the beta spectrum attain special attention, since the low-energetic part of the spectrum will be used to obtain the trigger function of detectors used in PERKEO III. The two main contributions to the beta decay spectrum are a second non-unique transition to the ground state of $^{137}_{56}$Ba, described by [BC83] and a first unique transition to the excited state $^{137m}_{56}$Ba:

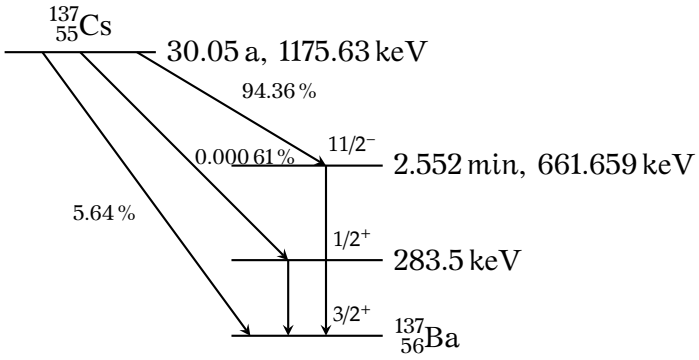

(2.7)

The transition to the $1/2^+$ excited state is neglected due to its low probability. The large impact of the Fermi function and the shape factor is visible in Figure 2.1a.

2.1.2 Electron Capture

In contrast to beta decay, where an electron and an antineutrino are emitted, in electron capture (EC) an electron from the atomic shell is captured and a neutrino emitted, leaving the daughter core in an excited state. The de-excitation can occur via gamma emission or internal conversion, where the emitted energy is transferred to a shell electron which then gets released from the atom.

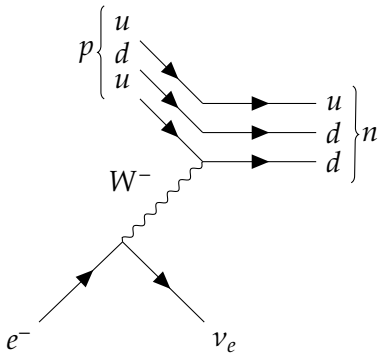

(2.8)

The energy of the gamma equals the difference of energy levels and allows a precise determination of nuclear excitation energies. The energy of emitted conversion electrons depends on the origin of the electron, i.e. the most likely emission of an electron from the K-shell carries less energy than electrons from outer shells, since the binding energy must be overcome. The small differences in electron binding energy between shells $\sim 10\,\mathrm{keV}$ compared to energy differences of nuclear excitation levels $\sim 100\,\mathrm{keV}$ - $1000\,\mathrm{keV}$ make electron capture transitions excellent calibration sources. The ratio of conversion electron emissions to gamma emissions is expressed by internal conversion coefficients (ICC) which can be measured, but usually are calculated to higher precision with knowledge about the multipolarity of the decay [Kib+08].

2.1.3 Auger Electrons

Electron capture and internal conversion remove an electron from one of the atomic shells and therefore create a vacancy, leaving the atom in an excited state. This vacancy gets filled by electrons from higher shells by fluorescence or Auger- and Coster-Kronig-transitions. While fluorescence most likely is not detected in PERKEO III, Auger and Coster-Kronig electrons are transmitted towards the detectors like any other decay electron and add up to the detected signal. With fluorescence shifting the vacancy to a higher shell and Auger and Coster-Kronig transitions even creating further vacancies, a cascade of electrons may be emitted after just a single nuclear decay. A simple approach for the calculation of electron combination probabilities is already described in [Roi10] where sub-shells were combined to one shell and Coster-Kronig transitions were neglected. However, for high-Z elements like lead – the daughter nucleus in Bi-decay – the energy difference within shells may be several keV.

By the means of gamma spectroscopy the binding energies of electron shells can be determined to very high precision, compared to uncertainties in beta spectroscopy. Therefore one is tempted to use electron capture transitions for the low-energy calibration of scintillation detectors: In absence of internal conversion, one vacancy in the electron shell is

left which potentially de-excites by Auger electron emission at low energies. However, the experimental knowledge about the fluorescence yields $\omega_{K,L,M}$ is limited [Dao+15], also due to the binding of elements in compounds. This adds up to large uncertainties in the relative amount of electron combinations and currently makes a precise determination of the detector function in the low-energy region difficult. For decays with internal conversion electrons, this argument does not hold, as the additional Auger electrons can be seen as a correction to the pure conversion electron spectrum.

2.1.4 Decay Cascades

Except for beta decay to (meta-)stable states, a typical decay seldom involves a single electron. The electronic signal of PERKEO processing is based on a charge integrating ADC (see section 2.8.3), acquiring signals over a period of 200 – 300 ns during one event, to allow detection of backscattering events below the trigger threshold, a subject described in more detail in sections 2.2.4 and 2.6. This long integration period leads to the acquisition of the summed up signal of a complete decay event, involving conversion electrons and Auger electrons.

The large number of subshells allows a huge number of different de-excitation chains following an electron capture event. An exemplary cascade up to the N-shell in chronological order might look as follows:

$$\begin{aligned} \mathrm{EC_K} \rightarrow & X_{\mathrm{KL_2}} + e_{\mathrm{L_2M_1M_1}} + e_{\mathrm{M_1M_3N_7}} + e_{\mathrm{M_3N_1N_3}} + e_{\mathrm{M_1N_1N_4}} + \cdots + \\ & e_{\mathrm{ICC\text{-}L_1}} + e_{\mathrm{L_1L_2N_3}} + X_{\mathrm{L_2N_1}} + \cdots , \end{aligned}$$

which is just one of many possible combinations. $X_{\mathrm{KL_2}}$ is a radiative transition of an electron of the $\mathrm{L_2}$-shell to the K-shell. $e_{\mathrm{M_1M_3N_7}}$ fills a hole in the $\mathrm{M_1}$-shell with an electron from the $\mathrm{M_3}$-shell by emitting an electron from the $\mathrm{N_7}$-shell. It cannot be distinguished from $e_{\mathrm{M_1N_7M_3}}$. The width of excited atomic states typically is much broader than nuclear excitation, which normally leads to atomic de-excitation before emission of a conversion electron. Emission from the N-shell and beyond are neglected due to their small energy.

To obtain the distribution of decay cascades for a specific isotope, in a first step, the probabilities for transition into the next atomic and nuclear state is calculated for each initial or intermediate state. A state can be identified by a number of base ($\#_{\text{subshells}} + \#_{\text{nuclear states}}$), using one digit per nuclear state or hole in the atomic shell. Duplicates are excluded by sorting the digits in ascending order. The lack of experimental data requires the use of approximative calculations relying on the Dirac-Hartree-Slater and Dirac-Fock models. [CCM79] provides theoretical subshell transition widths for K- and L-Auger transitions. M-Auger and -Coster-Kronig transition widths are taken from [McG72]. Fluorescence transition probabilities are provided by [Sco74] for K-shell de-excitation, by [Pur07] for L-shell de-excitation and M-shell de-excitation for $Z \geq 65$ and by [CC84] for M-shell de-excitation for $Z < 65$. Since the accuracy of overall fluorescence yields is likely to be more exactly determined than subshell yields, an overall correction is applied to the subshell transition widths to comply with empirical fits to experimental data by [Dao+15] or [Bam+72]. A program described by [Jön+07; Fri12] could provide easier access to atomic transition probabilities.

Electron capture ratios for calibration sources in PERKEO III are provided in [Bé+99; Bé+06; Bé+08; Bé+10], more detailed subshell probabilities are given in [Fir97].

In combination with internal conversion coefficients, each path of the complete decay and de-excitation tree diagram is traversed, keeping track of probabilities and transitions including electron emission. Some paths and branches have to be cut if they are unlikely to limit the number of possible paths. Furthermore, some electron emissions are merged into

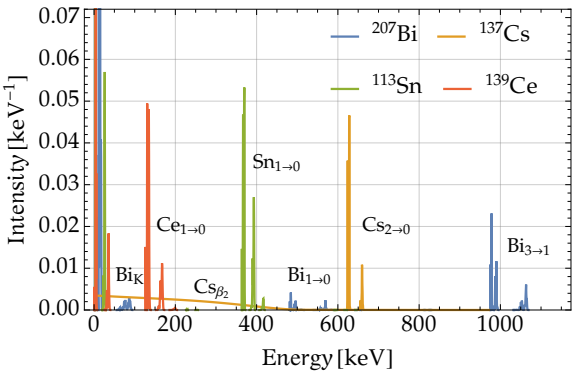

(a) Four different calibration source types cover the full detection range up to 1 MeV. The line sources have several branches for internal conversion transitions which depend on the emitted conversion electron and additional Auger electrons. The ^{137}Cs source additionally has two beta spectra, one of them being visible in the range < 500 keV.

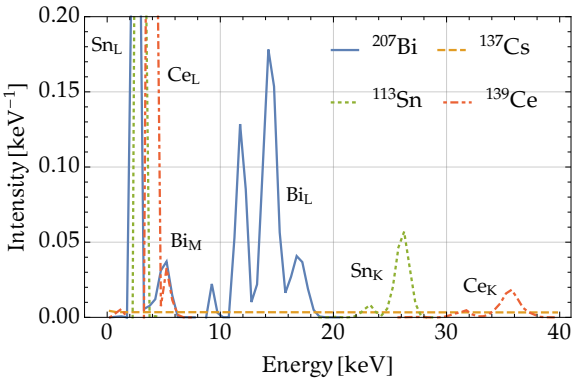

(b) In the low energy region, Auger electrons mark the end of the spectrum. The influence of electron cascades is visible especially for de-excitations with L-dominated Auger electrons (Bi_L). Electrons with energies below 1 keV are not considered. The graphs also show the energy resolution of 0.5 keV used for further calculations.

Figure 2.2: Theoretical energy spectra are calculated as input for further convolution. The presented lines show the sum of energies of all electrons from a single decay. Line spectra are either originating from internal conversion in the higher energy region or Auger electrons in the lower energy region. A gamma transition from excited nuclear states of electron capture must precede to allow pure Auger spectra.

one without altering initial and final state if their energies are the same within 0.2 keV or 0.5 keV in the case of Bismuth. Despite these simplifications, for the latter ≈ 9000 electron combinations are possible, where ≈ 16 million unique decay chains are combined. Caching is used to quickly access the condensed information about electron combinations and skip the time and memory consuming calculations. The resulting theoretical energy spectra are shown in Figure 2.2.

Usually the calculation of Auger cascades is done using Monte Carlo methods [PBC87; Gua+07], since there is interest in the investigation of sub-shells beyond the M-shell, which further blows up the number of possible de-excitation paths. So far, there seems to be no other tool than the one described in this work, which performs the described steps explicitly using the complete probability net.

2.2 Particle Transport

In PERKEO III electrons and protons, coming from a calibration source or the neutron beam, are guided to the detector by a magnetic field. For the recent measurement of the proton asymmetry, there are also electrostatic fields involved. Particle tracking in electromagnetic fields is done by [Klo18]. A study of electron motion in PERKEO III only for the magnetic field is described in [Roi10]. In addition to lossless movement in the magnetic field, there is interaction with matter, leading to energy loss and change of direction.

2.2.1 Energy Losses at Thin Layers

Electrons of the PERKEO III proton asymmetry measurement are not entirely transported to the detectors without energy loss. In contrast to synchrotron radiation which leads to losses in the sub-meV-range, passage through matter may lead to a significant loss of kinetic energy. For calibration sources which are positioned on a carbon holder foil, at least half of the calibration electrons are interacting with these foils of $\approx 200\,\mathrm{nm}$ thickness. Later on, the electrons have to pass the proton-to-electron converters, again being equipped with a thin carbon foil of 100 nm thickness at the maximum of the electric potential. Lastly, the electron detectors are covered with a non-scintillating layer of ITO (Indium-Tin-Oxide) which allows pulling the electric potential at the surface of the detector to ground even for a layer thickness of 20 nm.

Ionization

Charged particles in the low-energy range of keV to MeV mainly transfer their kinetic energy to matter by ionization. The material specific energy loss is described in [BS64] for electrons. For low-density materials such as carbon, the low-energy region of the ionization energy loss may be approximated by

$$\frac{\mathrm{d}E}{\mathrm{d}x} \approx -A\,\rho\,E^{1-B}, \quad E < 100\,\mathrm{keV}, \tag{2.9}$$

with path length x, material density ρ and arbitrary parameters A and B. The kinetic energy after a path length l is then extracted by solving the differential equation to

$$E_{\mathrm{out}}(l) = \left(E_{\mathrm{in}}^{B} - A\,B\,l\,\rho\right)^{1/B}. \tag{2.10}$$

For carbon $A \approx 0.65\,\mathrm{keV}^{1.74}\mathrm{cm}^2/\mathrm{g}$ and $B \approx 1.74$ are determined from a fit to material-specific data [Ber+14]. The effective path length increases with the polar angle by $\cos^{-1}\theta$ if straggling is neglected for very thin layers. The energy distribution of the outgoing particles then follows to be

$$\frac{\mathrm{d}(\cos\theta)}{\mathrm{d}E_{\mathrm{out}}} = \frac{AB^2 l\rho E_{\mathrm{out}}^{B-1}}{\left(E_{\mathrm{in}}^{B} - E_{\mathrm{out}}^{B}\right)^2}. \tag{2.11}$$

The relative number of particles getting stuck in the layer is $A\,B\,l\,\rho E_{\mathrm{in}}^{-B}$. Averaging over this distribution yields the mean energy for outgoing electrons. As an example, Figure 2.3 shows the energy loss at a carbon holder foil similar to the ones used in PERKEO III.

For the analysis of the electron asymmetry calibration data, it is assumed, that one of the detectors does not have direct sight onto the calibration sources. The visible energy spectrum per electron is therefore smeared out following the distribution (2.11). For very large polar angles and energy losses $\gtrsim 1\,\mathrm{keV}$, the assumption of the absence of straggling should be reevaluated to improve the loss model. Spectra from both detectors have to be combined in order to account for the detector mixing of multi-electron events. Not considering the effect of energy losses in the foils would lead to a relative underestimation of the electron asymmetry on the order of 10^{-4} corresponding to a tenth of the total uncertainty.

2.2.2 Flight Times

After leaving a calibration foil or being emitted from neutron decay, each electron requires a certain amount of time to reach one of the detectors. Typical flight times range from 15 to

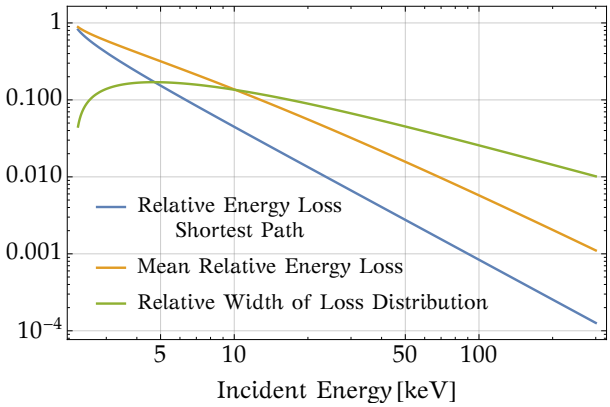

Figure 2.3: Energy loss at thin layers such as calibration source carrier foils may be treated as an energy offset, if the initial electron energy is $> 50\,\mathrm{keV}$. Below, an effective path length is not sufficient, but the width of the loss distribution should be considered for further evaluation of calibration spectra. The energy loss along the shortest path perpendicular to the surface is much smaller than the average energy loss for isotropic emission.

200 ns. This flight time depends on the starting position, the energy and the emission angle. For multi-electron events of calibration sources this allows every electron, even those with low relative energy, to be the first to be detected. From the center of the instrument, where the scanner device is located, the empirical formula

$$t(\theta, E) \approx \frac{1}{c\beta(E)} \left(\frac{b}{\sqrt{\pi^2 - 4\theta^2}} - a \right), \quad a = 2.277\,\mathrm{m}, \quad b = 18.74\,\mathrm{m}, \tag{2.12}$$

which is deduced from a fit to simulation data, may be used to estimate the flight time. Its simple invertibility enables an estimation of the probability that an electron e_1^- of a multi-electron event with n particles reaches a detector first:

$$p(e_1^- \text{ first}) = \frac{1}{100} \sum_{\cos\theta_1 = 0.01}^{1} \prod_{i=2}^{n} \int_{\theta(t_{\mathrm{Flight}}(\theta_1, E_1), E_i)}^{\theta(t_{\mathrm{Flight}}(\theta_1, E_1) + t_{\mathrm{Gate}}, E_i)} \sin\theta \mathrm{d}\theta. \tag{2.13}$$

The summation indicates discrete steps – in this case 100 – for possible emission angles of the considered first electron. t_{Gate} is used as upper integration limit after the start time and is defined by the electronic setup, c.f. section 2.8.3. This method therefore allows the determination of the number of delayed electrons per event, which had already been studied in [Roi10], where a less efficient algorithm is used however.

A particular application of this information arises from the combination with the detector trigger function from section 2.6. A low-energetic electron which reaches the detector first might not release a trigger signal and its energy information likely gets lost. Only one of the following electrons may then be the new first electron and a reduced number of electrons then is detected. This effect leads to a further distortion of the multi-electron event distribution. The effect on the electron asymmetry in the currently analyzed energy range is small $|\Delta A/A| < 10^{-4}$, but it allows a better description of calibration spectra in the low-energy region and may enable using a larger analysis window in energy in the future.

2.2.3 Point Spread Function

The movement of particles inside external fields is often predicted by applying particle tracking simulations. Many qualitative, but also quantitative insights can still be obtained from symbolical calculations. A particularly interesting information is the projection of a charged particle point source onto a detector by transport inside a magnetic field, the so-called point spread function (PSF) [Dub15b]. It can be used to calculate the probability that an electron will hit a detector and can also be combined with spatially dependent detector response functions.

Singularities

A charged particle emitted at a point $\vec{x_0} = (0,0,0)$ inside a magnetic field $\vec{B}$ initially will have a polar or pitch angle of θ and an azimuth of α. Assuming $\vec{B}$ to be constant, θ will remain constant as well and α will change constantly along the flight path z

$$\alpha(z) = \frac{z}{r_0 \cos\theta},\ r_0 = \frac{p}{eB}. \tag{2.14}$$

r_0 is the gyration radius for emission at $\theta = 90°$ and increases with particle momentum p. Now R is introduced to be the distance between the particle position $\vec{x} = (x,y,z)$ and the center of gyration $(0,0,z)$:

$$\frac{R}{r_0} = 2\sin\theta \left|\sin\frac{z}{2r_0\sin\theta}\right|. \tag{2.15}$$

The direct relation of R and θ for fixed distances z between source and detector now leads to divergences of the electron distribution along R as Figure 2.4 shows. This behavior may lead to unexpected signatures even in continuous energy spectra [Dub15a]. If z is not fixed, as for electrons coming from a neutron beam for instance, the divergences are smoothed out, and the radial distribution simply is

$$f(R < 2r_0, \phi) = \frac{1}{4\pi R r_0}, \quad \text{or} \tag{2.16}$$

$$g(R < 2r_0) = 2r_0 \int_0^{2\pi} f(R,\phi) R \mathrm{d}\phi = 1. \tag{2.17}$$

The maximum radius $2r_0$ cannot be exceeded. In section 2.4.6 it is worked out, why equation (2.17) is sufficient for electron detection in PERKEO III, even for calibration sources which are located at fixed distance from the detectors.

Asymmetric Point Spread Function

In the case of non-isotropic, but asymmetric emission of particles, the PSF naturally has to be adapted. Equation (2.17) now has an additional asymmetric part [Dub+14]

$$g_A(R) = 1 + A_{\text{exp}} \frac{2}{\pi} \sqrt{1 - \frac{R^2}{4r_0^2}}, \tag{2.18}$$

with asymmetry $A_{\text{exp}} = \beta(E) A P$ for neutron beta decay. This includes the polarization of the neutrons $P \in [-1,1]$ and the relative electron velocity β. It expresses what is expected intuitively: Emission to the preferred half space yields more particles in the center of gyration, while particles emitted in the suppressed direction end up further outside.

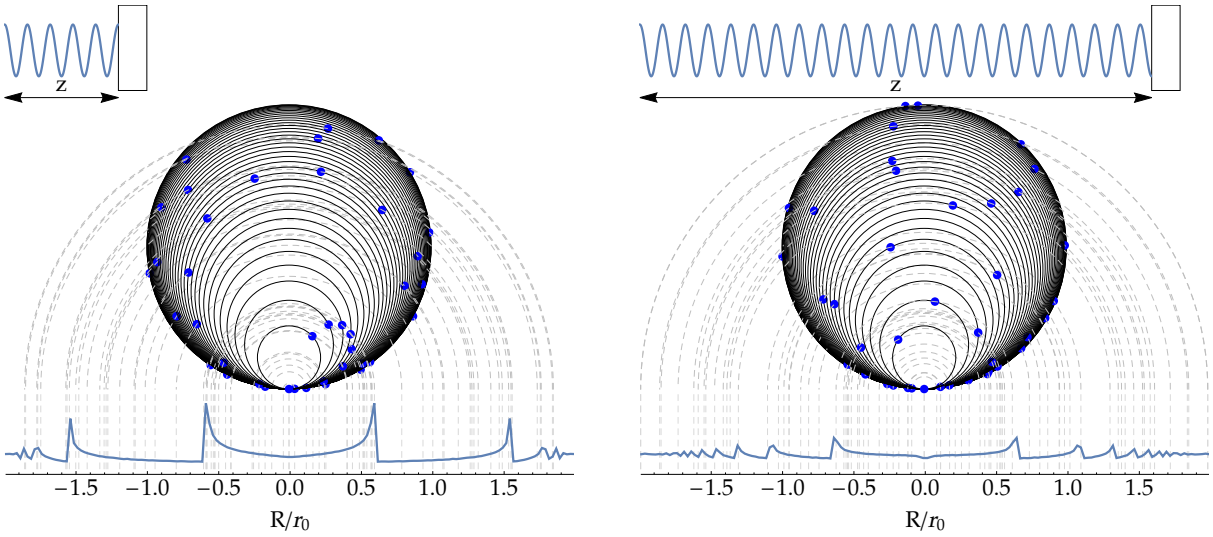

(a) For small ratios z/r, the number of divergences is small and the maxima are more prominent.

(b) If the distance to the detector is increased, the divergences are distributed more equally and washing out.

Figure 2.4: To illustrate the occurrence of divergences in the point spread function, the clockwise gyration movement is shown as solid black circles, for isotropically distributed polar angles and fixed azimuth. The blue dots represent the end position of the particle on a detector at distance z to the source. To show the radial distribution on the detector, the end positions are projected onto the horizontal axis by the gray dashed circles. The particle distribution, i.e. the density of gray lines, is finally shown below the sketch.

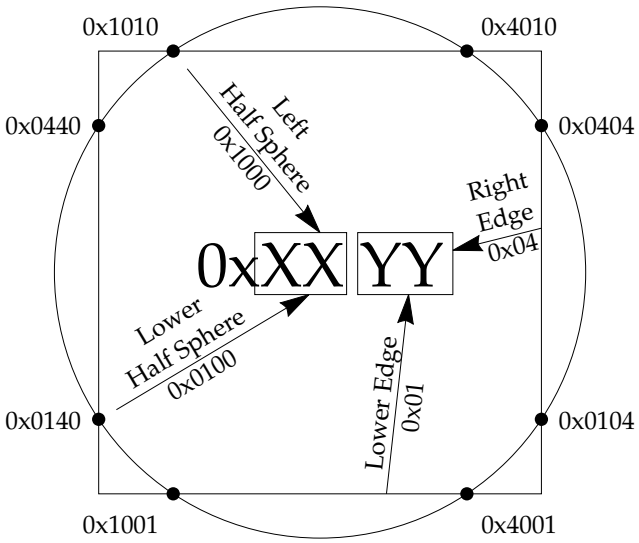

(a) Each cut between disk border and pixel border can be classified by a 16 bit value. The sum of all values yields the full pixel classification.

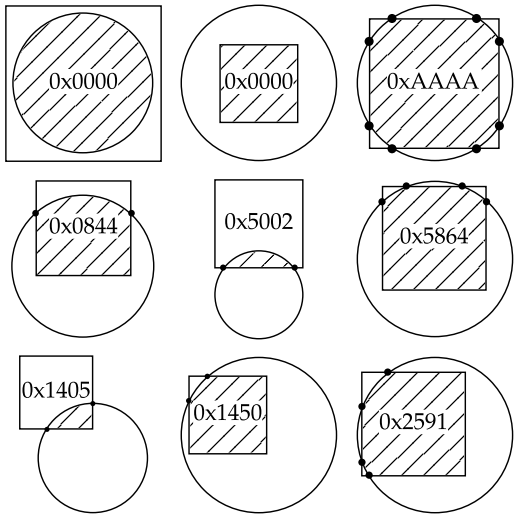

(b) There are many different ways to cut a rectangle with a circle. The obtained classifiers are shown for a selection of cuts.

Figure 2.5: To be able to calculate the integral of a rotational invariant function with maximum radius inside a pixel, partially or fully covered by the disk with that radius, the cuts of the disk border with the pixel border are used to classify the integration region.

Pixelized Point Spread Function

Section 2.4.6 will show, that the convolution of an advanced detector function with the PSF is hard to accomplish by means of symbolical calculations. To overcome this problem, the detector function, as well as the PSF, will be presented as pixels, a typical digital image representation. To comply with normalization and demanded precision, the probability for a particle to hit a pixel will be calculated exactly.

Classification To get a precise anti-aliased representation of a rotational invariant function $f(R)$ by pixels, a distinction of cases has to be done for the coverage of the pixels by a disk $\mathscr{D}$ which defines the domain of definition with values > 0. In the case of the PSF this would be a disk with radius $2r_0$.

The pixels can be cut by the disks border $\partial\mathscr{D}$ in many different ways, all leading to different descriptions of the intersection. To efficiently classify each type, combinations of 16 bits describing a cut of pixel borders $\partial\mathscr{P}$ and $\partial\mathscr{D}$ are introduced in Figure 2.5a, which are added up to yield pixel classifiers in Figure 2.5b. They are unique, as long as the disk may not completely fit into one pixel. A distinction of case has to be done, if this condition is not met.

If arbitrary rectangular shapes are allowed for the pixels, there are 46 distinct pixel classifiers which have to be handled independently. The trivial case is a pixel which fully covers $\mathscr{D}$. The pixel value would simply be the area of the disk. Another simple and typical case is the pixel which is fully covered by $\mathscr{D}$. Here the integral of $f(R,\phi)$ in the domain of definition of the pixel is to be evaluated. These types are an example for the special handling of small radii. Both types are classified as 0x0000 and must be distinguished by

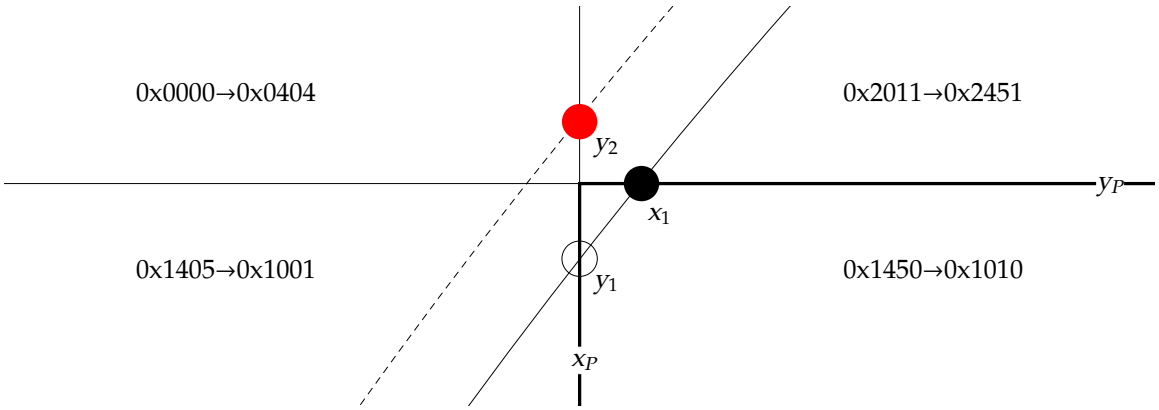

Figure 2.6: The loss of numerical accuracy may lead to a faulty cut assignment, ending up in wrong classifications. For a cut of the solid black disk border at y_P, the horizontal component is solved to be $x_1 > x_P$. The expected cut at x_P would be $y_1 < y_P$, however, the numerical accuracy is too low and the returned value is $y_2 > y_P$. The classification for the lower right pixel results in 0x1010 instead of the expected 0x1450.

the pixel size and radius ratios.

Special care has to be taken when determining the cut coordinates. For a vertical pixel border at x_P and a disk of radius R centered at (x_0, y_0), they are found by solving

$$(y - y_0)^2 + (x_P - x_0)^2 = R^2 \Rightarrow y = y_0 \pm \sqrt{R^2 - (x_P - x_0)^2}. \tag{2.19}$$

The numerical calculation of a square-root involves a loss of numerical accuracy. In particular cases, especially, when the disk is centered on a pixel border, an erroneous attribution of cuts to the wrong pixels might occur. This may lead to a situation presented in Figure 2.6. Problems can be identified by checking for even number of cuts per pixel. It is sufficient to correct the classification of the pixels, since differences in the spatial coordinates which are required to obtain the covered area are negligible. The correction simply ensures the application of the correct formulas. Except for pixels at the detector edge, there are always four pixels involved for one miscalculation of cuts. This allows the selection of the right correction.

Integration The integration over several shapes is required to obtain the correct pixel coverage:

- rectangles
- right triangles with catheti along x- and y-axes
- isosceles triangles with apex in the center of the disk
- circular segments
- circular sectors.

Figure 2.7a shows a possible composition of these shapes. Formulas which allow to calculate the respective PSF coverage by these shapes are given in the appendix A.1.

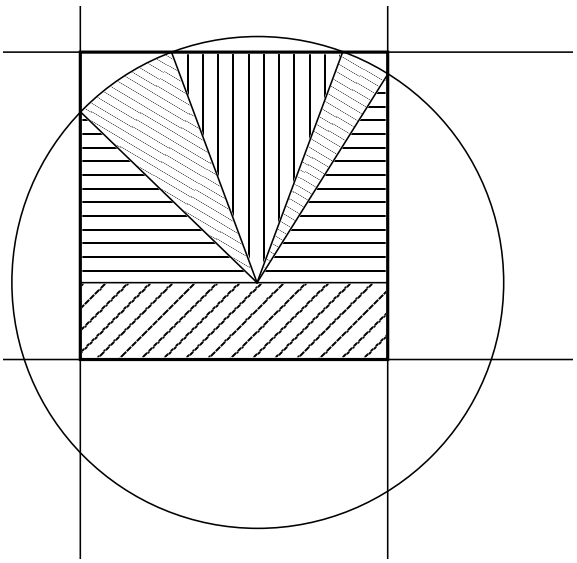

(a) A pixel cut by the disk border is segmented into different shapes to allow integration over the covered domain. The integral over a circular segment can be obtained by subtracting an isosceles triangle from a circular sector.

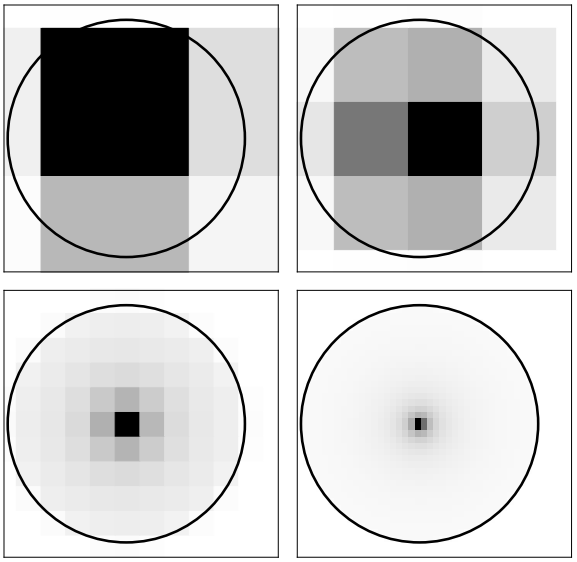

(b) The algorithm allows the calculation of the PSF at arbitrary resolutions. The final number of pixels is to be chosen depending on the use case. For the determination of the edge effect, a single pixel is sufficient, while a complex detector function may require a finer grid.

Figure 2.7: In order to simplify the application of the PSF to a detector or an opening function, the PSF is projected onto a grid of pixels. Common anti-aliasing algorithms [Bre65; Wu91] only yield approximate coverage for not fully covered pixels. Normalization is guaranteed by performing an exact piecewise calculation of the covered area.

Asymmetric Pixelized Point Spread Function

For the asymmetric point spread function (APSF) (2.18), no closed form solution could be found and the integration must be approximated:

$$\frac{1}{R}\sqrt{1-\frac{R^2}{4r_0^2}} \approx \frac{1}{R} - \frac{1}{2r_0}\left(\frac{R}{4r_0} + \frac{R^3}{64r_0^3} + \frac{R^5}{512r_0^5} + \ldots\right). \tag{2.20}$$

A final term $c(R/2r_0)^s$ can be added to assure that the series expansion is zero at $R = 2r_0$, as for the original expression. c is determined by the expansion prefactors, while s can be chosen, such that the expansion formula is optimized. For a series expansion to fifth order this can be done by minimizing

$$\int_0^1 \mathrm{d}x \left(\sqrt{1-x^2} - x\left(\frac{1}{x} - \frac{x}{2} - \frac{x^3}{8} - \frac{x^5}{16} - \frac{5x^s}{16}\right)\right)^2 \tag{2.21}$$

with respect to s, where $x = \frac{R}{2r_0}$. The best integer solution yields $s = 24$.

The integration over the required shapes yields trivial but lengthy integrals, not given here. Special care must be taken when implementing the formulas to evaluate higher order polynomials in the right order to prevent significant loss of numerical precision.

Application

Even without interest in the detector function, the pixelized point spread function can be a useful tool due to its intrinsic normalization. It allows an easy calculation of edge effects, i.e. the loss of events because of a limited detector size. In section 2.4.8 the PSF is extended to a beam spread function, by convolution of the neutron beam profile with the PSF for electrons of a specific energy. The larger coverage of the detector by high energetic electrons leads to a nonlinearity as a result of the non-uniformity of the scintillation light transport. The same cause changes the measured asymmetry, since the APSF leads to more electrons reaching the detector at large radii when they are emitted in neutron spin direction. This effect is investigated in section 2.4.7

2.2.4 Backscattering

A large source of uncertainty in the detection of low-energetic electrons is backscattering: The particle only deposits a fraction of its energy in the detector and then leaves again before being entirely stopped. The backscattering probability for silicon detectors is roughly three times as large as for plastic scintillators. Although the former provide a higher energy resolution for single events, the systematic error introduced by backscattering currently does not allow the use of semi-conductor detectors. This – next to economic reasons and a better timing resolution – is the main motivation to continue using plastic scintillators within PERKEO III.

Simulations

The absence of a comprehensive database requires the use of particle scattering simulations to estimate the energy deposition of electrons in plastic scintillators. In principle backscattering from a planar surface may be described by five observables:

- incoming energy E_{in}

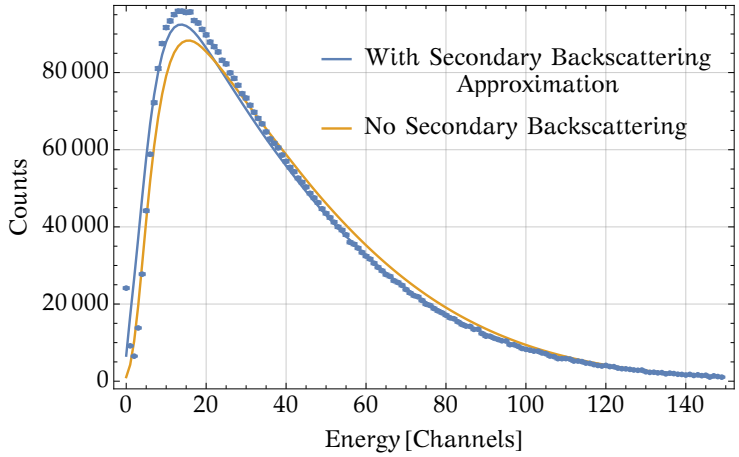

Figure 2.8: Backscattering simulations with `Geant4` show an excellent agreement with measured data, if backscattering of backscattered electrons is taken into account. The presented height of the spectrum is completely extracted from a fit to the sum spectrum of the neutron decay and only differs by up to 3 % from the data. The graph represents the integration $\int \frac{\mathrm{d}\eta \mathrm{d}\Gamma_\beta}{\mathrm{d}E_{\mathrm{in}}\mathrm{d}E_{\mathrm{out}}}\mathrm{d}E_{\mathrm{in}}$ over the incoming beta decay spectrum with a lower angular limit for θ_{out} to account for the magnetic mirror effect.

- incoming polar angle θ_{in}
- outgoing energy E_{out}
- outgoing polar angle θ_{out}
- outgoing azimuth ϕ relative to the incident azimuth.

The displacement of the outgoing electron which should not exceed 2 mm for $E_{\mathrm{in}} < 1\,\mathrm{MeV}$ is neglected in this case. A Monte Carlo simulation provides all of these parameters. Validation with experimental data can mostly only be done by integrating over some of them. In [Kim+15] several `Geant4` low-energy models are reviewed by comparing to multiple experiments. Therein the Single Coulomb Scattering model is tested to be the most precise choice. The authors do not provide details about the influence of the choice of the ionization model – namely the Livermore or Penelope model. They refer to insignificant differences, a statement which could not be confirmed in this work. The backscattering probability of both models differs by 10 %.

With PERKEO III, the absolute backscattering probability $\eta_{\mathrm{opp}}(E_{\mathrm{in}}, E_{\mathrm{out}})$ to the opposite detector can be extracted from neutron decay data. $\eta_{\mathrm{opp}} \approx 6\,\%$ and is about as large as η_{same}, which describes backscattering onto the same detector due to the magnetic mirror effect – see section 1.2.4. A comparison to simulations in Figure 2.8 shows the necessity to include secondary backscattering – backscattering of already backscattered electrons. A simplified correction for this effect finally shows, that the simulated backscattering coefficient only differs by up to 3 % relative to the data if the `Geant4` Livermore ionization model is used.

Backscattering with Elise

A setup to actually measure the backscattering dependence on all five observables could be realized with the magnet spectrometer Elise [Roi12; Gra13; Dai14; Lam15]. A closed ^{90}Sr beta source provides electrons with energies up to $\approx 2\,\mathrm{MeV}$ by emission from decaying daughter nuclei ^{90}Y. Energy selection is done by insertion of two pinholes, each after 90° of deflection. The provided electron beam has a low divergence, which allows to vary the incident angle by turning the primary detector. Properties of the outgoing electrons can then be measured by a moving secondary detector, which can be rotated around the primary detector. An exemplary sketch in [Gra13] shows a possible setup. An important feature is the possibility to calibrate the secondary detector with the primary electron beam to reduce the systematic uncertainty of detector calibration. Such a setup will allow to find a suitable set of simulation parameters, which can then be used to create reliable simulations of more complex detector geometries.

Backscattering Detection in PERC

For PERC, there will only be one main detector and backscattering detection is limited to energy and time resolving veto detectors. These detectors cannot be used for further data analysis, since they have to be placed in a region with high background rates. A collaborative study of the new systematic effects are summarized in the thesis by Carmen Ziener [Zie14]. The main difference between Perkeo measurements and PERC will be the use of the magnetic filter, which will only allow almost perpendicular incidence on the detector and suppress passage of backscatter electrons at the same time. A main concern is actually not backscattering from the main detector, but undetected backscattering from the veto detectors onto the main detector. The handling of this issue in section 2.7 will also be applied to upcoming measurements with PERC. An important improvement is the higher light extraction efficiency. It leads to a lower detection threshold [Bar17], compared to those considered in [Zie14] or used with Perkeo III.

2.3 Nonlinear Detector Response

An ideal calorimetric detector would provide an output signal which is perfectly proportional to the energy deposited. Real detectors usually do not fulfill this specification, but deviate from linearity. This shortcoming is usually called nonlinearity and may have several origins. A nonlinear detector response is not a problem per se, as long as it is sufficiently well known. In the following, theoretical and experimental approaches are presented to obtain a good detector description.

2.3.1 Scintillation Quenching

The transformation of kinetic energy of charged particles to light in organic scintillators is a multi-step process [Bir64]. A typical plastic scintillator is mainly made of a base material such as Polyvinyltoluene or Polystyrene and doped with fluorescing substances such as *p*-Terphenyl or POPOP, also called fluors. Traversing charged particles transfer their kinetic energy mainly to the base material by ionization and excitation, the latter being more likely for low particle energies. Electrons which are released by ionization themselves undergo the same energy loss processes, leading to cascades of secondary particles.

Excited base molecules may fluoresce or transfer their energy by Förster resonance energy transfer (FRET) [För48], a non-radiative energy transfer process, which is more likely since

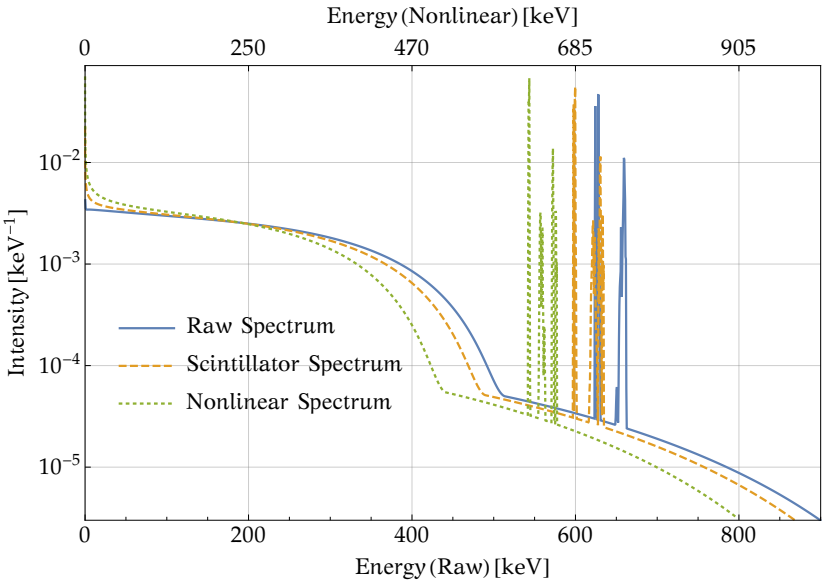

Figure 2.9: The detector nonlinearity is applied by shrinking theoretical input spectra from Figure 2.2 by applying nonlinear relations such as equations (2.22) or (2.28) to single electrons. The graph shows the impact of combined scintillator and electronics nonlinearity on the theoretical spectrum of ^{137}Cs. The upper energy scale is mapped onto the lower energy scale.

donor and acceptor spectra are overlapping. The energy may also be be transformed into vibrational excitation and finally dissipate as heat. A random walk of energy transfers or exciton diffusion [Pow71] may end up hitting a fluor acting as exciton trap, whose absorption spectrum overlaps with emission from the base material, but which emits at higher wavelengths. Here radiative de-excitation is more likely, since fluor donor and base acceptor spectra do not overlap. This largely extends the mean free path of a photon. To further limit self-absorption by the primary fluor with concentrations $\approx 1.5\,\%$, an additional secondary fluor with concentrations $\approx 0.1\,\%$ may further shift the wavelength and increase the absorption length.

A survey to find the source of the uncommonly large nonlinearity for PERKEO III detectors results in an extensive study of processes leading to nonlinearities in the scintillation process. A semi-empirical model was worked out by Birks [Bir52] and usually is applied to describe scintillation quenching:

$$\frac{\mathrm{d}L}{\mathrm{d}x} = \frac{g\frac{\mathrm{d}E}{\mathrm{d}x}}{1 + k_B\frac{\mathrm{d}E}{\mathrm{d}x}} \Leftrightarrow \frac{\mathrm{d}L}{\mathrm{d}E} = \frac{g}{1 + k_B\frac{\mathrm{d}E}{\mathrm{d}x}}. \tag{2.22}$$

Further models which evolved over time and an approach to simulate quenching effects using scattering simulations are presented in section 2.3.3.

For the nonlinearity of PERKEO III detectors it finally turned out, that bandwidth limitations in the signal processing are responsible for a similar behavior. A description using equation (2.22) with increased k_B yields a decent reproduction of measured data. It is important to note, that no good description of the measured spectra can be achieved if nonlinearity relations are applied after summing up electron energies of an electron cascade. More details about a comparison of several nonlinearity models are provided in [Sau18].

2.3.2 Detector Calibration via Time of Flight Measurement

The calibration of a calorimetric detector requires a reference measurement which allows to determine the energy of incident particles independently. This can be done by assuming a particular energy spectrum of the particle source – such as for radioactive calibration sources – or by determining a different quantity, which allows to draw conclusions on the individual particle energy. One of these quantities is the time of flight (ToF) which a particle requires to cover a well-known distance. It allows to determine the speed of the particle and therefore its energy.

The electron ToF was so far only used to separate events on two distinct detectors connected by a magnetic field. In particular, for Perkeo III, the time difference between two trigger signals during one event is used to decide which detector was hit first. In the case of neutron decay measurements the second trigger is then considered as a backscattered electron. So far, there were no attempts to use the timing information to draw conclusions on the electron energy. The main reason is the angular distribution of the electrons relative to the magnetic field which theoretically allows infinitely large flight times: The gross flight path to travel a distance l along the magnetic field increases by a factor $\cos^{-1}\theta$, for a polar angle θ.

[Dub16] proposes a method to overcome this problem which and is proven to be working in [Roi+18]. Here, the inverse magnetic mirror effect is used to project even large initial polar angles θ_0 of the momentum to the magnetic field to almost parallel movement along the magnetic field:

$$\sin\theta(z) = \sqrt{\frac{B(z)}{B_0}}\sin\theta_0. \tag{2.23}$$

If $B(z)/B_0$ is small for most of the distance l between start and stop point, the actual flight path can be considered to be almost l as well. Since the electron energy is solely determined from the ToF, it is not required to know the spectrum at the stop detector which is to be calibrated. Any electron source which provides a start signal and electrons in the required energy range is therefore suitable as calibration device. For this experiment a scintillator doped with ^{90}Sr fulfills this purpose. It is read out by a PMT connected by a light guide. Figure 2.10 shows a schematic overview of the experiment. The stop detector which is located in the low field region consists of a scintillator, light guide and PMT as well. The PMT signal therefore provides energy and timing information which can finally be used to determine the stop detector calibration. The following sections provide a more detailed insight to aspects which are not covered in [Roi+18].

Adiabatic Transport

The magnetic field densities at the starting point were varied to be 2.5 T, 1.3 T and 0.7 T, which quickly decreased to 22 mT of the 4.43 m of transport section. For the largest change of magnetic field from 2.5 T to 22 mT, perpendicular starting angles lead to the maximal angle of 5.3° within the transport section, which increases the flight path by a maximum of 4‰. However, good things often come for a price: The magnetic flux $\vec{B}\cdot\vec{A}$ must be conserved and as $\vec{B}$ is decreasing, the through-flown area A must increase, and therefore a starting section A_0 is widening to a covered area of $A_1 = A_0\cdot B_0/B_1$. An electron with center of gyration in distance r_0 to the center of the magnetic field, will finally have a center of gyration of $r_1 = r_0\cdot\sqrt{B_0/B_1}$. The energy dependent fraction of transmitted electrons can be

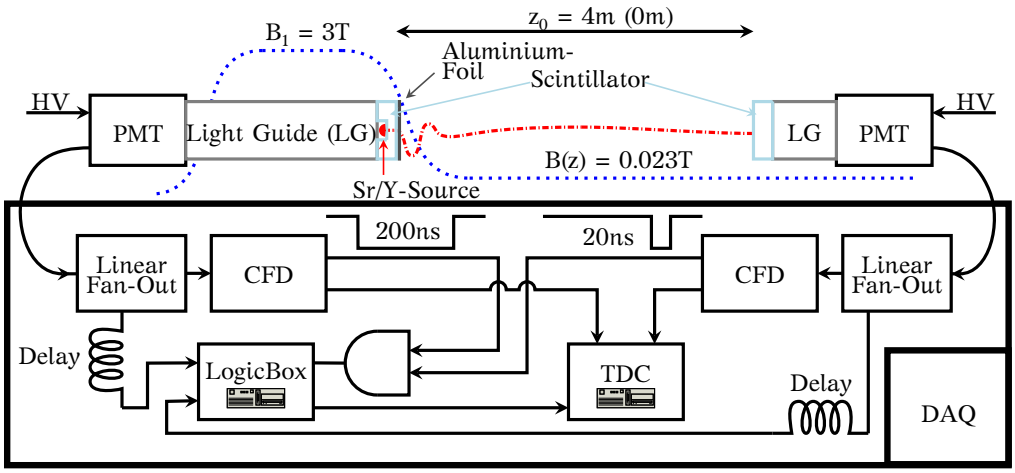

Figure 2.10: The ToF experiment was setup to trigger for coincident signals in start and stop detector. The upper part shows the decreasing magnetic field at the start in blue and the sketched particle movement in red. Photons which are released in the scintillators (light blue) are guided to photomultiplier tubes (PMTs). The trigger logic in the lower part registers an event if photons are detected in both of the PMTs. The signal amplitude in the right detector is then compared to the ToF – the time difference of the signals between right and left detector.

expressed as

$$\Omega(E) = \int \frac{\mathrm{d}I}{\mathrm{d}r_0 \mathrm{d}\theta} \max\left(1 - \sqrt{1 - B_0 \frac{a\sqrt{B_1/B_0} - r_0}{2\sin\theta\sqrt{E^2 + 2mE}}}, 0\right) \mathrm{d}r_0 \mathrm{d}\theta. \tag{2.24}$$

$I(r_0, \theta)$ denotes the distribution of electrons escaping the start detector depending on the distance to the center. a is the inner radius of the vacuum tube, where electrons eventually are absorbed if their distance to the central axis is too large. These calculations are only valid in the case of adiabatic transport, which in simple words means: The change of the magnetic field must be small for one gyration. This condition can be expressed by the adiabatic parameter:

$$\eta = \frac{2\pi p_e}{eB^2} \left|\frac{\mathrm{d}B}{\mathrm{d}z}\right| \ll 1. \tag{2.25}$$

The magnet Perkino is magnetically shielded and must allow access to the center of the solenoid at the same time. Figure 2.11 shows how end-plates with central holes fulfill both conditions but lead to a quick decrease of the magnetic field. The holes in the plates finally lead to an adiabatic parameter $\eta \approx 1$ for energies of $< 1\,\mathrm{MeV}$, estimated in Figure 2.12b, which contradicts the required condition. It is therefore not sufficient to simply assume equation (2.23), but it has to be checked by means of particle tracking calculations.

Magnetic Field Calculations In contrast to the typical approach of finite-element calculations, the `Mathematica` add-on `Radia v4.31` [CEC98] uses a boundary integral method to obtain static magnetic field densities created by coils and magnetized solids. The magnetization of ferromagnetic solids still is calculated by finite-element relaxation, however. The magnetic field was measured at 1T nominal magnetic field density along the central axis of the solenoids, by using a Hall probe. This data is used to tune the magnetic field

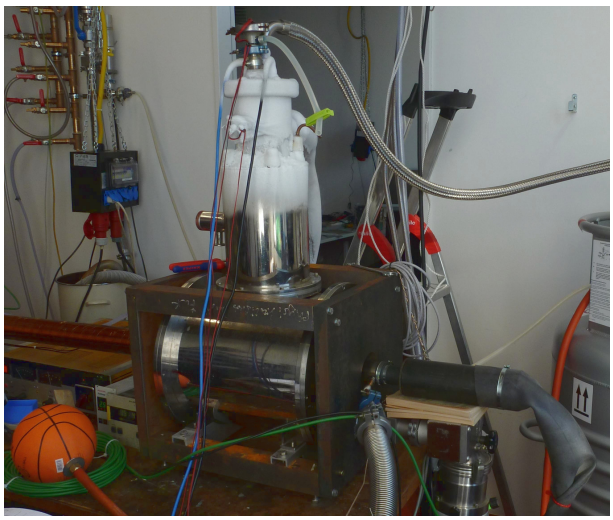

Figure 2.11: The superconducting magnet PERKINO is shielded by steel-plates which quickly decrease the magnetic field on the central axis. To the left, the beginning of the low field section is visible. A rubber hose is used as light-tight envelope for the start detector.

calculations and obtain the expected magnetic field at any point in the setup for arbitrary currents through the supraconducting solenoid. Figure 2.12a shows the resulting magnetic field along the central axis.

Particle Tracking To test the assumption of equation (2.23) an updated version of the particle tracking code which is described in [Roi10] is used. The initial parameters which allow a particle to reach the stop detector have to be found. A scan of the kinetic energy, the distance to the center of the start detector and the initial polar angle is done to obtain an allowed range for the azimuthal angle. To simplify calculations the vacuum vessel is assumed to be centered in the magnetic field. This allows to reduce the variation of the starting position along one axis, using the cylindrical symmetry to transform any starting point to the investigated parameter range by rotation:

$$\vec{x} \longrightarrow R\vec{x} = \begin{pmatrix} 0 \\ |\vec{x}| \end{pmatrix}, \ \vec{p} \longrightarrow R\vec{p}.$$

Scattering The initial kinematic parameters which are required to decide whether an electron will reach the stop detector are estimated by using the simulation toolkit `Geant4 v10.3.1` [All+16], carefully taking into account required adaptations to the default settings [Kim+15]. Good precision even at low energies requires more computation time and therefore only few events (300 000) are simulated using the single Coulomb scattering model. The start scintillator has a thickness of 5 mm and is doped with a ^{90}Sr source at a depth of 2.5 mm. To reach the stop detector, the decay electrons of ^{90}Sr or its daughter isotope ^{90}Y have to overcome the remaining 2.5 mm of scintillator, leading to an energy loss of at least 450 keV, which provides enough light emission from the start detector to be used as a start signal. Electrons which are able to interpenetrate the start detector are distributed around the center of the detector within a large radius of 1 cm and a mean distance to the center of 3.4 mm as Figure 2.13a shows. Finally the simulation provides all required parameters for these particles to decide whether they may hit the stop detector as well.

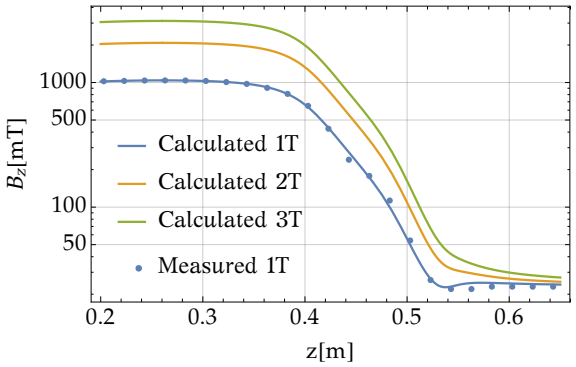

(a) The magnetic field of the setup is measured at 1T and calculated for all configurations. Calculation and measurement are in good agreement.

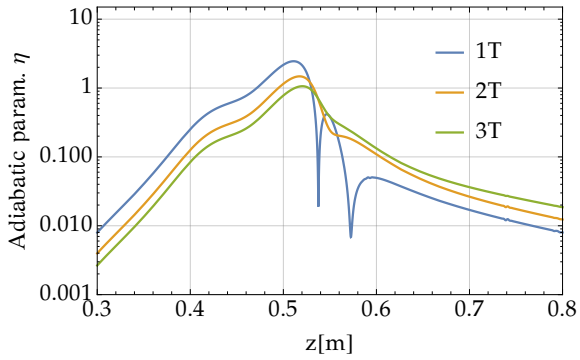

(b) By using the calculated magnetic field, an estimation of the adiabatic parameter shows, that the required condition (2.25) is not fulfilled. Consequently the evolution of the polar angle along the flight path must be analyzed in more detail.

Figure 2.12: Measurements of the magnetic field in the 1T configuration are used to tune the calculations. The calculated magnetic field allows an estimation of the adiabatic parameter.

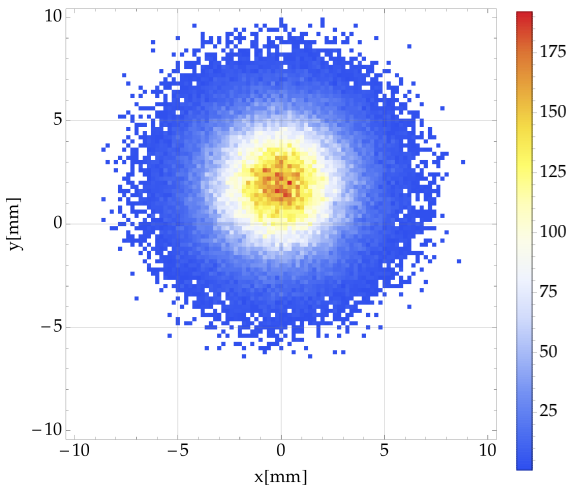

(a) At the surface of the scintillator the emitted electrons have a large spread with a radius of $\approx 1\,\mathrm{cm}$.

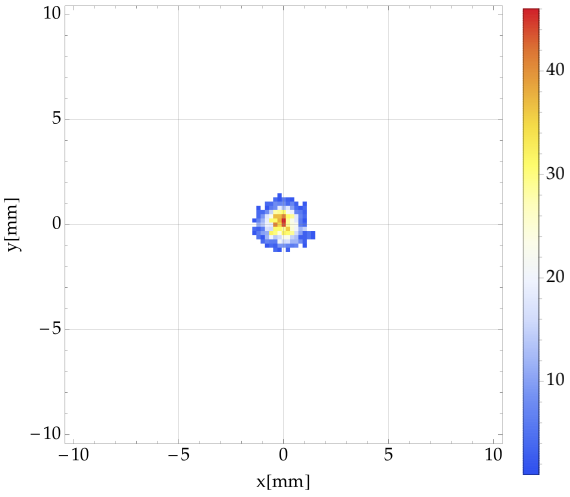

(b) The figure shows the distribution of electrons that can reach the detector in the low-field region. The magnetic flux leaves the inner region of the vacuum tube by large parts and only electrons at small distances to the center are transmitted.

Figure 2.13: The observed coincident count rate was much smaller than expected. The reason is the small diameter of the vacuum tube in the transport section. The figures show the distribution of simulated electrons originating from the ^{90}Sr source, after traversing the scintillator.

Despite the activity of 8 kBq, only a coincident rate of ≈ 30 events/s was observed at $B = 3\,\mathrm{T}$. This does not hint to a malfunction of the magnetic transport, but simply is an interaction of the electron distribution at the start detector and its imaging onto the stop detector. If the detector would be centered in the magnetic field, a coincident rate of ≈ 47 events/s would be expected from the simulation. A slight shift of the detector off axis by 2 mm may explain the deviation.

Data Analysis

In principle the ToF method does not depend on any knowledge about the energy spectrum at the stop detector. The energy of each particle is calculated by its ToF. Unfortunately the timing information depends on the signal pulse shape and therefore the whole apparatus must be calibrated. The scintillation light is guided to the PMTs by rather long light guides of lengths 50 cm for the start detector and 20 cm for the stop detector, which increases the probability for an early first photon for events with high photon yield compared to events with only few photons. Furthermore the employed constant fraction discriminator has a time-walk, delaying its output signal especially for low amplitudes.

The absolute timing of the time-to-digital converter can be calibrated by artificially extending the signal path of either the start or the stop detector by precisely known delays. The timing differences between separate measurements then yield a timing-channel-relation. For the determination of the time-walk characteristic, start and stop detector may be moved close to each other to effectively reduce the flight path to zero. The timing characteristic of coincident events in this configuration then yields the correction which has to be applied for the actual ToF measurement.

Timing Offset The minimal ToF for an electron is given by $t_{min} = l/c$ or, if the energy is known, by $t = l/(\beta c)$. During the analysis it turned out, that despite the application of the timing correction function, a considerable number of electrons would reach the detector quicker than light. Most likely, during the course of adapting the experiment to the calibration measurement, cables were switched, which would add a constant offset to the timing difference between both detectors. Although a lot of the theoretical precision is lost, this slip does not render the measurement useless:

The change of velocity is decreasing with increasing kinetic energy. Therefore the ToF is getting insensitive to the particle energy at high energies, which is confirmed by the measured time vs. energy distribution in Figure 2.14a. However, this also means, that the ToF of particles at high energies can be used for the determination of the timing offset.

$$\beta = \sqrt{1-\gamma^{-2}} = \sqrt{1-\frac{m_e^2c^4}{E^2}} \quad \Rightarrow \quad \frac{\mathrm{d}\beta}{\mathrm{d}E} = \frac{m_e^2c^4}{E^3\sqrt{1-\frac{m_e^2c^4}{E^2}}} \quad \Rightarrow \quad \Delta t \approx \frac{l m_e^2 c^3}{E^3\sqrt{1-\frac{m_e^2c^4}{E^2}}}\Delta E. \tag{2.26}$$

At 1.5 MeV kinetic energy, a precision of 1 % for the theoretical description of the spectrum would be sufficient to determine the additional constant offset with an uncertainty < 10 ps. To get an estimate of the offset, the detector function is fitted at low energies. Afterwards these parameters are fixed and only the offset is fitted. These steps are repeated until all parameters remain stable. A variation of parameters in the scattering simulation, as well as a variation of particle tracking parameters yields an estimate for the systematic uncertainty of the timing offset of 50 ps. This is not sufficient to obtain a reliable detector function, but allows to test the ToF calibration method to be applicable for electron detectors.

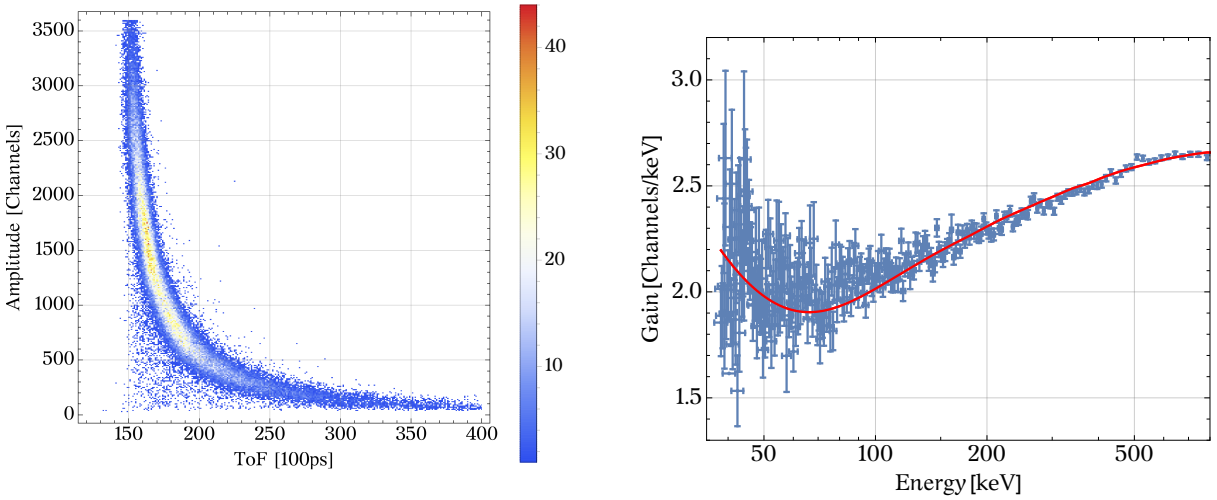

(a) At small flight times high energetic electrons are reaching the detector. Events with an amplitude > 3200 channels can be used to determine the timing offset. The low-energy events are used to determine the detector nonlinearity.

(b) The measured ToF data are used to extract a nonlinearity relation between energy and measured amplitude. The model gain curve, here defined as the ratio of mean amplitude and extracted energy, shows good agreement with the measured data.

Figure 2.14: A simultaneous fit to measured detector responses at different flight times allows the determination of the detector nonlinearity. A constant timing offset between both detectors can be fixed by exploiting the small change in ToF at high electron energies.

Detector Function Basically the same detection process as for the PERKEO III detectors must be applied here, except that only one PMT is used per detector, which largely simplifies the determination of the trigger function. The same toolkit which is used for the analysis of a Compton scattering calibration method [Sau18] is adapted to the energy determination by ToF. Results are therefore easily comparable and agree with a model assuming scintillation quenching according to Birks, presented in Figure 2.14b.

A method presented in [Roi+18] introduces an assumption about the asymptotic behavior of the detector gain at high energies. By requiring a constant gain at high energies, the timing offset can be fixed at higher precision. Incomplete energy deposition in the scintillator at high energies and electronics effects for large amplitudes may lead to nonlinearity even at high energies, though. Differences in the results between [Roi+18] and Figure 2.14b arise from releasing the restriction.

ToF Detector Charaterization in PERC

The instrument PERC is equipped with a filter magnet [Dub+08; Kon+12] which is used to enhance the sensitivity of the asymmetry measurements in neutron decay, but which could also be used as a starting field for a ToF measurement, similar to the presented measurement. Figure 2.15 shows how adiabatic transport of electrons is already guaranteed by the design of the coils and the magnetic field will be mapped and therefore well known to allow reliable tracking simulations. Assuming that the 8 m long central coil is operated at 2 % of its nominal current, the minimum magnetic field would be 30 mT. Starting at almost 6 T, starting angles of 90° would be projected onto 4°. However, the flip would not happen immediately and an intermediate flight path with $B \approx 100$ mT must be considered as

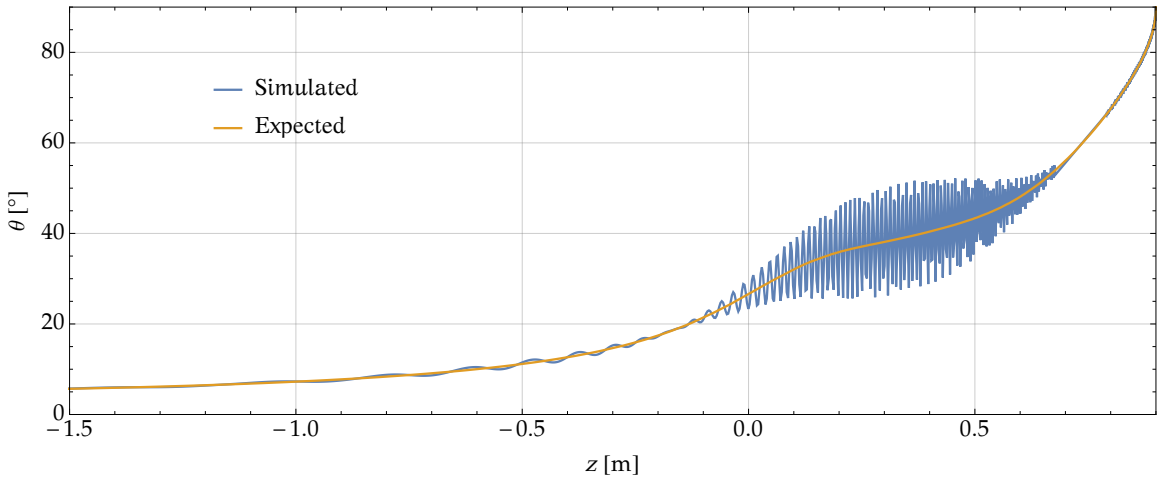

Figure 2.15: The coil configuration of PERC guarantees adiabatic transport of charged particles even for high energies (here: 800 keV) and allows the application of equation (2.23) to calculate the polar angle θ of the momentum. An initial polar angle of 90° is reduced to ≈ 6° in the long flight section.

well. A simulation of particles starting almost at 95 % of the field maximum yields a ToF difference of 10 % for particles emitted at 90° compared to particles emitted at 0°. This is comparable to the experiment performed with `Perkino`. A method to determine the angular spread of electrons at the start detector is proposed in [Dub16] and would only require minimal changes to the ToF setup.

2.3.3 Simulating Quenching

An inconvenient property of scintillation quenching as described by equation (2.22) [Bir52] is the dependency of the parameter k_B on the particle type and the inability to deduce it from first principles. The differential energy loss $\mathrm{d}E/\mathrm{d}x$, obtained from Bethe's formula or as an adaptation for electrons and positrons [RC54] tabulated in [BS64], does not express properties of the secondary particles which absorb the energy of the primary particle and are responsible for the excitation of the scintillator base material. Therefore a comprehensive description of the process cannot only depend on $\mathrm{d}E/\mathrm{d}x$. This can easily be seen by comparing the maximum energy transfer of an electron of mass m_e with kinetic energy E_{kin} to an electron and the maximum energy transfer of a proton with the mass m_p and the same kinetic energy to an electron, which classically is limited by momentum conservation:

$$\left.\frac{E_{\mathrm{max},e}}{E_{\mathrm{max},p}}\right|_{E_{\mathrm{kin}}} \overset{\text{nonrelativistic}}{=} \frac{\frac{1}{2}}{\frac{4m_p m_e}{(m_p+m_e)^2}} \approx \frac{m_p}{8m_e}. \tag{2.27}$$

The same holds for the mean energy transfer. Protons which generally have a higher energy loss than electrons [Ber+14] are releasing many low-energetic electrons, while primary electrons may release secondary electrons with energies comparable to their own. An approach, which tries to disentangle the secondary particle dependencies is presented by [Vol+66]. Therein quenching arises by quenching centers for high local energy deposition. However, there is an account for higher energetic secondaries, also called delta rays, by

assuming no quenching for these particles:

$$\frac{\mathrm{d}L}{\mathrm{d}x} = g\left[(1-F_s)\frac{\mathrm{d}E}{\mathrm{d}x}\exp\left(-\frac{k_B}{2}(1-F_s)\frac{\mathrm{d}E}{\mathrm{d}x}\right) + F_s\frac{\mathrm{d}E}{\mathrm{d}x}\right]. \tag{2.28}$$

The quenching parameter $k_B/2$ is inserted intentionally to be comparable to Birks' quenching (2.22) for small $\mathrm{d}E/\mathrm{d}x$. F_s accounts for the mean delta ray energy and depends on the energy of the primary particle and the mean excitation energy I, a material parameter:

$$F_s = \frac{1}{2}\frac{\ln\left(\frac{4m_eE}{MT_0}\right)}{\ln\left(\frac{4m_eE}{MI}\right)}. \tag{2.29}$$

T_0 is defined as the minimum energy a secondary particle must have to be considered as a delta ray and hence presents itself as second free parameter to describe scintillation quenching. Equation (2.29) assumes the primary mass $M \gg m_e$, neglecting delta rays for incident electrons, by stating that the integral energy loss of secondary particles be small for low primary particle energies; a strong statement, considering that only few eV are required to excite the scintillator. The relation also neglects quenching of secondary particles, which is considerable at energies in the 10 to 100 keV range.

A modern method which allows studying the basic idea of considering secondary electrons in more detail is the application of scattering simulations to track the particle movements. The low-energy electromagnetic Livermore physics model of `Geant4` allows tracking of electrons with energies down to 10 eV [Inc16; PCS91], which is close to energies required for atomic excitation. In this framework, any residual energy loss calculated by `Geant4` can be treated as energy that is locally transmitted to surrounding molecules.

To estimate the probability of energy transfer to one of the circumjacent fluors, a random walk Monte Carlo simulation is performed on a 3D grid representing the base molecules, doped with random occurrences of fluor molecules. The choice of a three dimensional grid is done due to observations by [Pow71], suggesting that sole one dimensional exciton migration along polymer chains is unlikely. The probability for Förster resonance energy transfer from a donor to an acceptor depends on the spectral overlap, which is assumed to be equal for all molecules, and the distance $\propto r^{-6}$. A random walk is assumed to be finished when a fluor is reached or the energy is not further non-radiatively transferred. As a result, in Figure 2.16 the overall probability of successful energy transfer to a fluor is determined, as well as the dependence on the distance between initial base excitation and final acceptor fluor. The probability for an initial excitation to be trapped by a fluor is found to depend on the fluor concentration c_f and the nonradiative transfer probability p_nr by

$$p_\mathrm{trap}(c_\mathrm{f}, p_\mathrm{nr}) = 1 - \left(1 + C_1\frac{c_\mathrm{f}}{1-p_\mathrm{nr}}\right)^{-1}, \tag{2.30}$$

with $C_1 = 0.87$, which is slightly higher than a nearest neighbor calculation by [Ros68; Rud66] who find $C_1 = 0.66$. The latter is intrinsic to nearest neighbor three dimensional random walks and denotes the probability of not returning to the origin.

The distance r of the origin to the point where the absorption takes place is distributed by

$$\frac{1}{p_\mathrm{trap}}\frac{\mathrm{d}p_\mathrm{trap}}{\mathrm{d}r} = \frac{C_{2,1}^2(1-p_\mathrm{nr}^{2C_{2,2}})}{d^2} r \exp\left(-C_{2,1}(1-p_\mathrm{nr})^{C_{2,2}}\frac{r}{d}\right), \tag{2.31}$$

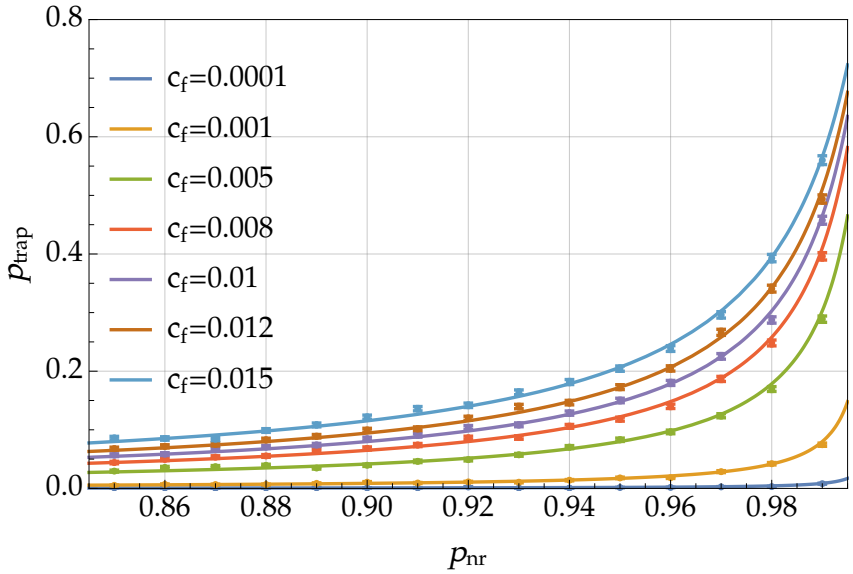

Figure 2.16: The probability of trapping an excitation is simulated by using a 3D random walk of Förster resonance energy transfers. Naturally the probability increases for larger fluor concentrations c_f. Radiative energy loss is considered as extinction of the excitation. Therefore, a large probability for non-radiative energy transfer p_{nr} also increases that probability. A simultaneous fit of equation (2.30) agrees well with simulated data.

with $C_{2,1} = 1.72$, $C_{2,2} = 0.45$ and $d = \sqrt[-3]{n}$ being the distance between two neighbouring base molecules at particle density n.

If an exciton hits an already excited fluor, either there is bimolecular excitation of a base molecule and the fluor, which could hinder fluorescence, or the random walk simply continues. For the latter case, the concentration of traps is reduced locally, also reducing the probability of hitting another fluor. A simulation taking this into account yields $C_1 = 0.78$, $C_{2,1} = 1.32$ and $C_{2,2} = 0.39$.

These simulations are performed outside of `Geant4` as the microscopic scale is beyond the scope of its particle tracking. The obtained relations can now be used to define a grid of fluors inside the detector which can be excited by neighbouring energy depositions. Since the time for emission of a fluorescence photon is much larger than the time a particle needs to be stopped, fluors can be considered to be saturated, once they are excited. In [PH71] bimolecular quenching – the formation of a higher excited state due to neighbouring excited molecules – for concentrations of *p*-Terphenyl of 0.35 % is considered to be unlikely but the depletion of unexcited fluors is assumed to be the main source of quenching. That is the crucial assumption which leads to quenching in the simulated model.

When a particle track including secondary electrons is finished, the number of excited fluors is counted and defines the number of emitted photons. By this step, reabsorption of first fluor photons is neglected, as it can be be applied later on. The free parameter range is limited by requiring an emission of ≈ 10 photons per keV [Sai14a].

Keeping these assumptions, the results of a quick first simulation are sobering: The obtained nonlinearity expressed by $k_B = (20.9 \pm 2.1)$nm/keV for equation (2.22) is too small. This is not unexpected however, since equation (2.30) is completely neglecting effects of self-quenching. Measurements by [SB53] show, that increasing concentrations of fluors lead to a saturation and later even to a decrease of the light response, reducing the effective fluor concentration.

In order to attain a realistic quenching parameter of $k_B \approx 120\,\mathrm{nm/keV}$, the effective fluor density must be decreased to 0.02 %, which is on the order of the secondary fluor concentration. It might therefore be concluded, that secondary fluor saturation is responsible for quenching effects in plastic scintillators. Further investigation to disentangle between static quenching and saturation effects will be required to gain deeper insight into scintillation processes. This might help to understand recently measured differences in $\mathrm{d}E/\mathrm{d}x$-dependencies for different types of scintillators (polyvinyltoluene and polystyrene) [Pös+18].

2.4 Light Extraction from Scintillator

Light that is produced by scintillation has to be transported to the edges of the scintillator to get detected by PMTs, which are coupled to the scintillator with light guides. Light transport is typically done via internal total reflection. Because of finite angles of total reflection and absorption, only a fraction of the initially emitted light reaches the PMTs. The effective intensity will be calculated in the first part of this section. For the PERKEO III 2014 detector, the light guides were not directly coupled to the scintillator, but a small gap with a thickness of about one sheet of paper is between the two parts. In the second part, losses resulting from this gap will be calculated.

2.4.1 Light Transport

As a good approximation, light in a scintillator gets emitted isotropically at its source. Light collection can be achieved by two methods:

1. read-out from the back
2. read-out from sides, exploiting total reflection

Both detector concepts have been applied for PERKEO measurements over the years, with different results. The first is less prone to surface deterioration and has a large overall light output when combined with a reflective coating. The second provides better detector uniformity, i.e. the independence of the light output on the impact position of the detected particle. It does not forgive careless handling however, as the concept depends on good light transport and reflection. Overall, read-out from sides has proven to be the better choice and will be treated in the following.

Light extraction from the sides is possible, because the refraction index of the scintillator of $n_S = 1.58$ [Sai14a] is quite high. This way, a large fraction of the emitted light (77 %) does not leave the scintillator through the front plane (i.e. the surface), but gets transported via total internal reflection. However, light can get absorbed in the material or the total reflection might not be perfect because of surface roughness. In the following, these effects will be investigated to calculate an effective light yield per PMT depending on the light source position.

Efforts to calculate the spatially dependent light output from surfaces have been made by [SJ49] and later, including light losses and more complicated geometries, by [Kei70]. In [Plo00] this was applied to one of the PERKEO II detectors. However, these calculations led to closed form solutions, whereas the distribution over multiple PMTs at one surface will have to be carried out numerically. More realistic results are finally obtained by ray-tracing simulations. A calculation yields quicker results however and allows to fix the principle geometry before studying higher order effects. Both methods are applied in Figure 2.24 and show comparable results.

Two cases will be covered for the following considerations:

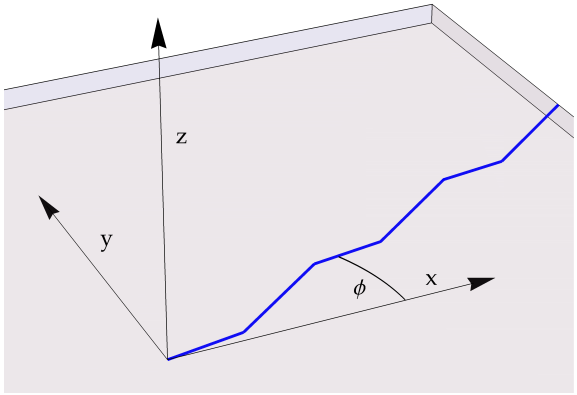

(a) In the plane parallel to the surface the light direction is defined by the azimuth ϕ. It varies between 0 and 2π.

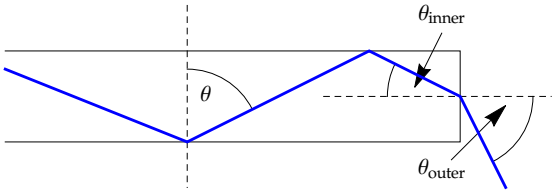

(b) The polar angle θ defines, whether the light exits through the surface or is transported through the edges.

Figure 2.17: The light direction is defined in standard spherical coordinates.

1. light guides at two edges of the scintillator and directly coupled to the scintillator,
2. light guides at four edges of the scintillator and coupled with a tiny gap in between scintillator and light guide.

These are two basic concepts for the detectors employed in PERKEO III.
The choice of these configurations is defined by a few conditions:

- maximize light output
- minimize intensity dependence on light source position
- detector must fit inside instrument

There is no optimal solution and the best compromise has to be found for each specific situation. A further simple but expensive concept is to directly couple PMTs or silicon photomultipliers to the edges of the scintillator. This yields the highest light collection efficiency, but decreases the overall detector uniformity for large scintillators.

Critical Angle

Before taking a look at special geometries, first the transport of light inside the scintillator will be considered, a process that has to be taken into account for all detectors of this kind.
The light direction is defined in spherical coordinates, which simplifies some of the calculation steps, but may quickly lead to false assumptions about the solid angle of light extraction. As in figure 2.17b, θ is the polar angle to the normal of the scintillator planes and ϕ the azimuth to the normal $\vec{n_x} = (1, 0, 0)$ of the outgoing edge.

Limits inside the Scintillator A distinction of cases provides an overview, of where light may leave the scintillator. α_{Gx}, α_{Gy} and α_{Gz} are used as critical angles of the respective planes:

$|\theta| < \alpha_{Gz}$
: The light gets lost through the surface.

$|\theta| > \alpha_{Gz}$

$|\phi| < \alpha_{Gx}$

$|\theta| < \arcsin(\frac{\cos\alpha_{Gx}}{\cos\phi})$

The light is stored in the scintillator.

$|\theta| > \arcsin(\frac{\cos\alpha_{Gx}}{\cos\phi})$

The light is emitted through the plane with normal $\vec{n_x}$.

$|\phi| > \alpha_{Gx} \wedge |\phi| < \frac{\pi}{2} - \alpha_{Gy}$

The light is stored in the scintillator.

$|\phi| > \frac{\pi}{2} - \alpha_{Gy}$

$|\theta| < \arcsin(\frac{\cos\alpha_{Gy}}{\sin\phi})$

The light is stored in the scintillator.

$|\theta| > \arcsin(\frac{\cos\alpha_{Gy}}{\sin\phi})$

The light is emitted through the y-plane.

The limits for θ are found, when applying Snell's law according to the planes, i.e.

$$\cos\phi\sin\theta = \cos\alpha_{Gx} = \sqrt{1 - n_x^{-2}} \tag{2.32}$$

$$\sin\phi\sin\theta = \cos\alpha_{Gy} = \sqrt{1 - n_y^{-2}} \tag{2.33}$$

$$\cos\theta = \cos\alpha_{Gz} = \sqrt{1 - n_z^{-2}}. \tag{2.34}$$

For now, light exiting through the x-plane will be considered. Therefore, only the angular limits of $\phi \in [-\alpha_{Gx}, \alpha_{Gx}] \ \wedge \ \theta \in \left[\arcsin(\frac{\cos\alpha_{Gx}}{\cos\phi}), \frac{\pi}{2} - \arcsin(\frac{\cos\alpha_{Gx}}{\cos\phi})\right]$ are taken into account for integration.

A further limitation of this range is introduced if a different material is used for the light guide. In the case of PERKEO III, the light guides are made of Poly(methyl methacrylate) (PMMA), or Plexiglas®. Since its refractive index is slightly smaller ($n_L \approx 1.50$ [Bea+15]) than the one of the scintillator, further photons get lost during the transport in this material.

Change of Light Direction The initial direction of light is described by the vector

$$\vec{v}_{\text{inner}} = \begin{pmatrix} \cos\phi\sin\theta \\ \sin\phi\sin\theta \\ \cos\theta \end{pmatrix}. \tag{2.35}$$

When the light reaches one of the edges of the scintillator, it will be refracted or reflected, depending on its angle to the edges normal. To simplify the calculation of the outer light direction vector $\vec{v}_{\text{outer}}$, the following transformations for a refraction at the y-z-edge are applied:

$$\vec{v}_{\text{inner}} \xrightarrow{R} \begin{pmatrix} \cos\theta_{\text{inner}} \\ 0 \\ \sin\theta_{\text{inner}} \end{pmatrix} \xrightarrow{D} \begin{pmatrix} \cos\theta_{\text{outer}} \\ 0 \\ \sin\theta_{\text{outer}} \end{pmatrix} \xrightarrow{R^{-1}} \vec{v}_{\text{outer}} \tag{2.36}$$

The rotation R is a rotation around the x-axis with the rotation angle θ_R such that $\sin\phi\sin\theta \to 0$.

$$R = \begin{pmatrix} 1 & 0 & 0 \\ 0 & \cos\theta_R & -\sin\theta_R \\ 0 & \sin\theta_R & \cos\theta_R \end{pmatrix}, \ \theta_R = \arctan(\sin\phi\tan\theta) \tag{2.37}$$

The refraction D maps the inner vector onto the outer vector following Snell's law

$$\frac{\sin\theta_{\text{outer}}}{\sin\theta_{\text{inner}}} = \frac{n_{\text{S}}}{n_{\text{L}}} = n \tag{2.38}$$

for the refraction from the scintillator into the light guide. With

$$\cos^2\theta_{\text{outer}} = n^2(\cos^2\phi\sin^2\theta - 1) + 1$$

and applying R^{-1} to rotate back into the initial frame, the direction of the outgoing light is expressed by

$$\vec{v}_{\text{outer}} = \begin{pmatrix} \sqrt{n^2(\cos^2\phi\sin^2\theta - 1) + 1} \\ \sqrt{n^2(1-\cos^2\phi\sin^2\theta)}\dfrac{\sin\phi\tan\theta}{\sqrt{1+\sin^2\phi\tan^2\theta}} \\ \sqrt{\dfrac{n^2(1-\cos^2\phi\sin^2\theta)}{1+\sin^2\phi\tan^2\theta}} \end{pmatrix} = \begin{pmatrix} \sqrt{n^2(\cos^2\phi\sin^2\theta - 1) + 1} \\ n\sin\phi\sin\theta \\ n\cos\theta \end{pmatrix} \tag{2.39}$$

The following relations were used:

$$\sin\Big(\arctan(\tan\theta\sin\phi)\Big) = \frac{\tan\theta\sin\phi}{\sqrt{1+\tan^2\theta\sin^2\phi}}$$

$$\cos\Big(\arctan(\tan\theta\sin\phi)\Big) = \frac{1}{\sqrt{1+\tan^2\theta\sin^2\phi}}$$

$$\frac{1-\sin^2\theta\cos^2\phi}{1+\tan^2\theta\sin^2\phi} = \cos^2\theta.$$

By setting $v_{\text{outer},x}$ to zero, it follows immediately, that the limits for light leaving the scintillator are given by

$$n^2(1-\cos^2\phi\sin^2\theta) = 1 \tag{2.40}$$

$$\Rightarrow \left|\frac{\pi}{2} - \theta\right| < \arcsin\left(\frac{\sqrt{1-n^{-2}}}{\cos\phi}\right) \tag{2.41}$$

$$\Rightarrow |\phi| < \arcsin n^{-1}. \tag{2.42}$$

For reasons of symmetry, the integration region for θ may be halved at $\theta = \frac{\pi}{2}$, simplifying inequation (2.41) to

$$\arcsin\left(\frac{\sqrt{1-n^{-2}}}{\cos\phi}\right) < \theta < \frac{\pi}{2} \tag{2.43}$$

Limits inside the Light Guide With the new light direction the limits from equations (2.33) and (2.34) now turn into

$$\frac{n_{\text{S}}}{n_{\text{L}}}\sin\phi\sin\theta = \sqrt{1-n_{\text{L}}^{-2}} \tag{2.44}$$

$$\frac{n_{\text{S}}}{n_{\text{L}}}\cos\theta = \sqrt{1-n_{\text{L}}^{-2}}. \tag{2.45}$$

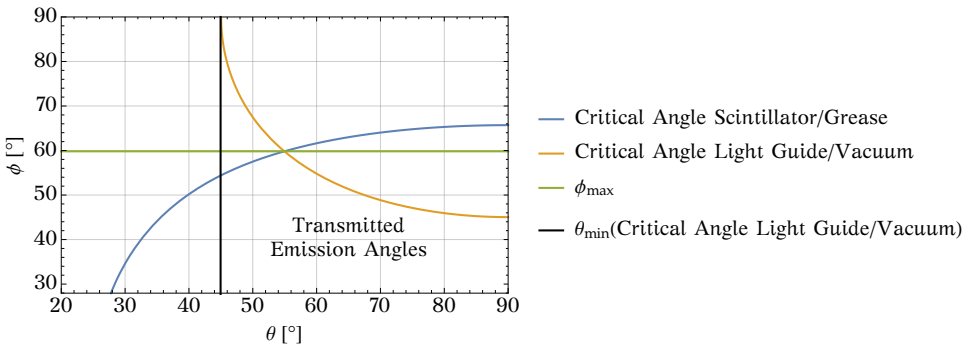

Figure 2.18: The combination of refractive indices for scintillator and light guide limits the angles taken into account for integration to the lower right part, i.e. small ϕ and large θ.

This further decreases the integration limits to

$$\theta \in \left[\max\left(\arcsin\left(\frac{\sqrt{1-\frac{n_L^2}{n_S^2}}}{\cos\phi} \right), \arccos\left(\frac{\sqrt{n_L^2-1}}{n_S} \right) \right), \begin{cases} \frac{\pi}{2}, & |\phi| < \arcsin\left(\frac{\sqrt{n_L^2-1}}{n_S} \right) \\ \arcsin\left(\frac{1}{n_S} \frac{\sqrt{n_L^2-1}}{\sin\phi} \right), & \text{otherwise} \end{cases} \right] \tag{2.46}$$

In particular, this also further limits ϕ, since

$$\frac{1}{n_S} \frac{\sqrt{n_L^2-1}}{\sin\phi_{max}} = \frac{\sqrt{1-\frac{n_L^2}{n_S^2}}}{\cos\phi_{max}} \text{ at } \phi_{max} = \arctan\left(\sqrt{\frac{n_L^2-1}{n_S^2-n_L^2}} \right) \tag{2.47}$$

Figure 2.18 shows the resulting limitations. The figure also considers the grease which is used to ensure an optical coupling between scintillator and light guide. See below for an estimate of its refractive index.

Attenuation

The employed materials polyvinyltoluene and PMMA have a finite attenuation length which leads to a decrease of the intensity of the light. In [Sai14a] the bulk attenuation length for the scintillator BC-400 is given as $\frac{1}{\lambda} = 250\,\text{cm}$ and in [Sai14b] $\frac{1}{\lambda} > 400\,\text{cm}$ for the scintillator BC-440. The attenuation length of PMMA is $\approx 1\,\text{m}$ but will be varied later on. Additionally, with each reflection, roughness of the surfaces can cause a loss of light. This can be accounted for by an additional approximative effective attenuation of $\lambda_{rough} = -\ln(\omega)(\frac{\cos\theta}{h} + \frac{\sin|\phi|\sin\theta}{w})$ with $1-\omega$ being the light loss per reflection, $h = 5\,\text{mm}$ the thickness of the detector and w the height of the scintillator or the light guide. Since the roughness is not known, the effective absorption length $(\lambda + \lambda_{rough})^{-1}$ is a free parameter which has to be deduced from the measurements.

A light beam starting from position $x = x_0$ with angles ϕ and θ traverses a path length $\frac{\frac{l_S}{2}-x}{\cos\phi\sin\theta}$ inside a scintillator of length l_S and a path length $\frac{l_L}{\sqrt{\frac{n_S^2}{n_L^2}(\cos^2\phi\sin^2\theta-1)+1}}$ inside a straight

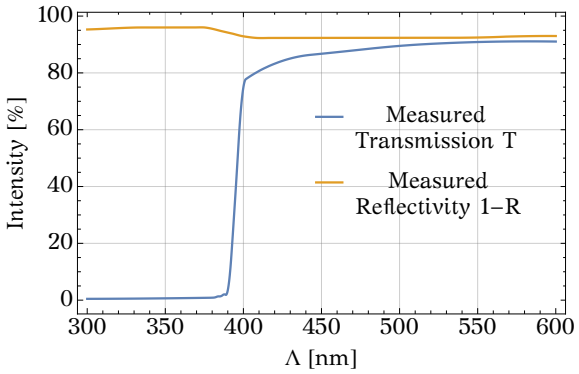

(a) The curves of reflectivity and transmittance for Plexiglas® GS 222, measured by the manufacturer, show that the light guides are almost opaque for UV-light.

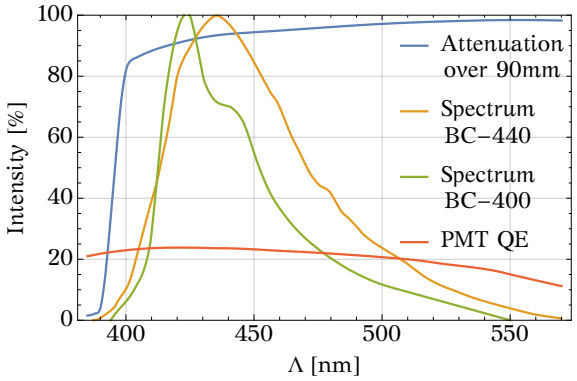

(b) The drop of transmittance t when attaining the UV-region affects the spectra of the scintillation light [Sai14a; Sai14b]. This effect is slightly compensated by the decreasing quantum efficiency of the PMTs [Ham95] for larger wavelengths.

Figure 2.19: The limited transmittance of the PMMA light guides affects the spectrum that reaches the PMTs. With increasing light path, the mean wavelength of the light reaching the PMTs is increasing as well.

light guide of length l_L. The final intensity after attenuation on the way to the PMT now is

$$I(x,\phi,\theta,\omega) = \omega^{n_{Ry}} \cdot \exp\left(\frac{-(\lambda_\mathrm{L} - \ln(\omega)(\frac{\cos\theta}{h} + \frac{\sin|\phi|\sin\theta}{w_\mathrm{L}}))l_\mathrm{L}}{\sqrt{\frac{n_\mathrm{S}^2}{n_\mathrm{L}^2}(\cos^2\phi\sin^2\theta - 1) + 1}} + \frac{-(\lambda_\mathrm{S} - \ln(\omega)\frac{\cos\theta}{h})\left(\frac{l_\mathrm{S}}{2} - x\right)}{\cos\phi\sin\theta}\right). \tag{2.48}$$

The part $\frac{\sin|\phi|\sin\theta}{w_\mathrm{S}}$ was omitted here and replaced by $\omega^{n_{Ry}}$, which accounts for the exact number of reflections n_{Ry} on the y-plane of the scintillator. This can be done, because n_{Ry} is known from the calculation of accepted angles.

So far, the attenuation length λ is assumed to be a constant, but for PMMA it actually depends on the wavelength. The wavelength dependent reflectivity and transmittance are shown in Figure 2.19a for light passing a block of $L = 90\,\mathrm{mm}$ of Plexiglas® GS 222. Since these are measured values – the measured reflectivity R and the measured transmission T – they have to be transformed to r – the probability for reflection at one surface – and t – the probability for transmission through one surface:

$$R = r + (1-r)trt(1-r) = r(1 + t^2(1-r)^2) \tag{2.49}$$

$$T = (1-r)^2 t. \tag{2.50}$$

Here up to one reflection is allowed. The solution to these equations are solutions to polynomials of third order and therefore expressed in closed form. The net transmittance t as well as the scintillation spectra of BC-400 from [Sai14a] and BC-440 from [Sai14b] are shown in Figure 2.19b.

The final light output after a path length l can be obtained by integrating over the complete

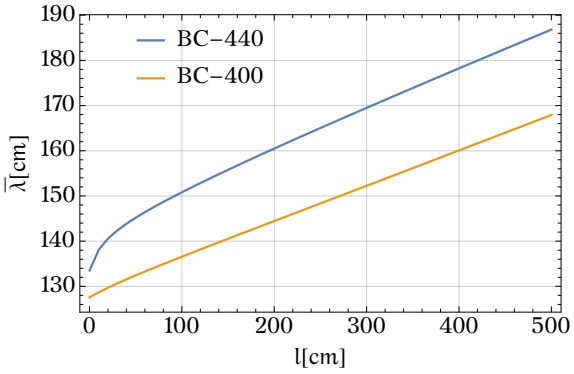

Figure 2.20: The attenuation depends on the wavelength. This leads to a different attenuation and scintillation spectrum at the PMT for different path lengths.

light path attenuation and the scintillation spectrum $\mathscr{S}(\Lambda)$.

$$I(l) = \frac{\int_{\Lambda_{\min}}^{\Lambda_{\max}} t(\Lambda)^{l/L} \mathscr{S}(\Lambda) \mathrm{d}\Lambda}{\int_{\Lambda_{\min}}^{\Lambda_{\max}} \mathscr{S}(\Lambda) \mathrm{d}\Lambda} = \int_{\Lambda_{\min}}^{\Lambda_{\max}} t(\Lambda)^{l/L} \iota(\Lambda) \mathrm{d}\Lambda \tag{2.51}$$

$$\overline{\lambda}_{\mathrm{L}}(l) = -\frac{\ln I(l)}{l} \tag{2.52}$$

In Figure 2.20 $\overline{\lambda}(l)$ displays an almost linear dependence on the path length l.

Fresnel Reflection

Light that moves between two media of different refractive indices can be reflected although its incident angle is below the critical angle. For non-magnetic materials and unpolarized light the probability of reflection can be expressed as [Hec02]

$$R = \frac{1}{2}\left[\left(\frac{n_{\mathrm{out}} \cos\alpha_{\mathrm{in}} - n_{\mathrm{in}} \cos\alpha_{\mathrm{out}}}{n_{\mathrm{out}} \cos\alpha_{\mathrm{in}} + n_{\mathrm{in}} \cos\alpha_{\mathrm{out}}}\right)^2 + \left(\frac{n_{\mathrm{in}} \cos\alpha_{\mathrm{in}} - n_{\mathrm{out}} \cos\alpha_{\mathrm{out}}}{n_{\mathrm{in}} \cos\alpha_{\mathrm{in}} + n_{\mathrm{out}} \cos\alpha_{\mathrm{out}}}\right)^2\right]. \tag{2.53}$$

Since α_{out} is connected to α_{in} by $\sin\alpha_{\mathrm{out}} = \frac{n1}{n2}\sin\alpha_{\mathrm{in}}$ and transmission to light guides corresponds to transitions through the x-plane, the relation changes to

$$R(n,\chi) = \frac{\left(n^2-1\right)^2\left(2n^2\chi^4 + \left(1-3n^2\right)\chi^2 + n^2\right)}{(n\chi + \sqrt{n^2\left(\chi^2-1\right)+1})^2(n\sqrt{n^2\left(\chi^2-1\right)+1}+\chi)^2}, \tag{2.54}$$

with

1. scintillator → grease

$$n_1 = \frac{n_{\mathrm{S}}}{n_{\mathrm{Grease}}}, \chi_1 = \cos\phi\sin\theta \tag{2.55}$$

2. grease ↔ light guide

$$n_{2,3} = \frac{n_{\mathrm{Grease}}}{n_{\mathrm{L}}}, \chi_{2,3} = \sqrt{\frac{n_{\mathrm{S}}^2}{n_{\mathrm{Grease}}^2}(\cos^2\phi\sin^2\theta - 1) + 1} \tag{2.56}$$

3. grease → PMT faceplate

$$n_4 = \frac{n_{\text{Grease}}}{n_{\text{PMT}}}, \chi_4 = \sqrt{\frac{n_{\text{S}}^2}{n_{\text{Grease}}^2}(\cos^2\phi \sin^2\theta - 1) + 1} \tag{2.57}$$

4. PMT faceplate → photocathode

$$n_5 = \frac{n_{\text{PMT}}}{n_{\text{PC}}}, \chi_5 = \sqrt{\frac{n_{\text{S}}^2}{n_{\text{PMT}}^2}(\cos^2\phi \sin^2\theta - 1) + 1}. \tag{2.58}$$

Since the Fresnel reflection slightly polarizes the outgoing light, the polarization in the case of transition from light guide to PMT could be taken into account. However, the probability for reflection in the latter case is rather small and later uncertainties are much larger, so this effect can be neglected.

By regarding Fresnel reflections, the probability of light being directly transmitted into the photocathode of the PMT decreases by a factor of

$$\prod_{i=1}^{5}(1 - R(n_i, \chi_i)).$$

In the case of reflection, the light path length increases, which leads to a higher absorption probability and allows to neglect more than one Fresnel reflection. The refractive index of the PMT faceplate is assumed to be $n_{\text{PMT}} \approx 1.50$ [Sch15] with borosilicate glass as the given material [Ham95] for the PMT R5924. The specific type of glass is not named, however the refractive index of 1.50 that is referenced in the data sheet of the comparable PMT R1307 [Ham98] leads to the assumption, that the glass type BK10 or similar is used. Absorption will be neglected, since the light loss for a thin window is smaller than 1‰.

More challenging are the properties of the vacuum grease that is used to connect optical elements without gaps. Both candidates, Dow Corning® High Vacuum Grease and Rhodorsil – Graisse pour Vide, formerly fabricated by Rhône-Poulenc, are based on the silicone Polydimethylsiloxane whose physical properties have been investigated by [Sch+09]. Although both greases share the same basis, [Plo00] showed significant differences in light transmission for both fabricates, which could be due to the additional substances inside the products. Especially the former seems a lot more opaque when taken in larger quantities, indicating a higher absorbance. For instance, [Lee+08] showed that it is possible to attain a large variation of the optical properties by adding e.g. ZrO_2-nanoparticles. Despite these facts, for further calculation the refractive index will be kept at $n_{\text{Grease}} \approx 1.44$ and absorption will be neglected due to the low thickness of the layer.

The optical properties of the directly attached photocathode – it is coated by evaporation – have been investigated by [MS05]. Hamamatsu® would not provide information about the exact composition of the photocathode, but the quantum efficiency curve in [Ham95] leads one to assume that it basically consists of RbCsSb. According to [Ham07] the measurement of the quantum efficiency already includes reflectivity effects. By assuming perpendicular incidence of light and PMTs coupled to air, the new quantum efficiency can be estimated to

$$\eta(\phi, \theta, \Lambda) \approx \frac{[1 - R(n_4, \chi_4)]\,[1 - R(n_5, \chi_5)]\,[1 + R(n_4, \chi_4)\,R(n_5, \chi_5)]}{\left[1 - R\left(\frac{1}{n_{\text{PMT}}}, 1\right)\right]\left[1 - R\left(\frac{n_{\text{PMT}}}{n_{\text{PC}}}, 1\right)\right]\left[1 + R\left(\frac{1}{n_{\text{PMT}}}, 1\right)R\left(\frac{n_{\text{PMT}}}{n_{\text{PC}}}, 1\right)\right]}\eta_{R5924}(\Lambda). \tag{2.59}$$

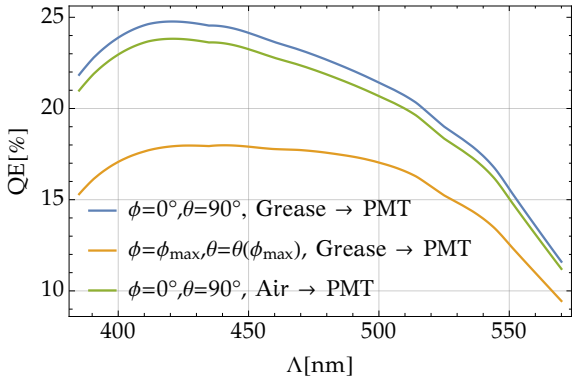

Figure 2.21: The quantum effeciency given in [Ham95] (green line) is corrected by calculating adapted reflectivities.

The impact of this correction is shown in Figure 2.21.

Double reflection inside the faceplate is included here, since the refractive index of the photocathode is quite large and thus also the probability for reflection. A photon that gets reflected at the PMT will henceforth be declared as lost, since it will likely be absorbed inside light guides or the scintillator and the actual endpoint of its path is hard to predict.

The increased absorbance for higher angle impinging photons due to the increased effective thickness, which is discussed in [MS05] is not included here. However, with increasing thickness, the absorbance of the photoelectron increases as well. A simple assumption for the probability of an electron to escape would be

$$p_{\mathrm{PE}} = \frac{1}{d}\int_0^d (1-\mathrm{e}^{-x/\lambda_\gamma})\mathrm{e}^{-(d-x)/\lambda_{e^-}}\,\mathrm{d}x = \frac{\lambda_{e^-}}{d}\left(1+\frac{1}{\lambda_{e^-}-\lambda_\gamma}\left(\lambda_\gamma \mathrm{e}^{-d/\lambda_\gamma}-\lambda_{e^-}\mathrm{e}^{-d/\lambda_{e^-}}\right)\right), \tag{2.60}$$

where λ_γ and λ_{e^-} are the mean free paths of photon and electron and d the thickness of the photo layer. For the conception of a PMT one would try to increase this probability, i.e. choosing the thickness d of the PMT such that the outcome of photoelectrons is maximized for a standardized setup. With increasing thickness d/χ, the quantum efficiency would therefore further diminish. While λ_γ can be calculated from the imaginary part of the refractive index n_{PC} and the thickness d from the transmission, the actual absorbance for electrons λ_{e^-} is still unknown and it cannot be proven that d was chosen to be at the maximum, therefore the effect will be neglected for now.

Integration

Up to now the intensity of one particular light beam at the PMT has been calculated. Since the PMT is covering a whole area, the full intensity of a particular light source is obtained by integration over a range of emission angles. Using the intensity from equation (2.48), the detected light emitted from a point (x,y) is written as

$$\begin{aligned} I(x,y,\omega) = \int_\Lambda \int_{\phi(x,y)} \int_{\theta_{\min}(\phi)}^{\theta_{\max}(\phi)} \sum_{n_R=0}^{1} \left[\prod_{i=1}^{3}(1-R(n_i,\chi_i))\right]\eta(\phi,\theta,\Lambda)\cdot \\ [R(n_1,\chi_1)+(1-R(n_1,\chi_1))^2 R(n_2,\chi_2)]^{n_R}\cdot \\ I(x+n_R\times l_S,\Lambda,\phi,\theta,\omega)\sin\theta\,\mathrm{d}\theta\mathrm{d}\phi\mathrm{d}\Lambda \end{aligned} \tag{2.61}$$

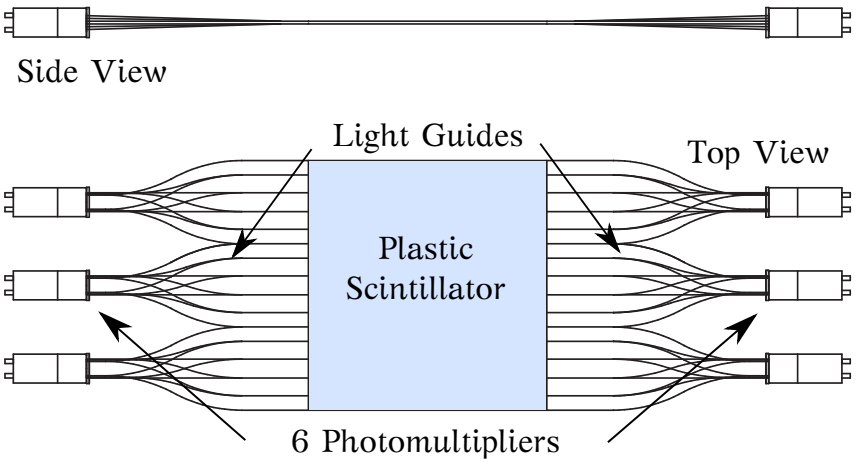

Figure 2.22: The PERKEO III 2009 detector was read out from the sides. The scintillators size was $43 \times 45\,\mathrm{cm}^2$, coupled to light guides of 40 cm length. To fit into the instrument, the vacuum vessels were extended by "ears". Figure adapted from a sketch by M. Schumann.

with θ being limited to the range (2.46) on page 53. The variables n_i and χ_i are defined in equations (2.54) – (2.58). Fresnel reflections at the scintillator-to-light guide edge are limited to the first order ($n_R \leq 1$). No closed form solution is found for this expression, which can be calculated numerically however.

2.4.2 Perkeo III 2009 Detector

For the beam time 2009, the detector was chosen to be read out from two sides. To increase the light output, the light guides were directly coupled to the scintillator using an optical grease.

This setup allows a direct application of equation (2.61). Since each side is split into three parts – one inner and two outer PMTs – first the limiting regions $\phi(x,y)$ have to be calculated. Figure 2.23 shows the mapped integration region.

The obtained formula allows to visualize the detected light intensity depending on the position of emission. Examples for single PMTs are shown in figure 2.25.

The exact geometry of the light guides as in 2.22 is not included in the calculations. Since five separate light guides per PMT lead to the centered PMT, the light guides are curved and therefore are not of equal length. This could be accounted for by splitting the detector in 15 separate sections and introducing adapted lengths for the light guide segments. Difference due to this effect are small, as a comparison to a Monte-Carlo simulation with a realistic geometry in Figure 2.24 proves.

2.4.3 Perkeo III 2014 Detector

For the PERKEO III 2014 detector from Figure 1.7b, the light guides were not directly coupled to the scintillator, but a small gap with the thickness of about one sheet of paper is between the two parts. This way, light losses inside the light guides are reduced, but light may actually be stored inside the scintillator. That simplifies the limits of the integral (2.61) to expressions (2.42) and (2.43). However, a non-negligible fraction of light gets lost in the newly created gap.

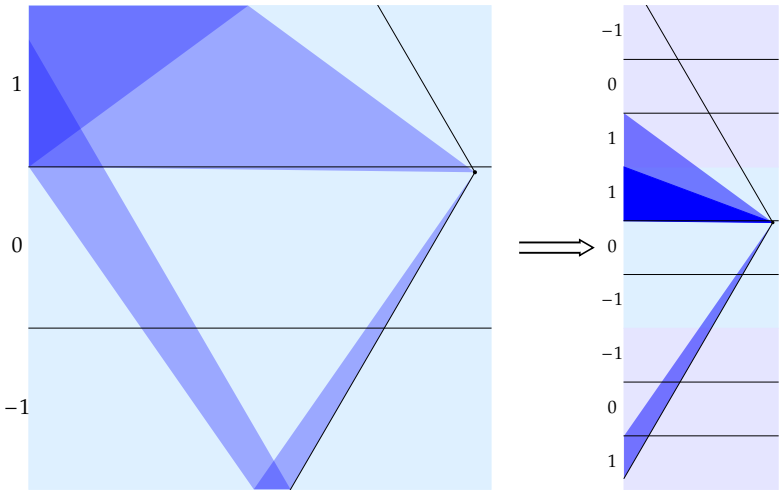

Figure 2.23: Multiple reflections at the top and bottom planes lead to multiple light cones mapped to the scintillators x-plane. Therefore a piecewise integration over ϕ has to be done. Horizontal lines depict the separation between PMTs/light guides. In this figure light cones which reach the top left PMT of the PERKEO III 2009 detector are drawn.

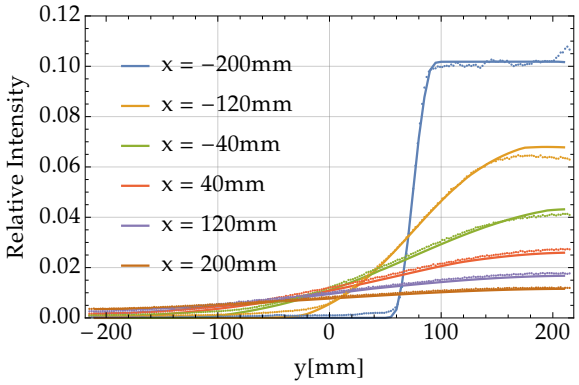

(a) The calculation (lines) for the light outcome at the outer PMTs compared to simulations (dots).

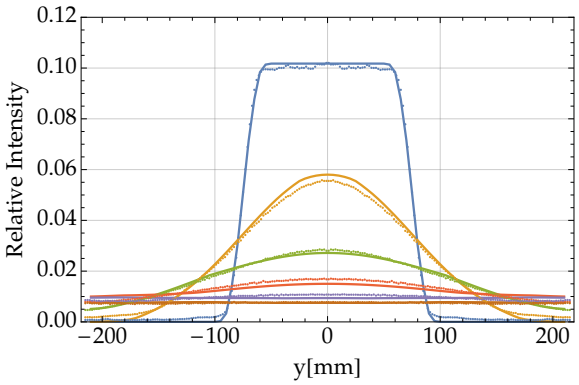

(b) The calculation (lines) for the light outcome at the middle PMTs compared to simulations (dots).

Figure 2.24: A comparison of the outcome of equation (2.61) with data from a simulation with `Geant4` done by [Sau15] shows good agreement. Larger differences are due to the form of the light guides, which has been approximated as straight and equally shaped in the calculation, whereas the simulation includes their real geometry. Furthermore, the simulation respects roughness by allowing isotropic reflection, while in the calculation it is accounted for by a fixed loss probability.

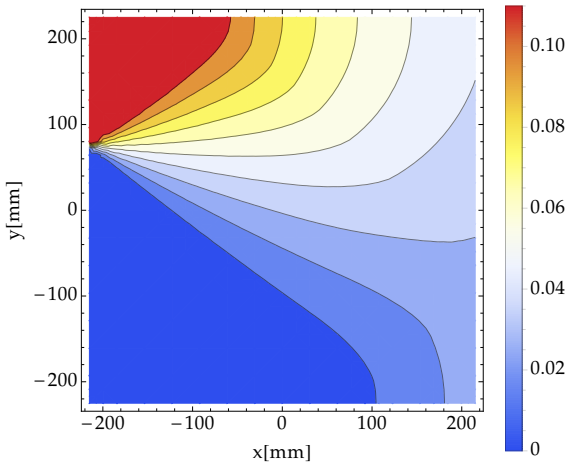

(a) Light intensity at the upper left PMT without roughness.

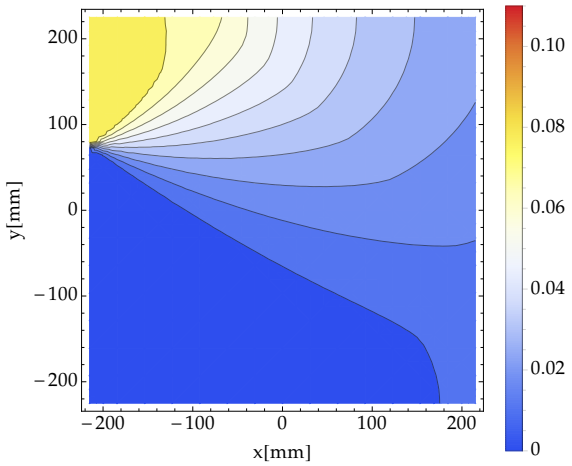

(b) Light intensity at the upper left PMT with a light loss of 1% per reflection.

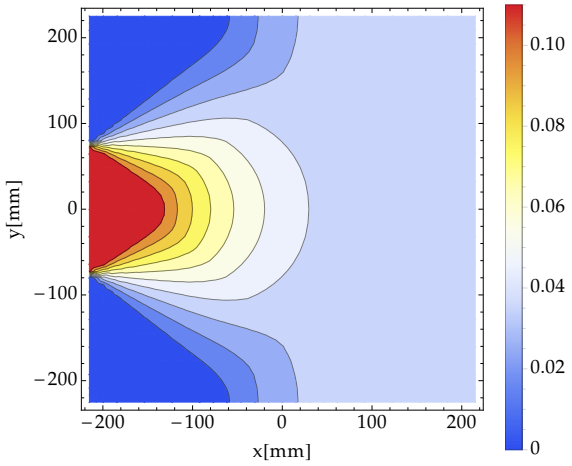

(c) Light intensity at the middle left PMT without roughness.

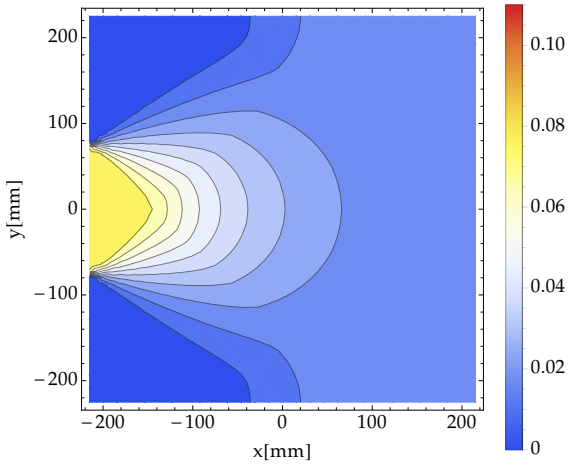

(d) Light intensity at the middle left PMT with a light loss of 1% per reflection.

Figure 2.25: The position dependent light intensity per PMT of the PERKEO III 2009 detector shows both, angular and distance dependence. Without losses, the maximum incoming light intensity is at 11% right before the light guides. A loss of 1% per reflection decreases the light intensity significantly.

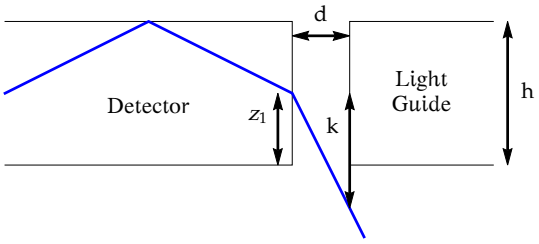

Figure 2.26: The refraction inside the gap between detector and light guide increases the light loss. If the projected path length k is larger than z_1, the light will not be coupled into the light guide.

Losses in the Gap between Scintillator and Light Guide

For now it will be assumed that light only gets lost in the z-direction, as if the scintillator would be infinitely large. Furthermore, the probability for light emission shall be equal at any depth z_0, such that the same can be said for the z_1-coordinate at the scintillator edge. Actually this would only apply for impinging electrons with high energies – most of the detected electrons do not penetrate deeper than 1 mm. The error introduced by this assumptions is negligible.

Figure 2.26 depicts the light loss in a gap of width d, if the projection k of the outgoing position z_1 of the photon onto the ingoing position is larger than the thickness h of the light guide allows. Expressed by the means of equation (2.39) this implies

$$k = \frac{d\ \cos\theta}{\sqrt{\cos^2\phi \sin^2\theta - 1 + n_S^{-2}}} > z_1 \tag{2.62}$$

Solving this equation leads to

$$\theta < \arctan\left(\frac{\sqrt{d^2\ n_S^2 + \left(n_S^2 - 1\right) z_1^2}}{z_1\sqrt{1 - n_S^2 \sin^2\phi}}\right), \tag{2.63}$$

which shows that the lower integration limit of equation (2.43) changes to

$$\arcsin\left(\frac{\sqrt{1 - n_S^{-2}}}{\cos\phi}\right) \rightarrow \arctan\left(\frac{\sqrt{d^2\ n_S^2 + \left(n_S^2 - 1\right) z_1^2}}{z_1\sqrt{1 - n_S^2 \sin^2\phi}}\right) \tag{2.64}$$

to compensate for the loss in the gap. At $d = 0$ this transformation is the identity as expected. The complete loss can be accounted for by integrating $I(x, \phi, \theta, \omega)$ over z from 0 to h, if the assumption of an equally distributed light output at the edge of the scintillator is kept. The variation of z will decrease the integration range for θ. Assuming a gap of about 100 um (one sheet of paper), the loss is about 2 %. Figure 2.27b illustrates that in the region of reasonable gap sizes, the light loss increases proportionally with the gap. The effect may be reduced by increasing the thickness of the light guide. This would require a larger read-out cross section at the end of the light guides, though.

Fresnel Reflections Increased

By increasing the number of boundary surfaces, i.e. using a gap, the probability for Fresnel reflections, which grows with $\frac{n_1}{n_2}$, gets larger as well. Furthermore, if light is reflected at

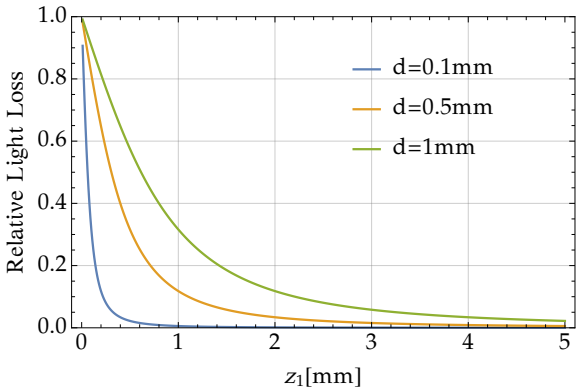

(a) With decreasing distance to the detector surface, the relative loss of light increases. Here, refraction is considered for one direction only.

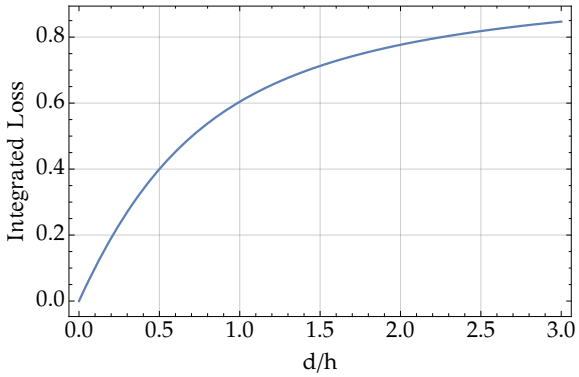

(b) The integrated light loss depends on the ratio d/h of gap size and light guide thickness, so the gap should be as small as possible.

Figure 2.27: Losses due to the gap, when assuming that no absorption takes place in the scintillator.

the surface of the light guide, the path length inside the gap doubles, compared to equation (2.62). These effects have to be taken into account when applying equation (2.61) to the new detector design. Figure 2.28 shows a typical light response distribution for the upper PMT on the left side of the detector.

Coupling Directly to the Light Guide

The decrease of integration range for a coupling with gaps shows that the overall light output for a detector with directly coupled light guides would be larger. On the other hand, the angular acceptance for the integrated light signal did not depend on the light source position so far. Figure 2.29 shows how direct coupling may increase position dependency of the light yield. Photons may enter the closest light guide, but eventually leave it again, whereas a gap ensures that light which enters a light guide should remain inside. In Figure 2.30a the angular acceptance of directly coupled light guides is shown to be larger. On the other hand, Figure 2.30b depicts the position dependence.

2.4.4 Monte Carlo Simulations

The simulations for light transport inside the PERKEO III 2009 [Sau15] and 2014 [Ber17] detectors are performed using `Geant4` [All+16]. These simulation include all features discussed here, but also allow surfaces to be defined as rough, which basically introduces a probability for non-planar reflection. This feature is superior to assuming a simple light loss probability, as it also allows a change of direction inside the scintillator.

2.4.5 Localization of Events

An event on one of the detectors consists of time information and amplitudes for each of the PMTs. As seen in the last section 2.4.1, the light response has a signature for specific regions over the detector. This should allow a reconstruction of the event position by analyzing the corresponding set of PMT amplitudes. This may be useful to verify the detector positioning

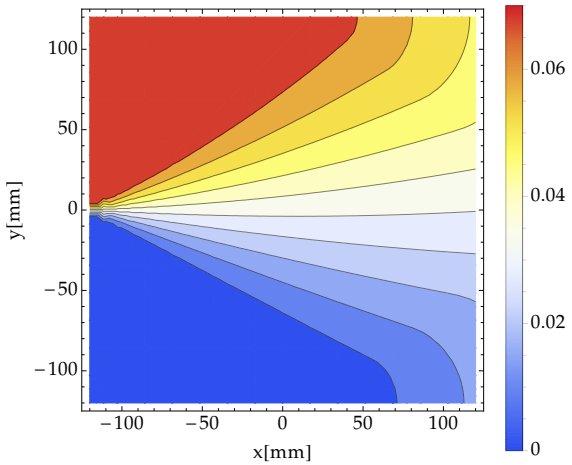

Figure 2.28: Here the position dependent light yield of the PERKEO III - 2014 detector is shown for the upper left PMT. It is similar to Figure 2.25a. The absolute value is smaller due to the losses in the gap between scintillator and light guide. This is compensated by using PMTs on all four sides of the scintillator.

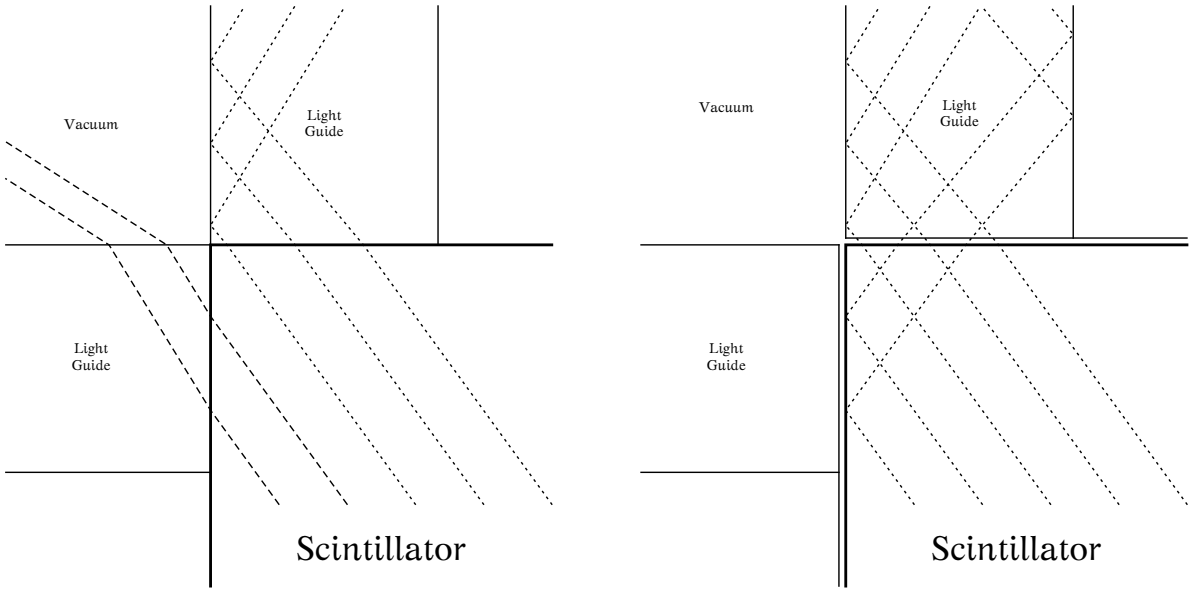

(a) Without gap, some of the photons entering the left guide are lost, since their angle is too large for total reflection on the upper face. Figure 2.30b shows the corresponding detector uniformity.

(b) With a tiny gap, photons should not leave through the light guides. Not shown here is that a part of the light is stored inside the scintillator, however.

Figure 2.29: For read-out from four sides direct coupling of the light guides to the scintillator should be avoided to keep the position dependency of the light yield low. The gaps reduce the overall light collection efficiency however.

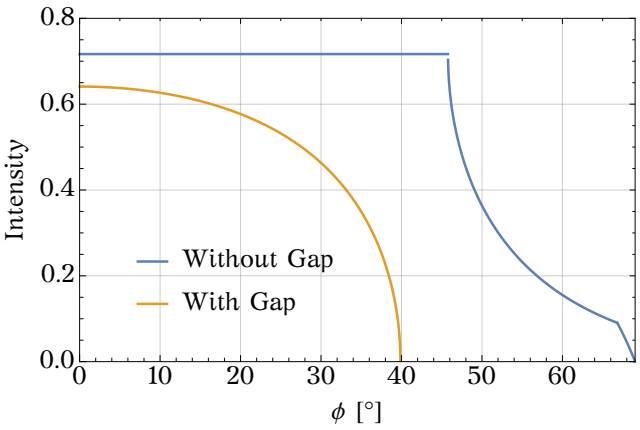

(a) Coupling the light guides directly to the scintillator reduces the number of interfaces and therefore increases the overall light output. With gaps, a part of the light is stored inside the scintillator and absorbed eventually.

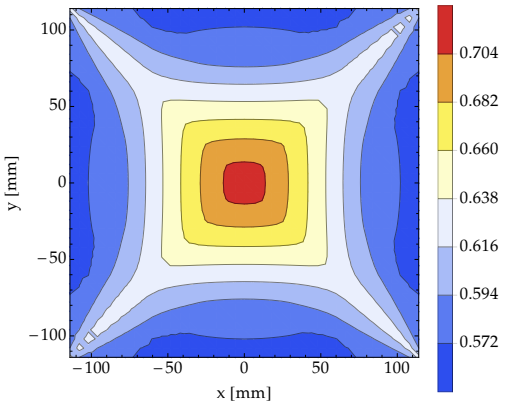

(b) Without gaps, light emitted along the detector diagonals has a higher probability to remain inside one of the light guides.

Figure 2.30: A calculation which neglects all absorption effects shows the accepted angles of light emission with and without gap between scintillator and light guides. The increased light yield without gaps comes at the price of a poor uniformity.

or identify and exclude anomalous events from the analysis. In section 3.4 the method is applied to identify a background source.

The emission of scintillation light is a statistical process and therefore subject to fluctuations following a Poisson distribution

$$p(n_\gamma, \lambda) = \frac{\lambda^{n_\gamma}}{n_\gamma!} \mathrm{e}^{-\lambda}. \tag{2.65}$$

The expected amount of light is expressed in λ, whereas the observed number of photons n_γ can vary around the mean value. The relative width of the distribution $\frac{n_\gamma}{\lambda}$ decreases with an increasing λ, so the better the light output, the better is the chance to get a reliable position reconstruction.

The number of photons per MeV of incident particle energy is given in [Sai14a] as a percentage of anthracene scintillator efficiency.

$$\lambda(E, x, y) = E \times 17\,400\,/\mathrm{MeV} \times 65\,\% \times \eta_{\mathrm{PMT}} \times I(x, y) \tag{2.66}$$

$$= \lambda_0(E) \times \eta_{\mathrm{PMT}} \times I(x, y). \tag{2.67}$$

An additional factor η_{PMT} is introduced here which accounts for quantum efficiency of the PMTs which describes how many of the incident photons actually get converted into a measurable signal. $I(x, y)$ from equation (2.61) returns the detection efficiency for light that originates from a position (x, y) on the detector. At low number of photons this process actually does not follow a Poisson distribution, but for the purpose of testing the method it fulfills the requirements. The nonlinear photon emission dependence on E can be accounted for by replacing λ_0 by a suitable nonlinear function from section 2.3.

The number of measured photons n_γ can be obtained from the PMT amplitude which is given in channels C by a gain factor $g = \frac{C}{n_\gamma}$. This factor, as well as the quantum efficiency is not exactly known and can also be obtained from the response function.

Likelihood Method

A common way to optimize a set of parameters is the minimum χ^2 estimation. However, the parameter finding for a relatively simple model can be accelerated by using the Likelihood method where the probability for the observed events is going to be maximized. I.e. for a probability density function $f(x_i \mid \theta)$ with a set of parameters θ, the so-called joint density function

$$f(x_1, x_2, ..., x_{n_E} \mid \theta) = \prod_{i=1}^{n_E} f(x_i \mid \theta) \tag{2.68}$$

has to be maximized. For the detector response function, f must be split into the product of the Poisson light distributions of each PMT. The set of gain g_j and quantum efficiency η_j for each PMT j has to be determined such that this product turns out to be the most likely combination for measured amplitudes C_{ij}:

$$\mathscr{L}_{max} = \max\left(\prod_{i=1}^{n_E} \prod_{j=1}^{n_{\mathrm{PMT}}} \frac{\lambda_{ij}^{\left\lfloor \frac{C_{ij}}{g_j} \right\rfloor}}{g_j \left\lfloor \frac{C_{ij}}{g_j} \right\rfloor !} \mathrm{e}^{-\lambda_{ij}} \right) \tag{2.69}$$

$$\lambda_{ij} = \lambda_{ij}(E, \eta_j, x_i, y_i) = \lambda_0(E) \times \eta_j \times I_j(x_i, y_i). \tag{2.70}$$

Since only integer values are allowed for the number of photons n_γ, the Poisson distribution has steps that are inconvenient for numerical minimizer algorithms. For this reason, the distribution can be transformed into a continuous approximation

$$\mathscr{L}_{max} \approx \max\left(\prod_{i=1}^{n_E} \prod_{j=1}^{n_{\mathrm{PMT}}} \frac{\lambda_{ij}^{\frac{C_{ij}}{g_j} - \frac{1}{2}}}{g_j \Gamma\left(\frac{C_{ij}}{g_j} + \frac{1}{2}\right)} \mathrm{e}^{-\lambda_{ij}} \right). \tag{2.71}$$

For a large number n_E of events, $\mathscr{L}$ will become very small, so a common way to calculate the maximum is to take the logarithm, which is a monotonically increasing function, of the product which turns the expression into a sum, the log-likelihood:

$$\hat{\ell}_{max} = \frac{1}{n_E} \ln \mathscr{L}_{max} \tag{2.72}$$

$$\approx \max\left[\frac{1}{n_E} \sum_{i=1}^{n_E} \sum_{j=1}^{n_{\mathrm{PMT}}} \left(\left(\frac{C_{ij}}{g_j} - \frac{1}{2} \right) \ln \lambda_{ij} - \ln g_j - \ln \Gamma\left(\frac{C_{ij}}{g_j} + \frac{1}{2} \right) - \lambda_{ij} \right) \right]. \tag{2.73}$$

A fixed set of parameters g and η can now be used to determine the approximate position (x_i, y_i) of each event i by minimizing

$$- \sum_{j=1}^{n_{\mathrm{PMT}}} \left(\left(\frac{C_{ij}}{g_j} - \frac{1}{2} \right) \ln \lambda_{ij} - \ln g_j - \ln \Gamma\left(\frac{C_{ij}}{g_j} + \frac{1}{2} \right) - \lambda_{ij} \right).$$

Furthermore, the detector parameters g and η can now be optimized as well in a superordinate process, yielding the localization of the events and the detector parameters in one action.

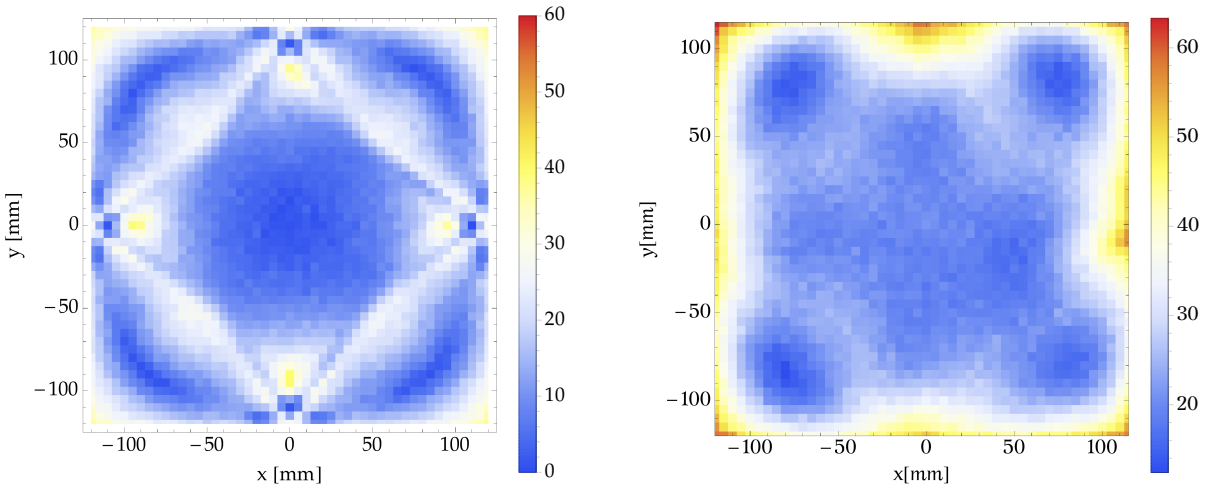

(a) Reconstruction of simulated data by the fitting method works well for events in the center of the detector. For events which end up further outside, basically only one of the corners may be assigned.

(b) By using a trained neural network to reconstruct data, the results are comparable, but not as good as for the fit. This method is much quicker than fitting every data point, however.

Figure 2.31: To test the capability to reconstruct the position of detector events, simulated data is applied to two methods. The colors show the mean deviation of the reconstruction from the actual position in mm.

Spatial Resolution

The quality of reconstruction is tested with simulated data before being applied to measurements. For a set of reasonable parameters g and η, simulated light output events whose distribution follows the parameter set can be used to test the goodness of reconstruction, which is presented in Figure 2.31a. It turns out, that in the center of the detector, an event position can be reconstructed with a precision $< 1\,\mathrm{cm}$.

While this is promising and can be verified with comparison to calibration data sets, the application of this method to more than sample data sets with a few hundreds of thousands of events is impractical. Therefore an alternative method with a large higher data throughput is considered in the following.

Neural Network

A well chosen fitting algorithm will find the optimal solution to given input parameters. Fitting the impact position of events occurring at rates of 1000 per second is not practial though due to time constraints.

The reduction of a set of input parameters to fewer output parameters can also be performed by the use of artificial neural networks, however. These networks consist of a set of neurons, each having a number of input and output connections. n_{in} input neurons are fed with the n_{in}-dimensional raw data, while n_{out} output neurons return the result. In the case of position reconstruction, there are eight PMT amplitudes for the input and two coordinates for the impact position as a result. In between there are hidden layers of neurons which may perform different, but usually simple operations on their inputs. The net used here is presented by Figure 2.32.

The quality of the reconstruction is tested by evaluating the output of a scanning data set.

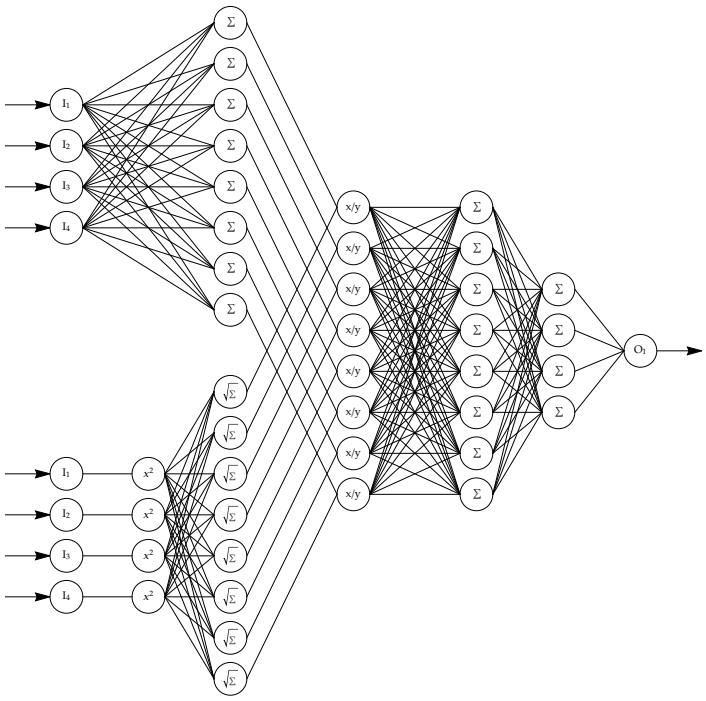

Figure 2.32: Schematic representation of the neural net used for position reconstruction. The actual network has twice as many neurons per layer. The lower branch allows data normalization. The mean deviation in the training set is $\approx 20\,\mathrm{mm}$. Training data is generated from a simulated light distribution and includes Poisson broadening and electronic noise.

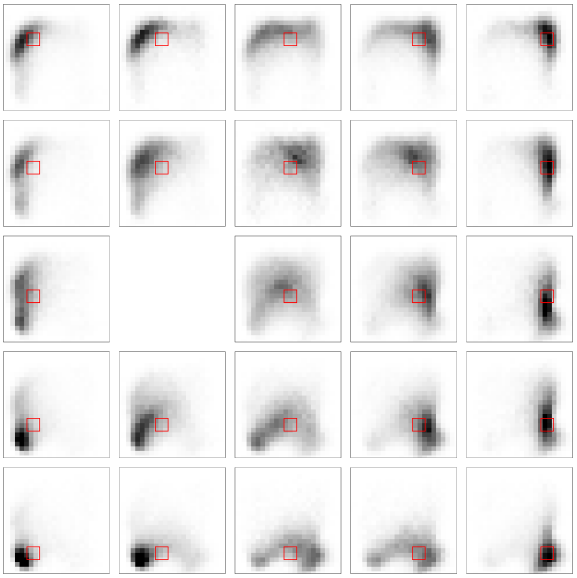

(a) Grenoble sided upstream detector. The goodness of the reconstruction can be estimated by comparing to scan measurements. Red boxes indicate the expected mean position, if the center of the magnetic field was mapped onto the center of the detectors.

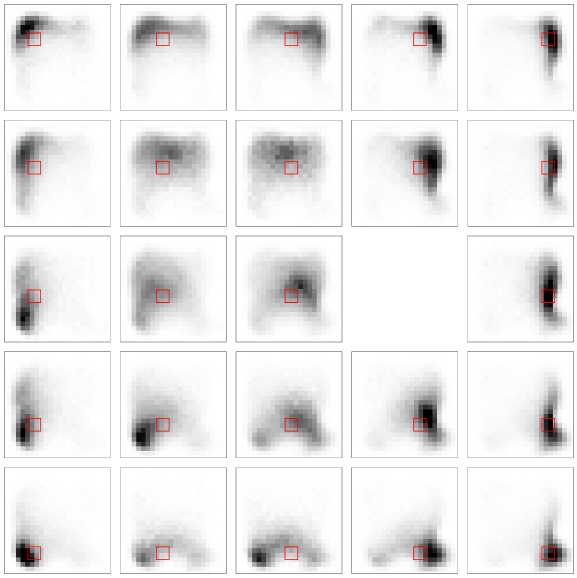

(b) Lyon sided downstream detector. Both detectors are installed slightly too low. This is in agreement with tracking simulations and pinhole measurements [Klo18]. A slight impact of the $\vec{R} \times \vec{B}$ drift in the horizontal direction is also visible.

Figure 2.33: Reconstructed electron impact positions on the detector ($24 \times 24\,\mathrm{cm}^2$) deduced from PMT amplitudes using a neural network. The reconstruction works especially well in the center of the detector, while near the edges the signature of the signal distribution basically only allows the assignment to one of the corners. The reconstructed events are collected in two-dimensional histograms.

In this set, a movable pointlike Bismuth source is put into the magnetic field region which connects central volume and electron detectors using the scanner device from section 1.2.2. This test proves the applicability of the method to a certain extend. Figure 2.33 shows that the reconstruction works well in the central region of the detector and also reveals a slight misalignment between the image of the central volume and the detector.

2.4.6 Detector Nonlinearity

For a scintillator edge which is entirely read out, the integrated light output approximately is $I(x) \sim \mathrm{e}^{-\lambda x}$ for x being the distance to the scintillator edge. For a scintillator being read out from two opposite sides, this transforms into

$$I(x) \sim \frac{a\left(\cosh\left(\frac{2x}{l}\right) - \cosh(1)\right)}{\cosh(1) - 1} + 1, \tag{2.74}$$

x now being the distance to the middle of the scintillator, l the complete width and a the fraction of light being lost at the middle compared to the edges [Fri08].

The smoothness of the detector response may now be used to motivate the use of an averaged point spread function (PSF) $f(r) = r^{-1}$ despite singularities which are introduced at the outset of section 2.2.3.

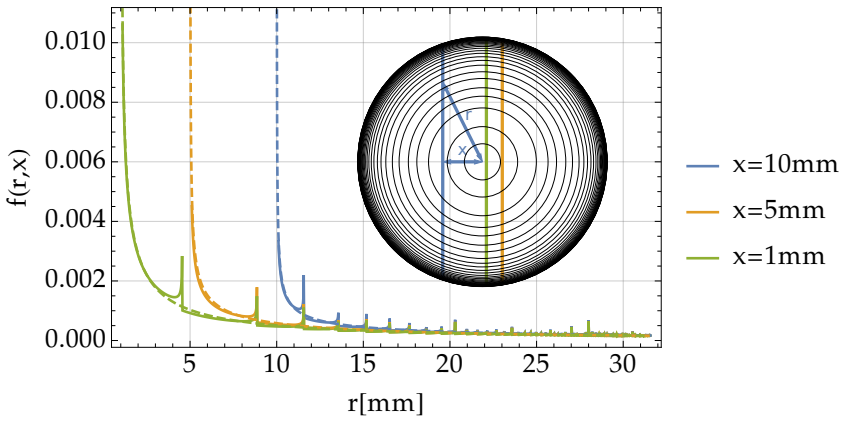

Figure 2.34: The real point spread function for a point source at fixed energy shows the occurrence of rings on the detector. However, when integrating over a line with distance x to the center, the rings are averaged out.

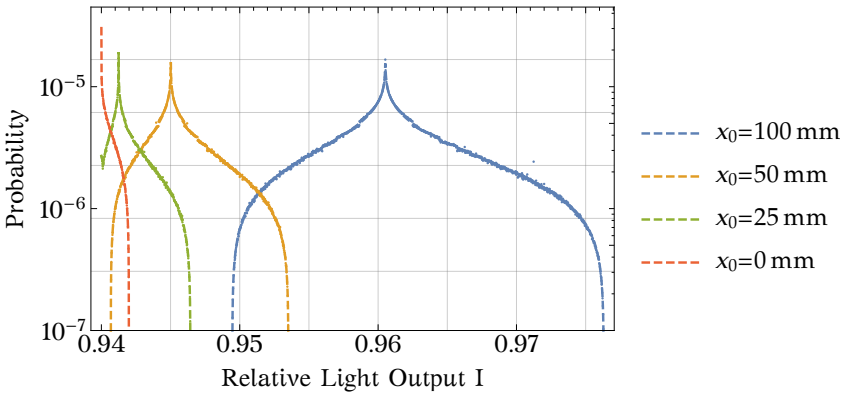

Figure 2.35: Light output at different x-positions as calculated with the real PSF (dots) and the conventional PSF (dashed lines) yields comparable results. Therefore the conventional PSF may be employed even for calibration sources when calculating the signal broadening due to light transport. The data correspond to an energy of 364 keV.

The $\cosh(x)$-dependence of the detector function is independent of the y-component on the detector. Therefore, integration over the PSF over the Cartesian coordinate $y = \sqrt{R^2 - x^2}$ at a fixed distance x to the projected source center yields the distribution $N(I)$ of the detector response, as illustrated by the blue line in Figure 2.34.

$$N(I) = \int_{x(I)}^{2r_0} \frac{1}{\sqrt{R^2 - x(I)^2}} \mathrm{d}R = \ln\left(\frac{2r_0 + \sqrt{4r_0^2 - x(I)^2}}{x(I)}\right). \tag{2.75}$$

Figure 2.35 compares the detector response of the real PSF including singularities to the conventional PSF without singularities. The integration over several of the rings is smoothing the divergences and justifies the application of the simple PSF which may more easily be mapped onto any detector function in section 2.2.3.

Figure 2.36 shows several effects of the broadening due to light transport in the Perkeo III 2009 detector. In the center of the detector, influences due to the finite coverage of the PSF are rather small. The effect becomes important, when the calibration by pointlike sources is

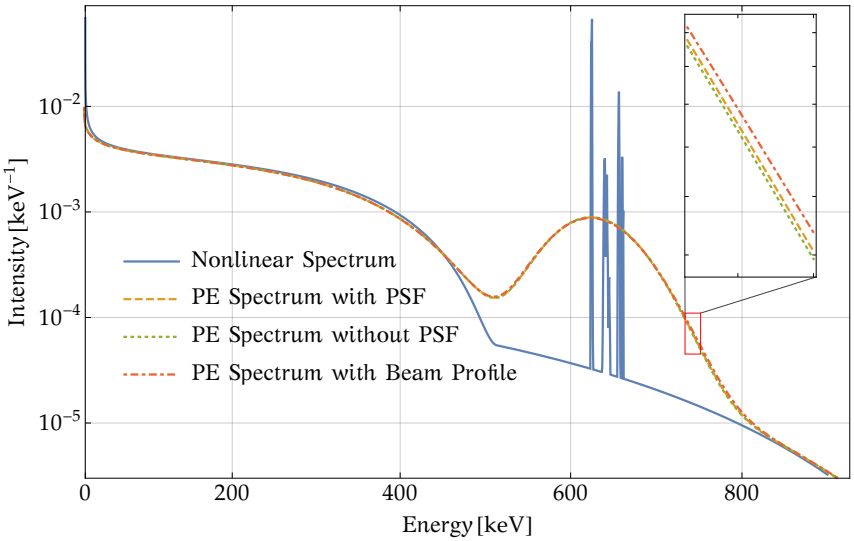

Figure 2.36: Pixelized point spread functions from section 2.2.3 are applied to a simulated detector function [Sau15] to obtain the effect of the detector response on the ^{137}Cs spectrum from Figure 2.9. The resulting photoelectron yield slightly depends on the extension of the source. A zoom shows the difference between pointlike ^{137}Cs-sources and a hypothetical extended ^{137}Cs-source. The transition from pointlike calibration source to the neutron beam leads to a relative change of $2 \cdot 10^{-4}$ of the electron asymmetry, as Figure 2.38 shows.

applied to an extended source such as the neutron beam. Here the increasing gradient of the $\cosh(2x/l)$-dependence for $|x| \to l/2$ becomes noticeable.

2.4.7 Asymmetric Point Spread Function

Effects of the asymmetric point spread function (APSF) (2.18) on asymmetry measurements are discussed in [Dub+14], but with emphasis on the edge effect. This effect which describes the incomplete coverage of the particle beam by a detector is not present in the measurement of the electron asymmetry with Perkeo III, however. Instead, a combination of the spatial inhomogeneity of the detector response function and the APSF comes into play.

An exaggerated example for spatial electron distributions following equation (2.18) with maximal asymmetry is shown in Figure 2.37. The actual differences of electron distributions are almost not visible by eye for a typical asymmetry $\beta AP \sim \pm 0.05$ at large electron energies.

A correction now arises from the fact that outer regions on the detector provide a larger light response than inner regions. Therefore electrons emitted at an energy E against neutron spin direction cause a smaller detector response $L^{\downarrow}(E)$ than electrons of the same energy emitted in neutron spin direction ($L^{\uparrow}(E)$). This decreases the measured asymmetry towards higher energies and increases the measured asymmetry towards lower energies.

The measured asymmetry then is

$$A_{\mathrm{exp,PSF}}(E) = \frac{N^{\uparrow}(L^{\uparrow}(E)) - N^{\downarrow}(L^{\downarrow}(E))}{N^{\uparrow}(L^{\uparrow}(E)) + N^{\downarrow}(L^{\downarrow}(E))}. \tag{2.76}$$

and provides the theoretical basis for the correction, which is obtained by comparing a flat detector response to a simulated [Sau15] realistic response using the pixelized APSF from section 2.2.3.

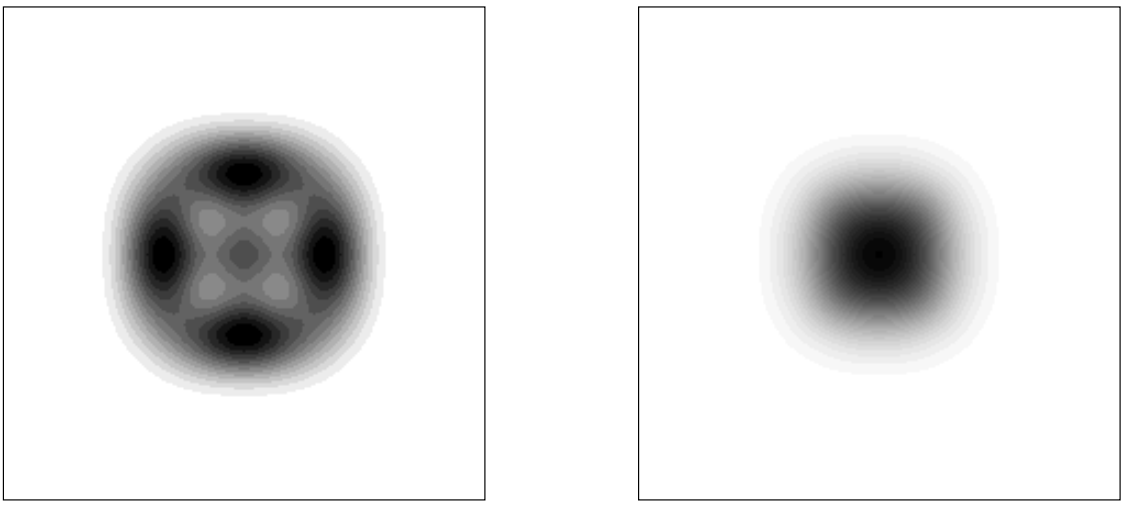

(a) For emission in spin direction of the neutron, most of the electrons would impinge outside the projected beam profile.

(b) Electrons emitted against spin direction are almost completely projected directly onto the detector.

Figure 2.37: To illustrate the effect of the asymmetric beam spread function, the asymmetry is set to $\frac{2}{\pi}\beta AP \equiv \pm 0.99$. The black regions show more likely electron impacts and lie wider outside if electrons are emitted against their preferred emission direction. The large radii stem from the high kinetic energy of 750 keV.

Uncertainties to the corrections mainly come from the model choice for the detector non-uniformity. The center position of the mapped beam is obtained by an analysis of scan data and single PMT spectra combinations, which is not described in this work. On both detectors the beam is displaced by (26.0 ± 5) mm in the vertical direction and in horizontal direction by (-7.1 ± 5)mm and (3.5 ± 5) mm on the Grenoble and the Lyon detector respectively. This difference shows the influence of $\vec{R} \times \vec{B}$ drifts in the separator section of the magnetic field. Uncertainties due to the beam positioning are estimated by shifting the horizontal position by 5 mm in both directions.

2.4.8 Point Spread Function to Beam Spread Function

In contrast to pointlike calibration sources, electrons from the neutron beam are coming from a spatially extended source. The PSF must therefore be extended to a beam-spread function (BSF), which implies a convolution of the point spread with the neutron beam profile, mapped onto the detector by the magnetic field. The average beam profile may be approximated by

$$\frac{\mathrm{d}f}{\mathrm{d}x\mathrm{d}y} = \frac{1}{4d^2\Gamma^2(5/4)} \exp\left(-\frac{(x-x_0)^4}{d^4}\right) \exp\left(-\frac{(y-y_0)^4}{d^4}\right), \quad d = 45.4\,\mathrm{mm}, \tag{2.77}$$

with its center at (x_0, y_0). Figure 2.40a illustrates the difference between a pointlike source and the neutron beam. The projected neutron beam covers more area with higher light response, and shifts small beta asymmetries at lower energies to higher ADC channels. Consequently, the uncorrected measured asymmetry obtained from a point-source calibration would be lower than the actual asymmetry. This effect overcompensates the correction due to the asymmetric point spread function, resulting in Figure 2.38 and an overall positive relative correction of $4.2 \cdot 10^{-4}$, where the effects from section 2.2.1 are included as well for technical reasons.

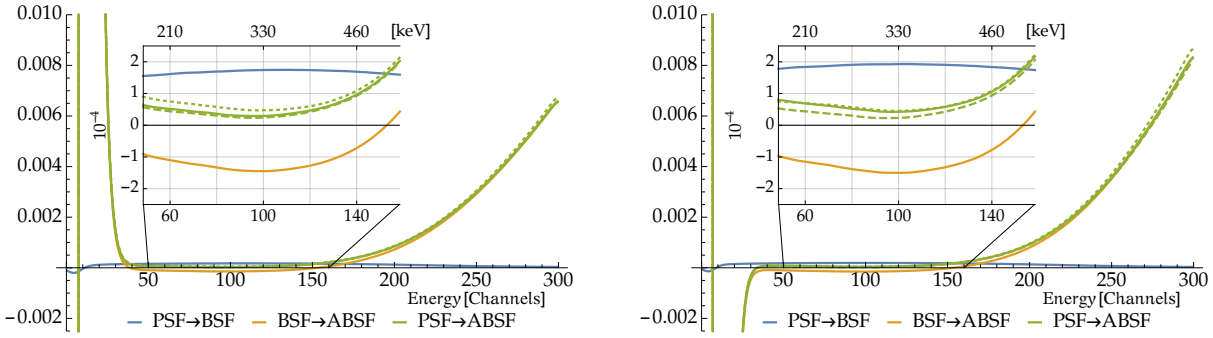

(a) Grenoble sided upstream detector.

(b) Lyon sided downstream detector.

Figure 2.38: The asymmetric BSF in combination with the detector inhomogeneity leads to a significant positive correction at higher energies (> 500 keV). The actual effect of the asymmetric PSF is negative in the low-energetic region, which is compensated for by a higher signal response in the outer detector region. The plots also include a correction for spin dependent pedestal widths, which only play a significant role in the very low energy range. The resulting corrections are shown as a green solid line for the assumed displacement to the center of the detector. Dashed lines indicate a displacement of −5 mm and dotted lines a displacement of 5 mm relative to the most likely position.

2.5 PMT Response

Counting of photons in PERKEO III is done with PMTs. Those consist of a photo layer which exploits the photoeffect to transform incident photons into electrons and several dynodes or meshes in order to amplify the charge of a single photoelectron. In the case of PERKEO III, mesh PMTs are used, since they are less sensitive to external magnetic fields. In contrast to classical dynode PMTs they require a larger number of amplification stages – 19 compared to 12 or eight – as the gain factor at each stage only is $\Lambda \gtrsim 2$.

Commonly [Plo00], primarily out of practical reasons, the PMT response to emitted photoelectrons is approximated by a Poisson distribution function, although the underlying statistical process is more complex. Especially for small numbers of photoelectrons, this approximation fails and does not reflect the actual signal response. A more realistic expression is deduced in [Sau18] and will be briefly summarized in the following:

For each amplification stage the probability of obtaining k_i electrons out of k_{i-1} incoming electrons is expressed by the Poisson probability distribution

$$p(k_i, k_{i-1}) = \frac{(\Lambda k_{i-1})^{k_i}}{k_i!} \mathrm{e}^{-\Lambda k_{i-1}}. \tag{2.78}$$

Consequently, the probability of obtaining $k_N > 0$ electrons in the N-th stage for k_0 initial photoelectrons is

$$P(k_N, k_0, N) = \sum_{k_1=1}^{\infty} \sum_{k_2=1}^{\infty} \cdots \sum_{k_{N-1}=1}^{\infty} \prod_{i=1}^{N} p(k_i, k_{i-1}), \tag{2.79}$$

which is a rather unhandy expression. The probability for zero electrons at any stage is already excluded since this leads to an extinction of the signal. The probability for extinction is expressed by

$$P(0, 1, N) = \exp\left[(\exp\left[(\exp\left[(\exp\left[\cdots\right] - 1)\,\Lambda\right] - 1)\,\Lambda\right] - 1)\,\Lambda\right], \tag{2.80}$$

which is nested N times up to the N-th innermost term $\exp(-\Lambda)$. Equation (2.80) may be evaluated exactly, but for any non-zero charge output of the PMT, equation (2.79) must be simplified to be of practical use.

For large electron numbers, the discrete probability distribution P may be approximated by a continuous probability distribution for a continuous number of electrons x using a diffusion approximation

$$P_{\text{Diff}}(x, k = k_0, N) = \mathrm{e}^{-A/B}\left(\delta(x) + \frac{\mathrm{e}^{-x/B}\sqrt{A/x}}{B} I_1\left(\frac{2\sqrt{Ax}}{B}\right)\right), \quad A = k\Lambda^N, \quad B = \frac{\Lambda^N - 1}{2(\Lambda - 1)}. \tag{2.81}$$

I_1 denotes the modified Bessel function of the first kind. [Sau18] now shows, that a very good description of experimental PMT responses can be obtained by combining equations (2.80, 2.79, 2.81):

$$\xi(x,k) = \begin{cases} (P(0,1,N))^k, & x = 0 \\ P(k_n, k, n) \cdot P_{\text{Diff}}(x, k_n, N-n), & \text{while } k_n \leq 20,\ n \leq 14 \\ P_{\text{Diff}}(x, k, N), & \text{otherwise.} \end{cases} \tag{2.82}$$

Henceforth $\xi(c,k)$, which relates measurable channels to a number of photoelectrons by a gain factor, will be used.

One consequence of the amplification process is a broadening of the detector function. In addition to the broadening due to the photoelectron statistics, the variance is increased by a factor of $\Lambda/(\Lambda - 1)$, resulting in a relative width increased by 30 % for a mesh PMT with a typical gain of $\Lambda = 2.4$.

2.6 Trigger Function

Before the data acquisition system starts recording an event, a trigger signal has to be emitted. For Perkeo III this signal is primarily created by a constant fraction discriminator. Subsequently the condition two-out-of-six triggers (or two-out-of-four, in the case of Perkeo III 2014) has to be fulfilled to start a new event. In the past, a simplified method was used to determine the trigger function while in section 2.6.2 a more complete description is derived.

2.6.1 Homogeneous Fixed Threshold Approximation

Underlying assumptions of the method described in [Fri08] are, that a fixed minimum number of photoelectrons releases a trigger pulse and that the light is equally distributed onto all PMTs. Using the binomial distribution, the probability for l out of n coincidentally triggering channels is

$$B(W, l) = \binom{n}{l} W^l (1 - W)^{n-l}, \tag{2.83}$$

with the probability $W(N)$ of a channel for releasing a trigger with N incoming photons. The trigger probability therefore is

$$T(W) = 1 - B(W,0) - B(W,1) = 1 - (1 - W)^n \left(1 + \frac{nW}{1 - W}\right). \tag{2.84}$$

With a threshold of one required photoelectron for a trigger signal this transforms into

$$T_1(N) = 1 - (1-q)^{nN}\left(\frac{n}{(1-q)^N} - n + 1\right) \tag{2.85}$$

or for a two-photoelectron-threshold into

$$T_2(N) = 1 - \left[(1-q)^N\left(1 + \frac{qN}{1-q}\right)\right]^n \left(\frac{n}{(1-q)^N(1 + \frac{qN}{1-q} - n + 1)}\right), \tag{2.86}$$

with quantum efficiency q for a conversion of a photon into a photoelectron. To obtain the trigger function in channels c, the number of photons was then replaced by

$$N = g \cdot c$$

using a gain factor g or an expression including a nonlinear description of the energy-channel-relation [Mes11]. An approximatic description of the measured trigger function succeeded with that model, but the obtained parameters are rather nonphysical.

While the functions T_1 and T_2 certainly cover a part of the detection process, the initial assumptions made are too strong and have to be refined in the following.

2.6.2 Almost Complete Trigger Model

In section 2.5 a quarter of the signal broadening is shown to result from the response of the PMTs. Therefore the signal transport has to be split into at least two parts:

1. light distribution onto the PMTs, depending on the light source position and its strength
2. transformation of a photoelectron into an electrical pulse

Furthermore, electronic noise adds an additional broadening which is only by parts the same for discriminator and QDCs, however this subtlety will be neglected here and the broadening of the detected signal and the discriminator threshold will be treated separately.

Following section 2.4, the light is not equally distributed onto all PMTs, but actually two PMTs take almost all of the light, depending on the position of the light sources. This is true even for a detector with an overall homogeneous light response. Therefore equations (2.85) or (2.86) cannot be used to obtain a physically correct description.

The mean number of **photons** reaching a specific PMT i per overall number of emitted photons can be obtained from dedicated simulations or calculations (see section 2.4). To get the mean number of **photoelectrons** per emitted photons λ_i, the quantum efficiency q has to be multiplied with the mean number of photons. Now the distribution of photoelectrons can be expressed in terms of a Poisson distribution:

$$p_i(k,N) = \mathrm{e}^{-\lambda_i N}\frac{(\lambda_i N)^k}{k!}. \tag{2.87}$$

Therefore the signal response $s(c,N)$ to N photons produced as output by the PMT is given by

$$s_i(c,N) = \sum_{k=0}^{\infty} \xi_i(c,k)p_i(k,N), \tag{2.88}$$

where $\xi(c,k)$ is the response of a PMT to k photoelectrons in terms of QDC channels c as described in section 2.5.

The threshold for a trigger signal is set in terms of channels to c_T, which like the measured channel c is subject to electronic noise. The probability of relasing a trigger from a single PMT signal is then $(\mathrm{erf}((c-c_T)/\sigma)+1)/2$, with noise σ. The overall signal distribution can be expressed as a sum of a triggered part $\underline{\xi}$ and an untriggered part $\overline{\xi}$:

$$\begin{aligned} s_i(c,N) &= t_i(c,N) && + u_i(c,N) \\ &= \frac{1}{2}\left(\mathrm{erf}\left(\frac{c-c_T}{\sigma\sqrt{2}}\right)+1\right)\sum_{k=0}^{\infty}\xi_i(c,k)p_i(k,N) && + \frac{1}{2}\left(\mathrm{erf}\left(\frac{c_T-c}{\sigma\sqrt{2}}\right)+1\right)\sum_{k=0}^{\infty}\xi_i(c,k)p_i(k,N) \\ &= \sum_{k=0}^{\infty}\underline{\xi_i}(c,k)p_i(k,N) && + \sum_{k=0}^{\infty}\overline{\xi_i}(c,k)p_i(k,N). \end{aligned} \tag{2.89}$$

For practical reasons the influence of a non-zero σ will be accounted for by adding up several spectra with different c_T. The error function term $(\mathrm{erf}(x)+1)/2$ can then simply be replaced by the Heaviside Θ.

The measured spectrum S for a fixed number of initial photons can then be calculated by convolution:

$$S(c,N) = (s_1(N) * s_2(N) * \cdots * s_n(N))(c). \tag{2.90}$$

Luckily, the properties of the Poisson distribution allow to combine this combinatorially complicated function into a single expression, namely

$$S(c,N) = \sum_{k=0}^{\infty}\Xi(c,k)P(k,N), \qquad P(k,N) = p_{1+2+\cdots+n}(k,N) \tag{2.91}$$

since the convolution of two Poisson distributions again yields a Poisson distribution:

$$\begin{aligned} p_{1+2}(k,N) &= (p_1(N) * p_2(N))(k) = \sum_{j=0}^{k} p_1(j,N)\cdot p_2(k-j,N) \\ &= \mathrm{e}^{-(\lambda_1+\lambda_2)N}\frac{((\lambda_1+\lambda_2)N)^k}{k!}\underbrace{\sum_{j=0}^{k}\frac{k!}{j!(k-j)!}\left(\frac{\lambda_1}{\lambda_1+\lambda_2}\right)^j\left(\frac{\lambda_2}{\lambda_1+\lambda_2}\right)^{k-j}}_{=1} \\ &= \mathrm{e}^{-(\lambda_1+\lambda_2)N}\frac{((\lambda_1+\lambda_2)N)^k}{k!}. \end{aligned} \tag{2.92}$$

To include the trigger condition and obtain a triggered spectrum S_T, certain parts of the spectrum have to be subtracted, however. For a one-out-of-n condition, the convolution of all untriggered spectra does not contribute to the measured spectrum:

$$S_{T,1}(c,N) = S(c,N) - U_0(c,N), \qquad U_0(c,N) = (u_1(N) * u_2(N) * \cdots * u_n(N))(c). \tag{2.93}$$

The cut which is introduced between the triggering and the non-triggering part of the single PMT spectra does not allow a simplification of this relation as in equation (2.91). Instead every possible combination of photoelectrons has to be taken into account:

$$U_0(c,N) = \sum_{c_1=0}^{c}\sum_{c_2=0}^{c-c_1}\cdots\sum_{c_{n-1}=0}^{c-c_1-c_2-\cdots-c_{n-2}} \underbrace{u_1(c_1,N)\cdot u_2(c_2,N)\cdots u_n(\overbrace{c-c_1-c_2-\cdots-c_{n-1}}^{=c_n})}_{=\prod_{i=1}^{n}\sum_{k_i=0}^{\infty}\overline{\xi_i}(c_i,k_i)p_i(k_i,N)}. \tag{2.94}$$

When the trigger condition is two-out-of-n, the contribution U_1 which includes one triggered (t_1 or t_2 or ...) and $n-1$ untriggered spectra has to be subtracted as well. For three coincident triggers, two triggered spectra must be subtracted, and so on.

This turns out to be a huge number of combinations which, numerically calculated, may consume a long time when fitting the spectra. To be of practical use, the relation must further be simplified.

The inner part of equation (2.94) is the product of n PMT response functions and n Poisson distributions, the latter indicating at which scale the normalized PMT response functions occur. If the same PMT gain $\xi_i = \Xi$ for every individual PMT is used, the number of performed convolutions is already largely reduced by symmetry $\xi_1(k_1)\xi_2(k_2) = \Xi(k_1)\Xi(k_2) = \Xi(k_2)\Xi(k_1)$. The remaining part may also be transformed:

$$\begin{aligned}\prod_{i=1}^{n} p_i(k_i,N) &= \exp\left(-N\sum_{i=1}^{n}\lambda_i\right)\cdot N^{\sum_{i=1}^{n}k_i}\cdot\frac{(\sum_{i=1}^{n}\lambda_i)^{\sum_{i=1}^{n}k_i}}{(\sum_{i=1}^{n}k)!}\cdot\frac{(\sum_{i=1}^{n}k_i)!}{(\sum_{i=1}^{n}\lambda_i)^{\sum_{i=1}^{n}k_i}}\cdot\prod_{i=1}^{n}\frac{\lambda_i^{k_i}}{k_i!}\\ &= \exp(-N\lambda)\frac{(N\lambda)^k}{k!}\cdot\frac{k!}{k_1!k_2!\cdots k_n!}\prod_{i=1}^{n}\left(\frac{\lambda_i}{\lambda}\right)^{k_i}\\ &= P(k,N)\cdot\binom{k}{k_1,k_2,\ldots,k_n}\prod_{i=1}^{n}\left(\frac{\lambda_i}{\lambda}\right)^{k_i},\end{aligned} \tag{2.95}$$

where $\lambda = \sum_{i=1}^{n}\lambda_i$ is the total combined relative mean light and photoelectron response and $k = \sum_{i=1}^{n}k_i$ the total number of photoelectrons. The probability for a certain distribution of photoelectrons onto all PMTs is a product of a Poisson distribution to the overall photoelectron yield and a multinomial distribution. This allows to pre-calculate triggered spectra only depending on the number of emitted photoelectrons which can afterwards simply be applied to theoretical photoelectron spectra.

A final remark must be made about the calculation of the multinomial distribution. Although the multinomial coefficient can be broken down into binomial coefficients

$$\binom{k}{k_1,k_2,\ldots,k_n} = \prod_{i=1}^{n}\binom{\sum_{j=1}^{i}k_j}{k_i}$$

whose calculation can easily be cached and optimized, for a large total number of photoelectrons the number of combinations still goes beyond all scope. To overcome this problem, a sensible numerical limit $I_{\min} \geq \sum_c \overline{\Xi}(c,k), \forall k \geq k_{\max}$ must be chosen, such that $\overline{\Xi}(c,k) \approx 0, \forall k \geq k_{\max}$ and the inner part of equation (2.94) transforms into

$$\prod_{i=1}^{n}\sum_{k_i=0}^{k_{\max}}\overline{\xi_i}(c_i,k_i)p_i(k_i,N).$$

2.6.3 Implications

Two major implications follow from the new approach that will make the handling of the trigger function less convenient. They both arise from the condition of at least two coincidentally triggering PMTs.

Formerly the trigger function could be calculated once and was then multiplied to any theoretical untriggered spectrum:

$$T(C) = t(C)\cdot S(C). \tag{2.96}$$

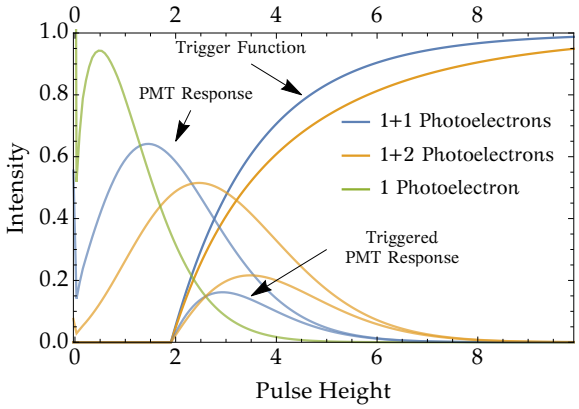

(a) A trigger threshold of 1 photoelectron (PE) equivalents for a 2-out-of-2 condition leads to different trigger functions for different numbers of PEs. The trigger function for one PE per PMT is steeper than for one and two PEs.

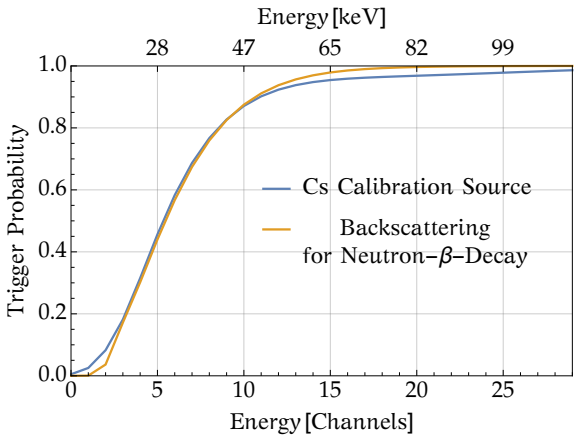

(b) Without changing the threshold parameters, the trigger function changes for different kinds of input spectra. In this plot also the spatial shape of the source distribution, as well as the timing differences have an influence.

Figure 2.39: The new approach to calculate the influence of the trigger threshold changes the trigger function between spectra. It is not possible to simply multiply a function $t(C)$ to the pulse height spectrum, but the triggered spectrum has to be evaluated for each source independently.

Now the shape of the input spectrum S also changes t. This comes from the nonlinear behavior of the cut in the signal due to the trigger threshold. The PMT response pulse height spectrum to a single photoelectron is differently shaped than the response to more photoelectrons (in terms of width and skewness of the distribution) and therefore a threshold cut breaks the convolution property

$$\xi(c,k_1) * \xi(c,k_2) = \xi(c,k_1+k_2), \text{ but} \tag{2.97}$$

$$\underline{\xi}(c,k_1) * \underline{\xi}(c,k_2) \neq \underline{\xi}(c,k_1+k_2), \tag{2.98}$$

with triggered spectra $\underline{\xi}$. Figure 2.39a shows how this affects the trigger function. A spectrum with increasing intensity towards zero signal (as the Cs spectrum) therefore has a different trigger function than a function with decreasing signal towards zero (as the neutron beta decay spectrum).

While the overall homogeneity is excellent for a plastic scintillator of this size, the distribution of the light is mostly a geometric consequence. Light being produced directly in front of a light guide will mostly enter only one light guide, while light being produced in the middle of the scintillator is by large parts distributed onto the two middle light guides and may also enter outer light guides. This makes the detection of events in the middle of the detector more likely. The neutron beam is spread over a rectangular shape and its events must be handled differently than pointlike calibration sources.

2.6.4 Extraction from Data

Two methods are used to extract the trigger function experimentally. One method is to use electron backscattering events from neutron decay data. Here electrons which hit one of the detectors do not deposit all of their energy, are leaving the detector again

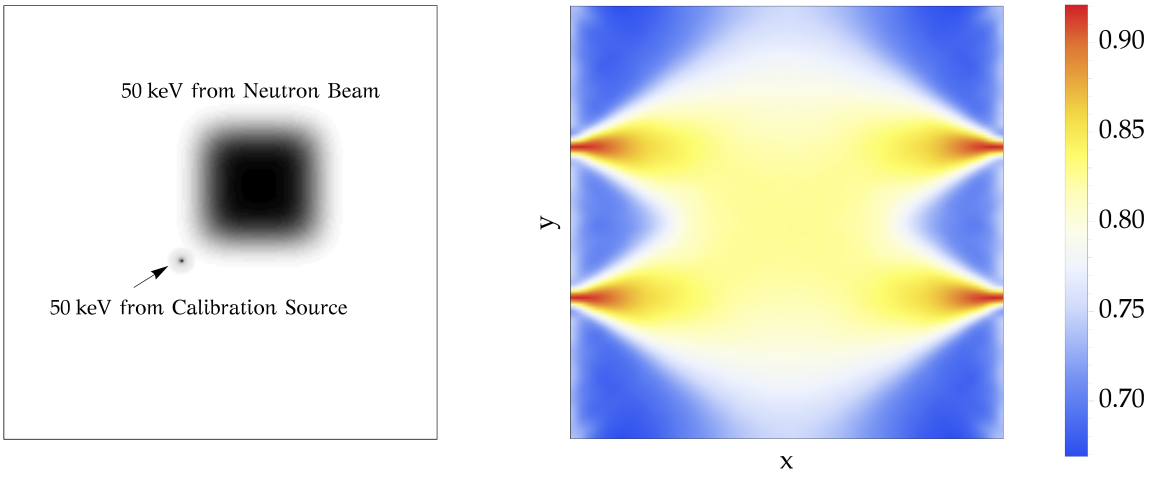

(a) The distribution for an electron of 50 keV is significantly different for different kinds of sources. The rectangular shape shows electrons from the neutron beam, while the circular shape is the point spread function stemming from a calibration source.

(b) The trigger probability also depends on the position of impact. Events in front of one of the light guides are less likely for a trigger signal, as most of the light is collected by a single PMT.

Figure 2.40: The new trigger function includes the light distribution for each PMT. A position dependence can therefore be included in the calculation of the theoretical spectra.

and eventually hit the opposite detector. The spectrum of triggering events on the second detector is compared to the spectrum of all events on the second detector. Dividing the first by the latter can be used to obtain the theoretical trigger parameters. This method has two potential problems: Backscattered electrons experience two additional $R \times B$-drifts in PERKEO III and therefore arrive with some displacement on the opposite detector compared to primary events. This displacement has been measured to be on the order of 1 cm and can be neglected. Furthermore the effect of late coming signals during the QDC integration window has not been investigated thoroughly and could introduce a time of flight effect to the measured trigger function.

A second method is to use the low-energetic region of the Cs calibration spectrum and compare it to the theoretical expectation. In this case the trigger function is obtained by fitting the theoretical spectrum including a trigger function to measured data. Despite the progress made in the description of the shape, a more detailed description of the screening function for the shape and Fermi functions as well as a description for the exchange effect is missing [Mou+14].

Figure 2.41 shows fits to the data performed with both methods and compares the resulting trigger functions. For the first time a physically motivated description of the trigger function is employed and satisfactorily agrees with the data. Differences between extraction from backscattering data and the Cs spectrum might arise from timing effects of the QDCs. For further application, the second method is used.

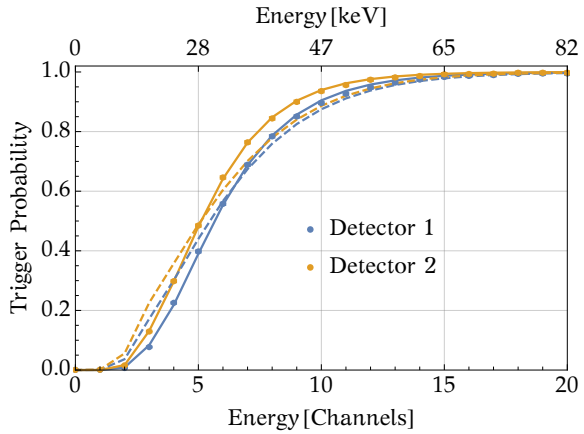

(a) When extracting the trigger function from the backscattering data of neutron decay, a late rise compared to the trigger function extracted from the Cs spectrum (dashed lines) is visible.

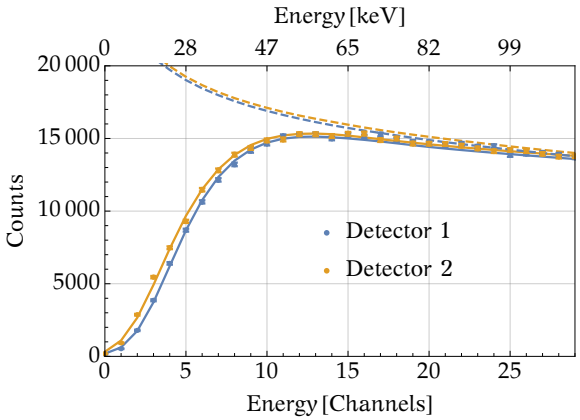

(b) The trigger function can also be extracted by fitting to an absolute spectrum of the Cs spectrum. The dashed lines show the theoretical signal without a trigger function.

Figure 2.41: Two methods are used to extract a trigger function from measured data. The extracted threshold parameters are differing but the obtained precision is sufficient for current purposes.

2.7 Undetected Backscattering

An important systematic effect on the determination of the electron asymmetry comes from the combination of electron backscattering – see section 2.2.4 – and the trigger function. An electron initially hitting one of the detectors might not fully deposit its energy, but leave the detector again. For this effect several cases have to be considered. Basically a backscattered electron may be transported to the opposite detector if the emission angle to the normal of the detector surface $\theta < \theta_{\text{lim}}$ or be reflected on the magnetic field for $\theta > \theta_{\text{lim}}$, impinging the same detector again. The limiting angle θ_{lim} is defined by the magnetic mirror effect – see section 1.2.4. The probabilities for backscattering onto the respective detectors are denoted as η_{opp} and η_{same}. A decision tree as in Figure 2.42 can be used to visualize possible event chains. For the measurement of the asymmetry, the first impact is crucial as it determines the measured emission direction. Here the trigger function plays an important role, since the deposited energy in the primary detector might not be sufficient to relase a trigger signal. Consequently the event could be assigned to the wrong emission direction. A theoretical description was done in [SA08] already, however the application to measured data underestimates the effect on the asymmetry, mainly due to false assumptions about the detector function when extrapolating the effect from the data.

Now a response function $L(E)$ describing the light response to an electron that completely deposits its energy inside one of the scintillators is introduced to account for quenching effects. If an electron gets backscattered from the first detector with remaining energy E_2, its light response is $L_1 = L(E) - L(E_2)$ in the first detector and $L_2 = L(E_2)$ in the second detector. With the trigger function $T(L)$ which describes the measured spectrum with included probability to start the acquisition of a signal L, for a backscatter event, the probability to correctly measure the full event is

$$p_{\text{Tbs}} = |T(L_1)| = |T(L(E) - L(E_2))|. \tag{2.99}$$

In this case it is irrelevant whether the second impact releases a trigger as well, as the

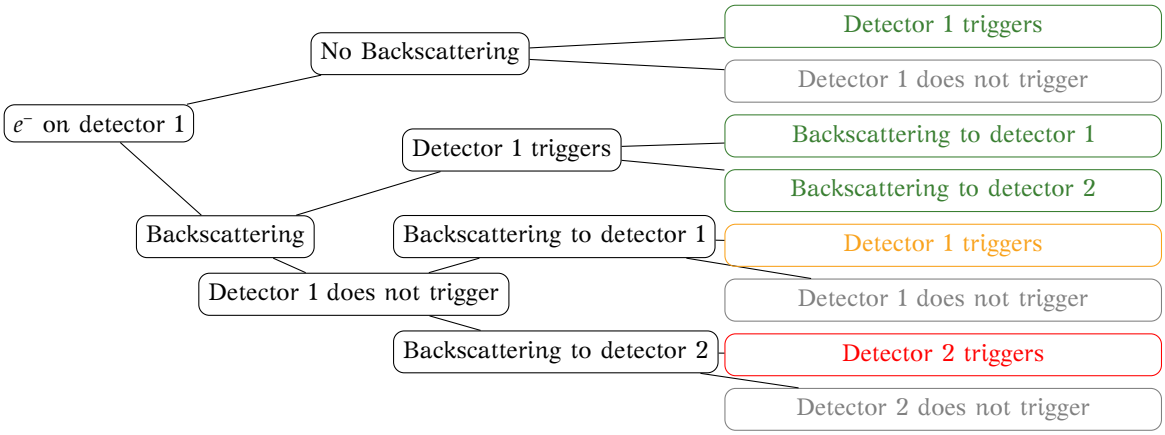

Figure 2.42: A first order decision tree is used to visualize the effects of backscattering. Green boxes denote events with correct emission direction and energy information. Gray boxes denote events without any trigger at all, while yellow stands for the right emission direction assignment, but detection at lower energy, and red misses both, emission direction and full energy reconstruction.

signal acquisition is running for both detectors during a reasonable time.

In case of undetected backscattering, i.e. the first impact does not release a trigger, but the second impact is registered, the probability is expressed as

$$p_{\text{Tubs}} = (1 - |T(L_1)|) \cdot |T(L_2)|. \tag{2.100}$$

Assuming two identical detectors, the spectrum of detected energy E_d of an initial electron with energy E now is

$$\begin{aligned} &I_T(E_d) = \\ &= \text{undetected backscattering} + (\text{no backscattering} + \text{detected backscattering}) \\ &= \underbrace{T(L(E_d)) \cdot (1 - |T(L(E) - L(E_d))|)}_{\substack{\text{spectrum/probability of} \\ \text{normalized undetected backscattering}}} \cdot (\eta_{\text{same}}(E, E_d) + \eta_{\text{opp}}(E, E_d)) \\ &\quad + \left(1 - \int_0^E \overbrace{(|T(L(E_2))| \cdot (1 - |T(L(E) - L(E_2))|)}^{\text{backscatter probability}} \cdot \overbrace{(\eta_{\text{same}}(E, E_2) + \eta_{\text{opp}}(E, E_2))}^{\text{backscatter probability}} \mathrm{d}E_2\right) \\ &\quad \cdot \delta(E_d - E), \end{aligned} \tag{2.101}$$

with $\eta_{\text{same/opp}}(E, E_2)$ being the probability of backscattering with incident energy E and emitting energy E_2 to the opposite or the same detector respectively. In this case it is assumed that the energy deposition of undetected events cannot be reconstructed. It depends on the time of flight between the two impacts and the QDC integration timing. A typical time of flight is 30 ns [Roi10] and it is possible to miss the energy which is deposited in the first detector for some of the events. If the energy can be reconstructed, only the number of detected events is reduced. Figure 2.43 shows the correction for both cases, with and without energy reconstruction.

The measured asymmetry including this effect now is

$$A_{exp} = \frac{N'_\uparrow - N'_\downarrow}{N'_\uparrow + N'_\downarrow} \tag{2.102}$$

$$= \frac{N^{\text{nbs}}_\uparrow + D^{\text{same}}_\uparrow + D^{\text{opp}}_\uparrow + U^{\text{same}}_\uparrow + U^{\text{opp}}_\downarrow - N^{\text{nbs}}_\downarrow - D^{\text{same}}_\downarrow - D^{\text{opp}}_\downarrow - U^{\text{same}}_\downarrow - U^{\text{opp}}_\uparrow}{N^{\text{nbs}}_\uparrow + D^{\text{same}}_\uparrow + D^{\text{opp}}_\uparrow + U^{\text{same}}_\uparrow + U^{\text{opp}}_\downarrow + N^{\text{nbs}}_\downarrow + D^{\text{same}}_\downarrow + D^{\text{opp}}_\downarrow + U^{\text{same}}_\downarrow + U^{\text{opp}}_\uparrow}, \tag{2.103}$$

where N^{nbs} is used for the spectrum without backscattering, D^{same} and D^{opp} for the spectra of detected backscattering onto the same or the opposite detector and U^{same} and U^{opp} for the respective undetected spectra. Assuming equal detector functions, (2.103) can also be simplified to

$$A_{exp} \approx \frac{(\alpha-\epsilon)N_\uparrow + \epsilon N_\downarrow - (\alpha-\epsilon)N_\downarrow - \epsilon N_\uparrow}{(\alpha-\epsilon)N_\uparrow + \epsilon N_\downarrow + (\alpha-\epsilon)N_\downarrow + \epsilon N_\uparrow} = \left(1 - 2\frac{\epsilon}{\alpha}\right)\frac{N_\uparrow - N_\downarrow}{N_\uparrow + N_\downarrow}, \tag{2.104}$$

with the triggered fraction without backscattering and with detected backscattering α and the fraction of undetected backscattering ϵ for clean and untriggered spectra N.

Since detector $S_{1(2)}$ and trigger functions $T_{1(2)}$ are different for both detectors, the measurement of decay products from neutrons which are polarized towards detector 1 is represented as follows:

$$\begin{aligned}
N'_\uparrow =& N'_\uparrow(E) \\
=& (1 - \eta_{\text{same}}(E) - \eta_{\text{opp}})N_\uparrow(E)\cdot T_1(L(E)) && \text{no backscattering (bs)} \\
&+ \int_0^E \eta_{\text{same}}(E,E_2)N_\uparrow(E)\cdot[T_1(L(E)-L(E_2)) * S_1(L(E_2))]\,\mathrm{d}E_2 && \text{detected bs to D1} \\
&+ \int_0^E \eta_{\text{opp}}(E,E_2)N_\uparrow(E)\cdot[T_1(L(E)-L(E_2)) * S_2(L(E_2))]\,\mathrm{d}E_2 && \text{detected bs to D2} \\
&+ \int_E^{E_{\max}} \eta_{\text{same}}(E_1,E)N_\uparrow(E_1)\cdot(1-|T_1(L(E_1)-L(E))|)\cdot T_1(L(E))\mathrm{d}E_1 && \text{undetected bs to D1} \\
&+ \int_E^{E_{\max}} \eta_{\text{opp}}(E_1,E)N_\downarrow(E_1)\cdot(1-|T_2(L(E_1)-L(E))|)\cdot T_1(L(E))\mathrm{d}E_1 && \text{undetected bs to D2}
\end{aligned} \tag{2.105}$$

The solid lines in Figure 2.43 show the resulting corrections.

2.7.1 Estimation of Systematic Effects

An important part of the correction is the determination of the actual trigger function. Both methods described in section 2.6.4 were used and differences for the corrections on the order of 2 % were obtained. Together with the uncertainties for the description of the underlying theoretical spectra (Cs and backscattering) and timing effects the uncertainty is estimated to 5 %.

Further uncertainties are the calculation of the backscattering probabilities η_{same} and η_{opp}, where the latter has the main contribution to the correction. The magnetic field in the detector region is known only on a 10 % level, which hardly changes $\eta_{\text{same}} + \eta_{\text{opp}}$, but shifts between η_{same} and η_{opp} due to a change of the limiting angle $\theta_{\text{lim}} = \arcsin\sqrt{B_1/B_0}$ of the

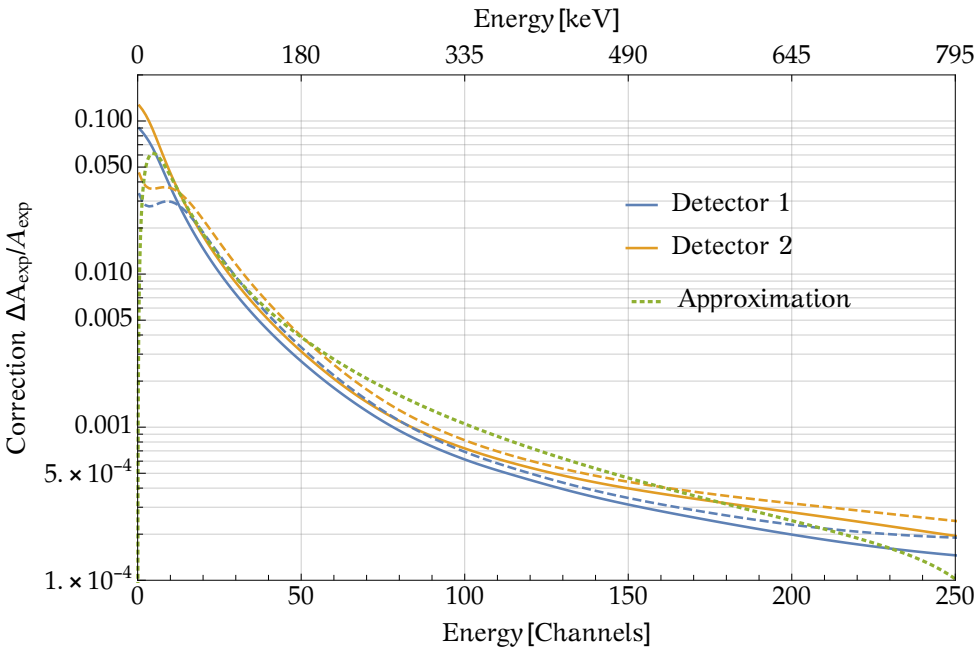

Figure 2.43: The correction has a positive sign, as undetected backscattering to the opposite detector decreases the measured asymmetry. It increases towards lower energies, as the probability for triggering decreases. Solid lines show the correction without energy reconstruction, dashed lines show the correction when the energy information of the undetected impact is not lost. The green dotted line shows an estimation with very simple assumptions.

magnetic mirror effect. Simplifying the angular distribution of backscattered electrons to $\sin 2\theta$ results in

$$\frac{\eta_{\text{opp}}}{\eta_{\text{same}} + \eta_{\text{opp}}} = \cos^2 \sqrt{B_1/B_0} \tag{2.106}$$

$$\Delta \frac{\eta_{\text{opp}}}{\eta_{\text{same}} + \eta_{\text{opp}}} = \frac{1}{2} \sqrt{\frac{B_0}{B_1}} \sin\left(2\sqrt{B_1/B_0}\right) \Delta \frac{B_1}{B_0} \approx 7\,\%, \tag{2.107}$$

which is increased to 10 % to account for the simplified angular distribution of backscattered electrons. The backscattering probability $\eta(E_{\text{in}}, \theta_{\text{in}}, E_{\text{out}}, \theta_{\text{out}})$ is obtained by performing a Monte Carlo simulation, briefly described in section 2.2.4. To account for the neglect of secondary backscattering, the choice of the ionization model and uncertainties in the angular distribution of the scattering model, an uncertainty of 20 % is assumed for the determination of energy dependent backscattering coefficients.

Another important uncertainty is the reconstruction of the energy of undetected events. The integration window starts a few ns before the triggering signal enters the QDC. If the time of flight for an undetected backscattered electron is smaller than this timing buffer, then the energy is reconstructed, otherwise it is lost or partly lost. The effect is maximized

if full energy reconstruction is assumed for all events, i.e.

$$\begin{aligned}
N'_{\uparrow} =& N'_{\uparrow}(E) \\
=& (1 - \eta_{\text{same}}(E) - \eta_{\text{opp}}) N_{\uparrow}(E) \cdot T_1(L(E)) && \text{no backscattering} \\
&+ \int_0^E \eta_{\text{same}}(E, E_2) N_{\uparrow}(E) \cdot [T_1(L(E) - L(E_2)) * S_1(L(E_2))] \, \mathrm{d}E_2 && \text{detected bs to D1} \\
&+ \int_0^E \eta_{\text{opp}}(E, E_2) N_{\uparrow}(E) \cdot [T_1(L(E) - L(E_2)) * S_2(L(E_2))] \, \mathrm{d}E_2 && \text{detected bs to D2} \\
&+ \int_0^E \eta_{\text{same}}(E, E_2) N_{\uparrow}(E_1) \cdot [1 - T_1(L(E) - L(E_2))] * T_1(L(E_2)) \mathrm{d}E_2 && \text{undetected bs to D1} \\
&+ \int_0^E \eta_{\text{opp}}(E, E_2) N_{\downarrow}(E_1) \cdot [1 - T_2(L(E) - L(E_2))] * T_1(L(E_2)) \mathrm{d}E_2 && \text{undetected bs to D2}
\end{aligned} \tag{2.108}$$

In contrast to backscattering without full energy reconstruction (2.105) spectra from both detectors are convoluted here. The correction increases by 15 %, shown with dashed lines in Figure 2.43.

systematic effect	magnitude
trigger function	5 %
magnetic field	10 %
simulation	20 %
energy reconstruction	15 %
combined	27 %

The combination of all effects yield an uncertainty of 27 %. Including the correction in the fit increases the absolute value of the asymmetry by a fractional amount of $5 \cdot 10^{-4}$. Conservatively the final uncertainty of the correction is set to $1.5 \cdot 10^{-4}$.

2.8 Signal Processing

Until here, all processes up to the plugs of the PMT bases are discussed. The remaining parts belong to the signal processing and cover the transformation of analog PMT signals into fitted spectra. For the electron asymmetry measurement, the electronic setup is described in [Mes11]. The following parts refer to changes which were applied for the proton asymmetry measurement. Figure 2.44 schematically shows the electronic signal processing.

For the measurement of PMT amplitudes charge integrating ADCs (QDCs) are employed. These are not self-triggering and therefore need an external start signal, which is provided by a constant fraction discriminator connected to a coincidence unit. The analog signals for the QDCs are bypassed in delay cables to allow processing time for the trigger signal. The discriminator output also provides a per-channel-input to a time-to-digital converter (TDC), which allows to separate signals with a resolution of 0.8 ns. One measurement cycle is defined by a fixed time of 10 s in the case of the electron asymmetry measurement and 700 chopper turns ($\simeq$ 9.2 s) for the proton asymmetry measurement. The time difference between PMT and chopper triggers allow an assignment of events to the signal and background time windows for later data analysis.

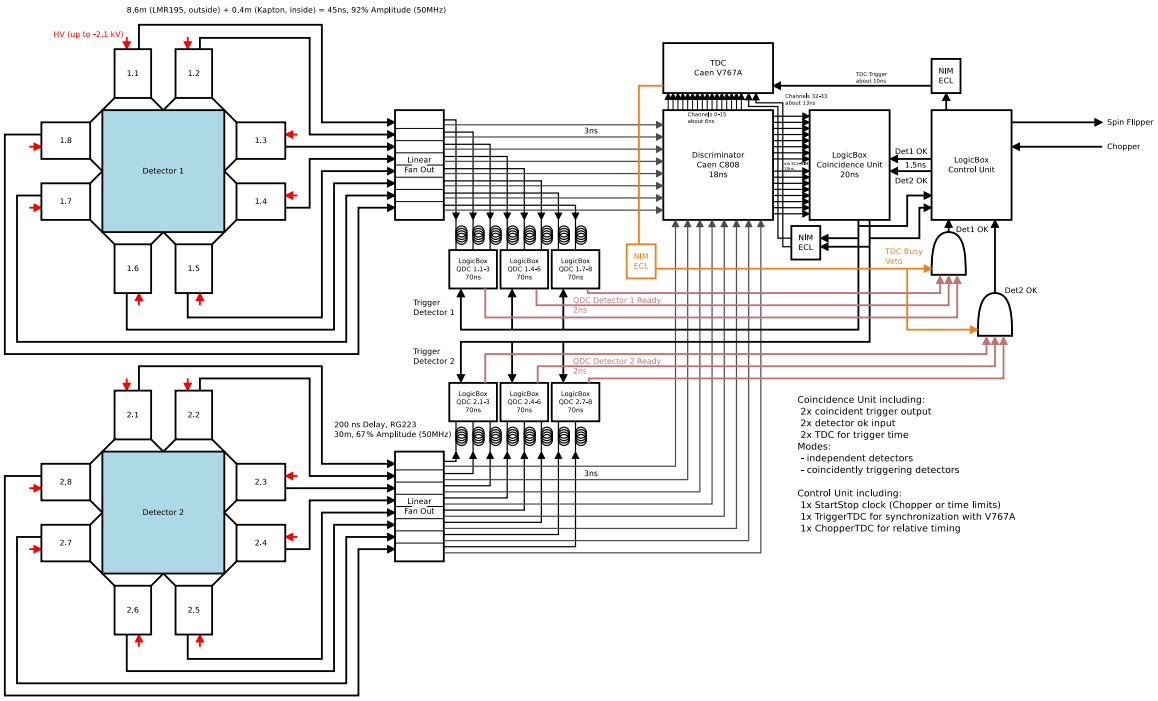

Figure 2.44: The schematic electronics setup for the proton asymmetry measurement is adapted from the electron asymmetry measurement [Mes11]. It is optimized for shorter delays and adapted to eight PMTs per detector. In principle, the detectors can be triggered individually, although this mode was not used during the beam time.

2.8.1 Cables

Since the electronic modules are not located near the detector, but in crates being accessible even when the neutron beam is switched on, the analog PMT signals have to be carried for a distance of approximately 8.6 m. Since a trigger logic is used to later start the charge integration, the signal has to be delayed by 200 ns, which is an equivalent of 40 m at a typical envelope velocity of $0.66 \times c$. Each meter of cable attenuates the signal and adds electronic noise at the same time. Therefore the main parameters are attenuation and shielding. The typical "cable from the cabinet" is an RG58, a cheap and robust choice, but with rather poor characteristics. An extensive survey of cable types yielded the best price-performance ratio for an LG-195 as the connection between detector vessel and electronics and an RG223 for the delay cables. While the typical rise time of a PMT pulse is 1 to 2 ns, the main part of the charge is carried by a wave packet of ≈ 20 ns length. To estimate the resulting signal loss of $\approx 38\,\%$, a signal frequency of 50 MHz is assumed. A special kind of cable is used inside the detector vessels to connect the PMTs with feed-throughs. To limit outgasing from the typical PVC sheathing, Kapton® is used instead. This kind of cable is rather hard to attach to a plug, though and should be avoided if possible.

2.8.2 Fan-Out and Trigger Logic

To split the analog signals between pulse analysis and trigger logic, a linear fan-out module Philipps Scientific Model 748 [Phi96] is used. Crosstalk is small for frequencies inferior to 100 MHz, for strong short PMT pulses small pulses related to neighboring channels are observed, however. As a consequence individual modules are used for each detector to

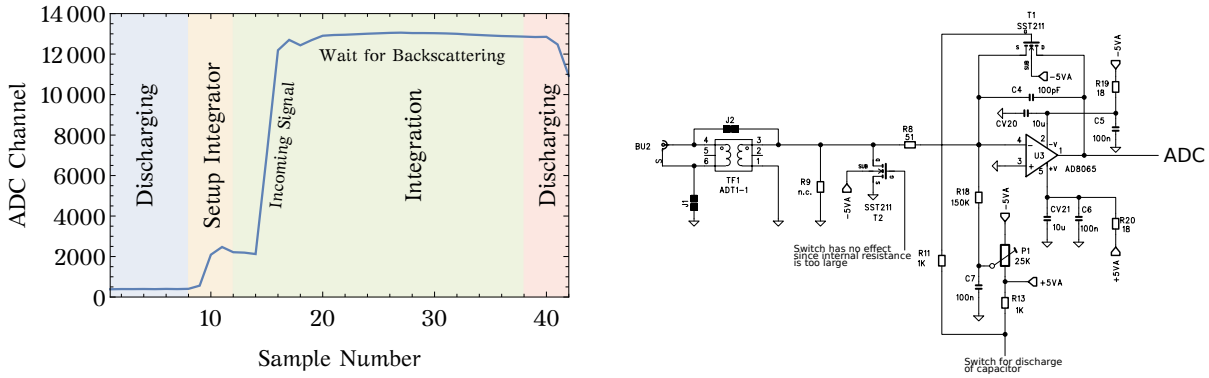

(a) The LogicBox firmware allows to read out all integration samples – one per 10 ns – of an event. To reduce the amount of data, only the first and the last sample of the integration region are kept.

(b) An active integrator circuit is used to measure the charge of incoming PMT signals. An external signal switches between integration and discharging.

Figure 2.45: Charge-integrating ADCs are used for pulse height analysis of PMT pulses. The system is not self-triggering and requires an external discriminator. The signal height is extracted from the difference of a start and a stop sample.

eliminate the detection of pseudo events on the opposite detector. In [Mes11] crosstalks related to the connected discriminator were investigated, an effect which could not be reproduced with a CAMAC based constant fraction discriminator CAEN C808 [CAE11]. Studies of the nonlinearity of the linear fan-out modules show [Sac16; Sau18], that the limited bandwidth of up to 250 MHz is the reason for a significant deviation from linearity on the same order of magnitude as scintillation quenching.

The use of a freely programmable so-called LogicBox, developed by the electronics workshop of the Physikalisches Institut, Universität Heidelberg, allowed to test different trigger patterns applied to the discriminator output. While typically, a two-out-of-all-PMTs trigger condition is imposed, this pattern was changed to a two-out-of-all-sides condition. This decreases the number of random afterpulses and background coincidences and conserves the spatial homogeneity of the trigger function.

A further LogicBox module, acting as the controlling unit, finally triggers the pulse integration of the individual QDCs. The controlling unit also receives trigger information from the chopper and sets the spin flipper state. For this measurement, always both detectors were triggered, a successful scheme which allows backscattering detection even below the trigger threshold. In principle it would also be possible to treat both detectors individually, which is an extension of the former electronic setup.

2.8.3 Charge Integrating ADCs

The QDCs, also part of the LogicBox family, allow sampling at 100 MHz, a mode which is used to investigate the timing, depicted in Figure 2.45a. To reduce the data load, only two samples, a start and a stop sample, were passed to the internal buffer during the productive measurement. To obtain the detected charge, a simple subtraction of the start sample value from the stop sample value has to be performed.

Although PMT pulses have a typical length of about 20 ns, the integration window is kept open to allow the energy detection of backscattered electrons. Particle tracking simulations in [Roi10] show, that a time window of 200 ns is sufficient to capture almost all backscat-

tering events. To allow a complete discharge of the integration unit, the trigger unit is blocking new incoming signals for 700 ns. A study of the nonlinearity of the QDCs [Sac16; Sau18] showed an integral nonlinearity of less than 1%. A rate dependent effect discovered in the PERKEO III 2009 measurements [Sau18] and described in a simulation using LTSpice [LTS; Raf17] can be corrected by applying an empirically determined offset. Unfortunately, the effect was only discovered after the beam time of 2014 and therefore renders a feature which automatically measures the pedestal before and after each cycle block of eight or 32 cycles useless. In this mode, every 10 µs an event is triggered, mainly without having any input signal. However, at this rate, the correction is maximal.

2.8.4 Data Acquisition Software

Electronic setup and data acquisition is done by the program `pudel`, which is a redesign of the formerly used `dackel` [Mes11; Kap07], the successor of `mops`. `pudel` is an acronym for "PERKEO's universal detector electronics library".

Next to the implementation by strictly following an object-oriented approach of `C++`, the main improvement is the use of separate CPU threads for the read-out of detector data, slow control data and the collection of event data inside ROOT [BR97] trees. This prevents overflows of buffers which could occur for `dackel` where all tasks are done sequentially. Furthermore the logging output is improved to give immediate feedback about event rates or erroneous data acquisition.

Part of `pudel` is PudelTV which is a browser based approach to present a quick online analysis of recently measured data. It provides a brief overview of signal and background measurements and slow control data.

2.8.5 Raw Data Processing

Before the raw data may be analyzed, it is processed in several steps by using the tool `p3reduce` by Heiko Saul [Sau18]. It allows a reduction of the event based data to multi-dimensional histograms by applying various cuts. All figures containing experimental data in this work are based on output of one of the many `p3reduce` analysis tools. A typical workflow is presented in section 3.5.

2.9 p3fit

All of the processes mentioned in this chapter are modeled in the in-house analysis software `p3fit`. Initially being a `FORTRAN` program, over time it was replaced by `C++` code, gained a terminal, configuration file and scripting interface, different fitter algorithms were included and its models were extended and optimized, also in the course of this work. The historical evolution makes it tedious to further extend the program however, motivating a code refactoring, which was implemented for this work.

Crucial parts for the implementation of different models are already described in the preceding sections, a few technical details of the implementation are found in appendices A.2 and A.3.

2.10 Conclusion

Figure 2.46 and Figure 3.14a present how well the combination of all detector effects applies to measured spectra. The knowledge about the detectors allows to keep its calibration

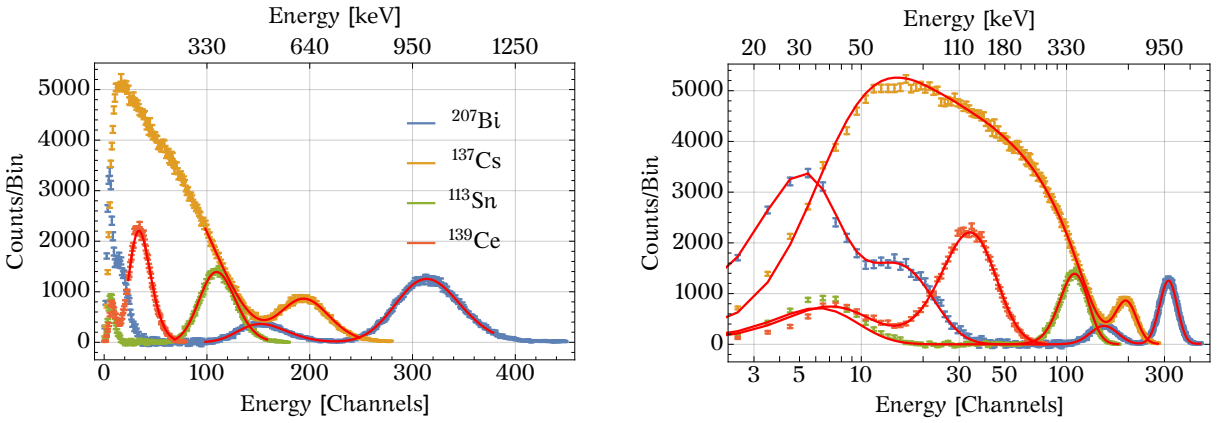

(a) Red lines indicate the actual fit regions for parameter extraction for the electron asymmetry analysis. Low energy effects do not play a role and are not considered.

(b) In logarithmic scale, the quality of detector and source description is demonstrated. Significant differences between model and data only appear at very low energies.

Figure 2.46: A combined fit of the detector function to measured calibration spectra is used to extract all detector parameters required for the determination of the electron asymmetry.

independent of the measured neutron beta decay spectrum and releases a former correlation between measured spectrum and detector function. It will allow to deduce a limit on the Fierz term using the sum of polarized beta spectra of Figure 2.47b.

The presented steps in this chapter allow the analysis of experimental beta asymmetry data collected with PERKEO III in 2009. It results in the new most precise ratio between axial-vector and vector coupling [Sau18]

$$\begin{aligned} \lambda &= -1.27641(45)_{\text{stat}}(33)_{\text{sys}} \\ &= -1.27641(56) \\ A &= -0.11985(17)_{\text{stat}}(12)_{\text{sys}} \\ &= -0.11985(21). \end{aligned} \tag{2.109}$$

In combination with the most recent neutron lifetime measurement [Pat+18], a competitive result for the CKM matrix element V_{ud}, solely from neutron measurements can be deduced [CMS18]:

$$V_{\text{ud}} = \sqrt{\frac{4908.6(1.9)\text{s}}{877.7(^{+0.8}_{-0.7})\text{s}(1+3\lambda^2)}} = 0.97462(^{+57}_{-53}), \tag{2.110}$$

which agrees well with $V_{\text{ud}} = 0.97420(21)$ [Tan+18] from superallowed beta decays, where large corrections for nuclear structure effects are required however.

The energy dependence of the electron asymmetry (1.4) may also be used to obtain a preliminary limit on the Fierz term [Sau18]:

$$b = 0.017(21) \tag{2.111}$$

This method is less sensitive to systematic uncertainties, but does not provide the same statistical precision as an extraction of this parameter from the neutron beta decay spectrum.

Direct contributions of this work to the final relative systematic uncertainty of $\Delta A_{\text{sys}}/A = 103 \cdot 10^{-5}$ of the electron asymmetry parameter are the correction for undetected backscattering of $50(20) \cdot 10^{-5}$ and the correction of $42(21) \cdot 10^{-5}$ for the detector non-uniformity and

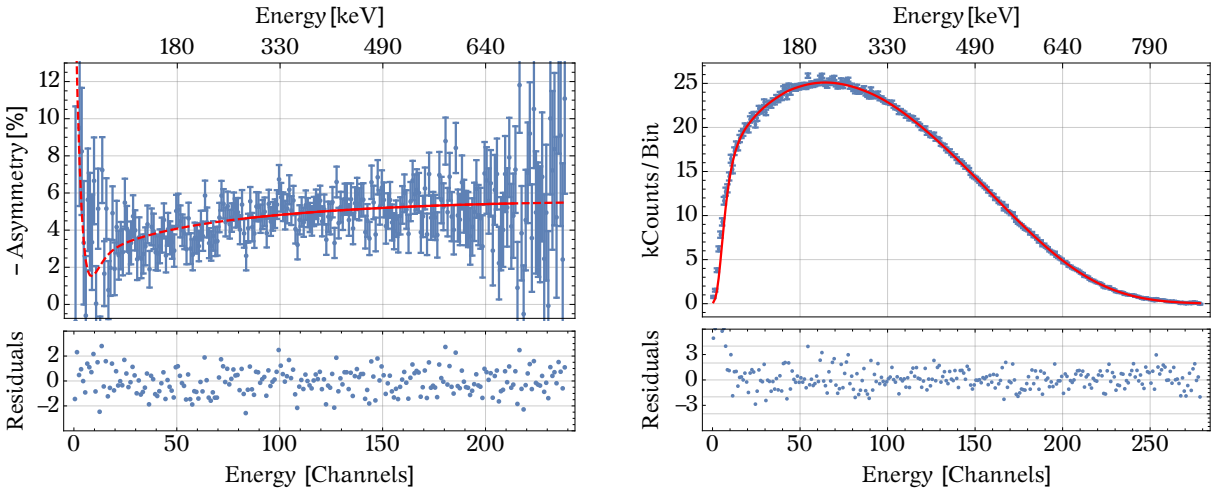

(a) The measured asymmetry spectrum is fully described by the model, including effects of spin dependent pedestals and undetected backscattering at low energies and the asymmetric PSF at high energies. The fit is performed for data between channel 85 and 215.

(b) The description of the neutron beta decay sum spectrum fits the data even below 100 keV. The detector function is entirely extracted from calibration fits. Here the Fierz term is fixed to be zero.

Figure 2.47: The figures show one out of 89 independent data sets for each detector. The asymmetry is extracted by averaging over individual fit results for all data sets [Sau18].

the finite thickness of the carrier foils. All systematic uncertainties of the measurement are listed in Table 1.1. The process of electron detection is described to a level that makes the analysis of the detector function independent of the actual subject of investigation, namely the neutron beta decay spectrum. The current analysis window sets the systematic uncertainty of the theoretical description of calibration sources to $10 \cdot 10^{-5}$. To preserve this uncertainty while decreasing the lower energy limit will require more precise data for the description of calibration sources or the application of new calibration techniques, such as energy determination using time-of-flight.

3 Proton Detection and Proton Asymmetry C

Compared to the TeV range of center-of-mass energy in collider facilities, beta decay measurements are considered to be low energy particle physics. This refers to the 10 keV to several MeV of maximum kinetic energy of the emitted electron. The actual low energy part is hidden in the recoil of the daughter nuclei, however. For heavy nuclei, the recoil can be neglected without hesitation, for the lightest, namely the proton, it plays an important role.

The maximum kinetic energy of the proton in neutron beta decay is 751.2 eV, as a result of energy and momentum conservation:

$$E_{p,\max} = \frac{m_n^2 - m_e^2 - 2m_n m_p + m_p^2}{2m_n}. \tag{3.1}$$

The so-called proton asymmetry parameter C does not appear in the differential decay width (1.2), but is directly related to electron asymmetry A and neutrino asymmetry B by a kinematical factor x_C [IPT13] due to energy and momentum conservation:

$$C = -x_C(A + B) = \frac{4x_C\lambda}{1 + 3\lambda^2} \quad \text{in the Standard Model.} \tag{3.2}$$

x_C includes access to the complete spectrum of the proton recoil and may be calculated to be $x_C = 0.275\,905(10)$ using [IPT13]. Additional contributions by radiative and recoil corrections are covered in section 3.1.3.

Equation (3.2) allows a test of the Standard Model, by comparing this result to measurements of λ by the means of a measurement of the electron asymmetry or the electron-antineutrino correlation. Extensions to the Standard Model affect the correlation coefficients differently and would manifest themselves as deviations between different results for λ.

The first and only successful experimental determination of the proton asymmetry was performed with the predecessor of Perkeo III, Perkeo II [Sch+08]. This chapter presents a new measurement of C with Perkeo III, which in its outline, similar to chapter 2, follows the track of the proton in the experiment. At first, the emission of the proton from neutron decay is discussed. The transport in the magnetic field is mainly covered in [Klo18], but two electrostatic devices are studied in more detail: Retardation electrodes and a wire grid are used to block protons depending on their energy and the proton detection system accelerates protons to release secondary electrons which are detected by an electron detector. Lastly the treatment of background events is described, before providing a preliminary error budget.

3.1 Proton Detection

The detection mechanism of this first measurement with Perkeo II in Figure 3.1a was similar to the one now used in Perkeo III in Figure 3.1b: Decay protons are guided along the magnetic field which connects two opposite detection systems. The magnetic field acts as a reference for the neutron spin and allows 4π coverage of the solid angle of the decay particle momentum. Since the kinetic proton energy is too low to allow direct calorimetric detection, the protons must be accelerated before detector contact. An electrostatic potential is inserted in the magnetic field region to achieve this. Since one requirement is the

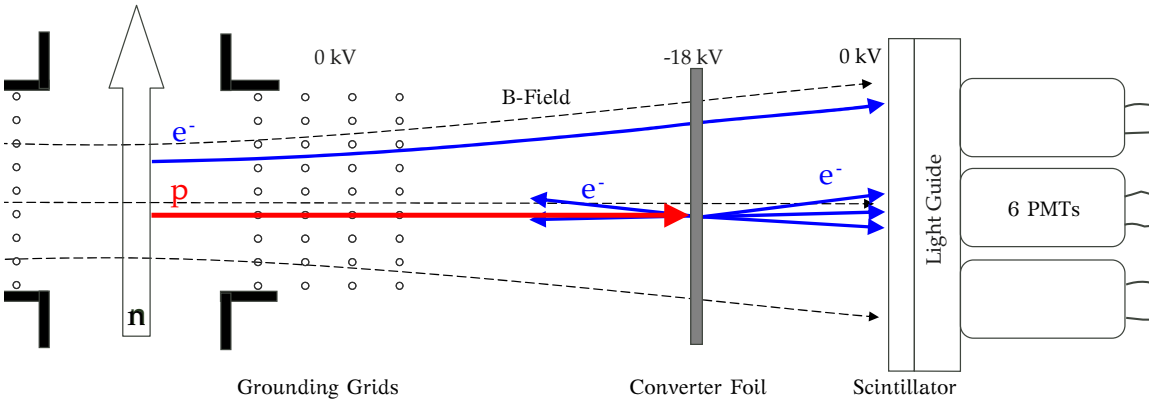

(a) In PERKEO II, protons were directly accelerated onto the converter foil. The electrostatic potential accelerates low-energetic secondary electrons onto a scintillator detector. Most electrons from beta decay are hardly affected by the foil and acceleration potential. Adapted from [Sch07].

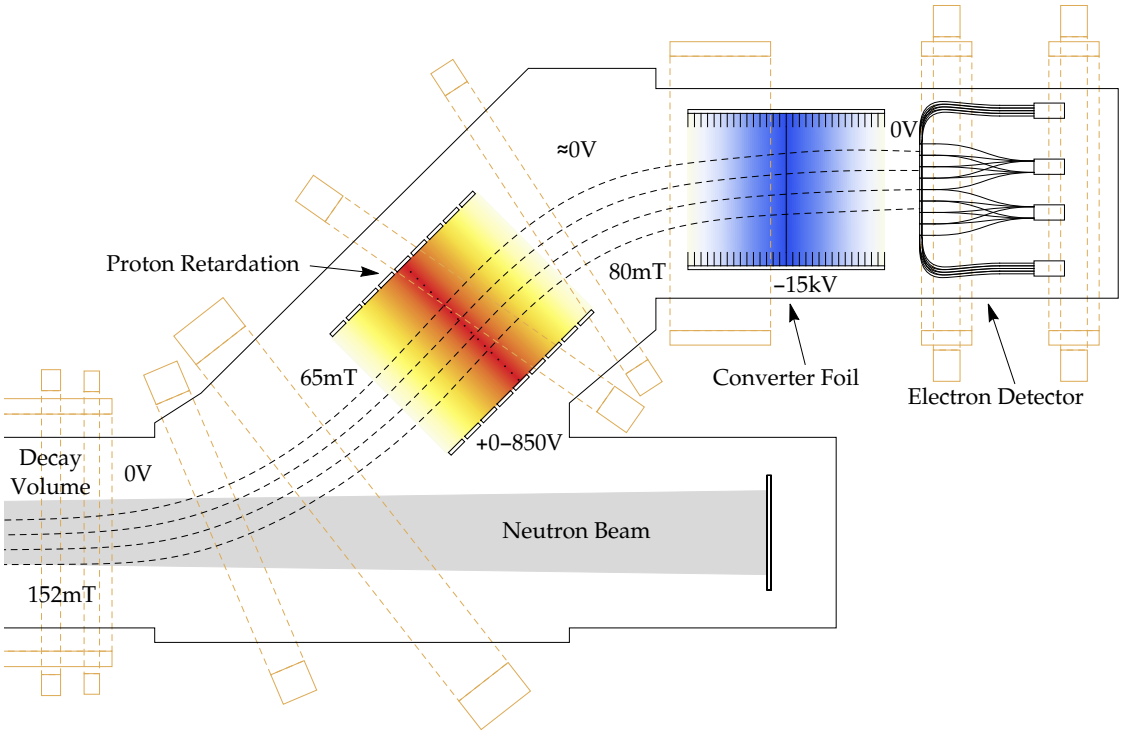

(b) The PERKEO III setup additionally provides proton energy information by a lite version of a MAC-E filter. A retardation plane before the acceleration section allows to block protons with energies below a threshold. The complete setup is shown in Figure 1.3.

Figure 3.1: Combined proton-and-electron detectors are used to determine the proton asymmetry parameter C and the antineutrino asymmetry parameter B. The low kinetic energy of the proton requires acceleration by electrostatic potentials. To allow detection of electrons in the 1 MeV range, an extremely thin carbon converter foil releases secondary electrons which are emitted by the impinging proton.

possibility of energy resolved electron detection during the same measurement period, no dedicated proton detector, such as avalanche photo diodes or microchannel plates can be used. Instead, the accelerated protons traverse an extremely thin carbon foil of $\approx 20\,\mu g/cm^2$ thickness, which leads to emission of secondary electrons, released by elastic scattering of the proton with carbon atoms. The secondary electrons themselves are accelerated onto the electron detector by the repelling electrostatic potential and have enough energy to release a trigger signal. Results of a measurement by Lukas Raffelt to characterize the required conductive coating on the surface of the electron detector is briefly described in section A.4 of the appendix.

3.1.1 Coincident Detection

The setup of Perkeo II in Figure 3.1a does not allow direct discrimination of proton and electron signals. Instead, the time of flight properties are exploited. A proton will always take more time to reach a detector, than its corresponding electron. Therefore, two successive detector events may be assigned to first an electron and second a proton, neglecting random coincidences. The distance from the decay volume to the detectors is sufficiently short to largely exclude random coincidences. This method yields four different detector hit dependent spectra $N^{\pm}_{\pm}$, whose upper index designates the detector hit by the electron, while the lower index indicates the detector hit by the corresponding proton [GJL95]:

$$r = \beta\frac{E}{E_\nu} \approx \beta\frac{E}{m_n - m_p - E} \tag{3.3}$$

$$N^+_+(E) = \Gamma(E)\begin{cases} 1 - \frac{r}{2} + \frac{a\beta}{4}\left(\frac{r^2}{2} - 1\right) + PA\beta\left(\frac{1}{2} - \frac{r}{3}\right) + P\frac{B}{2}\left(\frac{r^2}{3} - 1\right) & r \le 1 \\ \frac{1}{2r}\left(1 - \frac{a\beta}{4r} + P\frac{A\beta}{3r} - P\frac{2B}{3}\right) & r > 1 \end{cases} \tag{3.4}$$

$$N^-_-(E) = \Gamma(E)\begin{cases} 1 - \frac{r}{2} + \frac{a\beta}{4}\left(\frac{r^2}{2} - 1\right) - PA\beta\left(\frac{1}{2} - \frac{r}{3}\right) - P\frac{B}{2}\left(\frac{r^2}{3} - 1\right) & r \le 1 \\ \frac{1}{2r}\left(1 - \frac{a\beta}{4r} - P\frac{A\beta}{3r} + P\frac{2B}{3}\right) & r > 1 \end{cases} \tag{3.5}$$

$$N^+_-(E) = \Gamma(E)\begin{cases} 1 + \frac{r}{2} - \frac{a\beta}{4}\left(\frac{r^2}{2} - 1\right) + PA\beta\left(\frac{1}{2} + \frac{r}{3}\right) - P\frac{B}{2}\left(\frac{r^2}{3} - 1\right) & r \le 1 \\ 2 - \frac{1}{2r}\left(1 - \frac{a\beta}{4r} - P\frac{A\beta}{3r} + P\frac{2B}{3}\right) + PA\beta & r > 1 \end{cases} \tag{3.6}$$

$$N^-_+(E) = \Gamma(E)\begin{cases} 1 + \frac{r}{2} - \frac{a\beta}{4}\left(\frac{r^2}{2} - 1\right) - PA\beta\left(\frac{1}{2} + \frac{r}{3}\right) + P\frac{B}{2}\left(\frac{r^2}{3} - 1\right) & r \le 1 \\ 2 - \frac{1}{2r}\left(1 - \frac{a\beta}{4r} + P\frac{A\beta}{3r} - P\frac{2B}{3}\right) - PA\beta & r > 1 \end{cases}. \tag{3.7}$$

For $r < 1$ or $E_{\text{kin}} < 236\,\text{keV}$ there are two possible emission directions for the neutrino at fixed electron and proton emission directions, while for $r > 1$ the five parameters $(E, \theta_e, \phi_e, \theta_p, \phi_e)$ uniquely define the process. The sign of the polarization P can be changed by a neutron spin flipper.

The coincidental proton asymmetry

$$C_{\text{exp}}(E) = \frac{N^+_+(E) + N^-_+(E) - N^+_-(E) - N^-_-(E)}{N^+_+(E) + N^-_+(E) + N^+_-(E) + N^-_-(E)} = \frac{P}{6}\begin{cases} B(r^2 - 3) - 2Ar\beta & r \le 1 \\ A\left(\frac{1}{r^2} - 3\right)\beta - 2\frac{B}{r} & r > 1 \end{cases} \tag{3.8}$$

is therefore expressed depending on the electron energy E and obtained by a fit to the corresponding spectrum. In practice, in the fit A and B are expressed by λ which finally is used again to obtain C from equation (3.2). For systematic reasons the spin is flipped,

rather than mixing events from both detectors. Considering only electron events which hit the +-detector, the asymmetry reads

$$C_{\text{exp}}(E) = \frac{N_+^{\uparrow}(E) + N_-^{\downarrow}(E) - N_-^{\uparrow}(E) - N_+^{\downarrow}(E)}{N_+^{\uparrow}(E) + N_-^{\downarrow}(E) + N_-^{\uparrow}(E) + N_+^{\downarrow}(E)}. \tag{3.9}$$

$N^{\uparrow}$ and $N^{\downarrow}$ are events on the same detector with the spin flipper switched off (↑) or on (↓). Background subtraction was only performed by measurements without neutrons and the fit range was set to higher electron energies, which excludes the main background contributions [Sch07]. Probably to suppress random coincidence from background signals, the discriminator threshold of the electron detector was set quite high. This may have an impact on the proton energy dependence of the proton detection efficiency – see section 3.3.1 for reference. Therefore a different detector system is required to verify this first result.

3.1.2 Differential Detection

Similar to the approach of chopping the neutron beam to get a clean background subtraction, the proton asymmetry is directly measured with Perkeo III by chopping or rather blocking the protons – on a much longer time scale. A variable electrostatic potential between decay volume and the combined proton and electron detector allows to block protons away from detection. The electrodes which define this potential are installed in a magnetic field minimum and complete a simple MAC-E filter – compare to the experiments KATRIN [Ste+13] and *a*SPECT [Sim+09] – which allows some proton energy resolution for the blocking range. The setup is sketched in Figure 3.1b.

Many features of the measurement campaign 2014 to determine the proton asymmetry are described in [Raf16]. Therein an overview of the measurement setup, including the beam line and electron detectors, and an outline of steps towards the final result are presented. A detailed study of important systematic corrections related to particle propagation will be included in the dissertation by Michael Klopf [Klo18].

The experimental asymmetry now is measured by subtracting spectra $N^{\uparrow\downarrow}(U_{\text{block}})$ with all protons blocked from spectra with protons included $N^{\uparrow\downarrow}(U_R)$:

$$C_{\text{exp}}(U_R) = \frac{N^{\uparrow}(U_R) - N^{\uparrow}(U_{\text{block}}) - N^{\downarrow}(U_R) + N^{\downarrow}(U_{\text{block}})}{N^{\uparrow}(U_R) - N^{\uparrow}(U_{\text{block}}) + N^{\downarrow}(U_R) - N^{\downarrow}(U_{\text{block}})} \tag{3.10}$$

At the blocking voltage $U_{\text{block}} > E_{p,\text{min}}/e$, no protons may overcome the electrostatic barrier and only electrons may reach the detector, which for this measurement are considered to be background.

3.1.3 Proton Spectrum

The phase space (1.2) of neutron beta decay is expressed in terms of electron and antineutrino momenta, which makes analytical studies of proton properties not straightforward. In [IPT13; Iva17] numerically integrable expressions for the proton spectrum including first order radiative and recoil corrections are deduced. An additional contribution of proton-photon interaction is derived in [Iva+13].

Following the directions of [IPT13], the kinematical factor x_C from equation (3.2) may be

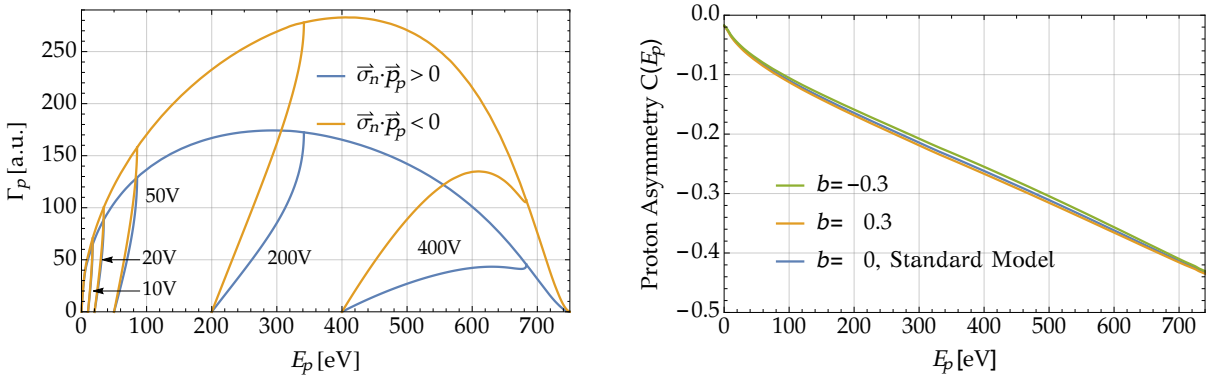

(a) Similar to the electron asymmetry A, the proton asymmetry C prefers emission against neutron spin direction over emission in spin direction. The various lines show the accessible spectra for different retardation modes.

(b) The proton asymmetry C increases almost linearly with the kinetic energy. It is sensitve to the Fierz term b and an additional scalar-and-tensor coupling contribution which could appear in the neutrino asymmetry B.

Figure 3.2: Theoretical calculations by [IPT13; Iva17] yield an easily numerical integrable representation of the proton recoil spectrum. Here, the spectra are presented for an axial-vector to vector coupling constant $\lambda = -1.275$.

calculated using

$$x_C = \frac{\int_0^{p_{p,\max}} \mathrm{d}p_p \int_{E_{e,\min}}^{E_{e,\max}} \mathrm{d}E_e \, E_e((E_0 - E_e)^2 + p_p^2 - p_e^2) F(E_e)}{\int_0^{p_{p,\max}} \mathrm{d}p_p \int_{E_{e,\min}}^{E_{e,\max}} \mathrm{d}E_e \, 4(E_0 - E_e) E_e p_p F(E_e)}, \qquad E_{e_{\min}}^{\max} = \frac{(E_0 \pm p_p)^2 + m_e^2}{2(E_0 \pm p_p)}, \tag{3.11}$$

where p_p is the proton momentum and E_e and E_0 are the electron energy and the endpoint of the electron spectrum. This relation does not include radiative and recoil corrections which yield a much more complicated function. Furthermore an additional contribution by the electron-antineutrino correlation parameter a must be added to the denominator, if low-energy parts of the proton spectrum are excluded from the integration – i.e. $p_{p,\min} > 0$. In the Standard Model recoil and radiative corrections result in a relative change of the proton asymmetry parameter C of about 1.7‰, which depends on the measured ratio of axial-vector and vector couplings. The neglect of higher order corrections is accounted for by an assumed relative uncertainty of $3 \cdot 10^{-4}$. Figure 3.2a shows the corresponding differential proton spectra for polarized neutrons.

A measurement of the proton recoil spectrum cannot be done by direct energy detection, but may only be derived from time of flight information like in the experiments aCORN [Dar+17] and Nab [Bae+13] or by an integral measurement, such as in the experiment aSPECT [Sim+09]. By applying a blocking voltage like in aSPECT, the sensitivity to scalar-and-tensor coupling contributions is enhanced – see section 1.1. An exemplary influence of a nonzero Fierz interference term on the differential proton asymmetry is sketched in Figure 3.2b.

Doppler Effect

Although it seems unlikely, the neutron velocity v_n has an influence on the measured proton asymmetry. By changing the reference from the neutron at rest to the lab frame, a

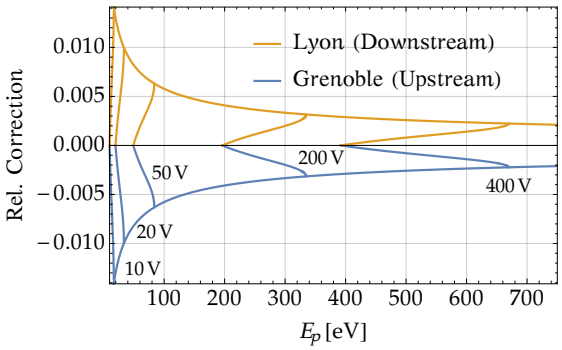

Figure 3.3: The Doppler effect increases the measured asymmetry on the upstream detector and must therefore be corrected by a negative correction factor. For the downstream detector the opposite correction is applied. By not mixing detectors for the evaluation of the asymmetry, the correction remains small. The correction is displayed for different retardation modes.

transformation of the polar angle θ to the magnetic field has to be done:

$$\cos\theta = \frac{v_p \cos\theta}{v_p} \xrightarrow{\text{to rest frame}} \frac{v_p \cos\theta - v_n}{\sqrt{v_p^2 \sin^2\theta + (v_p \cos\theta - v_n)^2}} = \frac{v_p \cos\theta - v_n}{\sqrt{v_p^2 + v_n^2 - 2v_p v_n \cos\theta}} = \cos\theta_n. \tag{3.12}$$

Here θ_n is used for the polar angle in the neutron rest frame, which is important for the asymmetric angular distribution, while θ denotes the observed polar angle. These calculations can be performed non-relativistically, since the kinetic energy of the proton is more than six orders of magnitude smaller than its rest energy.

Consequently there are more events observed on the downstream detector Lyon ($\theta < \pi/2$), than on the upstream detector Grenoble ($\theta > \pi/2$). The correction in Figure 3.3 for a neutron velocity $v_n = 800\,\text{m/s}$ becomes quite large at small proton energies where the phase space is rather small, but decreases to below $3 \cdot 10^{-3}$ towards the endpoint of the spectrum. The individual corrections for different measurement modes which are described in the following section yield:

Retardation	Rel. Correction (10^{-3})
10 V	3.59
20 V	3.51
50 V	3.31
200 V	2.52
400 V	1.25

The Doppler effect increases the measured asymmetry on the upstream detector and decreases it on the downstream detector. The sign for the correction must be chosen correspondingly. The uncertainty is estimated to be below 10 % by taking into account the neutron spectrum and divergence of the neutron beam.

3.2 Retardation System

The most important experimental difference to the measurement of the proton asymmetry parameter C with Perkeo II lies in the use of a set of retardation electrodes, which prevent

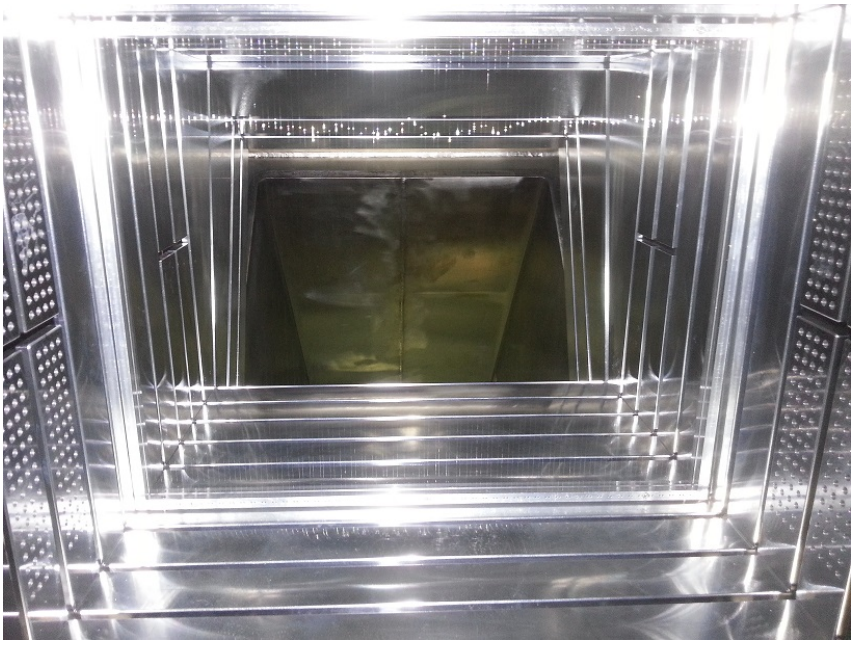

Figure 3.4: A photo of the retardation electrode system (opening diagonal $\approx 75\,\mathrm{cm}$) taken from the central volume [Klo15]. The wire grid which defines the retardation plane is visible, as well as the electrodes which can be set individually. The separation into upper and lower electrodes was foreseen to induce an $\vec{E}\times\vec{B}$ drift to residual gas ions.

particles from the decay region with kinetic energies below a certain threshold to reach the detectors.

The electrode system was designed by Michael Klopf [Klo18] and was initially foreseen to be used without any grid to circumvent background issues which were observed in the measurement with PERKEO II [Dei05]. This wireless concept has two drawbacks:

1. A plasma can build up undisturbed between both proton detectors.

2. The retardation region has an inhomogeneous potential which leads to a more complicated transmission function.

During the experiment the first point made at least one wire grid a requirement, while the second point hinted to the best position of the grid being the retardation plane. It finally turned out, that the grid in a region of low electric fields imposed no problems. This leads to the assumption, that the creation of ions in PERKEO II was solely related to the large potential gradient due to the vicinity of the grid to the acceleration potential of the converter foil.

The retardation electrode system in PERKEO III consists of several electrodes, which can be set to individual potentials. Strong electric fields at the wires can be avoided by increasing the electrode potential towards the wire grid. The photo in Figure 3.4 shows the electrodes after insertion of the grid.

3.2.1 Measurement Scheme

The measurement scheme was selected, such that most time is spend on measuring the proton asymmetry at blocking voltages at $U_R = 10\,\mathrm{V}$ and $U_R = 20\,\mathrm{V}$ as these provide most

statistics and have the smallest experimental uncertainties. For studies of the shape of the differential proton asymmetry, there were also measurements at 50 V, 200 V and 400 V retardation voltage. Protons were completely blocked at $U_R = 850$ V. The final scheme with the number of cycles per setting in consecutive order row-by-row was

Emptying	Ramping	Measurement	Emptying	Ramping	Measurement
8×0 V	8×10 V	32×10 V	8×0 V	8×850 V	32×850 V
8×0 V	8×50 V	32×50 V	8×0 V	8×20 V	32×20 V
8×0 V	8×850 V	32×850 V	8×0 V	8×10 V	32×10 V
8×0 V	8×400 V	32×400 V	8×0 V	8×850 V	32×850 V
8×0 V	8×20 V	32×20 V	8×0 V	8×850 V	32×850 V
8×0 V	8×200 V	32×200 V.			

One block consists of 528 cycles, running for ≈ 1.5 h, with 700 chopper turns $\simeq 9.2$ s per cycle. The spin flip pattern for eight cycles alternates between 01101001 and 10010110 (1 - spin flipper on, 0 - spin flipper off) between blocks, to cancel possible remaining ramping effects. Data from trap emptying and ramping cycles are not used for the final analysis. For emptying the particle trap, which is build up by the retardation potentials and the connecting magnetic field, the retardation electrodes are physically detached from the high voltage supply and connected to the environmental ground potential to ensure that no low-energetic ions may remain trapped. No measurement runs are performed at 0 V to ensure that hypothetical ionization related to the neutron beam cannot be detected and misinterpreted as real events.

In section 3.4, background issues related to the high voltage required for proton detection are addressed. To minimize the uncertainty of the dead time correction due to varying signal rates, only measurements which were performed in short succession are combined. Since more time is spend on signal measurements, than on background measurements, the latter have to be split onto signal data sets. The fraction of data from a background measurement which is assigned to a signal data set S follows

$$\frac{t_{\mathrm{bg}}^{S}}{t_{\mathrm{bg}}} = \frac{1}{\sum\limits_{S_i} \frac{\#_{\mathrm{cycles}}^{S_i} \times \#_{\mathrm{cycles}}^{\mathrm{bg}}}{\Delta T_{\mathrm{bg}}^{S_i}}} \frac{\#_{\mathrm{cycles}}^{S} \times \#_{\mathrm{cycles}}^{\mathrm{bg}}}{\Delta T_{\mathrm{bg}}^{S}}, \tag{3.13}$$

where $\Delta T_{\mathrm{bg}}^{S}$ denotes the time difference between signal and background measurement and accounts for background drifts. The number of background cycles $\#_{\mathrm{cycles}}^{\mathrm{bg}}$ – with protons fully blocked – cancels here, but plays a role when combining multiple background measurements into a single signal measurement. For S_i only signal measurements after the preceding and up to the following background measurement are considered. In practice, background data sets are not split, but statistical errors are scaled by $\sqrt{t_{\mathrm{bg}}/t_{\mathrm{bg}}^{S}}$. This leads to correlated statistical errors between measurements at different retardation voltage settings.

3.2.2 Asymmetric Retardation

All retardation voltages U_R mentioned so far are referring to a symmetrical setup, where both electrode systems are set to equal potentials. Driving both systems at different voltages opens up opportunities for systematic tests. For these tests, one of the electrode systems is set to full proton retardation, while the other is set to 10 V or 400 V potential.

First of all, accidental misassignments of secondary electron events to the wrong detector can be excluded. No proton signal is expected on the fully blocked detector. If however there is such a signature on this detector, this may hint to secondary electrons which are

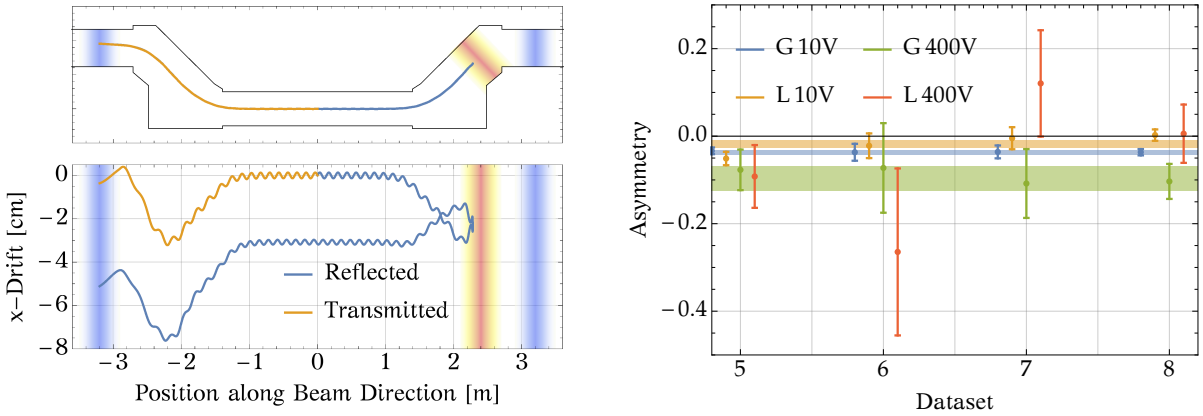

(a) Protons which directly reach the proton detector effectively experience almost no drift. Reflected protons are more unlikely to be detected, since they are shifted by up to several cm. The red region shows the retardation plane.

(b) Drifting protons are more likely to not reach the conversion foil, which is of finite size. Therefore an asymmetry is measured for asymmetrically blocking setups. A higher asymmetry for the Grenoble (G) detector agrees with positioning measurements using calibration sources.

Figure 3.5: Measurements with asymmetric retardation settings are very sensitive to the the magnetic field. Especially $\vec{R} \times \vec{B}$ drifts lead to shifts of the proton position perpendicular to the magnetic field.

emitted from the opposite proton conversion foil towards the blocked detector and are able to pass the blocked conversion foil and be detected. This effect is excluded for most of the data sets in section 3.3.1, with a different method, however. A second effect to be studied is related to $\vec{E} \times \vec{B}$ and $\vec{R} \times \vec{B}$ drifts. The first lets charged particles drift in the direction of $\vec{E} \times \vec{B}$ in combined electrical and magnetic fields. The latter induces drifts in curved magnetic fields perpendicular to curvature and magnetic field, such as in the separator section between neutron beam and charged particle path of PERKEO III. Both effects have an influence on the edge effect, which arrises due to a finite detector size and its incomplete coverage of the charged particle beam. In an ideal environment, the blocking electrodes would simply reflect any incoming protons, which were then registered by the unblocked detector. The measured asymmetry should therefore be zero. In the real environment, the mentioned effects lead to a measurable asymmetry in Figure 3.5b, hinting to a loss of protons which experience these drifts. Figure 3.5a illustrates the drift effect for two protons, one being directly transmitted, one being reflected first. In [Klo18], this effect is studied using particle tracking simulations which include the measured magnetic field of PERKEO III and calculated electric fields for retardation electrodes and proton detector. A validation of the electric field calculations follows in the next section.

3.2.3 Reach-Through

To minimize the reach-through of the electric potential at the blocking electrodes, the wire grid was inserted in the central proton blocking electrode. This grid also acts as an absorber for charged particles which are trapped in the magnetic field between the electric field boundaries of the Field Degrader.

While the grid already reduces the reach-through by a factor of ≈ 20, there still is a change of potential in the wire grid layer, depending on the distance to the wires. The grid extends

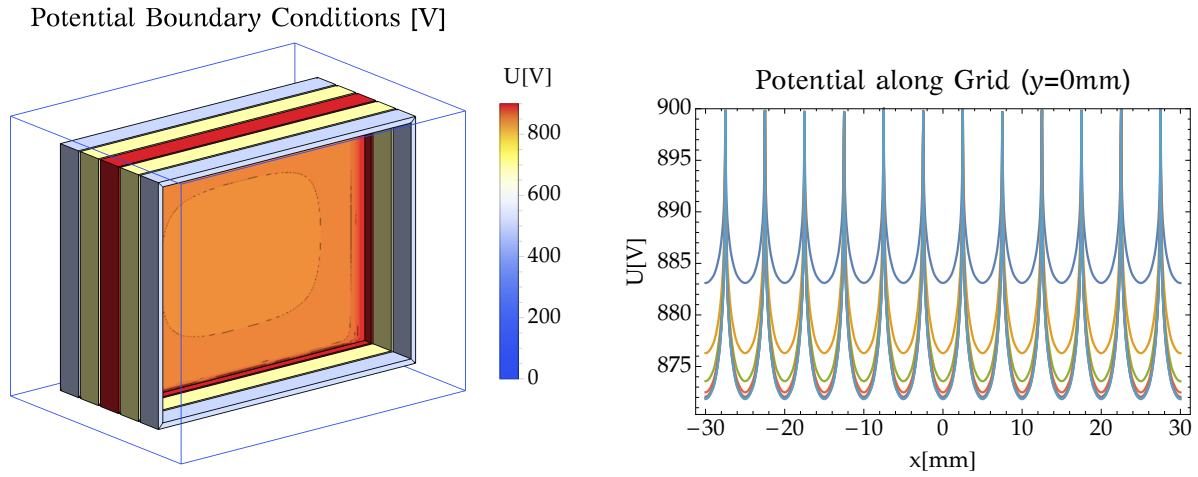

(a) The potentials are fixed at the electrodes and varying in the center. The latter can be calculated with the help of the near-region-simulation which is used as a boundary condition for the far region calculation.

(b) The calculation in the inner region shows a variation of the electric potential within 3 %, leading to an effective blocking potential. A comparison with other methods shows deviations < 0.05 % [Klo18].

Figure 3.6: To calculate the grid blocking potential, the boundary problem is split into two parts. A three dimensional outer region is mainly determined by the electrode potentials, while two dimensional slices of the inner region is dominated by the wire grid potentials. Within ten iterations indicated in b, a smooth transition between both models is obtained and converges to the final result.

over a width of 52.5 cm with wires of 25 µm diameter and a spacing of 5 mm. Since the dimension of the wires are much smaller than the overall dimensions of the system, it is difficult to find a reasonable finite element mesh that allows the calculation of the potential inside the space. In [Klo18] a simulation of the whole PERKEO III instrument is performed to obtain the electric potential at any point. This section shows a cross-check of the results obtained therein, using a different method.

Simulation

The problem can be expressed as the Dirichlet boundary problem with Laplace's equation

$$\begin{aligned} \Delta\Phi = 0, \text{where } \rho(\vec{x}) = 0 \\ \Phi|_{\partial V} = U_{\text{electrode}}. \end{aligned} \tag{3.14}$$

Only for a few geometries this can be solved analytically, so a numerical solution will be found using `Mathematica`'s numerical equation solver with finite elements. As already mentioned, the main task is to include the small wires within the large volume. One approach is to split the problem into a near-wire-region and a region which is far enough away from the wires such that the microscopic influence of the potential vanishes. The far-region can be implemented as seen in Figure 3.6a. The electrodes are at fixed potentials, while the inner end of the far-region is defined as a floating potential whose behavior is a result of the following calculations.

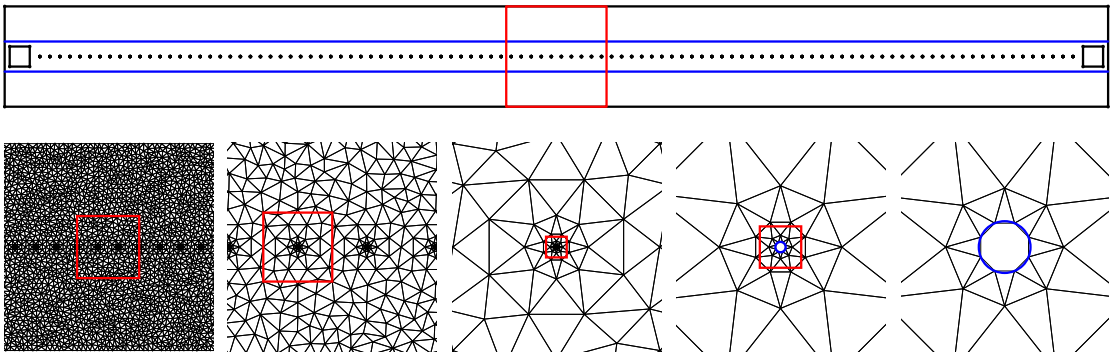

Figure 3.7: The horizontal blue lines show the boundary position used for the far-region boundary condition. The blue circle shows the theoretical shape of the wire, while the black lines show the 2D-mesh. Each red rectangle shows the next zooming stage.

2D-Approach

For this approach, the region inside the central electrode is separated into 2D-slices, such that the wires appear as circles as in Figure 3.7.

For each of these slices, the boundary conditions are taken from the far-region simulation. Since in 2D, the space has to be separated into triangular mesh elements – instead of tetrahedrons in 3D – the number of finite elements is largely reduced and the calculation accelerated. The slices are chosen in this way, because the potential between two slices only changes slowly and interpolation can be used to reconnect the result to a 2D surface such as in Figure 3.6a.

By applying these steps – calculating the far-region potential, afterwards the near-region potential – several times, a converging solution can be found. Possible initial parameters are:

1. setting the complete inner region to the potential of the inner electrode
2. do not use an inner boundary condition at all (as if there were no wires)

The convergence in Figure 3.6b is the result of the first approach.

Comparison to other Methods

In [Klo18] the presented geometry is implemented with COMSOL [COM] and `neBEM` [MM06] to compare the outcome of the simulations. Differences of the methods are $< 0.05\,\%$ which makes the computational error negligible compared to effects due to surface potentials. An advantage of the combination of two and three dimensional geometries is the quick convergence. However, the implementation of more complex geometries is time consuming, compared to a COMSOL model.

3.2.4 Grid Effect

The presence of wire grids in the retardation plane gives rise to the probability of protons hitting these wires. For these cases, two things have to be considered:

- Either the proton is lost or reflected.

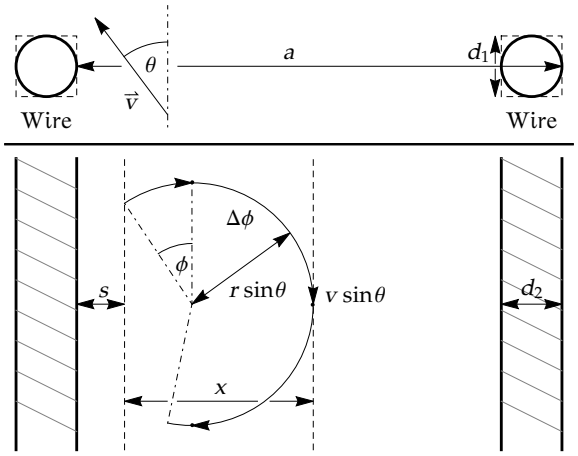

(a) Particle movement through a wire grid in the approximation of homogeneous magnetic and zero electric field. The wires are modeled by a rectangular shape of dimensions $d_1 \times d_2$. For a uniform distribution of s, the probability to hit a wire is $(x + d_2)/a$.

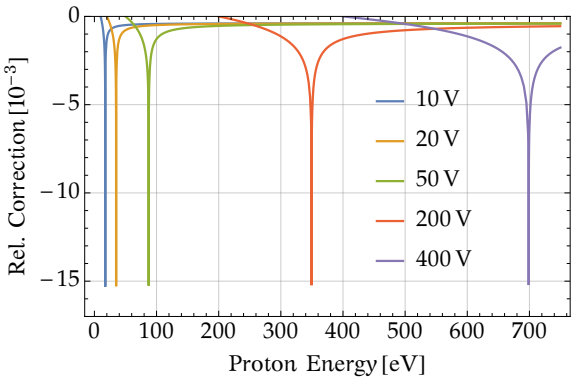

(b) Correction to the differential proton asymmetry for different retardation voltages when assuming no backscattering. Protons which are emitted in neutron spin direction have a higher probability to hit a wire, which relatively increases the measured asymmetry.

Figure 3.8: A wire grid which is installed in the retardation plane of the electrode system allows protons to hit these wires. In a model for an estimation of the influence on the measured proton asymmetry, the wires are rectangularly shaped and may be hit from the front or on the sides.

- The wires are made of aluminum – the proton might sputter an aluminum ion.

A simulation with TRIM [ZZB10] shows that the sputtering probability is ≈ 5 % and can therefore be neglected. Even if an ion is released, it only has a chance of being detected if at least three atomic shell electrons are missing, due to the thickness of the carbon foil in the proton-to-electron converter.

Proton reflection plays a role, however. Protons with an energy of 500 eV which hit an aluminum target under an angle of 45° have a probability of ≈ 35 % to be reflected. This probability increases towards lower energies. Depending on where the wire is hit, the proton might continue towards the originally aimed detector or the opposite detector. This effect was not considered for the measurement with Perkeo II [Sch07] and will be treated later on.

Hit Probability

First of all the overall probability that a proton hits one of the wires is obtained. Here a rectangular wire of thickness d_1 and width d_2 is considered. While the proton is passing the thickness d_1 in the wire grid plane, it covers a range x in Figure 3.8a.

The starting point s is considered to be uniformly distributed within 0 and the distance between two wires a. Following the sketch, the wire is hit, if $s > a - d_2 - x$ and therefore the probability to hit the wire is

$$P_{\text{hit}} = \begin{cases} \frac{x+d_2}{a}, & x + d_2 < a \\ 1, & \text{otherwise.} \end{cases} \tag{3.15}$$

The angle of gyration $\Delta\phi$ as a parameter for x can be expressed as follows:

$$d_1 = v\ t \cos\theta \tag{3.16}$$

$$\Rightarrow \Delta\phi = \frac{v\ t \sin\theta}{r \sin\theta} = \frac{d_1}{r\cos\theta}. \tag{3.17}$$

Here the proton moves with a total velocity v at polar angle θ to the magnetic field. The radius of gyration is defined by $r\sin\theta$, where

$$r = \frac{p_p}{e\ B_R}, \tag{3.18}$$

according to the Lorentz force in a magnetic field B_R in the retardation plane. An expression for x requires a distinction of cases. The azimuth ϕ is uniformly distributed between 0 and 2π. For reasons of symmetry however it can be limited to $(-\pi/2 - \Delta\phi/2, -\Delta\phi/2)$.

$$\frac{x}{r\sin\theta} = \begin{cases} \sin(\phi+\Delta\phi) - \sin\phi, & \phi > -\frac{\pi}{2} \\ 2, & \phi > \frac{\pi}{2} - \Delta\phi \\ 1 + \sin(\phi+\Delta\phi), & \text{otherwise.} \end{cases} \tag{3.19}$$

The first branch is only accessible for $\Delta\phi < \pi$, the second only for $\Delta\phi > \pi$. On average, the coverage reduces to

$$\overline{x} = 2r\sin\theta \begin{cases} \frac{\Delta\phi}{2\pi} + \frac{1}{\pi}\sin\left(\frac{\Delta\phi}{2}\right), & \Delta\phi < 2\pi \\ 1, & \text{otherwise.} \end{cases} \tag{3.20}$$

$\overline{x}$ cannot be used to calculate the average hit probability though, which would be overestimated for $\Delta\phi$ close to 2π. Instead it must be determined by integration:

$$\overline{P_{\text{hit}}}(\Delta\phi(r, \sin\theta, d_1), d_2) = \frac{2}{\pi} \int_{-\frac{\pi+\Delta\phi}{2}}^{-\frac{\Delta\phi}{2}} \mathrm{d}\phi \begin{cases} \frac{x(\phi,\ \Delta\phi)+d_2}{a}, & x + d_2 < a \\ 1, & \text{otherwise,} \end{cases} \tag{3.21}$$

which may be evaluated to analytical but unhandy expressions.

The corresponding correction to the measured asymmetry can now be calculated by assuming proton loss if a wire is hit:

$$C_{\text{measured}}(E_p) = 2C_{\text{real}}(E_p) \frac{\displaystyle\int_{\Re\sqrt{1-\frac{B_0}{B_R}\left(1-\frac{eU_R}{E_p}\right)}}^{1} \left(1 - \overline{P_{\text{hit}}}\left(r(E_p), \sqrt{\frac{B_R(1-\cos^2\theta)}{B_0\left(1-\frac{eU_R}{E_p}\right)}}, d_1, d_2\right)\right) \cos\theta\, \mathrm{d}(\cos\theta)}{\displaystyle\int_{\Re\sqrt{1-\frac{B_0}{B_R}\left(1-\frac{eU_R}{E_p}\right)}}^{1} \left(1 - \overline{P_{\text{hit}}}\left(r(E_p), \sqrt{\frac{B_R(1-\cos^2\theta)}{B_0\left(1-\frac{eU_R}{E_p}\right)}}, d_1, d_2\right)\right) \mathrm{d}(\cos\theta)} \tag{3.22}$$

Since the polar angle θ does not change the probability of whether the front face of the wire is hit, the width d_2 of a wire has no influence on the measured asymmetry, only the

thickness d_1 is crucial. For a thickness of $d_1 = 25\,\mu\text{m}$ Figure 3.8b shows the correction. Peaks occur at the energy where all of the protons emitted in one of the half-spheres start to overcome the electrostatic barrier. At this energy $E_p = \frac{eU_R}{1-\frac{B_R}{B_0}}$, the angular distribution of proton momenta has a singularity at 90°, where the correction is maximal. For lower energies the singularity does not overcome the potential, while at higher energies, it already occurs at smaller polar angles. The overall corrections to the measured integral proton asymmetries would then be

Retardation	Rel. Correction (10^{-4})
10 V	-4.3
20 V	-4.8
50 V	-6.3
200 V	-12.1
400 V	-13.7

Proton Backscattering

The situation changes, if backscattering is considered. If the backscattered proton continues to move towards the originally aimed detector, the correction simply gets smaller. If instead it moves towards the opposite detector, the measured asymmetry is reduced, which is very similar to undetected backscattering in electron detection as discussed in section 2.7:

$$C_{\text{measured}} \approx \frac{\left(N^{\uparrow} - N^{\downarrow}\right)(1 - \overline{P_{\text{hit}}}) + \left(N^{\uparrow} - N^{\downarrow}\right)(p_{\text{same}} - p_{\text{opp}})\overline{P_{\text{hit}}}}{\left(N^{\uparrow} + N^{\downarrow}\right)(1 - \overline{P_{\text{hit}}}) + \left(N^{\uparrow} + N^{\downarrow}\right)(p_{\text{same}} + p_{\text{opp}})\overline{P_{\text{hit}}}} \tag{3.23}$$

$$= \frac{\left(N^{\uparrow} - N^{\downarrow}\right)(1 - (1 - p_{\text{same}} + p_{\text{opp}})\overline{P_{\text{hit}}})}{\left(N^{\uparrow} + N^{\downarrow}\right)(1 - (1 - p_{\text{same}} - p_{\text{opp}})\overline{P_{\text{hit}}})} \tag{3.24}$$

$$= C_{\text{real}}\left(1 - 2\frac{p_{\text{opp}}\overline{P_{\text{hit}}}}{1 - (1 - p_{\text{same}} - p_{\text{opp}})\overline{P_{\text{hit}}}}\right) = C_{\text{real}}\left(1 - 2\frac{\epsilon}{\alpha}\right), \tag{3.25}$$

where p_{same} is the probability of reflection in forward direction and p_{opp} is the probability of reflection towards the wrong detector. The probability for false assignment ϵ and the overall detection probability α for not being lost in the wire correspond to the same notation used for undetected electron backscattering in equation (2.104).

This effect will be studied in more detail in [Klo18], including angular and energy distributions of the backscattering probability. To obtain an estimate for the expected order of magnitude, the following assumptions are made: The wires are still considered to be of rectangular shape. If a proton hits the front face of the wire, it will move towards the opposite detector in case of reflection. If one side of a rectangular wire is hit, it may continue to move in its original direction if it is backscattered. These cases can be accounted for by either setting the thickness d_1 or the width d_2 to zero when calculating $\overline{P_{\text{hit}}}$. For the backscattering probability, 35 % will be used in both cases. In Figure 3.9 it results in a measured asymmetry which is smaller than the actual asymmetry by a factor of about 3‰. Again, it must be noted, that this result is based on simple assumptions and a more realistic behavior is still to be evaluated. The correction may probably be determined with a relative uncertainty of 1‰ on the proton asymmetry.

For future measurements with PERC, proton backscattering from grid wires will not have the same influence on the measured asymmetry, since only one detector will be used and a

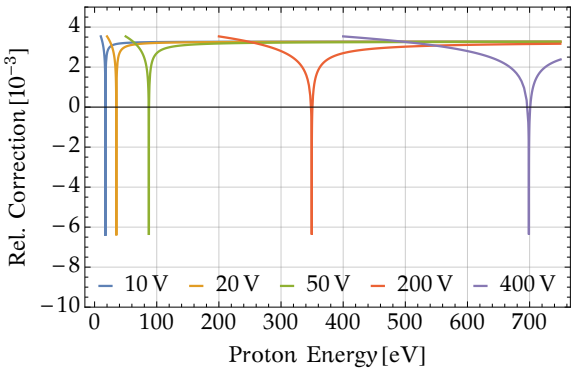

Figure 3.9: A rough estimate of the correction due to the grid effect yields 3‰ if proton backscattering is taken into account. In the simplified model, hitting the front face of a wire may result in backscattering in the opposite direction, while scattering off of the side of a wire lets the proton continue its movement in the same direction.

false assignment of the emission direction is excluded. Therefore the positive effect on the homogeneity of the electric potential may be exploited, as well as the disturbing influence on plasma build-up between magnetic filter and retardation potential, without the drawback of a relatively large correction. The transmission function of the blocking potential may be characterized experimentally by using the positron source CALIPSO which has been developed by Romain Virot for this purpose [Vir17].

3.3 Field Degrader

The key instrument of the proton asymmetry measurement is a proton-to-electron converter device, referred to as Field Degrader. It allows the detection of those protons that are able to overcome the electrostatic barrier of the retardation system. A photo with an installed converter foil is shown in Figure 3.10a. It is a symmetrical reflectron setup, consisting of 15 electrodes on each side, linearly increasing the electric potential up to the central potential, where a converter foil is installed. The foil "converts" accelerated protons into secondary electrons, which can then be detected by the electron detector on the other side of the foil. Each symmetric pair of electrodes is surrounded by a copper plated Kapton® foil to allow a step-wise potential reduction towards the detector vessels, depicted in Figure 3.11. This design works excellently under air, but has some drawbacks when employed in vacuum: The small space of 0.17 mm for each layer of shielding foils is hard to evacuate, such that the pressure inside the device is larger than expected. This gives rise to small discharges and subsequent photon and charged particle emission which leads to background events in the adjacent detector, investigated in section 3.4. A more detailed description of the Field Degrader design can be found in [Raf16].

3.3.1 Secondary Electrons

The key to an efficient proton detection, is an efficient production of secondary electrons. Naturally, the number of electrons produced along a path length $\mathrm{d}x$ is related to the proton energy loss $\mathrm{d}E/\mathrm{d}x$. Since the proton will lose all of its kinetic energy in the course of its detection, the first thing which comes into the mind is to increase the proton energy as far as possible. However, secondary electrons are produced at atomic scale energies of few

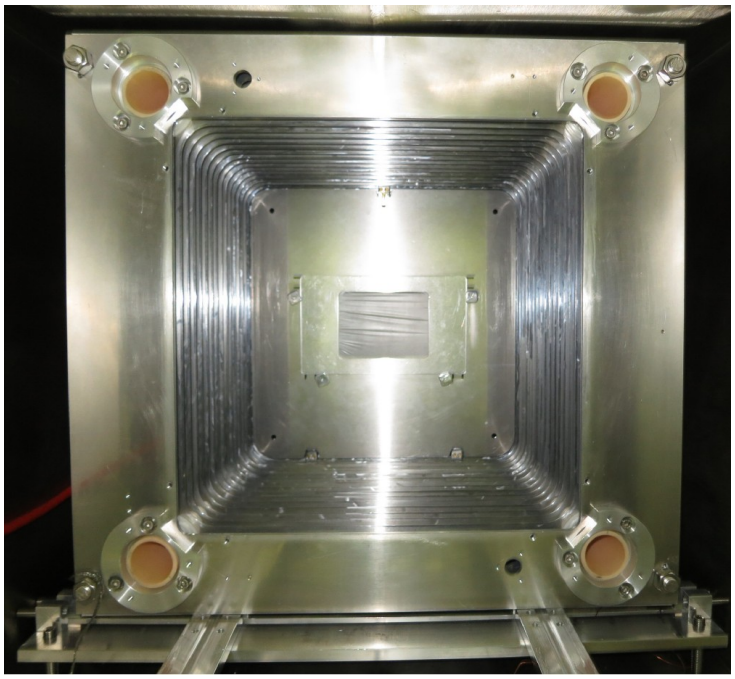

(a) The converter employed in PERKEO III has an opening diagonal of 47 cm and would have allowed a converter foil size of 34 cm diagonal. Installation could only be achieved once though and finally a much smaller foil had to be used.

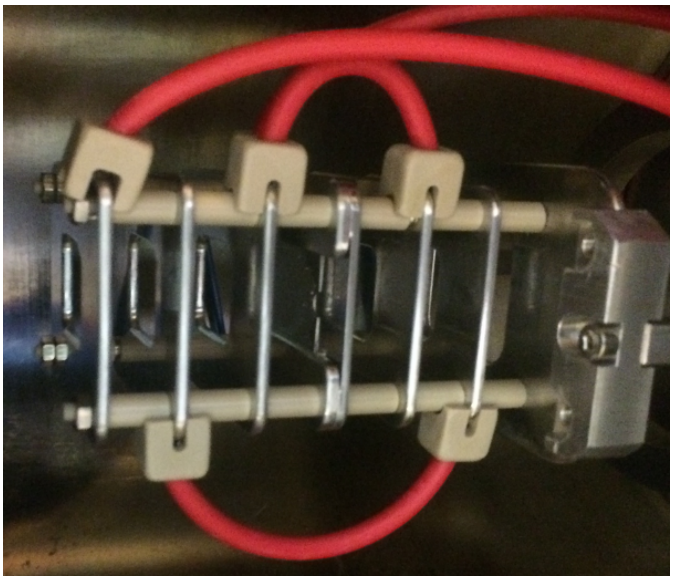

(b) A miniature version of the converter is used for test measurements to study conversion properties. Protons are accelerated onto the foil by up to −25 kV over a distance of 7 cm and release secondary electrons on the opposite side.

Figure 3.10: The proton-to-electron converters consist of several electrodes which generate a quasi-homogeneous electric field in the inner region towards the converter foil. Within the converter foil, the accelerated proton transfers its kinetic energy to secondary electrons which leave the foil eventually. The electrostatic potential accelerates these secondaries out of the device in turn.

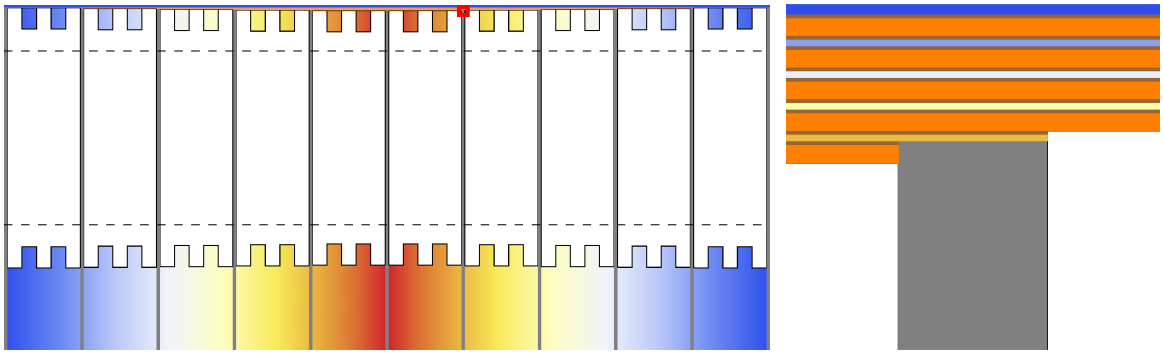

(a) The Teflon insulators used as spacers between the electrodes are supported by an inside ceramic tube (dashed lines). The grooves were added during the beam time to overcome issues with sparks along the surface of the hydrophilic Teflon. The red framed detail is shown in Figure 3.11b.

(b) The tiny spaces between the foils are at equal potential (colors blue to red), but not sufficient to efficiently evacuate the detector system.

Figure 3.11: The primary-proton-secondary-electron accelerator ("Field Degrader") creates a homogeneous electric field by step-wise increase of the acceleration potential applied to the electrodes. The figures show a cut through the white Teflon insulators at one of the edges of the device. In orange the insulating Kapton® foils are shown with brown copper plating. They allow a decrease of the maximum potential at the foil to the surrounding ground potential within a few millimeters. For the actual Field Degrader there are 15 outer electrodes. The colors from blue to red indicate the local potential, creating a nearly constant electric field in the inner region.

eV, such that their mean free path length is short. Usually one would try to set the Bragg peak of proton stopping to the detector sided surface of the foil to maximize the secondary production, but unfortunately the energy loss $\mathrm{d}E/\mathrm{d}x \propto \beta$ for small energies [Lin53] and the usually observed Bragg peak only appears at much higher energies.

The transport of secondary electrons may be treated as diffusion [Ste57] and the number of escaping electrons can then be regarded as exciton loss in scintillators [Bir52; Bir53]. The probability for an escaping electron, released at a distance r to the surface, is then

$$p(r) = \frac{1}{2}\left(\exp\left(-\frac{r}{\mathrm{a}_0}\right) + \frac{r}{\mathrm{a}_0}\mathrm{Ei}\left(-\frac{r}{\mathrm{a}_0}\right)\right), \tag{3.26}$$

where a_0 is a typical length on the order of the mean free path and Ei is the exponential integral function defined by $\mathrm{Ei}(z) = -\int_{\infty}^{z} \mathrm{e}^{-t}/t \,\mathrm{d}t$. This inclusion of the space element in the evaluation of Lambert-Beer's law is the main difference to a similar calculation performed in [Ber16]. The assumption of a constant secondary electron energy in the range of 20 to 30 eV [Ste57] which might certainly be true for high proton energies, cannot hold, due to the small maximum energy transfer which is possible at low proton energies. Therefore, Dirac scattering – describing the cross section of elastic scattering of two particles with spin – is assumed to obtain the number of secondary electrons with sufficient energy to overcome the work function. An empirical formula by [SD79] is used to estimate the mean free path of low-energetic electrons before inelastic scattering occurs. This value is set to a_0 in equation (3.26).

The only free parameter which remains for the secondary electron yield (SEY) is the energy required to overcome the surface potential. According to [Ste57] this barrier is expected to

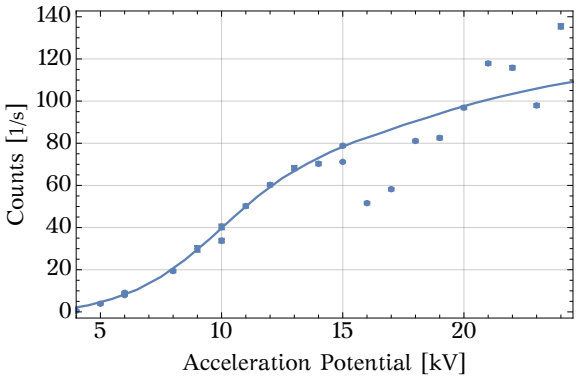

(a) For the measurements with the Mini Degrader, the detected SEY saturates in the region of 15 keV. This is related to the MCP detection efficiency. Variations at higher energies are due to the instable proton source.

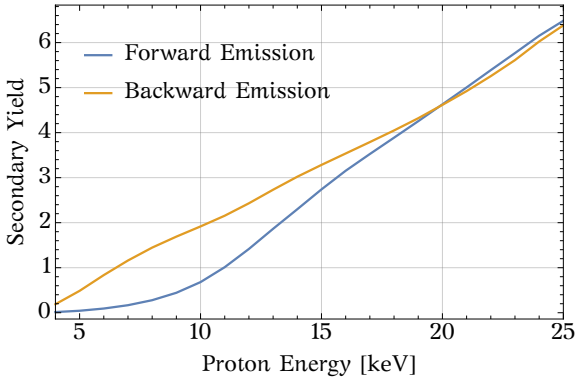

(b) The expected SEY from the model shows that more electrons are expected in backward direction than in forward direction for the foils employed in Perkeo III. This behavior was observed during a test measurement where only one Field Degrader was installed.

Figure 3.12: A test measurement with a thin foil of a thickness of 17 µg/cm^2 is used to tune the model for prediction of the secondary electron yield (SEY). For the thicker foils (20 µg/cm^2) employed in Perkeo III this allows to estimate the number of expected electrons per proton in dependence on the proton energy and to derive a corresponding correction to the measured asymmetry.

be lower than the actual work function. For graphite, from Figure 3.12a, 3.5 eV above the highest energy in the density of states is found to be of reasonable magnitude.

In preparation of the measurement of the neutrino asymmetry with Perkeo II, studies of converter foil properties were performed, with emphasis on proton energy [Rei99] and angular dependence [Bra00]. The use of a scintillator for electron detection makes disentangling of the SEY and the trigger function difficult at lower proton energies, though. To better understand the detection efficiency in relation to the acceleration voltage, a miniature version of the Field Degrader, called Mini Degrader, shown in Figure 3.10b was used to convert protons coming from a time of flight energy selector.

Test Measurements at BOB

Experiences with the high voltage system during the beam time point out the necessity of performing small scale test measurements to study the proton detection. A setup by Wolfgang Schott and Erwin Gutsmiedl in preparation of a bound beta decay measurement (BOB) provides low-energetic protons from a duoplasmatron source. The energy resolution of this source is enhanced by a time of flight selector, consisting of two Bradbury-Nielsen [BN36] gates which sequentially let protons pass. A microchannel plate (MCP) finally detects the protons, providing timing information of the event, relative to the gate switching.

In order to perform foil characterization studies, the Mini Degrader is put in front of the MCP, which now detects secondary electrons instead of protons. In contrast to scintillators, the detection efficiency of MCPs for electrons decreases with increasing energy. The setup provides a good means to disentangle the SEY and the detector function. The Bachelor thesis of Karina Bernert [Ber16] presents these measurement in detail. A recurring feature of all foils is the formation of an efficiency plateau in the region of $U_{\mathrm{FD}} \approx 15\,\mathrm{kV}$ acceleration voltage in Figure 3.12a. It can be explained by the decreasing MCP detection efficiency $\eta_{\mathrm{MCP}}(U_{\mathrm{FD}})$ [Ham06] for increasing electron energies.

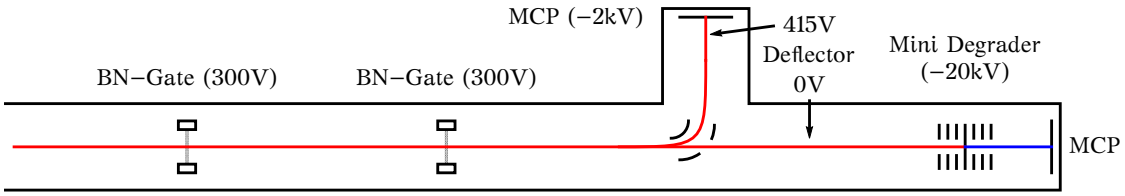

Figure 3.13: To resolve issues with an unstable proton source, which increase the uncertainty for measured SEYs, a deflector will be used, to alternate between a direct proton measurement and a secondary electron measurement. The rate of directly detected protons (red) can then be related to the measured electron (blue) rate.

To reproduce the measured curve, the ion stopping simulation tool TRIM [ZZB10] is used. TRIM does not provide information about secondary electrons, but can be used to simulate straggling of ions and returns the local energy loss. This information is sufficient to compile the complete SEY η_{SE} with the beforehand mentioned methods. Due to the long dead time of the detector, multiple secondary electrons may only lead to a single trigger. The event rate therefore is proportional to

$$p_{\mathrm{Detection}} = 1 - \exp\left(-n_{\mathrm{SE}}\eta_{\mathrm{MCP}}(U_{\mathrm{FD}})\right). \tag{3.27}$$

For small probabilities $n_{\mathrm{SE}}\eta_{\mathrm{MCP}}$ this increases linearly, but saturates when approaching unity. The spread in the SEY due to proton straggling is on the order of 10 % and may be neglected compared to the statistical spread of actually escaping electrons $\sim \sqrt{n_{\mathrm{SE}}}$.

A further rise of the SEY for acceleration potentials beyond 18 kV cannot be reproduced by the calculations. It is probably related to an instability of the flux from the proton source, which strongly increased after some time. Therefore measurements could not be reproduced on an absolute scale, especially calling the data points at high energies in question. Instead of stabilizing the proton source to the required rate, the actual proton flux could also be measured independently from the conversion detector.

This can be achieved by a electrostatic pinholed deflector, which allows normal operation when switched off, but deflects the proton beam onto a second MCP when switched on, shown as a sketch in Figure 3.13. A SEY measurement will then be improved significantly.

Energy Dependent Detection Efficiency

The observed plateau in the measurement at BOB is a consequence of the properties of the employed MCP. On the other hand, the measurement with Perkeo III is done with a scintillator whose trigger function is not yet saturating at similar electron energies. Therefore, there is no such plateau and the detection efficiency depends on the incident energy of the proton. The observations of the test measurements can be used to tune the theoretical SEY calculation and finally obtain a detection efficiency in dependence on the initial proton energy with Perkeo III. Direct measurement of this effect would be possible with the test setup as well, but will only be performed in combination with the new deflector electrodes.

The number of expected secondary electrons $n_{\mathrm{SE}}(E)$ can be read off in Figure 3.12b. The difference between measured and theoretical proton asymmetry can then be calculated by

plugging the electron trigger function $T(L(E))$ – see section 2.6.2 – into

$$N_{\downarrow}^{\uparrow} = \int_{\Re\mathrm{e}\sqrt{1-\frac{B_0}{B_R}\left(1-\frac{eU_R}{E_{\max}}\right)}}^{1} \mathrm{d}\cos\theta \int_{\frac{eU_R}{1-\frac{B_R}{B_0}\sin^2\theta}}^{E_{\max}} \mathrm{d}E \frac{\mathrm{d}\Gamma_P\left(E, \frac{\pi}{2} \mp (\frac{\pi}{2}-\theta)\right)}{\mathrm{d}E\mathrm{d}\Omega} \left(1-\left[1-T(n_{\mathrm{SE},1}(E))\right]\left[1-T(n_{\mathrm{SE},2}(E))\right]\right) \tag{3.28}$$

$$T(n_{\mathrm{SE}}) = \exp(-n_{\mathrm{SE}}(E)) \sum_{k=0}^{\infty} \frac{n_{\mathrm{SE}}(E)^k}{k!} T(k \cdot L(eU_{\mathrm{FD}})) \tag{3.29}$$

and comparing the resulting asymmetry to the same formula with $T = 1$. The lower integration limits are defined by the retardation potential U_R from section 3.2, which blocks protons depending on their kinetic energy, but also on their polar angle θ_R in the retardation plane:

$$E_{\min} = \frac{eU_R}{\cos^2\theta_R} = \frac{eU_R}{1-\frac{B_R}{B_0}\sin^2\theta} \tag{3.30}$$

The number of secondary electrons is assumed to follow a Poisson distribution with mean value n_{SE}, which agrees with measurements by [Rei99]. This value also depends on the incident angle of the proton on the converter foil

$$\theta_{\mathrm{FD}} = \arctan\sqrt{E_P \frac{\frac{B_{\mathrm{FD}}}{B_0}\sin^2\theta}{E_P\left(1-\frac{B_{\mathrm{FD}}}{B_0}\sin^2\theta\right)-eU_{\mathrm{FD}}}}, \tag{3.31}$$

but only changes the correction by 5 % with the maximum incident angle $\theta_{\mathrm{FD,max}} = 9.3°$ being small. However, the angular dependency is responsible for the overshoot of the correction in Figure 3.14b between 300 and 400 V.

Due to the relatively large flight times of the proton inside the field degrader, $n_{\mathrm{SE}}(E)$ is split into $n_{\mathrm{SE},1}(E)$ for the outgoing proton and $n_{\mathrm{SE},2}(E)$ for the reentering proton. The time between both electron emissions can be calculated by the reflectron time of flight

$$\Delta t = \frac{2L\sqrt{2E_{\mathrm{kin}}}}{U}\sqrt{\frac{m_p}{e}}, \tag{3.32}$$

which yields 300 to 500 ns for the expected kinetic energy of ≈ 6 keV when escaping the foil. This timing creates two well separated PMT pulses which have to be treated independently, leading to the combined trigger probability $1-(1-T_1)(1-T_2)$. Unfortunately Δt is too long to be identified as a double hit within one event, which would have allowed to confirm proton stopping simulations, but is short enough to not release a second event, however.

The required trigger function $T(L)$ from section 2.6 again is obtained by a fit to a measured ^{137}Cs spectrum. Additionally, a ^{207}Bi source is used to fix the remaining detector parameters. Figure 3.14a presents a simultaneous fit to both sources for the Lyon detector. The obtained trigger threshold of ≈ 0.5 photoelectron equivalent is a factor of 2.7 smaller than the corresponding threshold for the electron asymmetry measurement. On one hand this implies more detected background events, but allows the detection of single conversion electrons with a probability of ≈ 28 % on the other hand. Table 3.1 shows an overview of trigger probabilities where the complete detector function with individual scintillator quenching and coincident electronics nonlinearity are included.

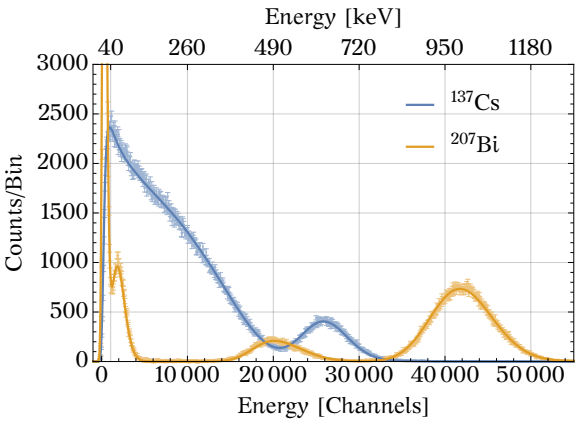

(a) A simultaneous fit to ^{137}Cs and ^{207}Bi calibration spectra yields the trigger function which is used to estimate the proton trigger efficiency. No edge effect was present for the calibration measurements, as they were performed without converter foils.

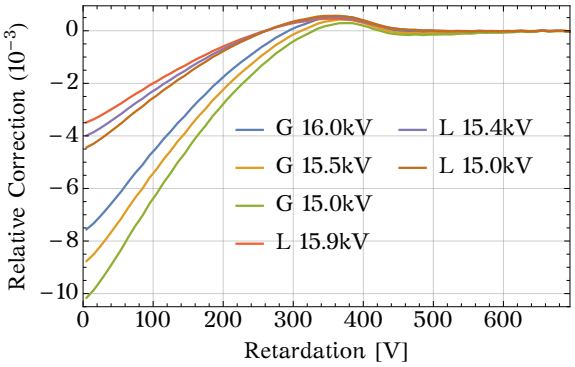

(b) The finite trigger efficiency requires the measured asymmetry to be corrected by −8‰ for the Grenoble detector and −4‰ for the Lyon detector. For increasing retardation voltages, the correction decreases, as the energy of the transmitted protons is less spread.

Figure 3.14: The secondary electron yield of the converter foil depends on the initial proton energy. As the differential proton asymmetry increases with the proton energy, this induces a correction on the measured integral proton asymmetry.

# of	Detector Grenoble			Detector Lyon		
Secondaries	16 kV	15.5 kV	15 kV	16 kV	15.5 kV	15 kV
1	26.7	28.6	30.5	30.5	32.6	34.6
2	67.3	69.6	71.8	70.7	72.9	74.9
3	87.6	89.0	90.3	88.9	90.2	91.3
4	95.6	96.3	96.8	96.0	96.6	97.1
5	98.5	98.8	99.0	98.6	98.9	99.1
6	99.5	99.6	99.7	99.5	99.6	99.7

Table 3.1: Probabilities of trigger signals by a certain number of coincident secondary electrons in %. In combination with the secondary electron yield distribution, the probability to detect a proton is obtained.

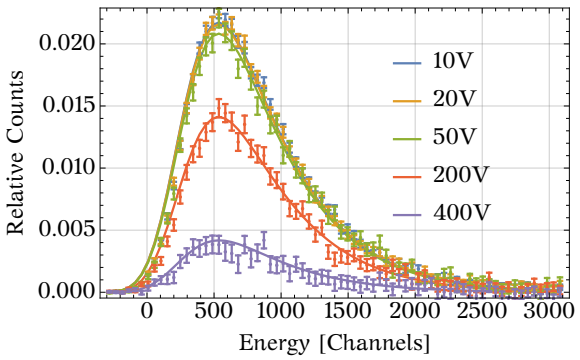

(a) Most data was collected at −15 kV acceleration voltage. All modes 10 V, 20 V, 50 V, 200 V and 400 V are used and the corresponding secondary electron spectra are well described.

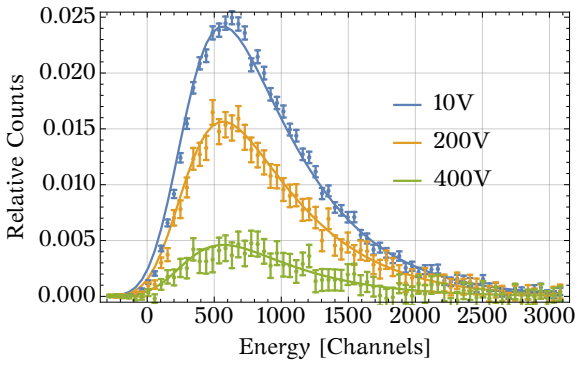

(b) At the beginning of the beam time, the retardation electrodes were driven at 10 V, 200 V and 400 V. The Grenoble Field Degrader was accelerating protons towards a potential of −16 kV.

Figure 3.15: To validate the asymmetry correction of the energy dependent proton trigger efficiency from Figure 3.14b, predicted secondary sum spectra are compared to measured spectra. The latter are scaled by the number of decay electrons detected in the same time. Electron detector parameters are fixed in Figure 3.14a. The only free parameters are the work function and the thickness of the converter foil.

The edge effect – the fraction of absorbed particles – for protons and electrons is considered to be 35 % and 30 % [Raf16; Dub+14]. From this, the obtained proton trigger efficiency can be validated by comparing to the measured spectrum of secondary electrons, relative to the number of detected decay electrons. The model for secondary electron emission has two parameters: The thickness of the carbon foil and the effective work function. Both have similar influence on the total trigger efficiency $1-(1-T_1)(1-T_2)$, but provide different signatures in the secondary spectrum. A parameter variation of the work function and the foil thickness while keeping the agreement with BOB measurement data yields the results in Figure 3.15. All other parameters are fixed.

The resulting corrections from Figure 3.14b are stable under parameter variation of the electron detector function. The corresponding uncertainties can be neglected compared to the uncertainty of the secondary emission model. The corrections may change by 20 % for different possible selections of the carbon foil work function. Further uncertainties of the Field Degrader voltage (5 %) and the ratio of the edge effect of electrons and protons (10 %) add up to ≈ 25 %. A more precise measurement of the SEY depending on foil thicknesses with BOB might significantly reduce the current error in the near future – see Figure 3.13.

Wrong Proton Detection

One implication of the secondary electron diffusion described by equation (3.26) is electron emission in backwards direction towards the source of proton emission. For the setup of PERKEO III this implies a transport of secondary electrons to the opposite detector. It is clear, that a correct measurement of the proton asymmetry may not allow transmission of these electrons through the converter foil, since they could then be registered by the wrong detector.

The arising question is: What is the minimum electron energy required to transmit the converter foil? A quick spot at the measurement data in Figure 3.16a reveals, that 3 keV

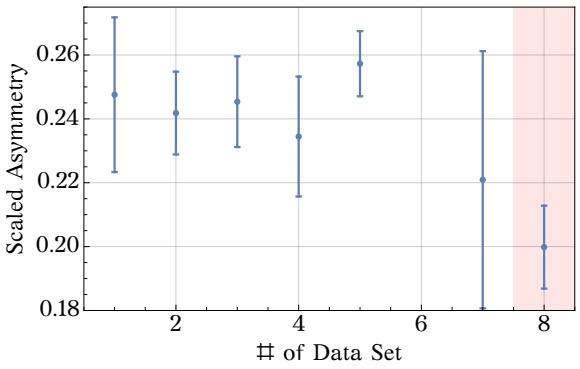

(a) The last production data set was taken with two different Field Degrader voltages: 15 keV Grenoble, 12 keV Lyon. The effect on the measured asymmetry is clearly visible by comparing the unused highlighted data point to the sane Lyon data sets.

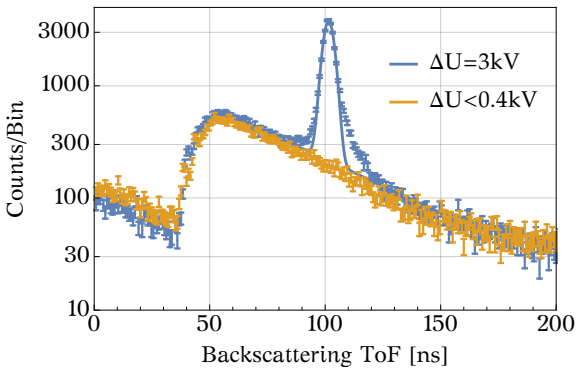

(b) Wrongly assigned proton events can be identified by a clear peak in the time of flight spectrum for backscattering events, i.e. events with hits on both detectors for a single proton. The effect is therefore excluded for data sets with similar Field Degrader voltages.

Figure 3.16: A possible systematic effect is the detection of secondary electrons from the converter foil, traveling to the wrong electron detector. If these electrons could transverse the opposite converter foil, they would be identified on the wrong detector.

are sufficient: The measured asymmetry of the Lyon-sided Field Degrader is clearly smaller for the late measurement set #8 with 12 kV, compared to the 15 kV measurements where the Grenoble-sided Field Degrader was set to the same potential. Although this data set clearly cannot be used for the determination of the proton asymmetry, further indications for this effect may be identified, to exclude any possible implication for the clean data sets. Here, the time of flight properties come into play. Electrons emitted backwards are accelerated to an energy equivalent to the Field Degrader potential, travel almost parallel along the magnetic field lines to the opposite Field Degrader and finally slow down to the potential difference between both devices. If they traverse the foil, they are accelerated onto the wrong detector. The time for this to happen is almost constant for every event and should show up as a peak in the backscattering time of flight spectrum. The time difference to the initial event on the primary detector is estimated to be

$$\Delta t = t_{\text{Backward}} - t_{\text{Forward}} \tag{3.33}$$

$$= \left(l_F \sqrt{\frac{2m}{U_1}} + l_{\text{PERKEO}} \frac{eU_1 + mc^2}{c\sqrt{(eU)^2 + 2mc^2 eU}} + 2l_F \sqrt{2m} \frac{\sqrt{U_1} - \sqrt{U_1 - U_2}}{U_2} \right) - \left(l_F \sqrt{\frac{2m}{U_1}} \right) \tag{3.34}$$

$$= \frac{1}{c} \left(l_{\text{PERKEO}} \frac{eU_1 + mc^2}{\sqrt{(eU_1)^2 + 2mc^2 eU_1}} + 2l_F \sqrt{2mc^2} \frac{\sqrt{U_1} - \sqrt{U_1 - U_2}}{U_2} \right) \tag{3.35}$$

from a reflectron setup, which includes acceleration, deceleration and the free flight path l_{PERKEO}. l_{PERKEO} is approximately 6.2 m, plus an additional transversal component due to slight gyration of the electron. The energy loss in the opposite converter foil is neglected. The expected time difference between primary and secondary event then is $\Delta t \gtrsim 95$ ns for $U_1 = 15$ kV and $U_2 = 12$ kV, which matches perfectly with the peak in Figure 3.16b for the data set #8. The absence of this peak in all other data sets with $U_1 - U_2 < 0.4$ kV allows to estimate the influence of the relative effect on the measured proton asymmetry to be

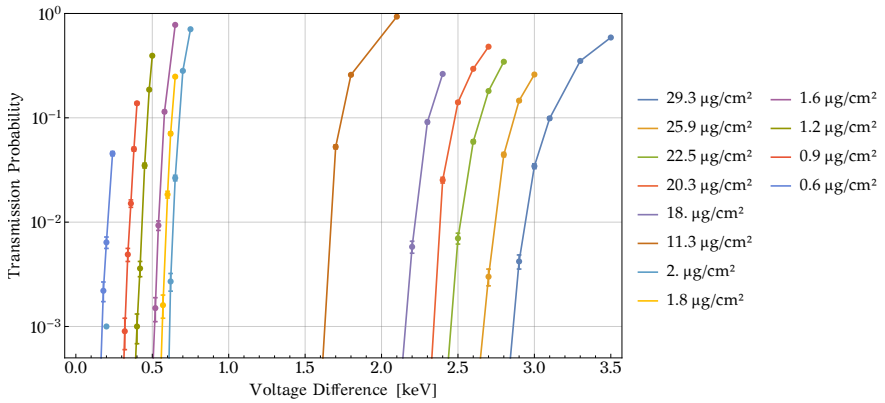

Figure 3.17: A simulation with Casino [Dro+16] to study the probability for secondary electron transmission through the opposite converter foil shows a strong dependence on the foil thickness. For the measurements with voltage difference $\Delta U < 0.4\,\mathrm{kV}$ no transmission is expected.

$< 3 \cdot 10^{-4}$. Here the number of observed electrons emitted backwards and the related change of the measured asymmetry are taken into account:

$$\Delta C_{<0.4\,\mathrm{kV}} = N_{<0.4\,\mathrm{kV}} \frac{\Delta C_{3\,\mathrm{kV}}}{N_{3\,\mathrm{kV}}} \tag{3.36}$$

$$< N_{<0.4\,\mathrm{kV}} \frac{\Delta C_{3\,\mathrm{kV}}}{N_{3\,\mathrm{kV}}} \sqrt{\left(\frac{\Delta(\Delta C_{3\,\mathrm{kV}})}{\Delta C_{3\,\mathrm{kV}}}\right)^2 + \left(\frac{\Delta N_{3\,\mathrm{kV}}}{N_{3\,\mathrm{kV}}}\right)^2 + \left(\frac{\Delta N_{<0.4\,\mathrm{kV}}}{N_{<0.4\,\mathrm{kV}}}\right)^2} \tag{3.37}$$

$$\approx N_{<0.4\,\mathrm{kV}} \frac{\Delta C_{3\,\mathrm{kV}}}{N_{3\,\mathrm{kV}}} \sqrt{0.2^2 + 0.01^2 + 1^2} \tag{3.38}$$

$$\approx \Delta N_{<0.4\,\mathrm{kV}} \frac{\Delta C_{3\,\mathrm{kV}}}{N_{3\,\mathrm{kV}}} = 20 \frac{0.05}{4500} < 3 \cdot 10^{-4}. \tag{3.39}$$

Another method is to consider data sets with only one detector being fully blocked by the retardation voltage. No proton signal should be visible, except if secondary electrons reach the blocked electron detector. Due to the strongly varying fraction of background events, this method is less reliable and does not yield similar limits.

A theoretical estimate for the maximum allowed potential difference that excludes electron transmission can also be acquired with the help of the simulation tool Casino [Dro+16]. It is designed to simulate low-energetic non-relativistic electron beams, using a method described in [Low96]. Although the specific energy loss is somehow uncertain and hence requires a tuning parameter, it still may provide a good estimate. Considering the foil thickness to be $20\,\mu\mathrm{g/cm^2} \pm 10\,\%$, the representation in Figure 3.17 excludes any secondary electron transmission for potential differences $\Delta U < 0.4\,\mathrm{kV}$. The data can be used however, to verify the foil thickness of $\approx 20\,\mu\mathrm{g/cm^2}$, by comparing the required fraction of wrongly assigned electrons to comply with the observed change in asymmetry for the $\Delta U = 3\,\mathrm{kV}$ data set:

$$C_{3\,\mathrm{kV}} = \frac{\alpha N_\uparrow + \alpha(1-\alpha)\epsilon N_\downarrow - \alpha N_\downarrow - \alpha(1-\alpha)\epsilon N_\uparrow}{\alpha N_\uparrow + \alpha(1-\alpha)\epsilon N_\downarrow + \alpha N_\downarrow + \alpha(1-\alpha)\epsilon N_\uparrow} \tag{3.40}$$

$$= \frac{N_\uparrow - N_\downarrow}{N_\uparrow + N_\downarrow} \frac{1-(1-\alpha)\epsilon}{1+(1-\alpha)\epsilon} \tag{3.41}$$

$$\frac{C_{3\,\mathrm{kV}}}{C_{<0.4\,\mathrm{kV}}} = \frac{1-(1-\alpha)\epsilon}{1+(1-\alpha)\epsilon}. \tag{3.42}$$

For a proton detection efficiency of $\alpha = 0.5$ and a change in asymmetry of 20 %, the probability for electron transmission to the opposite detector must be on the order of 25 %. Reading off the thicknesses from Figure 3.17 and considering the involved uncertainties, the values are in agreement.

To completely avoid possible electron backward emission in future experiments, the converter foil may simply be put behind the maximum of the electric potential, towards the electron detector. A few volts difference are sufficient to make secondary electrons in backwards emission turn around and hit the foil again. This feature is considered for a possible Field Degrader design for PERC which will be described in the following.

3.3.2 A Proton-to-Electron Converter for PERC

The experience made with the experimental setup for PERKEO III and test measurements at BOB allows to integrate many improvements into a new high voltage setup for PERC. The main features which are addressed by the new design are:

1. suitability for ultra-high vacuum
2. simplified mechanical converter foil installation
3. high voltage operation at low background
4. no backward secondary emission

All of these points are already improved by the smaller size of the instrument: If the converter is operated at 1 T, particles emitted inside the neutron guide of a cross section of up to 7 cm × 6 cm arrive at the converter within 8.5 cm × 8.5 cm. Therefore, a foil size of 10 cm × 10 cm is sufficient to detect all particles, still allowing a slight misalignment of the Field Degrader. In order to improve the vacuum suitability, surfaces are reduced and openings chosen large enough to allow efficient evacuation. Furthermore, resistors for the voltage divider are clamped instead of soldered. The resulting contact resistance can be neglected compared to the overall resistance of the voltage divider. For the measurements at BOB from section 3.3.1 this approach proved to have no visible side effects. A sketch in Figure 3.18a illustrates the insertion of the converter foil from the top, which prevents its error prone installation from the inside and omits sharp clamps required to keep the foil in place. Before installation, the foil holder is covered by a thicker electrode insert which avoids bending of the holder and subsequent foil damage. Adapting an idea by Michael Klopf, the overall insulation to the outer vessel is provided by four polyether ether ketone (PEEK) plates in Figure 3.18b, a material with excellent insulation properties at very low outgassing rates. Dimensional accuracy for the milled plates is maintained by outer reinforcing aluminum grids. The electrodes which define the inner potential are shut inside the insulator plates and do not require any kind of further fixation. The new device is small enough to be tested at BOB before employment in the real experiment.

3.4 Background

A major systematic advantage of PERKEO III over PERKEO II is the use of a pulsed neutron beam. A mechanical disk chopper allows slicing the neutron beam into pulses at several tens of Hz and allows a clean subtraction of background events with a time scale > 20 ms. The decreased average number of decays is compensated by the longer decay volume. Consequently a measurement is separated by the neutron flight time into a signal window,

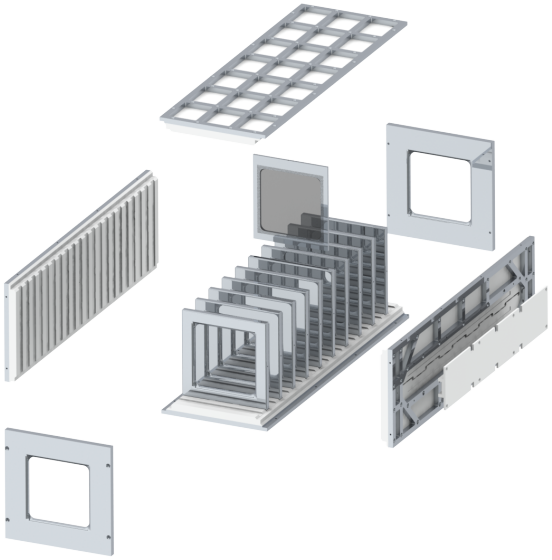

(a) Foil insertion will be done from the top again, as it was done for Perkeo II. This eases the last step of the delicate foil production and transport.

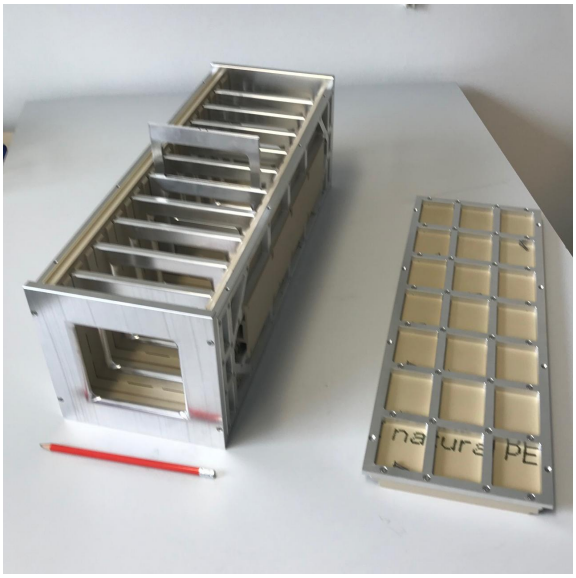

(b) The new device after production by the mechanical workshop[1] of the Physics Department, TUM. The top insulator is installed after the foil is put in place.

Figure 3.18: A new Field Degrader design foresees easier foil installation, is suitable for ultra high vacuum, can be operated at high voltages and suppresses backward emission of secondary electrons.

when neutron decay products are transported to the detectors, a beam stop peak, when the neutron pulse is absorbed by the beam stop and the background window, when no decay takes place in the central volume, but the background level is the same as during the signal window.

Experimental asymmetries are then obtained by subtracting spectra B in the background window from spectra N in the signal window:

$$A_{\text{exp}} = \frac{(N^{\uparrow} - B^{\uparrow}) - (N^{\downarrow} - B^{\downarrow})}{(N^{\uparrow} - B^{\uparrow}) + (N^{\downarrow} - B^{\downarrow})} \tag{3.43}$$

or for the differential proton asymmetry (3.10):

$$C_{\text{exp}} = \frac{(N_p^{\uparrow} - B_p^{\uparrow}) - (N_e^{\uparrow} - B_e^{\uparrow}) - (N_p^{\downarrow} - B_p^{\downarrow}) + (N_e^{\downarrow} - B_e^{\downarrow})}{(N_p^{\uparrow} - B_p^{\uparrow}) - (N_e^{\uparrow} - B_e^{\uparrow}) + (N_p^{\downarrow} - B_p^{\downarrow}) - (N_e^{\downarrow} - B_e^{\downarrow})} \tag{3.44}$$

The switch between $N^{\uparrow}$ and $N^{\downarrow}$ is performed by an adiabatic fast passage spin flipper, which flips the neutron polarization with 100 % efficiency before the neutrons enter the instrument. Switching of the flipper state is performed every $\approx 10\,\text{s}$, the time period which defines one measurement cycle. The influence of linear changes in the background, neutron flux or detector drifts can be canceled by selecting a special spin flip pattern: 01101001 or 10010110 (1 - spin flipper on, 0 - spin flipper off). Choosing this pattern and assuming the background to be spin independent and only drifting on larger time scales, the difference spectrum, namely the numerator of the experimental asymmetry (3.43), can be simplified to

$$(N^{\uparrow} - B^{\uparrow}) - (N^{\downarrow} - B^{\downarrow}) \overset{B^{\uparrow}=B^{\downarrow}}{\longrightarrow} N^{\uparrow} - N^{\downarrow}. \tag{3.45}$$

[1] Thanks to A. Kienle and T. Fechter for their diligent work.

Unfortunately, the assumption of slowly varying background levels does not hold for the measurement of the proton asymmetry and background subtraction must be performed as soon as possible after the signal measurement even in the difference spectrum. Therefore the complete equation (3.10) must be applied. The additional background contribution related to high voltage which is not present for a pure electron measurement is covered in the following section.

The necessity for a complete background subtraction can be tested by calculating the asymmetry of the background part

$$C_{\mathrm{exp}}^{\mathrm{bg}} = \frac{B_p^{\uparrow} - B_e^{\uparrow} - B_p^{\downarrow} + B_e^{\downarrow}}{(N_p^{\uparrow} - B_p^{\uparrow}) - (N_e^{\uparrow} - B_e^{\uparrow}) + (N_p^{\downarrow} - B_p^{\downarrow}) - (N_e^{\downarrow} - B_e^{\downarrow})}, \tag{3.46}$$

which results in non-negligible contributions of $C_{\mathrm{exp}}^{\mathrm{bg}} = 0.011(20)$ for the Grenoble and $C_{\mathrm{exp}}^{\mathrm{bg}} = 0.037(30)$ for the Lyon detector to the measured asymmetry.

3.4.1 High-Voltage Background

Typically, background events as well as decay events follow a Poisson distribution in time. That means, the probability for the next event to happen within time Δt is expressed by

$$p(t < \Delta t) = \int_0^{\Delta t} \frac{1}{\tau} \mathrm{e}^{-t/\tau} \mathrm{d}t = 1 - \mathrm{e}^{-\Delta t/\tau}, \tag{3.47}$$

for an average time τ between two events. The timing distribution of measurements with PERKEO III does not follow this law, however. In the case of the electron asymmetry measurement, afterpulsing of the PMTs – see section 3.4.2 – would only be completely suppressed by introduction of an artificial additional dead time of 10 µs [Mes11]. For the proton asymmetry measurement, there is a further component, which cannot be related to afterpulsing. A large number of events – compare signal and background rates in Figure 3.20 – have a small energy deposition in the scintillator and occur in short succession. These *bursts* are clearly related to the high voltage applied to the Field Degraders and require special attention in the data analysis.

Trapped Particles

PERKEO III in combination with the electric fields acts as a large Penning trap. Negatively charged particles are trapped between the Field Degraders, while positively charged particles could remain between the blocking electrodes. The latter is exploited to suppress potential neutron beam related background by only measuring the asymmetry at blocking voltages $> 10\,\mathrm{V}$. This trap is emptied every five minutes, following the measurement scheme. The larger trap between the Field Degraders cannot be emptied at similar frequencies, since in contrast to the blocking electrodes, ramping up of the high voltage can only be done within hours to prevent the destruction of the carbon foil by strong discharges.

Wire Grid as Background Absorber

Initially it was foreseen to operate the blocking electrodes without a wire grid to eliminate scattering of decay particles on the wire. Tests with both Field Degraders being ramped up synchronously with the magnetic field switched on showed immediately, that an absorber for charged particles is required: The electric system broke down even at low voltages of $\approx 1\,\mathrm{kV}$. Impurities of the Field Degrader electrodes probably led to field emission, constantly

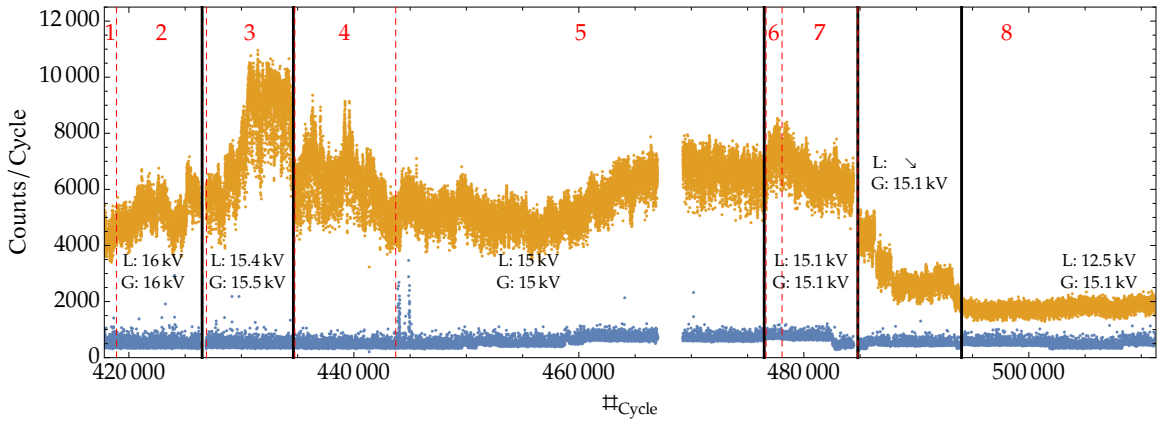

Figure 3.19: Trigger rates in the background time window of the downstream Lyon detector are strongly varying from cycle to cycle. Still, big "jumps" in the mean background rate are visible. The high rates forced a reduction of the proton acceleration voltage from 16 kV to 15.5 kV and 15 kV. Trigger rates at the upstream Grenoble detector are not affected. Numbers identifying the data sets head the figure.

filling the trap with low-energetic electrons. These quickly build up a plasma, which leads to a short circuit between electrodes. With insertion of a wire grid, even a very coarse one, the charge-up could be avoided and symmetric operation was possible. A detailed study [Frä+14] of undesired effects related to Penning traps was done for the KATRIN experiment. Therein, photons from small plasma discharges are identified as source for background events.

Surface Effects

Furthermore, rough electrode surfaces may induce field emission as a consequence of strong local electric fields. Impure tips and edges may create small plasmas which finally decharge by charge transport and light emission. Studies of high voltage breakdowns in vacuum were performed by [KS11] for CLIC, a linear TeV-collider. According to this work, a typical voltage breakdown has a short and intense ignition peak for $\approx 10\,\mathrm{ns}$ and subsequently emits light for a period of ≈ 3 to $4\,\mu\mathrm{s}$. For Perkeo III a similar behavior is observed, with time constants increased by a factor of ten; the following section will cover this in more detail. Also, voltage breakdowns be a source of further surface deterioration. This might be a reason for a sudden rise of the mean background rate. The rate could be reduced by reducing the proton acceleration voltage from 16 kV to 15.5 kV and later even 15 kV, visible in Figure 3.19. The hypothesis of background being related to photons can further be confirmed by using the position reconstruction of electron events from section 2.4.5. The positioning of background events does not hint to ions being converted in the carbon foil, but points to a light source in one of the upper corners of the Field Degrader.

Whether the background stems from photons from penning traps or high voltage breakdowns or detected ions emerging from plasmas, cannot ultimately be resolved. In any case, the strongly varying background level must be dealt with. It does not explicitly introduce a spin dependent background component, but still requires the background subtraction to be performed on much smaller time scales than the spin flip changes.

3.4.2 Dead Time Correction

As a consequence of the short, but intense background bursts, the number of background events can largely be reduced by introducing an artificial dead time, ignoring all events which occur within less than t_{dead} after the previous event. This kind of dead time is called extendible, as it resets with each new event, in contrast to the electronics dead time which does not reset. After applying this cut, the real number of events must be extrapolated to make proton measurements, electron measurements and background measurements comparable.

The actual event rate τ^{-1} depending on the measured event rate $\tau^{-1}_{\mathrm{measured}}$ with extendible dead time t_{dead} can be calculated with the help of equation (3.47):

$$N_{\mathrm{run}} = \frac{t_{\mathrm{run}}}{\tau_{\mathrm{measured}}} = \frac{t_{\mathrm{run}}}{\tau} \mathrm{e}^{-t_{\mathrm{dead}}/\tau} \Rightarrow \tau = -\frac{t_{\mathrm{dead}}}{W\left(-\frac{t_{\mathrm{dead}}}{\tau_{\mathrm{measured}}}\right)}, \tag{3.48}$$

where the Lambert-W function which solves the equation $z = W(z\mathrm{e}^z)$ is used. Equation (3.48) may be applied, if none of the events are correlated. In combination with a non-extendible electronics dead time, voltage breakdown bursts, afterpulsing and a correlated proton ToF, the applicability must be checked, however. Especially for the last point, care must be taken to not extend the artificial dead time over the minimum proton time of flight, which is $\gtrsim 5\,\mu\mathrm{s}$. In the following a model for the time distribution of background events is developed, verified by data and finally used to estimate the error which is introduced by applying the dead time correction (3.48).

Background Simulation

A Monte-Carlo simulation is used to estimate the error introduced by applying the simplified dead time correction (3.48). Three independent processes are involved which yield the complete event rate:

1. neutron decay
2. environmental background
3. high voltage bursts

Additionally, PMT afterpulsing plays a role: Residual gas inside the PMT gets ionized by the electron avalanche and leads to delayed pulses, emitted by the slowly propagating ions [Ham07]. These pulses occur within several hundred ns to µs and may be registered as independent events. Probability and amplitude of afterpulsing depend on the primary signal and therefore increase for larger signals. Afterpulsing may occur for all three event types. A short component by electron backscattering from the mesh electrodes does not play a role with respect to correlated events.

Environmental background due to fast neutrons from the reactor and the beam line or γ-radiation from neighbouring experiments is considered to be the only source of uncorrelated events. Fast neutrons or Compton electrons may create light in both detectors, but the time difference has an electron backscattering signature and are not registered as multiple events.

Neutron decay events consist of a fast electron with flight times of ~ 10 to 100 ns and a delayed proton which arrives at the detector at least 5 µs after the related electron. The relation of the momenta of both particles does not permit a fast proton and a slow electron at the same time. The timing distribution is modeled by a Landau distribution with a steep cut at 5 µs in the simulation, which fits simulated flight time spectra sufficiently well.

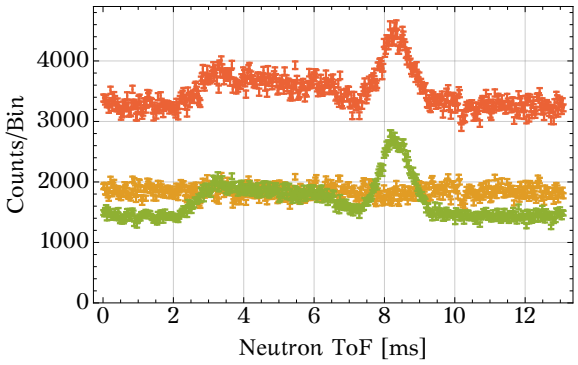

(a) By limiting event sequence probabilities (3.49) to $> 10^{-4}$, the related events of the high voltage background, but also afterpulsing, are suppressed by excluding the data in yellow.

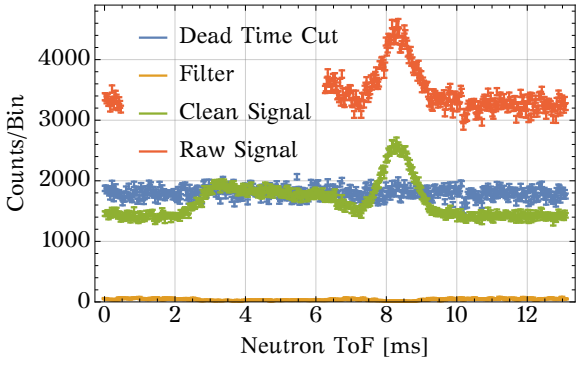

(b) The same effect can be obtained by introducing an artificial dead time of 5 µs. The corresponding uncertainty of the correction can be determined more reliably. Remaining bursts (yellow) can be neglected.

Figure 3.20: Two methods are considered to suppress bursts and afterpulsing to significantly improve the signal to background ratio. Both methods require a subsequent correction of the event rate to compensate for excluded false positives. The figures show raw data in red and filtered data in green.

Burst Filter

More detail is required to find a model for the bursts. Events from a burst are highly correlated and may be identified by evaluating the probability for a sequential occurrance of a number of uncorrelated events:

$$p_n(t_n - t_0 < \Delta t) = \frac{1}{\tau^n} \int_{t_0}^{t_0+\Delta t} \mathrm{e}^{-(t_n - t_{n-1})/\tau} \mathrm{d}t_n \cdots \int_{t_0}^{t_3} \mathrm{e}^{-(t_2 - t_1)/\tau} \mathrm{d}t_2 \int_{t_0}^{t_2} \mathrm{e}^{-(t_1 - t_0)/\tau} \mathrm{d}t_1 = \frac{\Gamma(n, \Delta t)}{\Gamma(n)}. \tag{3.49}$$

By defining a burst to be a set of at least n events to occur at a probability of at most $p_{\max} < 10^{-4}$, bursts can be found reliably with only a small number of false positives. An identified burst iteratively is extended to m events while $p_m(t_m - t_0) < p_{m-1}(t_{m-1} - t_0)$. Figure 3.20a shows how dropping identified bursts with $n > 3$ from further data analysis can improve the signal to background ratio significantly. On the other hand it is difficult to estimate a corresponding uncertainty for the application of the burst filter. An artificial extendible dead time of 5 µs has the same effect, shown in Figure 3.20b, and simplifies the determination of the uncertainty of the correction.

Burst Model

The filter is now used to collect information about burst events. It turns out that there is a short component, decaying with a life time of $\tau_{\text{short}} \approx 1.5\,\mu\text{s}$ and a delayed component, lasting for up to 50 µs. The corresponding probability distribution for events belonging to a burst, relative to the time of ignition, is approximated to

$$\frac{\mathrm{d}p_{\text{time}}}{\mathrm{d}t} = \frac{1}{\tau_{\text{short}} + c_{\text{long}}\tau_{\text{long}}} \left[\exp\left(-\frac{t}{\tau_{\text{short}}}\right) + c_{\text{long}} \frac{t}{\tau_{\text{long}}} \exp\left(-\frac{t}{\tau_{\text{long}}}\right) \right]. \tag{3.50}$$

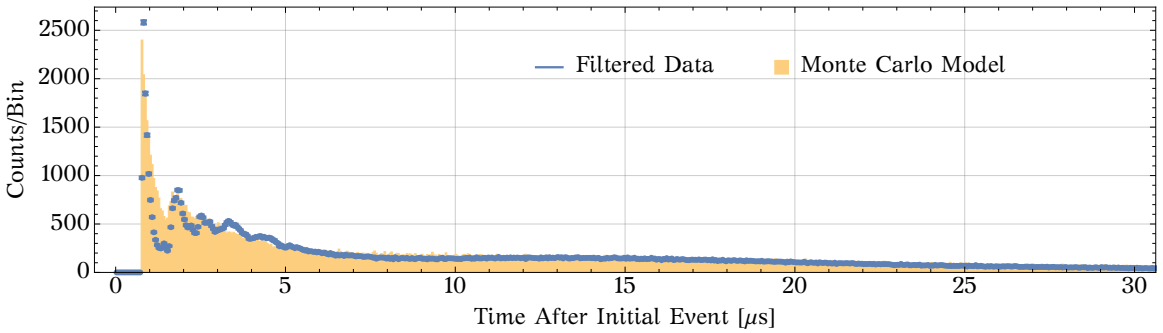

Figure 3.21: The model of the event distribution (3.50) in a burst is tested by a simulation which takes into account the electronics dead time – the source for the oscillatory structure up to 5 µs of the distribution.

The parameters are optimized to obtain a fit to filtered data in Figure 3.21. The number of events per burst is distributed by

$$\frac{\mathrm{d}p_{\mathrm{count}}}{\mathrm{d}N} = \frac{1}{\langle N\rangle}\exp\left(-\frac{N}{\langle N\rangle}\right), \tag{3.51}$$

with mean number of detectable events per burst $\langle N\rangle \approx 6$. The actual number of bursts is varying strongly, as Figure 3.19 testifies. The accuracy of the dead time correction must therefore be tested over a wide range of burst rates. Three different cases are considered:

1. signal window with protons and electrons

2. signal window with electrons

3. background window

To validate the dead time corrected number of events

$$N_C(N_{\mathrm{measured}}, t_{\mathrm{run}}, t_{\mathrm{dead}}) = -\frac{t_{\mathrm{run}}}{t_{\mathrm{dead}}} W\left(-\frac{t_{\mathrm{dead}} N_{\mathrm{measured}}}{t_{\mathrm{run}}}\right), \tag{3.52}$$

electronics dead time and artificial dead time are applied to simulated data. When subtracting a corrected number of events N_C from one time window from a corrected number of events from another, the remaining events should match the initially simulated number of unblocked events. The uncertainty δ_{ep} (3.56) for the determination of the asymmetry is obtained by comparing the number of corrected proton events to the number of completely randomly distributed electron events. N_p, N_e, N_{bg} and N_{burst} denote the actual number of protons, electrons, uncorrelated background and burst events in the detector, while N^{dead}

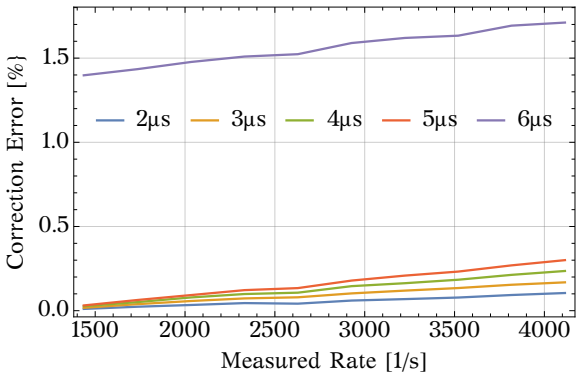

(a) Up to 5 µs dead time, the corrected overall number of detected protons is wrong at the permille level. For 6 µs, which is above the minimum proton ToF, the correction cannot be applied.

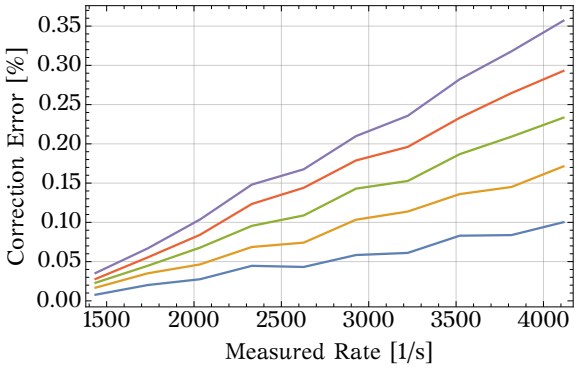

(b) The corrected number of electrons coincides with the number of protons. No jump for larger dead times is observed, since the electron events are not related to any other detector event.

Figure 3.22: The correction (3.52) for the dead time leads to an underestimation of the absolute number of electron and proton events in the simulation. The important quantity, namely the relative difference between electron and proton events is $< 2 \times 10^{-4}$, however.

are the number of events which are considered in the data analysis after dead time effects.

$$\begin{aligned} \{N_p, N_e, N_{\text{bg}}, N_{\text{burst}}\} &\longrightarrow \{N_p^{\text{dead}}, N_e^{\text{dead}}, N_{\text{bg}}^{\text{dead}}, N_{\text{burst}}^{\text{dead}}\} \\ \{N_e, N_{\text{bg}}, N_{\text{burst}}\} &\longrightarrow \{N_e^{\text{dead}}, N_{\text{bg}}^{\text{dead}}, N_{\text{burst}}^{\text{dead}}\} \\ \{N_{\text{bg}}, N_{\text{burst}}\} &\longrightarrow \{N_{\text{bg}}^{\text{dead}}, N_{\text{burst}}^{\text{dead}}\} \end{aligned} \tag{3.53}$$

$$\delta_e = 1 - \frac{N_C(N_e^{\text{dead}} + N_{\text{bg}}^{\text{dead}} + N_{\text{burst}}^{\text{dead}}) - N_C(N_{\text{bg}}^{\text{dead}} + N_{\text{burst}}^{\text{dead}})}{N_e} \tag{3.54}$$

$$\delta_p = 1 - \frac{N_C(N_p^{\text{dead}} + N_e^{\text{dead}} + N_{\text{bg}}^{\text{dead}} + N_{\text{burst}}^{\text{dead}}) - N_C(N_e^{\text{dead}} + N_{\text{bg}}^{\text{dead}} + N_{\text{burst}}^{\text{dead}})}{N_p} \tag{3.55}$$

$$\delta_{ep} = 1 - \frac{N_C(N_p^{\text{dead}} + N_e^{\text{dead}} + N_{\text{bg}}^{\text{dead}} + N_{\text{burst}}^{\text{dead}}) - N_C(N_e^{\text{dead}} + N_{\text{bg}}^{\text{dead}} + N_{\text{burst}}^{\text{dead}})}{N_C(N_e^{\text{dead}} + N_{\text{bg}}^{\text{dead}} + N_{\text{burst}}^{\text{dead}}) - N_C(N_{\text{bg}}^{\text{dead}} + N_{\text{burst}}^{\text{dead}})}. \tag{3.56}$$

The individual errors δ_e and δ_p of the correction in equations (3.54) and (3.55), namely the deviation from the actual number of electrons or protons after background subtraction, is $< 4 \times 10^{-3}$ as Figure 3.22 shows. It is a relative error of 15 % on the correction of the order of 1 %. The relative particle related error δ_{ep} is $< 2 \times 10^{-4}$ however and limits the relative uncertainty of the measured asymmetry to 8×10^{-4}.

3.4.3 Beam Related Background

A major concern of the measurement are so-called *beam related background* events which are related to the number of neutrons inside the instrument. This kind of background would induce a different number of background events in the signal time window, than in the background time window for decay times on the order of ms. One possible source could be residual gas ionization by trapped protons. Another source of beam related ionized particles are α particles, Lithium ions or Compton electrons emerging from the beam stop. They may be released by neutrons captured by Boron.

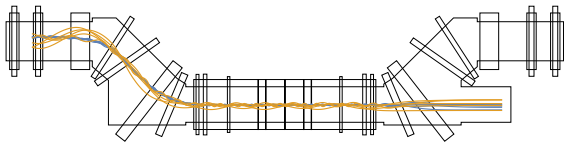

(a) To measure the neutron polarization, the downstream Lyon detector coils are switched off, which allows adiabatic passage of the neutrons to the polarization analyzer. When the latter is replaced by a beam stop, emerging α-particles (yellow, up to 20 keV) and Compton-electrons (blue, full energy range) may be transported to the Grenoble detector.

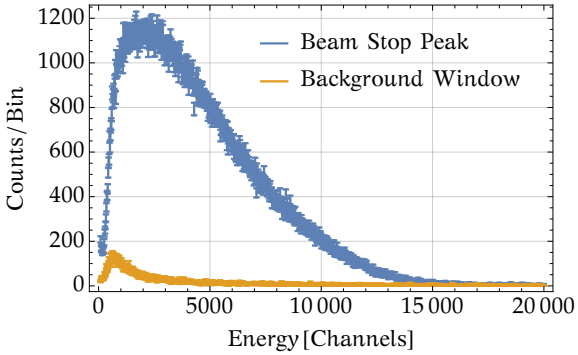

(b) When the beam stop is magnetically connected to the Grenoble detector, charged particles related to neutron capturing are detected. A β-like spectrum then adds to the usual γ-background while neutrons are hitting the beam stop. The spectrum is most likely related to electrons which are released by Compton scattering inside the beam stop.

Figure 3.23: A measurement with the Lyon detector coils switched off, reveiled the large number of charged particles escapting the beam stop. In the normal magnetic configuration these particles may not reach the detectors, but might still be responsible for residual gas ionization.

In the course of polarization measurements before the final beam time, only the Grenoble (upstream) and the central coils were switched on to allow adiabatic passage of polarized neutrons to the ^{3}He analyzer. Electron measurements performed during that period revealed an unusually large number of events on the Grenoble detector when the neutron beam hit the beam stop. In the normal configuration, neutrons arriving at the beam stop are detected by the Lyon (downstream) detector due to gammas traversing the lead shielding. Apparently the magnetic connection between Grenoble detector and beam stop shown in Figure 3.23a allows transport of charged particles released at the beam stop. The large number of the detected particles in Figure 3.23b certainly coming from the beam stop, resulted in covering the beam stop plate with an aluminum foil to stop all highly ionizing ions and also reduce the number of emerging electrons. While these particles themselves may not reach the main flux tube, they can ionize residual gas which then can be detected in any of both detectors. A small number of ions may still escape from the uncovered neutron backscattering absorber.

To allay remaining concerns, the last hours of the beam time were dedicated to a measurement with a chopper frequency of 6 Hz at equal neutron wavelength distribution. This configuration provides 13 times as many neutrons as usual in one pulse and leaves enough time to observe a potential decaying background component. Beam stop events and neutron decay events cannot be disentangled however, making this mode unsuitable for asymmetry measurements. Figure 3.24a shows a corresponding neutron ToF spectrum, zoomed to the background signals. For the Grenoble detector, an oscillating structure is apparent after the beam stop peak. This structure is related to neutrons being stopped by LiF chopper tiles of different quality which emit fast neutrons and gammas. A small fraction of the fast neutrons is detected by the close electron detector [Wer09]. No particular structure can be

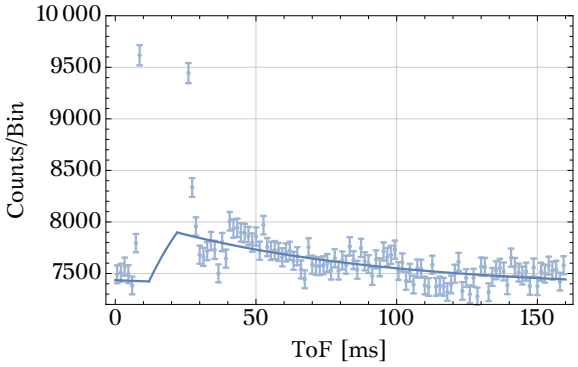

(a) A measurement with a chopper frequency of 6 Hz is used to estimate time constants of varying background rates. The fit is performed after the signal and beam stop peak and can be described by an exponential function (3.59).

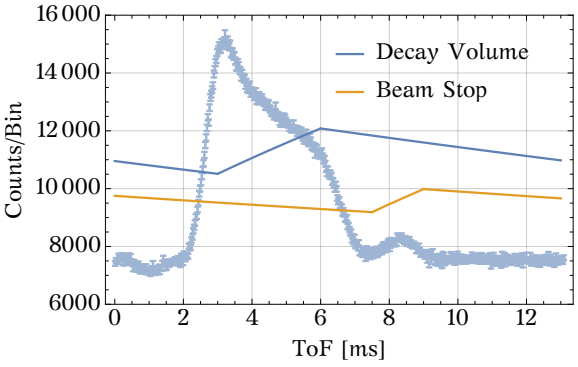

(b) The obtained background decay constant can be translated into the ToF spectrum of the actual measurement. Two possible background sources are illustrated: Decay volume or beam stop. The time dependent effect is exaggerated for illustration.

Figure 3.24: Background subtraction in PERKEO III is performed under the assumption, that background remains equal in signal and background time window. There are possible sources of beam related background however which could break this assumption. This is checked for by performing a measurement at slow chopper frequencies.

observed on the Lyon detector. The structure is only related to the chopper rotation angle and therefore cancels by subtracting the pure electron measurements – with protons blocked – from proton measurements.

Assuming that the time dependent background rate piles up linearly within a certain time window t_0 and t_1 – either while the neutron pulse is in the decay volume or it is hitting the beam stop – the time dependent background rate can be expressed as

$$r_{\mathrm{BG}}(t) \approx \int_{\min(t_0,t)}^{\min(t_1,t)} c_{\mathrm{BG}} \exp\left(-\frac{t+t'}{\tau}\right) \mathrm{d}t' + \sum_{n=1}^{\infty} \int_{t_0+n\cdot t_C}^{t_1+n\cdot t_C} c_{\mathrm{BG}} \exp\left(\frac{-(t+t')}{\tau}\right) \mathrm{d}t' \tag{3.57}$$

$$= \tau c_{\mathrm{BG}} \exp\left(-\frac{t}{\tau}\right)\left[\exp\left(-\frac{\min(t_0,t)}{\tau}\right) - \exp\left(-\frac{\min(t_1,t)}{\tau}\right) + \frac{\exp\left(-\frac{t_0}{\tau}\right) - \exp\left(-\frac{t_1}{\tau}\right)}{\exp\left(\frac{t_C}{\tau}\right) - 1}\right] \tag{3.58}$$

$$\overset{t>t_1}{=} \tau c_{\mathrm{BG}} \exp\left(-\frac{t}{\tau}\right) \frac{\exp\left(-\frac{t_0}{\tau}\right) - \exp\left(-\frac{t_1}{\tau}\right)}{1 - \exp\left(-\frac{t_C}{\tau}\right)} \equiv c'_{\mathrm{BG}} \exp\left(-\frac{t}{\tau}\right), \tag{3.59}$$

with a constant c_{BG} and the time t_C for one chopper turn. The time constant τ can be extracted from a fit of equation (3.59) to the ToF dependent background rate of the slow chopper data. In this fit, a constant background rate C_C must be included and can be related to the time dependent background rate by the ratio $R = (\tau c_{\mathrm{BG}})/C_C$.

Equation (3.58) can now be used to calculate the contribution of the time dependent background rate S_{BG} in the signal window and B_{BG} in the background window to the measured events by integrating $r_{\mathrm{BG}}(t)$ over the signal window $[t_{S_0} : t_{S_1}]$ and the background window $[t_{B_0} : t_{B_1}]$:

1. background rate piles up when neutrons are in the decay volume: $t_0 = t_{S_0}$, $t_1 = t_{S_1}$

$$S_{\mathrm{BG}} - B_{\mathrm{BG}} = R\left(\int_{t_{S_0}}^{t_{S_1}} \exp\left(-\frac{t}{\tau}\right)\left[\exp\left(-\frac{t_{S_0}}{\tau}\right) - \exp\left(-\frac{t}{\tau}\right) + \frac{\exp\left(-\frac{t_{S_0}}{\tau}\right) - \exp\left(-\frac{t_{S_1}}{\tau}\right)}{\exp\left(\frac{t_C}{\tau}\right) - 1}\right] - \int_{t_{B_0}}^{t_{B_1}} \exp\left(-\frac{t}{\tau}\right)\frac{\exp\left(-\frac{t_{S_0}}{\tau}\right) - \exp\left(-\frac{t_{S_1}}{\tau}\right)}{1 - \exp\left(-\frac{t_C}{\tau}\right)}\right) \tag{3.60}$$

2. background rate piles up when neutrons hit the beam stop from t_{D_0} to t_{D_1}

$$S_{\mathrm{BG}} - B_{\mathrm{BG}} = R\left(\int_{t_{S_0}}^{t_{S_1}} \exp\left(-\frac{t}{\tau}\right)\frac{\exp\left(-\frac{t_{D_0}}{\tau}\right) - \exp\left(-\frac{t_{D_1}}{\tau}\right)}{\exp\left(\frac{t_C}{\tau}\right) - 1} - \int_{t_{B_0}}^{t_{B_1}} \exp\left(-\frac{t}{\tau}\right)\frac{\exp\left(-\frac{t_{D_0}}{\tau}\right) - \exp\left(-\frac{t_{D_1}}{\tau}\right)}{1 - \exp\left(-\frac{t_C}{\tau}\right)}\right) \tag{3.61}$$

Contributions from pile-up in the decay volume (3.60) underestimate the background contribution ($S_{\mathrm{BG}} \gtrsim B_{\mathrm{BG}}$) but are almost canceling, while for background rate pile-up from beam stop interaction (3.61) the background contribution is overestimated ($S_{\mathrm{BG}} < B_{\mathrm{BG}}$). Assuming, that the time dependent effect scales with the number of neutrons and that the constant background rate C_C does not depend on the chopper frequency, the ratio R must be scaled by 6 Hz/76 Hz. The difference in the number of events is finally obtained by scaling with the signal to background ratio $(S - B)/B \approx 0.8$. Relative uncertainties for the relevant contributions on the Grenoble detector are listed in the following table. Uncertainties for the Lyon detector can be neglected since the measurement with slow chopper does not reveal any time dependent signature.

Retardation Voltage	Uncertainty (10^{-3})
10 V	+0.2, −0.7
20 V	+0.2, −0.8
50 V	+0.1, −0.4
850 V	+0.0, −0.1

Negative values increase the measured asymmetry. From slow chopper measurements it cannot be concluded what the source of the time dependent background contribution is. Therefore only uncertainties and no correction is deduced.

3.5 Results

The final analysis of proton asymmetry data is performed with the tool `p3reduce`, which is initiated and mainly implemented by Heiko Saul [Sau18]. The tool reduces the raw data compiled by the data acquisition software `pudel` – see section 2.8.4 – in several steps, which results in the final asymmetry histograms per data set. `p3reduce` is a framework around ROOT [BR97]. Each analysis step is defined in a configuration file, which allows to reproduce the analysis later on. The data reduction includes the following steps:

1. extraction of QDC pedestals – width and channel number of zero amplitude – from raw data

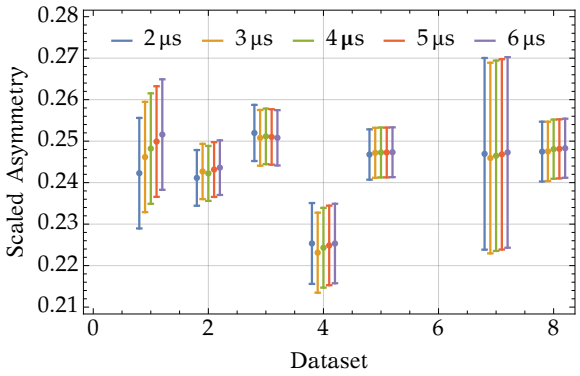

(a) The upstream Grenoble detector only was affected indirectly by the background issues and therefore has smaller statistical errors. The proton acceleration voltage was set to 16 kV for the first two data sets and later decreased to 15 kV.

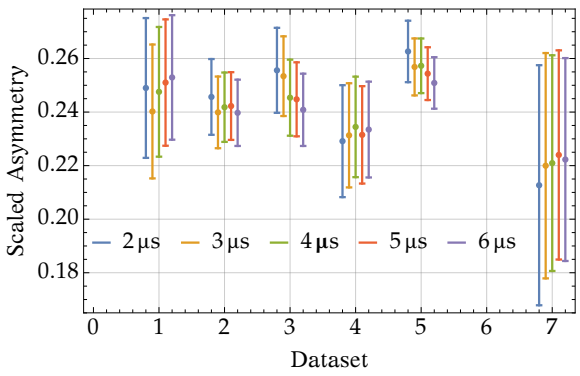

(b) The statistical error for the downstream Lyon detector is dominated by background events. The eighth data set cannot be used, since the acceleration voltage was significantly below the one of the opposite detector. For the final result, a dead time cut 4 µs is used.

Figure 3.25: The raw measured asymmetries are split into several data sets with different setup parameters, such as retardation settings and converter acceleration voltage. The asymmetry shown is scaled by a blinding factor. The results are correlated with other retardation modes due to the way the background is subtracted. Therefore the scattering of data points is smaller than the statistical error bars are suggesting. Different data sets in these figures represent different timing cuts in order to test the influence of artificial dead times. Data set #6 only includes systematic tests and does not contribute to the average.

2. creation of 2D histograms depending on neutron ToF and QDC signal
   - application of artificial dead time
   - application of burst filter on request
   - rescaling of PMT signals to reduce spatial dependence of the detector signal
3. project 2D histograms to one dimensional histograms of the QDC signal for signal and background time window
   - dead time correction is applied to the number of events per time window
4. assign pure electron measurements to proton measurements according to section 3.1.2
5. combine related histograms from the last step
6. add up all spectra of one data set and calculate average histograms

Since the secondary electron spectra do not provide enough about the proton energy except for a cross-check for the trigger efficiency, the integrals of difference and sum spectra are used to obtain the proton asymmetry. Figure 3.25 shows the obtained asymmetries at 10 V retardation voltage with different dead time cuts. To keep the remaining analysis unbiased, the results are scaled by a blinding factor $\mathscr{O} \approx -1 \pm \epsilon$.

A cross-check for measurements of the retardation voltage and magnetic field is done by comparing the expected change of number of proton counts depending on the retardation voltage in Figure 3.26. This method is comparable to the measurement of the proton

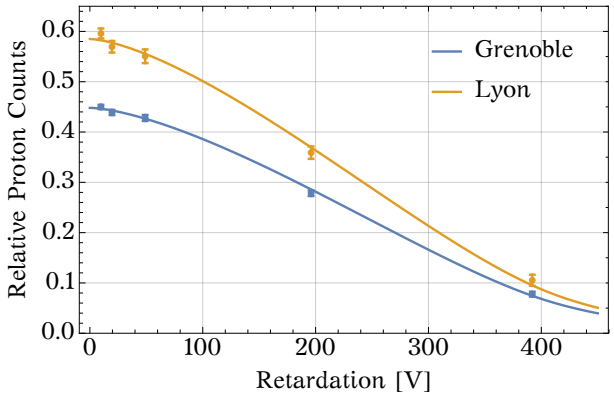

Figure 3.26: The number of detected protons relative to the number of detected electrons can be used to verify measurements and calculations of the magnetic field [Mos16] and electric potentials [Klo18]. The influence of the proton energy on the trigger efficiency from section 3.3.1 is only a small correction here.

spectrum with *a*SPECT and therefore depends on the electron-antineutrino-correlation $a(\lambda)$. The influence of the experimental uncertainty of a is negligible for the proton asymmetry measurement. The exact transmission function – the probability for protons of a certain momentum to overcome the electric barrier – is evaluated in [Klo18] and its effects on the determination of C may be estimated with precision better than 0.5‰.

For the first time, the energy dependent proton asymmetry can be evaluated in Figure 3.27. The combined representation of all measurements agrees well with the expectation.

It remains to evaluate a few systematic contributions. The most important correction will be the neutron polarization which is linearly related to the proton asymmetry. The depolarization of a few percent can be determined to a precision of better than 2‰. The most important correction is related to the size of the carbon foils and will contribute the largest systematic error despite an optimistic estimation in [Raf16]. Drifts in the retardation region such as in Figure 3.5a, as well as an $\vec{E} \times \vec{B}$-component in the acceleration region of the Field Degraders play an important role here and are investigated in [Klo18]. The uncertainty due to this effect will be smaller than 5‰. This analysis and an investigation of the magnetic mirror effect requires good knowledge about the magnetic field, which is investigated by Daniel Moser [Mos16].

As the final result, the uncertainty for the proton asymmetry will be smaller than 1% and improve the so far only measurement with PERKEO II. Table 3.2 lists all error contributions and the final relative uncertainty.

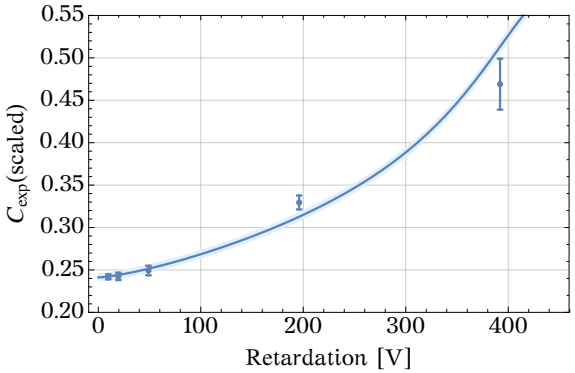

(a) Measured proton asymmetry on the Grenoble detector. The 2σ-band of the statistical errors is shown as well.

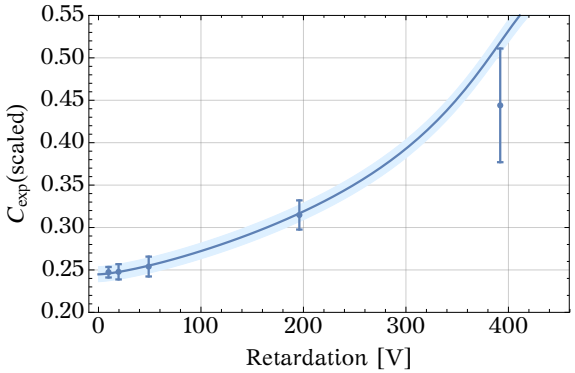

(b) Measured proton asymmetry on the Lyon detector. The statistical error is twice as large as for the Grenoble detector due to the large background rate.

Figure 3.27: For the first time, the proton asymmetry is measured as a function of the proton recoil energy. Because of the way the beta spectrum is subtracted – see section 3.1.2 – values do not scatter according to their statistical error bars. Several corrections which are evaluated in [Klo18], as well as the neutron polarization, are not yet included in these results.

Contribution	Section	Correction Grenoble (10^{-3})	Uncert. Grenoble (10^{-3})	Correction Lyon (10^{-3})	Uncert. Lyon (10^{-3})
Polarization & Spin Flip[§]		blind	< 2	blind	< 2
Doppler Effect[†]	3.1.3	-3.3	0.3	$+3.3$	0.3
Magnetic Mirror Effect[*]		blind	< 1	blind	< 1
Edge Effect[*]	3.2.2	blind	< 5	blind	< 5
Transmission Function[*]		blind	< 0.5	blind	< 0.5
Grid Effect[*]	3.2.4	≈ 3	≈ 1	≈ 3	≈ 1
Theory[+]	3.1.3	≈ 1.7	0.3	≈ 1.7	0.3
Detection Efficiency	3.3.1	-8.3	2.1	-3.4	0.9
Wrong Detector Assignment	3.3.1		0.3		0.3
Dead Time Correction	3.4.2		0.8		0.8
Background ToF Variation	3.4.3		$+0.1\ -0.7$		0.1
Systematic Uncertainties			6.1		5.7
Statistical Uncertainty			8.8		18.1
Total Uncertainty			10.5		18.7

Table 3.2: The error budget yields a combined relative error of at most $9.5 \cdot 10^{-3}$, where some of the uncertainties apply for both detectors simultaneously. All values in the table are relative to the measured proton asymmetry. Doppler and magnetic mirror effects actually cancel to some extent in the combined result of both detectors. [§]Measured and analyzed by Wilfried Mach and Heiko Saul; [*]evaluated in [Klo18]; [†]verified against [Raf16]; [+]theoretical corrections depend on λ.

4 Summary

In the course of this work significant process in the understanding of particle detection in neutron beta decay has been achieved. Neutron decays are used to determine the ratio between axial-vector and vector couplings in semi-leptonic decays. It allows tests of the Standard Model of particle physics by searches for scalar and tensor couplings.

Using the electron asymmetry measurement with the instrument PERKEO III, the major effects of electron detection with plastic scintillators are identified and modeled. The studies allow a fourfold improvement on the leading systematic uncertainty of the currently most precise measurement of the electron asymmetry with PERKEO II and finally lead to the determination of a new value for the ratio of axial-vector to vector couplings

$$\lambda = -1.27641(56) \quad \text{[Sau18]},$$

which improves the precision of the current world average by a factor of four.

The first step towards a better understanding of the measured electron spectra is a reevaluated and refined description of beta decay and electron capture source spectra. The latter is particularly challenging due to the large number of coincidentally emitted electrons. The impact of energy loss of electrons in thin films on measured calibration spectra is evaluated. A discretized representation of the point spread function of magnetically guided particles which describes the spatial distribution of electrons coming from a pointlike source is implemented. This function is applied to spatially dependent detector response functions to correct for shifts in the electron energy response. Detector response functions are deduced from calculations of the scintillation light distribution onto coupled light guides and photomultiplier tubes. A new method to simulate quenching of scintillation light – a major source of nonlinearity effects in scintillation detectors – is proposed. An experiment to calibrate detectors by using the electron time-of-flight information is realized and opens up a new way of calibrating detectors. The trigger function of the electron detector is described for the first time with detector light distribution and photomultiplier response function taken into account. It is used to identify and correct for the important systematic effect of undetected backscattering on the determination of the electron asymmetry. The combination of these complex models is implemented in a new fit program and now even allows the preliminary determination of the Fierz term from the beta asymmetry to

$$b = 0.017(21) \quad \text{[Sau18]}$$

and in the near future even from the beta decay spectrum to higher precision. The limits can be used to test the Standard Model for "new physics", i.e. test for hypothetical scalar and tensor interactions.

The second major part of this work is the preparation, realization and analysis of a measurement of the proton asymmetry parameter C with PERKEO III. It is a complementary correlation coefficient to the electron asymmetry parameter A and may disentangle the connection between scalar and tensor couplings. In combination with [Raf16; Klo18] the first and so far only measurement with PERKEO II, where a different measurement scheme was used, will be improved to a relative precision

$$\Delta C/C < 1\,\%.$$

For the first time, the energy dependence of the proton asymmetry is tested. The kinetic energy of the proton is three orders of magnitude smaller than the one of the electron and requires different techniques to allow proton detection. Studied effects in this work include the Doppler effect due to the moving neutron, the interaction with wire grids, which are required for energy resolution, the energy dependence of the efficiency of proton detection and the influence of high background rates on the background subtraction.

Both parts also are preparatory work to new measurements with the upcoming instrument PERC. The major systematic uncertainties which are identified in the measurements with PERKEO III – such as detector drift and nonlinearity for electron measurements and edge effect, grid effect and detection efficiency for proton measurements – can be reduced for PERC, which will further improve the precision of future correlation coefficient measurements in neutron beta decay.

Appendix

A.1 Formulas for the Pixelized Point Spread Function

In section 2.2.3 a point spread function (PSF) covering a number of pixels is divided into different shapes to enable an exact calculation of the coverage in every pixel. The different formulas for the required shapes are given here.

The radial symmetry of $f(R)$ makes the calculation of an integral F_{Sec} over a circular sector trivial, as long as the normalization F_{N} of f is known, like in the case of the PSF:

$$F_{\mathrm{Sec}}(\phi_0, \phi_1) = F_{\mathrm{N}} \frac{\phi_1 - \phi_0}{2\pi} \tag{A.1}$$

The isosceles triangle integral F_{I} can actually be obtained from two right triangles. Since the apex is lying in the center of the disk, the formula can be heavily simplified however and it makes sense to explicitly implement this special case. The cathetus connected to the center of the circle ($x_0 = 0, y_0 = 0$) is assumed to lie on the axis at $x = x_0$, which can always be achieved by rotation.

$$2\pi r_0 F_{\mathrm{I}}(x_1, y_1) = \int_0^{x_1} \mathrm{d}x \int_{\frac{xy_1}{x_1}}^{y_1} \mathrm{d}y \frac{1}{\sqrt{x^2 + y^2}} = \int_0^{x_1} \mathrm{d}x \log\left(\frac{x_1 \left(\sqrt{x^2 + y_1^2} + y_1 \right)}{x \left(\sqrt{x_1^2 + y_1^2} + y_1 \right)} \right) \tag{A.2}$$

$$= y_1 \log\left(\frac{\sqrt{x_1^2 + y_1^2} + x_1}{y_1} \right), \tag{A.3}$$

where (x_1, y_1) identifies the other end of the hypotenuse. A circular segment is calculated by subtracting F_{I} from F_{Sec}.

The most often required value for large circles is the rectangle F_{R}, defined by the points (x_1, y_1) and (x_2, y_2).

$$4\pi r_0 F_{\mathrm{R}}(x_1, x_2, y_1, y_2) = \int_{y_1}^{y_2} \mathrm{d}y \int_{x_1}^{x_2} \mathrm{d}x \frac{1}{\sqrt{x^2 + y^2}} = \int_{y_1}^{y_2} \mathrm{d}y \left(\log\left(\sqrt{x_2^2 + y^2} + x_2 \right) - \log\left(\sqrt{x_1^2 + y^2} + x_1 \right) \right) \tag{A.4}$$

$$= \sum_{i=1}^{2} \sum_{j=1}^{2} (2\delta_{ij} - 1) \left(x_i \log\left(y_j + \sqrt{x_i^2 + y_j^2} \right) + y_i \log\left(x_j + \sqrt{y_i^2 + x_j^2} \right) \right) \tag{A.5}$$

No dependence on r_0 appears in the formula for F_{R} except for the normalization factor $(4\pi r_0)^{-1}$, which makes the integration over a full pixel predestined for caching of results, which is an excellent way of optimization, since r_0 depends on the particle energy, and requires to calculate multiple PSFs over the whole spectrum. The calculation itself can be optimized by using vectorization: Sufficient numerical precision can be achieved by using 64 bit floating point numbers. However, modern CPUs allow floating point operations with 256 bits or more. This means, the same operation can be applied to four different

numbers in the same register and therefore at the same time, without requiring additional CPUs. This speeds up the calculation by a factor of four less overhead for data alignment. Furthermore individual summands can be reused in neighbouring pixels. This would add further overhead to the vectorization though.

The most complex calculation has to be done for a right triangle F_T with points (x_1, y_1), (x_1, y_2) and (x_2, y_1). Here no caching can be used, since it is required for the calculation of cut pixels which change for every r_0.

$$4\pi r_0 F_\mathrm{T}(x_1, x_2, y_1, y_2) = \int_{x_1}^{x_2} \mathrm{d}x \int_c^{\frac{(x_2-x)(y_2-y_1)}{x_2-x_1}+y_1} \frac{1}{\sqrt{x^2+y^2}} \tag{A.6}$$

$$= \int_{x_1}^{x_2} \mathrm{d}x \log\left(\frac{\frac{(x_2-x)(y_2-y_1)}{x_2-x_1} + y_1 + \sqrt{\left(\frac{(x_2-x)(y_2-y_1)}{x_2-x_1} + y_1\right)^2 + x^2}}{y_1 + \sqrt{y_1^2+x^2}} \right) \tag{A.7}$$

$$\begin{aligned} = \quad & x_1 \left(\log\left(y_1 + \sqrt{x_1^2+y_1^2} \right) - \log\left(y_2 + \sqrt{x_1^2+y_2^2} \right) \right) \\ & + y_1 \left(\log\left(x_1 + \sqrt{y_1^2+x_1^2} \right) - \log\left(x_2 + \sqrt{y_1^2+x_2^2} \right) \right) \\ & + \frac{(x_2 y_2 - x_1 y_1)}{\sqrt{(x_1-x_2)^2+(y_1-y_2)^2}} \\ & \cdot \Big(\log\left(x_1(x_2-x_1) + y_2(y_1-y_2) - \sqrt{\left(x_1^2+y_2^2\right)\left((x_1-x_2)^2+(y_1-y_2)^2\right)} \right) \\ & - \log\left(x_2(x_2-x_1) + y_1(y_1-y_2) - \sqrt{\left(x_2^2+y_1^2\right)\left((x_1-x_2)^2+(y_1-y_2)^2\right)} \right) \Big) \end{aligned} \tag{A.8}$$

A.2 p3fit: Bins and Bunches

Every step of the model calculation in `p3fit` takes an input spectrum and applies a convolution to generate an output spectrum. Since closed form expressions are usually not available, every spectrum is represented as a histogram, a collection of bins. For instance, the energy input spectra are binned in steps of 0.5 keV, which is more precise than the resolution of single scintillation events. Nevertheless, for line spectra, bins are included using interpolation such that the mean energy translated into the histogram is conserved, adding an additional but negligible smearing.

A typical operation which has to be performed is the convolution of two spectra, for the evaluation of the total energy of multi-electron events of section 2.1.3 or the sum of all PMT signals of section 2.6.2 for instance. For simplicity, a histograms with linear binning and the zeroth bin with center at zero is considered:

$$\mathrm{Bin}_i^{A*B} = \sum_{k=0}^{n_\mathrm{bins}-1} \mathrm{Bin}_k^A \mathrm{Bin}_{i-k}^B \tag{A.9}$$

To obtain the complete histogram $A * B$, n_bins^2 multiplications and additions, generally very cheap operations, but also the same amount of memory accesses, would be required. Figure A.1 shows how equation (A.9) can be efficiently implemented, using vectorization and parallelization for contiguous aligned bin data. A typical histogram in the course of model

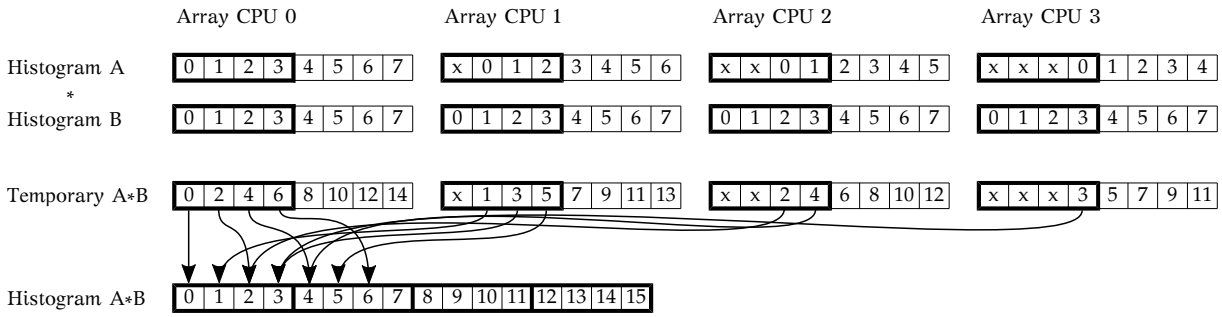

Figure A.1: Vectorization and parallelization can be used to quickly convolute two histograms of the same type, energy spectra for instance. The contiguous bin data of one of the histograms is temporarily copied into n arrays, the alignment of each array being shifted by one value for each new copy. The thick frames show the vector alignment for each array, the numbers indicate bin indices. The number of copies is defined by the size of a vector register n. Assuming that n CPUs are available, this way, n^2 multiplications and additions can be performed in the same time. The resulting data later have to be added up to one histogram, adding some overhead of complexity $n_{\text{bins}} \times n$.

calculation is not completely filled however, wasting computational time and memory by including bins without content in the calculation. In the case of very few bins, a tree structure to store bin contents including the corresponding bin position can be used, which allows easy insertion of new bin contents and saves memory. This approach does not allow quick convolution calculations however, as the data is fragmented in the memory.

The typical use case of histograms in `p3fit` is either the continuous filling of raw spectra, the convolution of histograms of the same type or continuous reading of contents to apply a model or to export the final histogram. Random access usually is not required. To combine the advantages of contiguous and tree storage, bunches of data are introduced. A bunch is defined as a set of contiguous bins and a set of bunches makes up a histogram. The data of bunches is stored in arrays, while the location of the bunches in memory is stored in a sorted list. This way, optimized operations on the histogram can be performed without giving away memory and computing time to empty bins. Additional effort has to be made to merge overlapping bunches in the course of random insertion or after the convolution of two histograms.

A.3 p3fit: Abstract Detection Unit

In the former productive version of the detection model, each part has its own specific implementation, depending on the former detection step and defining a hard-coded interface to the next detection unit. The new class layout is based on an abstract detection unit which allows a general use of models at any stage of the detection process. All used classes of the following example are children of the same base class and therefore interchangeable.

```
NuclearData nd("Cs"); // select Cs-137 data
ElecDistSpec espec; // create multielectron spectrum
PSFSpec psf(x, y, Bsource, Bdet, beamsize, asymmetry); // PSF at x, y
PixelDetector detector("detector.tiff"); // load detector function from TIFF image
PMTResponseHist pmt(2.4, "pmt.cache"); // set PMT gain per stage to 2.4
LightConvolutionSpec convolution(detector, pmt, 12.); // create 12 photons/keV

auto raw_spec = espec * nd; // calculate spectrum at source
```

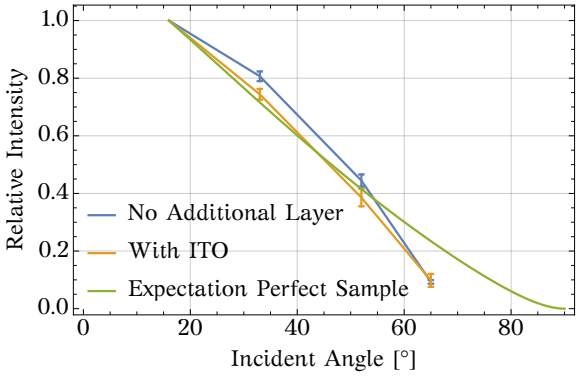

Figure A.2: The scintillator surface needs to be covered with a conductive coating to define the potential difference between conversion foil and detector surface. Aluminum or a different metallic coating is not applied since light absorption is dominant for the number of reflections required. Test measurements with ITO coated and uncoated scintillator samples [Raf15] show no significant differences in light conduction. The coating could therefore be applied to the surface of the electron detector.

```
auto light_spec = convolution * raw_spec; // calculate spectrum after PMTs
```

Inserting a nonlinearity model before the light distribution now is as easy as switching the last lines to

```
NonlinSpec nl(nonlin_birks, 6, 120.); // Birks model implementation 6

auto raw_spec = espec * nd; // calculate spectrum at source
auto light_spec = convolution * (nl * raw_spec); // calculate spectrum after PMTs
```

In this case, the nonlinearity model simply shrinks the bin borders of the input spectrum according to Birks' quenching model, effectively reducing the detected energy. More details about the nonlinearity implementations can be found in [Sau18].

A.4 Conductive Layer

Polyvinyltoluene as a base material for the scintillator is an insulator and therefore has an undefined surface potential. This requires a conductive coating which allows grounding of the detector surface to define the potential difference between conversion foil and scintillator and also to eliminate charging up by incoming electrons and high voltage bursts. As the light transport relies on total reflection, a metallic coating, such as aluminum is not optimal: An absorption coefficient of $> 10\,\%$ [Raf16] would significantly reduce the light yield. Instead, a transparent conductive coating of ITO, a material used for touch screens and anti-glare coatings, is used. To prove its suitability Lukas Raffelt performed tests with 420 nm LED pulses which were transferred through samples of coated and uncoated scintillator in Figure A.2. A small thickness of $15\,\text{nm} \pm 20\,\%$ is sufficient – only very small currents are expected – and is required to minimize the impact on the detected energy of incident electrons.

Bibliography

[Abe+06] H. Abele et al. “Characterization of a Ballistic Supermirror Neutron Guide”. In: *Nuclear Instruments and Methods in Physics Research Section A: Accelerators, Spectrometers, Detectors and Associated Equipment* 562.1 (June 15, 2006), pp. 407–417. ISSN: 0168-9002. DOI: 10.1016/j.nima.2006.03.020.

[Abe+97] H. Abele et al. “A Measurement of the Beta Asymmetry A in the Decay of Free Neutrons”. In: *Physics Letters B* 407.3 (Sept. 4, 1997), pp. 212–218. ISSN: 0370-2693. DOI: 10.1016/S0370-2693(97)00739-9.

[Abe00] Hartmut Abele. “The Standard Model and the Neutron β-Decay”. In: *Nuclear Instruments and Methods in Physics Research Section A: Accelerators, Spectrometers, Detectors and Associated Equipment* 440.3 (Feb. 11, 2000), pp. 499–510. ISSN: 0168-9002. DOI: 10.1016/S0168-9002(99)01027-X.

[All+16] J. Allison et al. “Recent Developments in Geant4”. In: *Nuclear Instruments and Methods in Physics Research Section A: Accelerators, Spectrometers, Detectors and Associated Equipment* 835 (Nov. 1, 2016), pp. 186–225. ISSN: 0168-9002. DOI: 10.1016/j.nima.2016.06.125.

[AM13] I. Angeli and K. P. Marinova. “Table of Experimental Nuclear Ground State Charge Radii: An Update”. In: *Atomic Data and Nuclear Data Tables* 99.1 (Jan. 1, 2013), pp. 69–95. ISSN: 0092-640X. DOI: 10.1016/j.adt.2011.12.006.

[Bae+13] S. Baeßler et al. “Neutron Beta Decay Studies with Nab”. In: (2013), pp. 114–116. DOI: 10.1063/1.4826731. arXiv: 1209.4663 [nucl-ex].

[Bam+72] Walter Bambynek et al. “X-Ray Fluorescence Yields, Auger, and Coster-Kronig Transition Probabilities”. In: *Reviews of Modern Physics* 44.4 (Oct. 1, 1972), pp. 716–813. DOI: 10.1103/RevModPhys.44.716.

[Bar17] Matteo Bartolini. *Personal Communication*. E-mail. Nov. 2017.

[BB82] Heinrich Behrens and Wolfgang Bühring. *Electron Radial Wave Functions and Nuclear Beta-Decay*. 67th ed. Oxford University Press, USA, 1982.

[BC83] H. Behrens and P. Christmas. “The beta decay of ^{137}Cs”. In: *Nuclear Physics A* 399.1 (May 9, 1983), pp. 131–140. ISSN: 0375-9474. DOI: 10.1016/0375-9474(83)90598-5.

[Bé+06] M.-M. Bé et al. *Table of Radionuclides*. Vol. 3. Monographie BIPM-5. Pavillon de Breteuil, F-92310 Sèvres, France: Bureau International des Poids et Mesures, 2006. ISBN: 92-822-2218-7. URL: http://www.bipm.org/utils/common/pdf/monographieRI/Monographie_BIPM-5_Tables_Vol3.pdf.

[Bé+08] M.-M. Bé et al. *Table of Radionuclides*. Vol. 4. Monographie BIPM-5. Pavillon de Breteuil, F-92310 Sèvres, France: Bureau International des Poids et Mesures, 2008. ISBN: 92-822-2230-6. URL: http://www.bipm.org/utils/common/pdf/monographieRI/Monographie_BIPM-5_Tables_Vol4.pdf.

[Bé+10] M.-M. Bé et al. *Table of Radionuclides*. Vol. 5. Monographie BIPM-5. Pavillon de Breteuil, F-92310 Sèvres, France: Bureau International des Poids et Mesures, 2010. ISBN: 92-822-2234-8. URL: http://www.bipm.org/utils/common/pdf/monographieRI/Monographie_BIPM-5_Tables_Vol5.pdf.

[Bé+99] M.-M. Bé et al. *Table de Radionucléides*. Vol. 1. DAMRI/LPRI BP 52, F-91193 Gif-sur-Yvette Cedex, France: Commissariat `a l'Énergie Atomique, 1999. ISBN: 2-7272-0200-8.

[Bea+15] G. Beadie et al. "Refractive Index Measurements of Poly(Methyl Methacrylate) (PMMA) from 0.4–1.6 Mm". In: *Applied Optics* 54.31 (Nov. 1, 2015), F139. ISSN: 0003-6935, 1539-4522. DOI: 10.1364/AO.54.00F139.

[Ber+14] M.J. Berger et al. *ESTAR, PSTAR, and ASTAR: Computer Programs for Calculating Stopping-Power and Range Tables for Electrons, Protons, and Helium Ions*. 2014. URL: http://physics.nist.gov/Star.

[Ber16] Karina Bernert. "Nachweis von Niederenergetischen Protonen". Bachelor Thesis. München: Technische Universität München, 2016.

[Ber17] Karina Bernert. *Personal Communication*. E-mail. Aug. 30, 2017.

[Bir52] J. B. Birks. "Theory of the Response of Organic Scintillation Crystals to Short-Range Particles". In: *Physical Review* 86.4 (May 15, 1952), pp. 569–569. DOI: 10.1103/PhysRev.86.569.

[Bir53] J. B. Birks. "Theory of the Response of Organic Scintillation Crystals to Short-Range Particles". In: *Physical Review* 90.6 (June 15, 1953), pp. 1131–1131. DOI: 10.1103/PhysRev.90.1131.5.

[Bir64] J. B. Birks. "Chapter 9 - Organic Plastic Scintillators". In: *The Theory and Practice of Scintillation Counting*. International Series of Monographs in Electronics and Instrumentation. Pergamon, 1964, pp. 321–353. ISBN: 978-0-08-010472-0. DOI: 10.1016/B978-0-08-010472-0.50014-8.

[BN36] Norris E. Bradbury and Russell A. Nielsen. "Absolute Values of the Electron Mobility in Hydrogen". In: *Physical Review* 49.5 (Mar. 1, 1936), pp. 388–393. DOI: 10.1103/PhysRev.49.388.

[Bop+88] P. Bopp et al. "The superconducting neutron decay spectrometer PERKEO". In: *Nuclear Instruments and Methods in Physics Research Section A: Accelerators, Spectrometers, Detectors and Associated Equipment* 267.2 (May 1, 1988), pp. 436–447. ISSN: 0168-9002. DOI: 10.1016/0168-9002(88)90485-8.

[BR97] R. Brun and F. Rademakers. "ROOT: An Object Oriented Data Analysis Framework". In: *Nucl.Instrum.Meth.* A389 (1997), pp. 81–86. DOI: 10.1016/S0168-9002(97)00048-X.

[Bra00] Bernhard Brand. "Ein Detektor Für Die Messung Der Neutrinoasymmetrie Beim Zerfall Freier Neutronen". Diplomarbeit. Heidelberg: Universität Heidelberg, 2000.

[Bre65] J. E. Bresenham. "Algorithm for Computer Control of a Digital Plotter". In: *IBM Systems Journal* 4.1 (1965), pp. 25–30. ISSN: 0018-8670. DOI: 10.1147/sj.41.0025.

[Bro+18] M. A.-P. Brown et al. "New result for the neutron β-asymmetry parameter A_0 from UCNA". In: *Physical Review C* 97.3 (Mar. 26, 2018), p. 035505. DOI: 10.1103/PhysRevC.97.035505.

[BS64] M. J. Berger and S. M. Seltzer. *Tables of Energy Losses and Ranges of Electrons and Positrons*. Jan. 1, 1964. URL: https://ntrs.nasa.gov/search.jsp?R=19650002905.

[CAE11] CAEN S.p.A. *C808 User Manual*. 2011. URL: http://www.caen.it/servlet/checkCaenManualFile?Id=7711.

[CC84] Mau Hsiung Chen and Bernd Crasemann. "M X-Ray Emission Rates in Dirac-Fock Approximation". In: *Physical Review A* 30.1 (July 1, 1984), pp. 170–176. DOI: 10.1103/PhysRevA.30.170.

[CCM79] Mau Hsiung Chen, Bernd Crasemann, and Hans Mark. "Relativistic Radiationless Transition Probabilities for Atomic K- and L-Shells". In: *Atomic Data and Nuclear Data Tables* 24.1 (July 1, 1979), pp. 13–37. ISSN: 0092-640X. DOI: 10.1016/0092-640X(79)90037-8.

[CEC98] Oleg Chubar, Pascal Elleaume, and Joel Chavanne. "A Three-Dimensional Magnetostatics Computer Code for Insertion Devices". In: *Journal of Synchrotron Radiation* 5.3 (May 1, 1998), pp. 481–484. ISSN: 0909-0495. DOI: 10.1107/S0909049597013502.

[Cha+18] C. C. Chang et al. "A Per-Cent-Level Determination of the Nucleon Axial Coupling from Quantum Chromodynamics". In: *Nature* (May 30, 2018), p. 1. ISSN: 1476-4687. DOI: 10.1038/s41586-018-0161-8.

[CMS18] Andrzej Czarnecki, William J. Marciano, and Alberto Sirlin. "Neutron Lifetime and Axial Coupling Connection". In: *Physical Review Letters* 120.20 (May 16, 2018), p. 202002. DOI: 10.1103/PhysRevLett.120.202002.

[COM] COMSOL. *COMSOL Multiphysics*. URL: http://www.comsol.com/comsol-multiphysics.

[Dai14] Benjamin Daiber. "Charakterisierung von Elektronendetektoren Für Messungen Am Beta-Zerfall Des Neutrons". Bachelor Thesis. Heidelberg: Universität Heidelberg, 2014.

[Dao+15] Salim Daoudi et al. "New K-Shell Fluorescence Yields Curve for Elements with $3 \leq Z \leq 99$". In: *Journal of the Korean Physical Society* 67.9 (Nov. 2015), pp. 1537–1543. ISSN: 0374-4884, 1976-8524. DOI: 10.3938/jkps.67.1537.

[Dar+17] G. Darius et al. "Measurement of the Electron-Antineutrino Angular Correlation in Neutron β Decay". In: *Physical Review Letters* 119.4 (July 25, 2017), p. 042502. DOI: 10.1103/PhysRevLett.119.042502.

[Dei05] Marc Deissenroth. "Optimization and Realization of a Neutrino Asymmetry Measurement in the Decay of Polarized Neutrons". Diplomarbeit. Heidelberg: Universität Heidelberg, 2005.

[Dro+16] Dominique Drouin et al. *Casino*. Version 3.3.0.4. Sherbrooke, 2016. URL: http://www.gel.usherbrooke.ca/casino/What.html.

[Dub+08] D. Dubbers et al. "A Clean, Bright, and Versatile Source of Neutron Decay Products". In: *Nuclear Instruments and Methods in Physics Research Section A: Accelerators, Spectrometers, Detectors and Associated Equipment* 596.2 (Nov. 1, 2008), pp. 238–247. ISSN: 0168-9002. DOI: 10.1016/j.nima.2008.07.157.

[Dub+14] D. Dubbers et al. “The Point Spread Function of Electrons in a Magnetic Field, and The Decay of the Free Neutron”. In: *Nuclear Instruments and Methods in Physics Research Section A: Accelerators, Spectrometers, Detectors and Associated Equipment* 763 (Nov. 1, 2014), pp. 112–119. ISSN: 0168-9002. DOI: 10.1016/j.nima.2014.06.020.

[Dub15a] Dirk Dubbers. “Generation of Narrow Peaks in Charged-Particle Magnetic Spectroscopy”. In: (Aug. 12, 2015). arXiv: 1508.02880 [hep-ph, physics:physics]. URL: http://arxiv.org/abs/1508.02880.

[Dub15b] Dirk Dubbers. “Magnetic Guidance of Charged Particles”. In: *Physics Letters B* 748 (Sept. 2, 2015), pp. 306–310. ISSN: 0370-2693. DOI: 10.1016/j.physletb.2015.07.004.

[Dub16] Dirk Dubbers. “Characterization of electron detectors by time-of-flight in neutron -decay experiments”. In: (Nov. 1, 2016). arXiv: 1611.00192 [nucl-ex, physics:physics]. URL: http://arxiv.org/abs/1611.00192.

[Fer34] E. Fermi. “Versuch einer Theorie der β-Strahlen. I”. In: *Zeitschrift für Physik* 88.3-4 (Mar. 1, 1934), pp. 161–177. ISSN: 0044-3328. DOI: 10.1007/BF01351864.

[FG58] R. P. Feynman and M. Gell-Mann. “Theory of the Fermi Interaction”. In: *Physical Review* 109.1 (Jan. 1, 1958), pp. 193–198. DOI: 10.1103/PhysRev.109.193.

[Fie37] Markus Fierz. “Zur Fermischen Theorie des β-Zerfalls”. In: *Zeitschrift für Physik* 104.7-8 (July 1, 1937), pp. 553–565. ISSN: 0044-3328. DOI: 10.1007/BF01330070.

[Fir97] Richard B. Firestone. *Table of Isotopes, 2 Volume Set*. Ed. by Virginia S. Shirley. 8th edition. New York: Wiley-VCH, Nov. 28, 1997. 3168 pp. ISBN: 978-0-471-14918-7.

[För48] Th. Förster. “Zwischenmolekulare Energiewanderung Und Fluoreszenz”. In: *Annalen der Physik* 437.1-2 (Jan. 1, 1948), pp. 55–75. ISSN: 1521-3889. DOI: 10.1002/andp.19484370105.

[Frä+14] F. M. Fränkle et al. “Penning Discharge in the KATRIN Pre-Spectrometer”. In: *Journal of Instrumentation* 9.07 (2014), P07028. ISSN: 1748-0221. DOI: 10.1088/1748-0221/9/07/P07028.

[Fri08] Felix Friedl. “Einfluss Der Detektorfunktion Auf Die Messung Des Schwachen Magnetismus Im Neutronzerfall”. Diplomarbeit. Heidelberg: Universität Heidelberg, 2008.

[Fri12] S. Fritzsche. “The Ratip Program for Relativistic Calculations of Atomic Transition, Ionization and Recombination Properties”. In: *Computer Physics Communications* 183.7 (July 1, 2012), pp. 1525–1559. ISSN: 0010-4655. DOI: 10.1016/j.cpc.2012.02.016.

[GJL95] F. Glück, I. Joó, and J. Last. “Measurable Parameters of Neutron Decay”. In: *Nuclear Physics A* 593.2 (Oct. 16, 1995), pp. 125–150. ISSN: 0375-9474. DOI: 10.1016/0375-9474(95)00354-4.

[GN16] M. González-Alonso and O. Naviliat-Cuncic. “Kinematic sensitivity to the Fierz term of β-decay differential spectra”. In: *Physical Review C* 94.3 (Sept. 28, 2016), p. 035503. DOI: 10.1103/PhysRevC.94.035503.

[Gra13] Jascha Grabowski. “Detektoreichung Mithilfe Eines Elektronenspektrometers”. Bachelor Thesis. Heidelberg: Universität Heidelberg, 2013.

[Gua+07] S. Guatelli et al. “Geant4 Atomic Relaxation”. In: *IEEE Transactions on Nuclear Science* 54.3 (June 2007), pp. 585–593. ISSN: 0018-9499. DOI: 10.1109/TNS.2007.896214.

[Ham06] Hamamatsu Photonics K.K. *MCP Assembly*. Sept. 2006.

[Ham07] Hamamatsu Photonics K. K. *Photomultiplier Tubes - Basics and Applications*. 3a. 2007. URL: https://www.hamamatsu.com/resources/pdf/etd/PMT_handbook_v3aE.pdf.

[Ham95] Hamamatsu Photonics K. K. *Photomultiplier Tube 5924*. Oct. 1995.

[Ham98] Hamamatsu Photonics K. K. *Photomultiplier Tubes R1307, R1307-01*. 1998. URL: https://www.hamamatsu.com/resources/pdf/etd/R1307_TPMH1214E.pdf.

[Hec02] Eugene Hecht. *Optics*. 4th ed., International ed. San Francisco, London: Addison-Wesley, 2002. vi, 698. ISBN: 978-0-321-18878-6.

[Hic+17] K. P. Hickerson et al. “First direct constraints on Fierz interference in free-neutron β decay”. In: *Physical Review C* 96.4 (Oct. 30, 2017), p. 042501. DOI: 10.1103/PhysRevC.96.042501.

[Inc16] Sebastien Incerti. *Livermore Low-Energy Electromagnetic Models*. Feb. 22, 2016. URL: https://twiki.cern.ch/twiki/bin/view/Geant4/LoweMigratedLivermore.

[Ins17] Institut Laue-Langevin. *The World's Flagship Centre for Neutron Science*. 2017. URL: https://www.ill.eu/.

[IPT13] A. N. Ivanov, M. Pitschmann, and N. I. Troitskaya. “Neutron Beta-Decay as Laboratory for Test of Standard Model”. In: *Physical Review D* 88.7 (Oct. 10, 2013). ISSN: 1550-7998, 1550-2368. DOI: 10.1103/PhysRevD.88.073002. arXiv: 1212.0332.

[Iva+13] A. N. Ivanov et al. “Proton recoil energy and angular distribution of neutron radiative β^- decay”. In: *Physical Review D* 88.6 (Sept. 24, 2013), p. 065026. DOI: 10.1103/PhysRevD.88.065026.

[Iva17] A. N. Ivanov. *Personal Communication*. E-mail. Nov. 12, 2017.

[Jön+07] P. Jönsson et al. “The grasp2K Relativistic Atomic Structure Package”. In: *Computer Physics Communications* 177.7 (Oct. 1, 2007), pp. 597–622. ISSN: 0010-4655. DOI: 10.1016/j.cpc.2007.06.002.

[JTW57] J. D. Jackson, S. B. Treiman, and H. W. Wyld. “Possible Tests of Time Reversal Invariance in Beta Decay”. In: *Physical Review* 106.3 (May 1, 1957), pp. 517–521. DOI: 10.1103/PhysRev.106.517.

[Kap07] Alexander Kaplan. “Preparing a weak magnetism measurement in free neutron decay with the new spectrometer PERKEO III”. Diplomarbeit. Heidelberg: Universität Heidelberg, 2007. URL: http://www.physi.uni-heidelberg.de/Publications/dipl_kaplan.pdf.

[Kei70] G. Keil. “Design Principles of Fluorescence Radiation Converters”. In: *Nuclear Instruments and Methods* 89 (Dec. 1970), pp. 111–123. ISSN: 0029554X. DOI: 10.1016/0029-554X(70)90813-X.

[Kib+08] T. Kibédi et al. “Evaluation of Theoretical Conversion Coefficients Using BrIcc”. In: *Nuclear Instruments and Methods in Physics Research Section A: Accelerators, Spectrometers, Detectors and Associated Equipment* 589.2 (May 1, 2008), pp. 202–229. ISSN: 0168-9002. DOI: 10.1016/j.nima.2008.02.051.

[Kim+15] S. H. Kim et al. “Validation Test of Geant4 Simulation of Electron Backscattering”. In: *IEEE Transactions on Nuclear Science* 62.2 (Apr. 2015), pp. 451–479. ISSN: 0018-9499. DOI: 10.1109/TNS.2015.2401055.

[Kla+13] Christine Klauser et al. “Ultra-Sensitive Depolarization Study of Polarizing CoTi Supermirrors with the Opaque Test Bench”. In: *Physics Procedia*. 9th International Conference on Polarised Neutrons in Condensed Matter Investigations 42 (Supplement C Jan. 1, 2013), pp. 99–105. ISSN: 1875-3892. DOI: 10.1016/j.phpro.2013.03.181.

[Klo15] Michael Klopf. *Personal Communication*. E-mail. 2015.

[Klo18] Michael Klopf. “TBA”. Atominstitut der Technischen Universität Wien, 2018.

[Kon+12] G. Konrad et al. “Neutron Decay with PERC: A Progress Report”. In: *Journal of Physics: Conference Series* 340 (Feb. 8, 2012), p. 012048. ISSN: 1742-6588, 1742-6596. DOI: 10.1088/1742-6596/340/1/012048.

[KS11] Jan Wilhelm Kovermann and Achim Stahl. “Comparative Studies of High-Gradient Rf and Dc Breakdowns”. Dissertation. Aachen, Techn. Hochsch., Diss., 2010, 2011. DOI: 3460,urn:nbn:de:hbz:82-opus-34604,30390,999910024774.

[KU41] E. J. Konopinski and G. E. Uhlenbeck. “On the Fermi Theory of β-Radioactivity. II. The ”Forbidden” Spectra”. In: *Physical Review* 60.4 (Aug. 15, 1941), pp. 308–320. DOI: 10.1103/PhysRev.60.308.

[Lam15] Max Lamparth. “Experiment Zur Bestimmung Der Niederenergetischen Nichtlinearität Und Rückstreuverhalten von Elektronen an Szintillatoren”. Bachelor Thesis. Heidelberg: Universität Heidelberg, 2015.

[Lee+08] Sangkyu Lee et al. “Refractive Index Engineering of Transparent ZrO2–Polydimethylsiloxane Nanocomposites”. In: *Journal of Materials Chemistry* 18.15 (Apr. 1, 2008), pp. 1751–1755. ISSN: 1364-5501. DOI: 10.1039/B715338D.

[Lin53] J Lindhard. “On the Properties of a Gas of Charged Particles”. In: *Mathematisk-fysiske Meddelelser* 28.8 (1953). URL: http://gymarkiv.sdu.dk/MFM/kdvs/mfm%2020-29/mfm-28-8.pdf.

[Low96] Jeremiah R. Lowney. “Monte Carlo Simulation of Scanning Electron Microscope Signals for Lithographic Metrology”. In: *Scanning* 18.4 (June 1, 1996), pp. 301–306. ISSN: 1932-8745. DOI: 10.1002/sca.1996.4950180406.

[LTS] LTSpice. *Linear Technology - Design Simulation and Device Models*. URL: http://www.linear.com/designtools/software/.

[LY56] T. D. Lee and C. N. Yang. “Question of Parity Conservation in Weak Interactions”. In: *Physical Review* 104.1 (Oct. 1, 1956), pp. 254–258. DOI: 10.1103/PhysRev.104.254.

[Mär+09] B. Märkisch et al. “The new neutron decay spectrometer PERKEO III”. In: *Nuclear Instruments and Methods in Physics Research Section A: Accelerators, Spectrometers, Detectors and Associated Equipment*. Particle Physics with Slow Neutrons 611.2 (Dec. 1, 2009), pp. 216–218. ISSN: 0168-9002. DOI: 10.1016/j.nima.2009.07.066.

[Mär06] Bastian Martin Märkisch. “Das Spektrometer PERKEO III und der Zerfall des freien Neutrons”. Dissertation. Heidelberg: Universität Heidelberg, 2006. DOI: 10.11588/heidok.00006927.

[McG72] Eugene J. McGuire. “M-Shell Auger and Coster-Kronig Electron Spectra”. In: *Physical Review A* 5.3 (Mar. 1, 1972), pp. 1052–1059. DOI: 10.1103/PhysRevA.5.1052.

[Mes11] Holger Frank Mest. “Measurement of the β-Asymmetry in the Decay of Free Polarized Neutrons with the Spectrometer PERKEO III”. Dissertation. Heidelberg: Universität Heidelberg, 2011. DOI: 10.11588/heidok.00012198.

[MM06] N. Majumdar and S. Mukhopadhyay. “Simulation of Three-Dimensional Electrostatic Field Configuration in Wire Chambers: A Novel Approach”. In: *Nuclear Instruments and Methods in Physics Research Section A: Accelerators, Spectrometers, Detectors and Associated Equipment* 566.2 (Oct. 15, 2006), pp. 489–494. ISSN: 0168-9002. DOI: 10.1016/j.nima.2006.06.035.

[MM33] N. F. Mott and Harrie Stewart Wilson Massey. *The Theory of Atomic Collisions*. The international series of monographs on physics. Oxford: Clarendon Press, 1933. 283 pp.

[Mos16] Daniel Moser. “Magnetic Field Investigation of the PERKEO III Experiment”. Master Thesis. Vienna: Atominstitut der Technischen Universität Wien, 2016.

[Mou+14] X. Mougeot et al. “Corrections for Exchange and Screening Effects in Low-Energy Beta Decays”. In: *Nuclear Data Sheets* 120 (June 2014), pp. 129–132. ISSN: 0090-3752. DOI: 10.1016/j.nds.2014.07.026.

[Mou15] X. Mougeot. “Reliability of usual assumptions in the calculation of β and ν spectra”. In: *Physical Review C* 91.5 (May 18, 2015), p. 055504. DOI: 10.1103/PhysRevC.91.055504.

[MS05] D. Motta and S. Schönert. “Optical Properties of Bialkali Photocathodes”. In: *Nuclear Instruments and Methods in Physics Research Section A: Accelerators, Spectrometers, Detectors and Associated Equipment* 539.1–2 (Feb. 21, 2005), pp. 217–235. ISSN: 0168-9002. DOI: 10.1016/j.nima.2004.10.009.

[Mun+13] D. Mund et al. “Determination of the Weak Axial Vector Coupling $\lambda = g_A/g_V$ from a Measurement of the β-Asymmetry Parameter A in Neutron Beta Decay”. In: *Physical Review Letters* 110.17 (Apr. 23, 2013), p. 172502. DOI: 10.1103/PhysRevLett.110.172502.

[Mun06] Daniela Mund. “Messung der Betaasymmetrie A im Neutronenzerfall”. Dissertation. Heidelberg: Universität Heidelberg, 2006. DOI: DOI:10.11588/heidok.00006576.

[Pat+18] R. W. Pattie et al. “Measurement of the Neutron Lifetime Using a Magneto-Gravitational Trap and in Situ Detection”. In: *Science* 360.6389 (May 11, 2018), pp. 627–632. ISSN: 0036-8075, 1095-9203. DOI: 10.1126/science.aan8895. pmid: 29731449.

[PBC87] E. Pomplun, J. Booz, and D. E. Charlton. “A Monte Carlo Simulation of Auger Cascades”. In: *Radiation Research* 111.3 (1987), pp. 533–552. ISSN: 0033-7587. DOI: 10.2307/3576938. JSTOR: 3576938.

[PCS91] S. T. Perkins, D. E. Cullen, and S. M. Seltzer. *Tables and Graphs of Electron-Interaction Cross Sections from 10 eV to 100 GeV Derived from the LLNL Evaluated Electron Data Library (EEDL), Z = 1 to 100*. UCRL-50400-Vol.31. Lawrence Livermore National Lab, Nov. 1991.

[Pet+16] A. K. Petukhov et al. “A Concept of Advanced Broad-Band Solid-State Supermirror Polarizers for Cold Neutrons”. In: *Nuclear Instruments and Methods in Physics Research Section A: Accelerators, Spectrometers, Detectors and Associated Equipment* 838 (Supplement C Dec. 1, 2016), pp. 33–38. ISSN: 0168-9002. DOI: 10.1016/j.nima.2016.09.023.

[PH71] R. C. Powell and L. A. Harrah. “Nonlinear Responses of Poly(Vinyl Toluene) Plastic Scintillators at High Excitation Doses”. In: *The Journal of Chemical Physics* 55.4 (Aug. 15, 1971), pp. 1878–1884. ISSN: 0021-9606. DOI: 10.1063/1.1676322.

[Phi96] Philipps Scientific. *Octal Linear/Logic Fan-Out NIM Model 748 Datasheet*. 1996. URL: http://www.phillipsscientific.com/pdf/748ds.pdf.

[Plo00] Christian Plonka. “Verbesserung der Lichtauskopplung zur Messung der Neutrinoasymmetrie mit PERKEO II”. Diplomarbeit. Heidelberg: Universität Heidelberg, Jan. 2000. URL: http://www.physi.uni-heidelberg.de//Publications/dipl_plonka.pdf.

[Pös+18] Thomas Pöschl et al. *(To Be Published)*. 2018.

[Pow71] R. C. Powell. “Energy Transfer in Poly(Vinyl Toluene)”. In: *The Journal of Chemical Physics* 55.4 (Aug. 15, 1971), pp. 1871–1877. ISSN: 0021-9606. DOI: 10.1063/1.1676320.

[Pur07] Sanjiv Puri. “Relative Intensities for Li (i = 1–3) and Mi (i = 1–5) Subshell X-Rays”. In: *Atomic Data and Nuclear Data Tables* 93.5 (Sept. 2007), pp. 730–741. ISSN: 0092-640X. DOI: 10.1016/j.adt.2007.05.002.

[Raf15] Lukas Raffelt. *Personal Communication*. E-mail. 2015.

[Raf16] Lukas Michael Raffelt. “Measurement of the Proton Asymmetry (C) in free neutron β-decay with PERKEO III”. Dissertation. Heidelberg: Universität Heidelberg, 2016. DOI: 10.11588/heidok.00022095.

[Raf17] Lukas Raffelt. *Personal Communication*. E-mail. 2017.

[RC54] F. Rohrlich and B. C. Carlson. “Positron-Electron Differences in Energy Loss and Multiple Scattering”. In: *Physical Review* 93.1 (Jan. 1, 1954), pp. 38–44. DOI: 10.1103/PhysRev.93.38.

[Rei99] Jürgen Reich. “Winkelkorrelationen Im Zerfall Polarisierter Neutronen”. Dissertation. Heidelberg: Universität Heidelberg, 1999.

[Roi+18] C. Roick et al. “Electron time-of-flight: A new tool in β-decay spectroscopy”. In: *Physical Review C* 97.3 (Mar. 7, 2018), p. 035502. DOI: 10.1103/PhysRevC.97.035502.

[Roi10] Christoph Roick. “Simulation von Elektronenbahnen in PERKEO III”. Bachelor Thesis. Heidelberg: Universität Heidelberg, 2010.

[Roi12] Christoph Roick. “Untersuchungen zur Elektronendetektion in Neutronenzerfallsexperimenten”. Master Thesis. Heidelberg: Universität Heidelberg, 2012.

[Ros68] Herbert B. Rosenstock. “Energy Transfer in Organic Solids”. In: *The Journal of Chemical Physics* 48.1 (Jan. 1, 1968), pp. 532–533. ISSN: 0021-9606. DOI: 10.1063/1.1667978.

[Rud66] M. Rudemo. “On an Absorption and Emission Problem for Random Walk”. In: *SIAM Journal on Applied Mathematics* 14.6 (Nov. 1, 1966), pp. 1293–1297. ISSN: 0036-1399. DOI: 10.1137/0114103.

[SA08] M. Schumann and H. Abele. “Unrecognized Backscattering in Low Energy Beta Spectroscopy”. In: *Nuclear Instruments and Methods in Physics Research Section A: Accelerators, Spectrometers, Detectors and Associated Equipment* 585.1–2 (Jan. 21, 2008), pp. 88–92. ISSN: 0168-9002. DOI: 10.1016/j.nima.2007.11.016.

[Sac16] Regina Sachsenhauser. “Detektorkalibration Für Präzisions-Beta-Spektroskopie”. Bachelor Thesis. Garching: Technische Universität München, 2016.

[Sai14a] Saint-Gobain Crystals. *Premium Plastic Scintillators Data Sheet (BC-400, BC-404, BC-408, BC-412, BC-416)*. June 2014. URL: http://www.crystals.saint-gobain.com/uploadedFiles/SG-Crystals/Documents/SGC%20BC400-404-408-412-416%20Data%20Sheet.pdf.

[Sai14b] Saint-Gobain Crystals. *Premium Plastic Scintillators Data Sheet (BC-440, BC-440M, BC-448, BC-448M)*. June 2014.

[Sal+87] F. Salvat et al. “Analytical Dirac-Hartree-Fock-Slater screening function for atoms (Z=1–92)”. In: *Physical Review A* 36.2 (July 1, 1987), pp. 467–474. DOI: 10.1103/PhysRevA.36.467.

[Sau15] Heiko Saul. *Personal Communication*. E-mail. Dec. 14, 2015.

[Sau18] Heiko Saul. “Energy Dependence of the Beta Asymmetry in Neutron Decay”. Dissertation. München, Wien: TU München, TU Wien, 2018.

[SB53] Robert K. Swank and Warren L. Buck. “The Scintillation Process in Plastic Solid Solutions”. In: *Physical Review* 91.4 (Aug. 15, 1953), pp. 927–933. DOI: 10.1103/PhysRev.91.927.

[Sch+07] M. Schumann et al. “Measurement of the Neutrino Asymmetry Parameter B in Neutron Decay”. In: *Physical Review Letters* 99.19 (Nov. 8, 2007), p. 191803. DOI: 10.1103/PhysRevLett.99.191803.

[Sch+08] M. Schumann et al. “Measurement of the Proton Asymmetry Parameter in Neutron Beta Decay”. In: *Physical Review Letters* 100.15 (Apr. 14, 2008), p. 151801. DOI: 10.1103/PhysRevLett.100.151801.

[Sch+09] Florian Schneider et al. “Process and Material Properties of Polydimethylsiloxane (PDMS) for Optical MEMS”. In: *Sensors and Actuators A: Physical* 151.2 (Apr. 29, 2009), pp. 95–99. ISSN: 0924-4247. DOI: 10.1016/j.sna.2009.01.026.

[Sch07] Marc Schumann. “Measurement of Neutrino and Proton Asymmetry in the Decay of Polarized Neutrons”. Dissertation. Heidelberg: Universität Heidelberg, 2007. DOI: DOI:10.11588/heidok.00007357.

[Sch15] Schott. *Optical Glass Data Sheets*. July 22, 2015, p. 16.

[Sco74] James H. Scofield. “Exchange Corrections of K X-Ray Emission Rates”. In: *Physical Review A* 9.3 (Mar. 1, 1974), pp. 1041–1049. DOI: 10.1103/PhysRevA.9.1041.

[SD79] M. P. Seah and W. A. Dench. “Quantitative Electron Spectroscopy of Surfaces: A Standard Data Base for Electron Inelastic Mean Free Paths in Solids”. In: *Surface and Interface Analysis* 1.1 (Feb. 1, 1979), pp. 2–11. ISSN: 1096-9918. DOI: 10.1002/sia.740010103.

[Sha71] R. T. Shann. “Electromagnetic Effects in the Decay of Polarized Neutrons”. In: *Il Nuovo Cimento A (1965-1970)* 5.4 (Oct. 1, 1971), pp. 591–596. ISSN: 1826-9869. DOI: 10.1007/BF02734566.

[Sim+09] M. Simson et al. “Measuring the Proton Spectrum in Neutron Decay—Latest Results with aSPECT”. In: *Nuclear Instruments and Methods in Physics Research Section A: Accelerators, Spectrometers, Detectors and Associated Equipment*. Particle Physics with Slow Neutrons 611.2 (Dec. 1, 2009), pp. 203–206. ISSN: 0168-9002. DOI: 10.1016/j.nima.2009.07.068.

[Sir67] A. Sirlin. “General Properties of the Electromagnetic Corrections to the Beta Decay of a Physical Nucleon”. In: *Physical Review* 164.5 (Dec. 25, 1967), pp. 1767–1775. DOI: 10.1103/PhysRev.164.1767.

[SJ49] W. A. Shurcliff and R. Clark Jones. “The Trapping of Fluorescent Light Produced within Objects of High Geometrical Symmetry”. In: *Journal of the Optical Society of America* 39.11 (Nov. 1, 1949), p. 912. ISSN: 0030-3941. DOI: 10.1364/JOSA.39.000912.

[SM58] E. C. G. Sudarshan and R. E. Marshak. “Chirality Invariance and the Universal Fermi Interaction”. In: *Physical Review* 109.5 (Mar. 1, 1958), pp. 1860–1862. DOI: 10.1103/PhysRev.109.1860.2.

[Ste+13] Nicholas Steinbrink et al. “Neutrino Mass Sensitivity by MAC-E-Filter Based Time-of-Flight Spectroscopy with the Example of KATRIN”. In: *New Journal of Physics* 15.11 (2013), p. 113020. ISSN: 1367-2630. DOI: 10.1088/1367-2630/15/11/113020.

[Ste57] E. J. Sternglass. “Theory of Secondary Electron Emission by High-Speed Ions”. In: *Physical Review* 108.1 (Oct. 1, 1957), pp. 1–12. DOI: 10.1103/PhysRev.108.1.

[Tan+18] M. Tanabashi et al. “Review of Particle Physics”. In: *Physical Review D* 98 (Aug. 6, 2018), p. 030001. DOI: 10.1103/PhysRevD.98.030001.

[Vir17] Romain Virot. “Development of Calibration Sources for Proton Spectroscopy”. Dissertation. Grenoble: Université Grenoble Alpes, 2017.

[Vol+66] R. Voltz et al. “Influence of the Nature of Ionizing Particles on the Specific Luminescence of Organic Scintillators”. In: *The Journal of Chemical Physics* 45.9 (Nov. 1, 1966), pp. 3306–3311. ISSN: 0021-9606. DOI: 10.1063/1.1728106.

[Wan13] Xiangzun Wang. “The Free Neutron β-Decay: A Powerful Tool for the Investigation in Particle Physics”. Dissertation. München: Technische Universität München, 2013. URL: http://nbn-resolving.de/urn:nbn:de:bvb:91-diss-20130320-1121297-0-0.

[Wer09] Dominik Werder. “Development and Characterization of a Pulsed Beam for Neutron Decay Experiments”. Diplomarbeit. Heidelberg: Universität Heidelberg, 2009.

[Wil07] Daniel Wilkin. “Aufbau eines Kollimationssystems und Entwicklung eines Scanners für das Spektrometer PERKEO III”. Diplomarbeit. Heidelberg: Universität Heidelberg, 2007.

[Wil82] D. H. Wilkinson. “Analysis of Neutron β-Decay”. In: *Nuclear Physics A* 377.2 (Mar. 22, 1982), pp. 474–504. ISSN: 0375-9474. DOI: 10.1016/0375-9474(82)90051-3.

[Wu91] Xiaolin Wu. “An Efficient Antialiasing Technique”. In: *Proceedings of the 18th Annual Conference on Computer Graphics and Interactive Techniques*. SIGGRAPH ’91. New York, NY, USA: ACM, 1991, pp. 143–152. ISBN: 978-0-89791-436-9. DOI: 10.1145/122718.122734.

[Zie14] Carmen Regina Ziener. “Das Spektrometer PERC zur Untersuchung des Neutron-Beta-Zerfalls”. Dissertation. Heidelberg: Universität Heidelberg, 2014. DOI: 10.11588/heidok.00017949.

[ZZB10] James F. Ziegler, M. D. Ziegler, and J. P. Biersack. “SRIM – The Stopping and Range of Ions in Matter (2010)”. In: *Nuclear Instruments and Methods in Physics Research Section B: Beam Interactions with Materials and Atoms*. 19th International Conference on Ion Beam Analysis 268.11 (June 1, 2010), pp. 1818–1823. ISSN: 0168-583X. DOI: 10.1016/j.nimb.2010.02.091.

Acknowledgment

At this point I would like to thank those people who supported me in the context of this work:

- Bastian Märkisch who supervised and supported this work and continues in the tradition of giving students the freedom to follow their own ideas.
- Stefan Schönert for accepting to review this work.
- Ulrich Schmidt for being my mentor and sharing his wide knowledge whenever time and presence allows.
- Torsten Soldner who helped with his expertise about cold neutron and proton experiments over the whole beam time and always kept an objective attitude towards our measurements.
- Gertrud Konrad who tried to keep the working moral in Grenoble up and kept and keeps an eye on probably all aspects of our measurement.
- Prof. Dubbers for entrusting me with the data taking of the time of flight measurements and giving insight into his pragmatic way of doing experiments.
- Wolfgang Schott for his help and enthusiasm about the proton test setup.
- Heiko Saul for not refusing any of our many ideas and instead pushing them towards world changing theories and methods.
- Michi Klopf with whom I would polish meters and meters of Field Degrader electrodes at any time again.
- Lukas Raffelt for keeping on with the measurement despite all doubts.
- Willi Mach for his cheerful attitude.
- Daniel Moser who decided to keep on working on PERKEO III although he had insight into the experiment before starting his Masters thesis.
- "My" Bachelor students Jascha Grabowski, Benjamin Daiber and Karina Bernert for their motivation for their projects. Especially Karina, who shared my office and continues to work with us.
- Max Lamparth who took over the remaining parts of improvement of ELISE and is heading towards actual measurements.
- Camille Theroine, whom I could share the office in Munich with, Romain Virot and Felix Rosenau who certainly contributed to the fun of our stay in Grenoble.
- Despite seeming far in history, the ANP group at the PI in Heidelberg for the familiar atmosphere, which was always present.
- Kathrin Lehmann, Ina Lommatzsch and Jens Klenke for giving me membership in their lunch group.
- All people of E18 for socially integrating us in their chair.
- Special thanks to Matteo Bartolini, Karina Bernert and Daniel Moser for proofreading this work.

Just as much gratitude I want to express to those who supported me despite this thesis:

- Meinen Eltern und Großeltern möchte ich dafür danken, mich in allen Lebenslagen zu unterstützen und mich nach meinen Entscheidungen zu fragen, ohne sie zu hinterfragen.
- Merci à François, qui m'avait proposé d'être son colocataire une autre fois et qui est le meilleure hôte que l'on peut imaginer.
- Merci aussi aux kayak-poloïstes de Grenoble qui m'ont permit d'avoir une place dans cette merveilleuse équipe, sachant que je partira après la saison. Bisous !
- Und vor allem danke ich Ksenia, die mir liebevoll zur Seite steht und Verständnis selbst für über ein Jahr Strahlzeit gezeigt hat.